Aspects of Highly-Entangled Quantum Matter:
From Exotic Phases, to Quantum Computation, and Dynamics

by

Ksheerasagar Vijay

A.B., Princeton University (2013)

Submitted to the Department of Physics
in partial fulfillment of the requirements for the degree of

Doctor of Philosophy

at the

MASSACHUSETTS INSTITUTE OF TECHNOLOGY

June 2018

© Massachusetts Institute of Technology 2018. All rights reserved.

Signature redacted

Author.......................................   .....
Department of Physics
May 21, 2018

Signature redacted

Certified by...
Liang Fu
Associate Professor of Physics
Thesis Supervisor

Signature redacted

Accepted by................................   ...
Scott A. Hughes
Interim Associate Head of Physics

MITLibraries

DISCLAIMER NOTICE

Due to the condition of the original material, there are unavoidable flaws in this reproduction. We have made every effort possible to provide you with the best copy available.

Thank you.

The images contained in this document are of the best quality available.

Aspects of Highly-Entangled Quantum Matter:
From Exotic Phases, to Quantum Computation, and Dynamics

by

Ksheerasagar Vijay

Submitted to the Department of Physics
on May 21, 2018, in partial fulfillment of the
requirements for the degree of
Doctor of Philosophy

Abstract

We explore three incarnations of highly-entangled quantum matter: as descriptions of exotic, gapped phases in three spatial dimensions, as resources for fault-tolerant quantum computation, and as the by-product of the unitary evolution of a quantum state, on its approach to equilibrium. In Part I, we study quantum information processing in platforms hosting Majorana zero modes. We demonstrate that certain highly-entangled states may be engineered in arrays of mesoscopic topological superconducting islands, and used for fault-tolerant quantum computation. We then discuss measurement-based protocols for braiding Majorana zero modes and detecting their non-Abelian statistics in on-going experiments on proximitized, semiconductor nanowires, before proposing new families of error-correcting codes for fermionic qubits, along with concrete realizations. In Part II, we study gapped, three-dimensional phases of matter with sub-extensive topological degeneracy, and immobile point-like excitations – termed "fractons" – which cannot be moved without nucleating other excitations. We find two broad classes of fracton phases in which (i) composites of fractons form topological excitations with reduced mobility, or (ii) all topological excitations are strictly immobile. We demonstrate a duality between these phases and interacting systems with global symmetries along sub-systems, and use this to find new fracton phases, one of which may also be obtained by coupling an isotropic array of two-dimensional states with Z_2 topological order. We introduce a solvable model in which the fracton excitations are shown to carry a protected internal degeneracy, which provides a generalization of non-Abelian anyons in three spatial dimensions. In Part III, we investigate the dynamics of operator spreading and entanglement growth in quantum circuits composed of random, local unitary operators. We relate quantities averaged over realizations of the circuit, such as the purity of a sub-system and the out-of-time-ordered commutator of spatially-separated operators, to a fictitious, classical Markov process, which yields exact results for the evolution of these quantities in various spatial dimensions. Operator spreading is ballistic, with a front that broadens as a dimension-dependent power-law in time. In this setting, we also map the dynamics of entanglement growth in one dimension to the stochastic growth of an interface and to the Kardar-Parisi-Zhang equation, which leads to a description of entanglement dynamics in terms of an evolving "minimal cut" through the quantum circuit, and provides heuristics for entanglement growth in higher-dimensions.

The material presented here is based on Ref. [1, 2, 3, 4, 5, 6, 7, 8, 9, 10]. Ref. [11, 12] are not discussed in this thesis, but were completed during my time at MIT.

Thesis Supervisor: Liang Fu
Title: Associate Professor of Physics

Acknowledgments

My time at MIT has been intellectually stimulating and exciting, and it is difficult for me to believe that the past five years have so quickly come to a close. It is a pleasure to thank the many people whose support made my work possible, and my time at MIT incredibly enjoyable.

First, I am grateful beyond words to my advisor, Liang Fu. His enthusiasm for research is infectious, and I have learned a great deal under his mentorship over the past five years. I am thankful for the flexibility that he gave me to explore research problems, and for his eagerness to discuss a variety of topics at length. I will fondly remember our many engaging conversations in his office, and how the process of reconciling our often complementary perspectives on problems led us to fascinating research questions. Working with Liang has been a humbling experience. I want to thank him for teaching me to believe in the simplicity of significant ideas, the importance of maintaining a broad range of research interests, and for being an invaluable mentor and friend. I sincerely hope that we continue to stay in touch and collaborate in the indefinite future.

I am deeply indebted to many others at MIT. I am incredibly grateful to Jeongwan Haah for our thought-provoking conversations over the past few years, and for his friendship. Indeed, a large portion of this thesis would have been impossible without these discussions, in which I learned quite a bit of math and quantum information, and which revealed glimpses of Jeongwan's quiet genius. I thank him for teaching me to prioritize thinking methodically and precisely about difficult research questions. Second, I absorbed a large amount of physics from Adam Nahum, who has been one of the sharpest minds that I have had the privilege to encounter. Conversations with Adam are intellectual marathons that I thoroughly enjoy, and I learned much from watching him triangulate interesting theoretical predictions from established results. I am fortunate to count him as a collaborator, and as a wonderful friend.

Other students and postdocs at MIT, especially Tim Hsieh, Jonathan Ruhman, Michael Pretko, Liujun Zhou, Vlad Kozii, and Huitao Shen, have significantly shaped my intellectual trajectory; I have had the privilege of collaborating with Tim and Jonathan on projects. I am fortunate to count still others – my former officemate Jörn Venderbos, as well as Lucile Savary and Brian Skinner – as great friends. I also want to thank the professors in the condensed matter theory group for being a valuable source of intellectual inspiration. I particularly enjoyed the stimulating lunch conversations in the department, which provided a fantastic opportunity to learn new physics from Senthil, Patrick, and Xiao-Gang, and to tap into their encyclopedic knowledge. I hope to return for lunch often, to continue my edification.

I owe my fascination with theoretical physics to my experience at Princeton, and I am deeply thankful for my time there. As an undergraduate, I had the privilege of working with Duncan Haldane, and my interest in condensed matter physics was borne from multi-hour conversations with him, of which I only understood a small fraction in real-time. However, I distinctly recall being captivated by what I understood, and deeply inspired by Duncan's dedication. I am certain that my intellectual life would be different, had he not been so generous with his time.

My family has made me all that I am: my parents – Sheela Vijay and Vijay Pitchumani

– have provided incredible emotional and moral support throughout my life, and their lives inspire me to show strength of character. I thank them for instilling in me a belief in the value of hard work, without feeling entitled to the fruits of my labors, or having undue concern for the consequences of my actions that lie outside of my control. This thesis is dedicated to them. My brother, Madhu, has been an incredible friend; I fondly remember our many dinners during his time at Harvard, and I have learned much from his insightfulness, intelligence, and generosity of spirit. My wife, Ginny, is my best friend, and has been my pillar of strength during the past five years. I am, in the words of Bertrand Russell, occasionally "prone to the malady of the introvert, who, with the manifold spectacle of the world spread out before him, turns away and gazes only upon the emptiness within" [13]; I thank my wife for her love and remarkable understanding, and for being the one to help me see the "manifold spectacle" in challenging times.

Many of my friends began shaping me before my time at MIT, and an unmeasurable part of my intellectual journey will always be attributable to their influence. I want to thank Will Rafey, Evan Larson, Erik Johnson, Akhil Reddy, and Amaresh Sahu, for their incredible friendship, for excelling in their own endeavors, and as a consequence, for inspiring me and motivating me to challenge myself. I am fortunate that Will and I have overlapped at MIT, and his proximity has made the past few years significantly more enjoyable.

Finally, I want to thank our cat, Boo. His callous indifference to my research is regularly on display when he sits on my laptop and demands affection; worse still, he has conditioned me to find this behavior endearing. I do enjoy his company very much, especially when I am working in the late hours of the night, and I thank him for it.

Cambridge, MA
May 17, 2018

Contents

List of Figures

13

17

20

24

List of Tables

28

Chapter 1

Introduction

Quantum mechanics is replete with strange phenomena that defy classical Newtonian intuition. At the heart of quantum "weirdness" is entanglement, a correlation in the density matrix of a quantum system which is experimentally manifest when local measurements affect subsequent measurement outcomes in a spatially distant region. Einstein, Podolsky, and Rosen (EPR) originally objected to this feature of quantum theory as a bizarre "action-at-a-distance" that violated a natural principle of locality – that spatially well-separated phenomena are relatively independent – and appeared to make possible instantaneous communication [20]. EPR's criticisms revealed a conceptual lapse in early understandings of the relationship between quantum physics and information, which took decades to resolve. Since that time, however, quantum entanglement has remained an intellectual point of contact between theoretical physics and information science, and at the forefront of deep questions in both disciplines.

In recent years, the exploration of the landscape of entangled quantum matter has attracted significant research interest. For the condensed matter physicist – concerned with cateloguing emergent phenomena in quantum many-body systems – the patterns of entanglement in the sub-atomic world reveal certain striking macroscopic properties of quantum matter, while the growth of entanglement sheds light on the dynamics of a closed quantum many-body system on its approach to a steady-state, equilibrium configuration. For the quantum information scientist – interested in the scale-up of controllable quantum phenomena – entanglement provides a resource for encoding and processing information in ways that are intractable on a classical computer, and quantifies the difficulty in classically simulating a quantum system.

The goal of this thesis is to explore the boundaries of our understanding of complex quantum states, the "entanglement frontier" [21], in order to uncover new equilibrium phases of matter, dynamical phenomena, and protocols for fault-tolerant quantum computation. We remain somewhat agnostic to the background of the reader, since the questions that we tackle sit at the intersection of condensed matter physics and quantum information science. As a result, this thesis will attempt to be self-contained in its presentation of both subjects.

Before embarking on our journey, we must define a complex quantum state and elaborate on the specific motivations for our study. First, we identify our domain of exploration: what

are the complex quantum states of interest? Our answer is defined by practical considerations, and a dose of optimism. Even a complex quantum state should be reasonably easy to prepare if it is to be used for quantum information processing, by starting from a classical, direct-product state (e.g. a ferromagnet) which has a low degree of entanglement. If this state is, instead, the ground-state of a quantum many-body system, then the degree of entanglement of a sub-system should be quantifiably small, even if the state is far from being a product state[1].

These considerations motivate a definition of the quantum states of interest that appeals to the ease of quantum state preparation [21]. In this thesis, a highly-entangled state will be one that can be obtained from a direct-product state by the unitary time-evolution generated by a local Hamiltonian, and for a time that scales polynomially in the system size. This definition encompasses a wide range of states, from ones that have an extensive entanglement entropy, to the ground-states of topologically-ordered phases of matter. A particularly simple example of a state that is highly-entangled according to this definition, is a Schrödinger cat state of spins, i.e. $|\psi\rangle \sim |\downarrow\downarrow \cdots \downarrow\rangle + |\uparrow\uparrow \cdots \uparrow\rangle$, for which the von Neumann entanglement entropy for any bi-partitioning of the system – even spatially non-local partitions – is non-zero.

Our definition is also quite restrictive. Indeed, the unitary evolution of a product state by a local, time-dependent Hamiltonian for a time scaling polynomially in the system size is known to only cover a fraction of the entire space of states of the system which is exponentially small in the Hilbert space dimension [22][2]. Put simply, Hilbert space is a vast, uncharted wilderness, but the pragmatist need only concern themselves with a comparatively small patch of real-estate. Rich equilibrium and dynamical phenomena abound here, and if our exploration is fruitful, we may yet count ourselves "king[s] of infinite space" [23].

The theoretical impetus to study highly-entangled states of this form has emerged in recent decades, and we now present the specific reasons for our undertaking:

1.0.1 Quantum Computation and Error-Correction

Highly-entangled states of matter provide a powerful resource for fault-tolerant quantum computation. Theoretically, a quantum computer would take advantage of quantum interference to perform certain computations more efficiently than a classical computer. Shor's algorithm for factorizing prime numbers [24] provides a celebrated example. A quantum computer would also speed up classical algorithms for searching an unsorted database [25] and for solving certain constrained satisfaction problems that are NP-complete [26]. For the physicist, a quantum computer would be useful for simulating the real-time dynamics and equilibrium properties of model quantum systems.

---

[1]More precisely, in the ground-state of a gapped quantum system, the von Neumann entanglement entropy should scale with the area of the boundary of the sub-system of interest – so-called "area-law" behavior.

[2]The proof of this statement follows from a simple parameter-counting argument, by comparing the surface area of the Bloch sphere for an L-spin system with the states that can be reached by local, unitary circuits with depth scaling polynomially in L.

Performing a successful, long-term quantum computation (simulation) requires accounting for errors in implementing gate operations, and in spurious noise from the environment. Since it is impossible to "clone" an unknown quantum state, robust information storage requires preserving a *single* instance of a qubit, making fault-tolerant quantum computation extremely challenging. The preservation of quantum information requires designing quantum codes, which map the relatively few states of a qubit of interest (the logical qubit), into the states of a much larger Hilbert space, often referred to as the codespace. Errors are generated when a coupling between the system and the environment leads to the unwanted unitary evolution of the logical qubit outside of the codespace.

The redundant encoding of the logical qubit permits us to leverage the entanglement between degrees of freedom in the larger Hilbert space, in order to recover the original state of the qubit *without* disturbing the encoded information. This protocol for "detecting without disturbing" leads to a precise criterion for the correctability of an error: a quantum error-correcting code with a codespace spanned by the orthonormal states $\{|\psi_i\rangle\}$ can recover from a set of errors, as specified by a collection of unitary operators $\{U_a\}$ acting on the logical qubit, iff [27]

$$\langle \psi_i \,|\, U_a^\dagger U_b \,|\, \psi_j \rangle = C_{ab}\delta_{ij} \tag{1.1}$$

where the matrix C_{ab} is independent of the states in the codespace. Colloquially, a correctable error process is one that can be undone without revealing the state of the logical qubit.

Successful quantum codes require that the states in the codespace are highly entangled. For example, consider a code in which some logical qubits are encoded in the states of m physical qubits. If the code can recover from an arbitrary n-qubit error – an error process where up to n of the physical qubits are affected by spurious unitary evolution – then any n-qubit reduced density matrix must be *independent* of the state of the logical qubit; this requires, of course, that the states in the codespace exhibit an intricate pattern of entanglement, since sufficiently non-local observations are required in order to interfere with encoded information.

On the other hand, the monogamy of entanglement also provides a limitation on the performance of quantum codes. From the criterion for correctability (1.1), a code that can recover from arbitrary n-qubit errors, can recover from $2n$-qubit "erasure" errors, where $2n$ *known* physical qubits in the system are replaced by spins in a trivial product state [27]. If $2n \geq m/2$, then such a code would be able to *clone* an arbitrary state in the codespace, which we know to be impossible. This means, for example, that the smallest encoding of a single logical qubit that can also recover from single-qubit errors, is into the Hilbert space of five physical qubits [28]. Such an encoding indeed exists, and the states in the codespace of the five-qubit code [29] are particularly remarkable, since they are *maximally entangled* for any spatial bi-partitioning.

It is important to determine how highly-entangled code states can be created, and how quantum error-correcting codes can be implemented in experimental platforms. Quantum computation in Fermi systems has also received recent interest, since the fermion parity can form the basis for a protected qubit. Are there differences between error-correcting codes in Fermi and

31

Bose systems? What are the natural ways to build a fault-tolerant quantum computer in this setting? We will provide partial answers to these questions, with a focus on physical platforms that host "Majorana zero modes", in Part I.

1.0.2   Equilibrium Phenomena: Highly-Entangled Quantum Phases

Highly-entangled quantum states provide a useful playground for uncovering exotic equilibrium phenomena in quantum many-body systems. Phases of matter are defined by the expectation values of measurable quantities, and, as a consequence, by their response to external probes. A conventional phase of matter is one in which a *local* order parameter develops an expectation value, thereby breaking a manifest symmetry of the system. This "symmetry-breaking" paradigm, as introduced by Lev Landau, has led to the categorization of an impressive panoply of phases, from classical phenomena such as ferromagnetism to fundamentally quantum-mechanical ones such as superfluidity.

The discovery of the fractional quantum Hall effect dramatically changed the landscape of possible quantum phases. In 1982, Tsui, Stormer, and Gossard observed that a two-dimensional electron gas subject to a strong magnetic field at temperatures of a few degrees Kelvin exhibited a Hall conductance which was robustly quantized to 1 part in 10^5 in rational fractional multiples of e^2/h [30]. Trial wavefunctions for this exotic state were soon proposed [31, 32], from which it was argued that the elementary, gapped quasiparticles of this state carried fractional electrical charge. As a striking consequence, the ground-states of the quantum Hall fluid at fractional filling $\nu = p/q$ were predicted to give rise to a q-fold degeneracy on the torus [33], and no *local* observables could distinguish the degenerate ground-states. This phenomenology gave rise to a paradigm shift: distinct fractional quantum Hall states, each a different phase of matter, were not distinguished by symmetries of the electron gas, in apparent violation of Landau's criterion.

In decades since, a zoo of these "topological phases", gapped states of matter in two spatial dimensions which are not characterized by broken symmetries, have been explored. We review this theoretical progress before proceeding into the unknown. First, gauge theory provides a framework for understanding a large class of topological phases, from quantum Hall states to quantum spin liquids [34, 35, 33, 36, 37, 38, 39, 19, 40]. The fractional statistics of the gapped topological excitations [41, 42], or anyons, arises from the Aharanov-Bohm phase of a charge moving around a flux. The origin of a non-local order parameter is similarly understood; the effective potential between gapped charges determines whether these are (de-)confined excitations, and this requires measuring the scaling of the expectation value of a gauge-invariant, non-local operator – the Wilson loop – with its size.

More generally, the low-energy effective theory for any gapped, two-dimensional topological phase is a topological quantum field theory (TQFT), and studies of the algebraic structure behind TQFT's – modular tensor categories – have led to a near-complete understanding of two-dimensional topological phases. Consistency conditions between the universal data in a
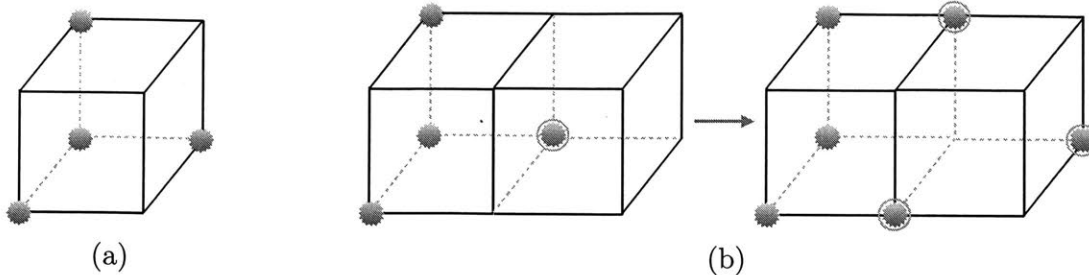
Figure 1-1: **Excitations in Haah's Code:** One type of gapped excitation in Haah's code lives on the sites of a dual cubic lattice. The excitation can only be created in clusters of four, in the geometric arrangement shown in (a). A single excitation cannot be moved without nucleating other gapped excitations, as indicated in (b). As a result, separating the excitations shown in (a) by a distance ℓ requires overcoming an intermediate energy barrier that grows as $\log \ell$.

topological phase, including quasiparticle content, braiding statistics, and fusion rules, lead to algebraic equations that determine the possible phases, even ones that lie outside of conventional gauge theory [43, 44]. Due to the presence of fractionalized excitations and the absence of local observables that can distinguish degenerate ground-states, topological phases exhibit a pattern of entanglement that cannot be generated from a product-state with a finite-depth quantum circuit [45]. This is quantifiably manifest in a sub-leading correction to the area-law behavior of the von Neumann entanglement entropy of an appropriate region, which is *universal* for a given topological phase, and a function of the quantum dimension of the fractionalized excitations.

Exactly solvable models have provided a powerful tool for studying these highly-entangled states of matter, and in the development of fault-tolerant architectures for quantum computation. Importantly, these exactly solvable models provide an invaluable foothold for beginning to explore similarly exotic phases of matter in *three* spatial dimensions. Here, very little is understood about gapped phases that lack a local order parameter, apart from the deconfined phases of lattice gauge theories with a finite gauge group, which typically have gapped, point-like charges and loop-like flux excitations; the former are restricted to have Fermi or Bose statistics. Even here, however, what constitutes a "universal" set of data that characterizes a three-dimensional topological phase is unknown.

Remarkable progress was made by Haah [46], who discovered a previously unknown phase of matter in a solvable model for interacting, spin-1/2 degrees of freedom on the cubic lattice. The model describes the zero correlation-length limit of a stable, gapped phase with the following properties, which are robust to perturbations:

1. The ground-state exhibits a *sub-extensive* degeneracy on the torus, and all of the degenerate ground-states are locally indistinguishable. Specifically, the ground-state degeneracy (D) on an $L \times L \times L$ cubic lattice with periodic boundary conditions is given by the

33

following expressions for the indicated values of L [47]:

$$\log_2 D = \begin{cases} 2 & L = 2^n + 1 \text{ or } L = 2^{2n+1} - 1 \\ 4L - 2 & L = 2^n \\ 4L - 10 & L = 4^n - 1 \end{cases} \tag{1.2}$$

with the integer $n \geq 1$.

2. There are two types of gapped, point-like excitations that are created by acting with a local operator on the ground-state. These excitations may only be created in clusters of four, and in particular geometric arrangements. One type of excitation lives on the sites of a dual cubic lattice, and can only be created in the arrangement shown in Fig. 1-1a. As a consequence, these point-like excitations are immobile; attempting to move any collection of them with a local operator nucleates other gapped excitations, as shown in Fig. 1-1b. It is only possible to separate the four excitations in Fig. 1-1a by a distance ℓ, by overcoming an intermediate energy barrier that scales as $E \sim \log \ell$.

While Haah's code is only a stable phase at zero temperature, the degenerate ground-states of the code can be used to robustly encode qubits at finite temperature. When Haah's code is coupled to a bath at inverse temperature β, there is a known algorithm for correcting thermally-induced errors such that the lifetime of an encoded qubit scales as $t \sim \exp(c\beta^2 \Delta^2)$ [48] where Δ is the energy cost for creating the point-like excitations shown in Fig. 1-1a, and c is an $O(1)$ constant. This should be contrasted with more conventional topological phases with point-like excitations in d spatial dimensions, in which the lifetime of an encoded qubit should only grow exponentially $t \sim \exp(c\beta\Delta)^3$, as is known to be the case for the two-dimensional toric code [49].

A number of questions remain about Haah's code, and the possible phases of matter in three-dimensional quantum systems that lack a local order parameter. What can solvable models tell us about this spectrum of phases, and is Haah's code an isolated phenomenon? What is the relation between two-dimensional topological phases and these exotic states? We will explore systematic ways to understand these states of matter, and other related questions in Part II.

1.0.3 Dynamical Phenomena: Propagation of Quantum Information

While the von Neumann entanglement entropy encodes universal properties of quantum ground states, the dynamics of the entanglement are far less understood. Since the entanglement entropy is non-local and is not conserved, its dynamics are distinct from energy, charge, or other local densities. Traditional many-body tools therefore do not provide much intuition about how

---

[3]For point-like excitations that can be created in pairs, the density of thermally excited excitations is $\sim \exp(-2\beta\Delta)$, so the distance between excitations will be $\ell_{\text{sep}} \sim O(\exp(2\beta\Delta/d))$ in d dimensions. Recovery of the initial state becomes difficult at a time when the excitations have diffused over a length $\ell_{\text{diff}} = \sqrt{Dt} \sim \ell_{\text{sep}}$, which leads to the quoted estimate of the lifetime.

entanglement spreads with time, for example, after a quantum quench, when a "sudden" change is made to the Hamiltonian.

If a many-body system is initialized in a state with low entanglement, unitary dynamics will typically generate entanglement between increasingly distant regions. The effectively irreversible growth of the von Neumann entanglement entropy is an essential part of the thermalization of a quantum system, when local observables relax to the their thermal expectation values at a temperature set by the energy density of the state. Entanglement growth has been addressed in diverse contexts ranging from conformal field theory [50, 51, 52, 53], to integrable [54, 55, 56, 57, 58, 59, 60], non-integrable [61, 62, 63, 64], and strongly disordered spin chains [65, 66, 67, 68, 69, 70, 71]. Entanglement growth is also of practical importance as the crucial obstacle to classical simulations of quantum dynamics using matrix product states or the density matrix renormalization group (DMRG) [72]. The entanglement entropy, and even its time dependence, is beginning to be experimentally measurable in cold atom systems [73, 74, 75]. For integrable 1D systems and rational CFTs, there is an appealing heuristic picture for entanglement growth following a quench in terms of spreading quasiparticles [50, 52]. However this picture does not apply to general interacting systems [52, 53, 76, 77].

Apart from entanglement growth, unitary evolution also gives rise to an effectively irreversible process, in which initially locally accessible quantum information becomes practically irretrievable. The timescale over which this "scrambling" of quantum information occurs is parametrically smaller than the time for thermalization[4]. Scrambling may be quantified by certain *out-of-time-ordered* correlation functions, such as the out-of-time-ordered commutator

$$C_\beta(t) \equiv -\frac{1}{2} \left\langle [V(t), W(0)]^2 \right\rangle_\beta \qquad (1.3)$$

with the expectation value taken at inverse temperature β. This correlation function effectively measures the spreading of the Hermitian operator $V(t) = e^{-iHt}V(0)e^{iHt}$ under Heisenberg evolution. For a generic choice of spatially separated operators, (1.3) will grow in time, before reaching an appreciable $O(1)$ value at the scrambling time (t_s), when the operator $V(t)$ has become significantly spatially de-localized. Importantly, the size of a growing operator – as measured by (1.3) – can exhibit ballistic growth, even when all conserved quantities in the system are transported diffusively.

There are several important reasons to study these out-of-time-ordered correlation functions. First, the scrambling time quantifies the speed at which unitary dynamics proceeds. In a system with $\mathcal{N}$ degrees of freedom (e.g. spins), and with a typical strength of local interactions J, the scrambling time for a generic choice of local operators that are separated by a distance $O(\mathcal{N})$

---

[4]This point – if not already clear to the reader – will be elaborated upon in Part III.

exhibits a wide range of behavior. Representative examples are given below:

$$t_s \sim \begin{cases} (J\mathcal{N})^{-1} & \text{Random matrix theory [12]} \\ \beta \log \mathcal{N} & \text{Chaotic system at low temperatures} \\ J^{-1}e^{\mathcal{N}/\xi} & \text{Many-body localized phase (1d) [78]} \end{cases} \tag{1.4}$$

A Hamiltonian chosen from a random matrix ensemble scrambles the fastest [12], due to the non-local nature of a typical interaction. Out-of-time-ordered correlations are also of interest, since their decay is believed to give rise to bounds on scattering rates in quantum systems and, by extension, on the diffusion constants for conserved quantities [79]. Finally, the infinite-temperature behavior of $C_\beta(t)$, after averaging over the choice of operators appearing in (1.3) is related to the level statistics of a Hamiltonian, and to the complexity of the unitary evolution generated by an ensemble of Hamiltonians [80].

Since operator spreading and entanglement growth are important dynamical phenomena that characterize quantum systems, it is important to study toy models in which their dynamics can be calculated precisely. Does this lead to heuristics for the growth of these quantities that can be applied to a generic many-body system? These questions will be addressed in Part III.

1.0.4 Plan of this Thesis

Motivated by this discussion, we embark on our exploration of the entanglement frontier. In this thesis, we will study new phases of matter in exactly solvable models, realize entangled states in physical platforms that can be used for fault-tolerant quantum computation, and find heuristics for the dynamics of quantum information and entanglement in our studies of toy models for chaotic quantum systems.

In Part I, we study quantum information processing in platforms with Majorana zero modes, where the fermion parity is used to encode logical qubits. We first demonstrate a protocol for engineering an entangled state of fermions in an array of mesoscopic, topological superconductor islands that can be used for fault-tolerant, universal quantum computation [1, 2]. To complement this long-term goal, we propose a measurement-based scheme for performing braiding operations on Majorana zero modes and for detecting their non-Abelian statistics without moving or hybridizing them [3]. Finally, we consider the problem of quantum error-correction in Fermi systems, which requires error-correcting codes that can recover from fermion parity-violating (quasiparticle poisoning) and parity-conserving errors. We relate fermion codes to weakly self-dual *classical* error-correcting codes, and use this mapping to find the shortest fermion code, and to construct translationally-invariant codes and their physical realizations [4].

In Part II, we turn our attention to "fracton" topological phases [7], gapped, three-dimensional phases of matter such as Haah's code, that are characterized by immobile, point-like excitations (fractons), and a sub-extensive topological degeneracy. Importantly, this phenomenology

emerges in translationally-invariant lattice models, so the immobility of the fracton excitations is not due to the presence of a potential landscape, but rather, to the intricate patterns of entanglement in the ground-state. Our exploration reveals three classes of unconventional, gapped quantum phases that emerge in solvable models in three spatial dimensions:

Type I fracton phases have immobile (fracton) excitations, but composites of these form topological excitations that exhibit dimensionally-reduced mobility. For example, certain composite excitations are restricted to move in two spatial dimensions, and exhibit fractional statistics. In certain phases, the fractons can carry a protected internal degeneracy.

Type II fracton phases, such as Haah's code [46] have fracton excitations that appear at the corners of fractal operators. All topological excitations are strictly localized and there are no mobile topological quasiparticles.

The third type of unconventional phase is one in which there are gapped quasiparticle excitations that have reduced mobility, but there are no stricly immobile, fracton excitations.

In Part II, we first construct a family of exactly solvable models of interacting fermions in $d \geq 3$ spatial dimensions that have a hierarchy of point-like excitations with dimensionally reduced mobility, and sub-extensive topological degeneracy [6]. We proceed to demonstrate that fracton topological phases are dual to interacting quantum systems with global symmetries along lower-dimensional sub-systems. We use this duality between symmetry-breaking states and fracton topological order to find new fracton phases in spin systems [7]. We show that one of these – the "X-Cube" model – may be obtained by coupling an isotropic array of states with Z_2 topological order, which leads, in turn, to a natural Z_N generalization of this fracton phase [5]. We conclude by presenting a solvable model for a fracton topological phase in which immobile topological excitations carry a protected internal degeneracy. This provides a previously unknown generalization of non-Abelian anyons – which arise in two-dimensional topological phases – to three spatial dimensions [8].

Commutative algebra provides an indispensable tool for deriving the results in Part II. Solvable models rapidly become difficult to study, since we must show (*i*) that the ground-state lacks a local order parameter and (*ii*) that certain gapped excitations are truly immobile; even if (*i*) is true, it is dangerously easy to convince oneself of (*ii*) in situations when it is patently false[5]. A purely algebraic representation also aids in efficiently searching the space of solvable models for exotic phenomena. As we discuss, properties of fracton topological phases in solvable models – including degeneracy, mobility of excitations, absence of local observables that distinguish ground-states – are encoded in an algebraic variety [47], defined by the common zeros of a collection of polynomials over a finite field. In bosonic systems, this variety is invariant under the action of certain quantum circuits [81]. We show that the existence of fracton excitations is determined by studying points on this variety. The absence of a local order parameter gives rise

---

[5]This provided a source of initial frustration for the author.

to an exact chain complex of free modules over a polynomial ring, leading to a derivation of the duality between fracton topological phases and interacting systems with sub-system symmetries.

We conclude, in Part III, by studying operator spreading and entanglement growth in random quantum circuits, in which a quantum state is evolved using local, unitary operators that are chosen randomly from an appropriate distribution. This least-structured model for quantum dynamics preserves the locality and unitarity of time-evolution, but has no conserved quantities. We demonstrate that after averaging over the choice of local unitaries in the circuit, certain quantities – such as the evolving purity of a subsystem, and the out-of-time-ordered commutator (OTOC) – may be exactly determined by a classical Markov process. We show, for example, that if q is the dimension of the Hilbert space at each lattice site ($q = 2$ for spins), then

$$\overline{C(r,t)} = \frac{q^2}{q^2 - 1} \langle n(r,t) \rangle_{\text{class}} \tag{1.5}$$

On the left-hand side of (1.5) is the OTOC for two operators separated by distance r, with the bar denoting an appropriate average over the choice of unitaries in the circuit, while the right-hand side denotes an average of the occupation number in a classical stochastic process, which describes biased diffusion in one dimension ($d = 1$), and cluster growth in $d \geq 2$. From this relationship, we determine the exact form of the averaged OTOC in one and two spatial dimensions, and that operators spread ballistically, with a front that broadens as a power-law in time ($\sim t^\alpha$) with

$$\alpha = \begin{cases} 1/2 & d = 1 \\ 1/3 & d = 2 \\ 0.24 & d = 3 \end{cases} \tag{1.6}$$

We then show that in one spatial dimension, the entanglement entropy of a subsystem grows under random unitary dynamics according to the celebrated Kardar-Parisi-Zhang equation (KPZ) [82]; we explicitly derive this behavior in two distinct random circuit models. In one of these, the KPZ equation emerges from a description of the collective hydrodynamics of operators spreading throughout the system. Furthermore, the relation between the stochastic growth of a one-dimensional interface, as described by the KPZ equation, and the dynamics of a directed polymer in a random environment, leads to heuristics for entanglement growth in higher-dimensions. Importantly, the leading order time dependence of the entanglement entropy is deterministic even in the presence of noise, which motivates us to propose that these heuristics apply to generic many-body quantum systems undergoing Hamiltonian evolution.

Part I

Quantum Computation and Majorana Zero Modes

We begin this section with a very brief review of the emergence of Majorana zero modes in quantum condensed matter. As originally proposed by Ettore Majorana, the Majorana fermion is a spin-1/2 particle that is its own anti-particle [83]. The existence of a "fundamental" particle with this property seemed mathematically possible to Majorana, through the structure of the Dirac equation. However, it seems peculiar that such a particle could easily emerge in the condensed matter setting, since fermionic excitations in materials naturally carry electric charge, and this quantum number prevents these excitations from acting as their own anti-particles.

The motivation to search for these exotic excitations in materials arises both from fundamental physics – to validate Majorana's original proposal – and from quantum information science. A physical fermion may be naturally decomposed into a pair of Majorana fermions, i.e. the operators c, $c^\dagger$ for physical electrons, which satisfy canonical anti-commutation relations, may be re-written as[6]

$$c = \frac{\gamma_1 + i\gamma_2}{2} \qquad\qquad c^\dagger = \frac{\gamma_1 - i\gamma_2}{2} \qquad\qquad (1.7)$$

with the Majorana operators $\gamma_i = \gamma_i^\dagger$ satisfying $\{\gamma_i, \gamma_j\} = 2\delta_{ij}$. This algebraic trick reflects a simple fact: since a Majorana fermion is its own anti-particle, it makes no sense to speak of a Majorana fermion "occupation number", and a pair of Majorana fermions is needed to describe a fermionic, two-level system. Given a collection of Majorana fermions, one must specify how these excitations are paired together to form the physical Hilbert space of fermions.

The importance of Majorana fermions for quantum information processing is now apparent. First, a hypothetical system that supports a pair of spatially separated Majorana fermions, should have two degenerate ground-states – corresponding to the occupation number parity of a single, complex fermion – that are indistinguishable by local observables [84]. Therefore, qubits defined by well-separated Majorana fermions should be insensitive to de-phasing errors. Second, exchanging a collection of well-separated Majorana fermions corresponds to a change of basis in the underlying, physical Hilbert space of complex fermions; in other words, "braiding" Majorana fermions affects a unitary transformation on an encoded state. This is of fundamental importance since this implies that Majorana fermions exhibit "non-Abelian statistics" [85, 86, 16] – in contrast to ordinary fermions or bosons – as their exchange leads to a *quantized* unitary operation acting within a degenerate Hilbert space. This provides the basis for the topological quantum computing architecture, in which logical qubits are encoded in the degenerate states of non-Abelian anyons and qubit operations are performed by braiding [19].

Superconductors provide the most natural host for Majorana zero modes, since the elementary excitations consist of electron particle-hole superpositions. In a superconductor with even parity pairing (e.g. *s*-wave), however, these excitations involve an electron and a hole with opposite spins, and no particle-hole superposition can give rise to a Majorana fermion. In a spinless superconductor (with odd-parity pairing), however, one could imagine the perfect electron-hole

---

[6]We have suppressed indices of other quantum numbers carried by the physical fermion, e.g. spin.

superposition, e.g. $\gamma \sim c + c^\dagger$, and indeed, for *topological* p-wave superconductors, Majorana fermions can emerge as a special type of zero-energy quasi-particle that is bound to vortices or defects [87, 88]. Of course, even ordinary superconductors with odd-parity pairing are extremely rare, and as a result, experiments hunting for Majorana fermions have had to resort to "engineering" topological superconductivity by proximitizing an s-wave superconductor with a helical metal [14, 89, 90, 91, 92]. Many encouraging physical signatures of Majorana zero modes have been observed in these platforms – in vortices in the proximitized surface state of a topological insulator, the edges of proximitized semiconductor nanowires, etc. – such as the presence of zero-energy tunneling conductance peaks [93, 94, 95, 96]. Majorana fermions in topological superconductors are also predicted to produce exotic quantum phenomena such as a fractional Josephson effect [84, 97, 98] and the phase-coherent transport of electrons through Majorana bound-states, termed "electron teleportation" [99].

The absence of de-phasing errors in a qubit encoded in well-separated Majorana zero modes is a double-edged sword, since this also makes manipulation and validation of the qubit difficult. Demonstrating the non-Abelian statistics of Majorana fermions also requires braiding, fusing, and measuring the fusion outcome, which is a challenging task, as each of these operations is yet to be experimentally achieved. Furthermore, braiding Majorana fermions alone is insufficient to perform the necessary gate operations for universal quantum computation. Finally, for a long-term quantum computation at finite temperature, it is important to address errors caused in the process of manipulating a fermionic qubit, or while storing this qubit for subsequent readout.

The purpose of this section is to demonstrate that the charging energy in a *mesoscopic* topological superconductor can be used to prepare exotic entangled states that can be used for fault-tolerant, universal quantum computation with Majorana zero modes. We propose experiments to detect the non-Abelian braiding statistics of Majorana zero modes, and measurement-based protocols for braiding them. We also introduce a large collection of new quantum error-correcting codes that can be used for the robust information storage in a fermionic qubit. This section is based on Ref. [1, 2, 3, 4].

Chapter 2

The Majorana Fermion Surface Code

In this chapter, we propose a concrete platform for universal quantum computation using Majorana zero modes, by utilizing quantum phase slips in an array of Josephson-coupled mesoscopic topological superconductors, which can be implemented in a wide range of solid state systems, including topological insulators, nanowires or two-dimensional electron gases, proximitized by s-wave superconductors. We present protocols for measurement-based gate operations and for qubit readout. Our proposal is based on a solvable model of interacting Majorana zero modes that we introduce, and our presentation of the model, and of the platform for quantum computation is self-contained, and is inspired by existing architectures for quantum computation [19, 100, 101]

The "surface code" architecture [100, 101] provides an approach to universal quantum computation that uses measurements in an Abelian topological phase for gate operations and error correction. In the surface code, measurements of non-trivial commuting operators (stabilizers) are used to project onto a "code state" and logical qubits are effectively encoded in the anyon charge of a region by ceasing certain stabilizer measurements [102, 103, 15, 104]. The logical gates necessary for universal quantum computation are realized through sequences of measurements used to move and braid the logical qubits. An advantage of the surface code architecture is its remarkable ability for error detection and subsequent correction during qubit readout, as the nucleation of anyons through the action of a random operator can be reliably tracked through stabilizer measurements. For a sufficiently low error rate per physical qubit measurement, scaling the size of the surface code produces an exponential suppression in propagated errors [105]. Remarkably, recent experiments with superconducting quantum circuits have demonstrated the ability to perform high-fidelity physical gate operations and reliable error correction for a surface code of small size [106, 107, 108].

We introduce a new scheme for surface code quantum computation that uses Majorana fermions as the fundamental physical degrees of freedom and exploits their unique properties for encoding and manipulating logical qubits. Our surface code is based on a novel Z_2 topological order with fermion parity grading (defined below), which we demonstrate in a class of exactly solvable Hamiltonians of interacting Majorana fermions. We demonstrate that charging

energy-induced quantum phase slips in superconducting arrays with Majorana fermions generate the required multi-fermion plaquette interactions, providing a physical realization of our model. We then describe a detailed physical implementation of the "Majorana fermion surface code", including physical qubit and stabilizer measurements, the creation of logical qubits, error correction, and logical gate operations required for universal quantum computation.

The Majorana fermion surface code poses significant benefits over a surface code with bosonic physical qubits. First, stabilizer measurements in the Majorana surface code can be performed in a *single step*, whereas this requires several physical gate operations in the conventional surface code [104, 15]. As a result, we anticipate that the Majorana surface code has a significantly higher error tolerance. Furthermore, our Majorana surface code operates with substantially less overhead, as it requires fewer physical qubits per encoded logical qubit, and uses no physical ancilla qubits. Second, we may tune the energy gap for anyon excitations in our physical realization of the Majorana plaquette Hamiltonian, increasing error suppression in the Majorana fermion surface code. Finally, the lattice symmetries in the Majorana plaquette model permute the three fundamental anyon types, allowing a much simpler realization of the logical Hadamard gate. As we will show, the above advantages arise from the unique approach taken by our Majorana fermion surface code and the use of Majorana fermions as fundamental degrees of freedom. In particular, the unique property that a Majorana fermion is half of an ordinary fermion, with the consequence that two of them form a single physical qubit, is crucial to the Majorana fermion surface code. On the other hand, the non-Abelian statistics of Majorana-carrying vortices or defects is of no relevance to our code, as our code does not involve braiding these objects.

This chapter is organized as follows. First, we introduce a solvable model of interacting Majorana fermions on the honeycomb lattice realizing a novel Z_2 topological order with a Z_2 fermion parity grading and an exact S_3 anyon symmetry. We propose a physical realization of this model, using charging energy in an array of mesoscopic superconductors [99] to implement the required non-local interactions between multiple Majorana fermions. Next, we demonstrate that our model provides a natural setting for the Majorana fermion surface code, in which a logical qubit is encoded in a set of physical qubits formed from Majorana fermions. We present a physical implementation of the Majorana surface code and propose detailed protocols for performing gate operations for universal quantum computation.

2.1   Majorana Plaquette Model

We begin by considering a honeycomb lattice with one Majorana fermion (γ) on each lattice site; the Majorana fermions satisfy canonical anti-commutation relations $\{\gamma_n, \gamma_m\} = 2\delta_{nm}$. The Hamiltonian is defined as the sum of operators acting on each hexagonal plaquette:

$$H = -u \sum_p \mathcal{O}_p \qquad \mathcal{O}_p \equiv i \prod_{n \in \text{vertex(p)}} \gamma_n. \tag{2.1}$$
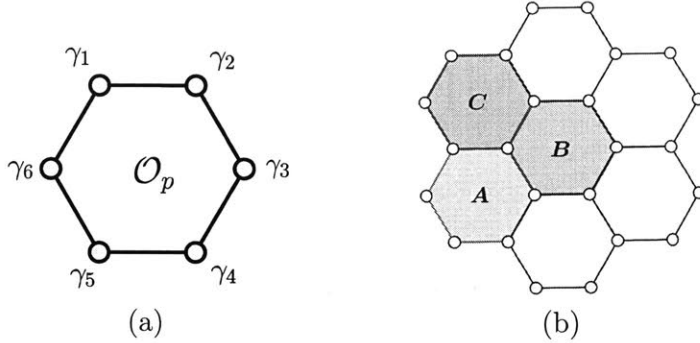
Figure 2-1: We consider a honeycomb lattice with (a) a single Majorana fermion on each lattice site, so that the $\mathcal{O}_p$ operator is the product of the six Majorana fermions on the vertices of a hexagonal plaquette. The colored plaquettes in (b) correspond to the three distinct bosonic excitations that may be obtained by violating a plaquette constraint.

We note that (1) this model was mentioned in a work by Bravyi, Terhal and Leemhuis [109], although its novel topological order and anyon excitations were not studied there; (2) a closely related model in the same topological phase was introduced and studied by Xu and Fu [110].

It suffices to consider $u > 0$ below, as the case of $u < 0$ can be mapped to $u > 0$ by changing the sign of the Majorana fermions on one sublattice. The operator $\mathcal{O}_p$ is the product of the six Majorana fermions on the vertices of plaquette p as shown in Figure 5-5a. Since any two plaquettes on the honeycomb lattice share an even number of vertices, all of the plaquette operators commute, and the ground-state $|\Psi_0\rangle$ is defined by the condition

$$\mathcal{O}_p |\Psi_0\rangle = |\Psi_0\rangle , \tag{2.2}$$

for all plaquettes p. We note that quite generally, Hamiltonians of interacting Majorana fermions with commuting terms may be realized on any lattice, so long as any pair of operators in the Hamiltonian only has overlapping support over an even number of Majorana fermions.

We demonstrate that the above Majorana plaquette model (5.1) realizes a Z_2 topological order of Fermi systems by considering the ground-state degeneracy and elementary excitations. First, we place the system on a torus by imposing periodic boundary conditions, and find a four-fold degenerate ground-state by counting the number of degrees of freedom and constraints on the full Hilbert space. For an N-site honeycomb lattice, the $2^{N/2}$-dimensional Hilbert space of Majorana fermions is constrained by the fixed total fermion parity:

$$\Gamma \equiv i^{N/2} \prod_n \gamma_n \tag{2.3}$$

For convenience, we choose a unit cell for the honeycomb lattice consisting of three plaquettes labeled A, B and C, as shown in Figure 5-5b. We observe that on the torus, the product of plaquette operators on each of the A, B and C-type plaquettes is equal to the total fermion

parity:

$$\Gamma = \prod_{p \in A} \mathcal{O}_p = \prod_{p \in B} \mathcal{O}_p = \prod_{p \in C} \mathcal{O}_p \qquad (2.4)$$

The operators $\{\mathcal{O}_p\}$ on any one type of plaquette fix one-third of the plaquette eigenvalues via the condition (2.2), and impose $2^{N/6-1}$ constraints on the Hilbert space. The number of unconstrained degrees of freedom is therefore given by:

$$D = 2^{\frac{N}{2}-1} / \left(2^{\frac{N}{6}-1}\right)^3 = 4, \qquad (2.5)$$

which yields a four-fold ground state degeneracy for the Majorana plaquette model on the torus.

The ground state degeneracy is of a topological nature, as the four ground-states are distinguished only by non-local operators. To see this, we construct a Wilson loop operator W_ℓ, defined as a product of Majorana bilinears on a non-contractible loop ℓ on the torus:

$$W_\ell \equiv \prod_{n,m \in \ell} (i\gamma_n \gamma_m). \qquad (2.6)$$

such that $W_\ell^2 = 1$, so that the Wilson loop has eigenvalues ± 1. Consider the operators W_x and W_y on the two non-trivial cycles of the torus ℓ_x and ℓ_y, as shown in Figure 2-2. Since ℓ_x and ℓ_y traverse an even number of vertices over any plaquette and do not contain any common lattice sites, we have $[W_x, W_y] = [W_x, H] = [W_y, H] = 0$. Furthermore, we may construct Wilson loop operators $W_{\tilde{x}}$ and $W_{\tilde{y}}$ on loops $\tilde{\ell}_x$ and $\tilde{\ell}_y$, where $\tilde{\ell}_x$ is shifted from ℓ_x by a basis vector parallel to ℓ_y and likewise for $\tilde{\ell}_y$, such that $\{W_{\tilde{x}}, W_y\} = \{W_{\tilde{y}}, W_x\} = 0$. As before, $W_{\tilde{x}}$ and $W_{\tilde{y}}$ commute with each other and with the Hamiltonian. Therefore, the four degenerate ground-states may be distinguished by their eigenvalues under W_x and W_y, with $W_{\tilde{x}}$ and $W_{\tilde{y}}$ transforming the ground-states between distinct sectors. In analogy with conventional Z_2 gauge theory, we may identify the Wilson loop operators $W_{x,y}$ with electric charges traversing the torus in two different directions, and $W_{\tilde{x},\tilde{y}}$ as magnetic fluxes on a dual lattice.

Gapped excitations above the ground state are obtained by flipping the eigenvalue of $\mathcal{O}_p$ from $+1$ to -1 on one or more plaquettes. Since the total fermion parity is fixed and equal to the product of all plaquette operators of each type, plaquette eigenvalues can only be flipped on pairs of plaquettes of the *same* type. This is achieved by string operators of the form (2.6), now acting on open paths and anti-commuting with the plaquette operators at the two ends of the path, thereby creating a pair of anyon excitations.

An important feature of our Majorana plaquette model, the conservation of total fermion parity—a universal property of Fermi systems—makes it impossible to create or annihilate two excitations living on different types of plaquettes, or change one type of plaquette excitation into another. As a result, there are three distinct elementary plaquette excitations, labeled A, B and C, by plaquette type. To determine their statistics, we braid these excitations by acting
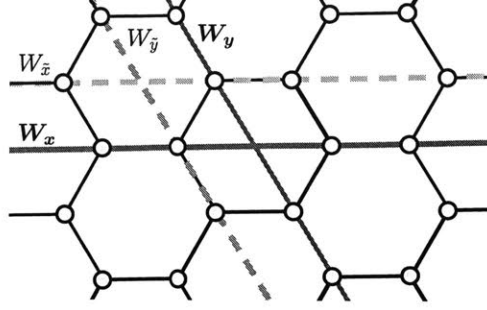
Figure 2-2: The action of the commuting Wilson loop operators W_x and W_y is shown above as the product of the Majorana fermions on the lattice sites intersected by the appropriate colored lines. The operator w_x anti-commutes with W_x and takes the ground-state between two topological sectors.

with Majorana hopping operators $i\gamma_n\gamma_m$ on lattice bonds [?]. We find that all three types of plaquette excitations have boson self-statistics and mutual semion statistics, i.e., braiding two distinct plaquette excitations generates a quantized Berry phase of π. From the elementary plaquette excitations we may build composite excitations AB, BC, AC and ABC by flipping the eigenvalues of the $\mathcal{O}_p$'s on two or three adjacent plaquettes. Among these, the composite excitation ABC is simply a physical Majorana fermion, since the Majorana operator γ_n acting on a lattice site flips the eigenvalues of the $\mathcal{O}_p$'s on the three surrounding A, B and C plaquettes. In contrast, the composite excitations AB, BC, AC are anyons, with fermion self-statistics and mutual semion statistics with the elementary excitations. We call these excitations composite Majorana fermions, as they are created by a string of physical Majorana fermions. A summary of the braiding statistics for all anyons in our Majorana plaquette model is given in the following table:

	1	A	B	C	AB	BC	AC	ABC
1	+1	+1	+1	+1	+1	+1	+1	+1
A	+1	+1	−1	−1	−1	+1	−1	+1
B	+1	−1	+1	−1	−1	−1	+1	+1
C	+1	−1	−1	+1	+1	−1	−1	+1
AB	+1	−1	−1	+1	−1	−1	−1	+1
BC	+1	+1	−1	−1	−1	−1	−1	+1
AC	+1	−1	+1	−1	−1	−1	−1	+1
ABC	+1	+1	+1	+1	+1	+1	+1	−1

Strange as it may appear, the existence of eight types of quasiparticle excitations is a generic property of Z_2 topologically ordered phases in Fermi systems, due to the conservation of fermion parity. Consider artificially dividing the above quasiparticles into two groups: $(1, A, B, AB)$ and $(ABC, BC, AC, C) = ABC \times (1, A, B, AB)$. The former is equivalent to the four quasi-particles

in Z_2 gauge theory coupled to a bosonic Ising matter field, as realized in Kitaev's toric code [19] or Wen's plaquette model [111]. The latter group of quasiparticles is obtained by attaching a physical Majorana fermion to the former. The conservation of total fermion parity guarantees that the two groups of quasi-particles cannot transform into each other in a closed system, and thus have separate identities. We refer to the presence of two groups of excitations with different fermion parity as a Z_2 fermion parity grading.

A remarkable property of the Majorana plaquette model is that crystal symmetries of the honeycomb lattice permute the three fundamental anyon excitations, A, B and C, by interchanging the three types of plaquettes. Examples of such lattice symmetries include $\pi/3$ rotations about the center of a plaquette, and translation by any primitive lattice vector. These symmetries of the honeycomb lattice provide a microscopic realization of the S_3 anyon symmetry that permutes quasiparticle sectors, as recently studied in the abstract formalism of topological field theory by considering the symmetries of the K-matrices of Abelian topological states [112, 44].

2.2 Physical Realization

In this section, we show that the Majorana plaquette model can be physically realized in an array of mesoscopic topological superconductors that are Josephson coupled. A wide range of material platforms for engineering a topological superconductor have been proposed and are being experimentally studied [87, 88]. As it will be clear in the following, the scheme we propose for realizing the Majorana plaquette model is independent of which platform is used. For the sake of concreteness, we use a platform based on topological insulators in describing the general scheme below, and discuss other platforms based on nanowires and two-dimensional electron gas with spin-orbit coupling in section II.C.

We place a array of hexagon-shaped s-wave superconducting islands on a topological insulator (TI) to induce a superconducting proximity effect on the TI surface states. The Hamiltonian for this superconductor-TI hybrid system is given by

$$
\begin{aligned}
H_0 \;=\; & \int d\mathbf{r}(-iv)\psi^{\dagger}(\mathbf{r})\left(\partial_x s_y - \partial_y s_x - \mu\right)\psi(\mathbf{r}) \\
& + \sum_j \int d\mathbf{r}_j \left[\Delta e^{i\varphi_j}\psi_{\uparrow}^{\dagger}(\mathbf{r}_j)\psi_{\downarrow}^{\dagger}(\mathbf{r}_j) + \text{h.c.}\right],
\end{aligned}
\tag{2.7}
$$

where $\psi = (\psi_{\uparrow}, \psi_{\downarrow})^T$ is a two-component fermion field and $s_{x,y}$ are spin Pauli matrices. The first term describes the pristine TI surface states, with a single spin-non-degenerate Fermi surface and helical spin texture in momentum space. The second term describes the superconducting proximity effect: $\mathbf{r}_j$ belongs to the region underneath the j-th superconducting island, whose phase is denoted by φ_j.

As found by Fu and Kane [14], a vortex or anti-vortex trapped at a tri-junction, where three islands meet, hosts a single Majorana fermion zero mode. Let us consider setting up
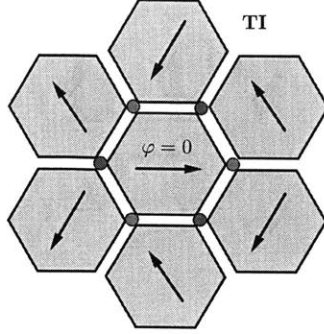
Figure 2-3: Array of hexagonal *s*-wave superconducting islands placed on a TI surface. Each arrow points in the direction of the relative phase of the associated island, with $\varphi = 0, \pm 2\pi/3$. This produces a honeycomb lattice of vortices (blue) and anti-vortices (red) at tri-junctions, hosting Majorana fermions.

the phases of superconducting islands to realize an array of vortices and anti-vortices at tri-junctions. For example, the phases can be set to $\varphi_j = 0, 2\pi/3$ and $-2\pi/3$ on the A, B and C-type islands respectively, as shown in Fig. 2-3. This yields a 2D array of Majorana fermions on a honeycomb lattice. In practice, the desired phase configuration can be engineered by external electrical circuits [113] and/or magnetic flux. Alternatively, applying a perpendicular magnetic field generates a vortex lattice. These vortices may naturally sit at these tri-junctions where the induced superconductivity is weak, leading to the desired lattice of Majorana fermions.

We take the size of the islands to be larger than the coherence length of the superconducting TI surface states. Under this condition, Majorana fermions at different sites have negligible wavefunction overlap, preventing any unwanted direct coupling between them. (We note that even weak couplings from wavefunction overlap will not affect the Z_2 topological order of the Majorana plaquette model, due to its finite energy gap.) Nonetheless, as we show below, the charging energy of superconductors induces a nonlocal interaction between the six Majorana fermions on each island, providing the key ingredient of the Majorana plaquette model.

2.2.1   Phase-Slip Induced Multi-Fermion Interactions

The important but subtle interplay between Majorana fermions and charging energy was first recognized by Fu and formulated for superconductors with a fixed number of electrons [99]. Later works have extended it to multiple superconductors connected by Josephson coupling and single-electron tunneling [110, 114, 115, 116]. In all of these cases, the charging energy of a given superconductor induces quantum phase slips $\varphi \to \varphi \pm 2\pi$, from which the Majorana fermions in the superconductor acquire a minus sign: $\gamma_i \to -\gamma_i$. This property is due to the inherently double-valued dependence of Majorana operators on the superconducting phase [99].

In our setup for the Majorana plaquette model, the charging energy of the superconducting islands exerts even more dramatic and interesting effects on the Majorana fermions at tri-
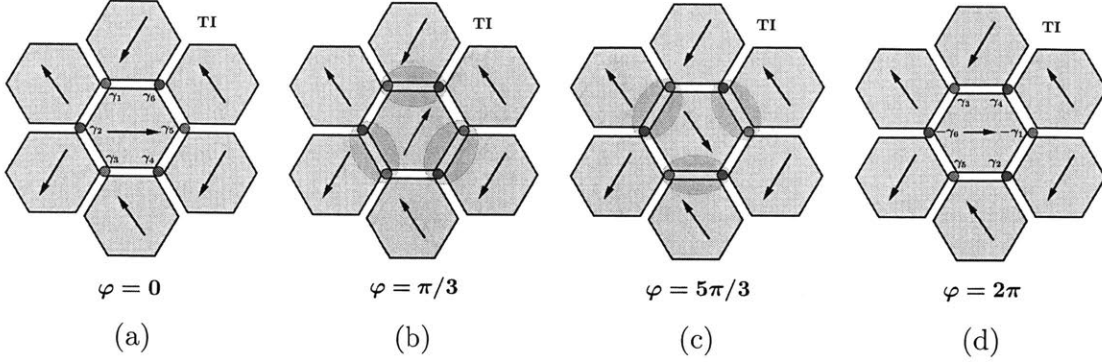
Figure 2-4: Schematic of a 2π phase-slip on the central superconducting island in a hexagonal superconducting array on a TI surface, with the phase of the central island indicated in each panel. When the phase difference between neighboring islands is π, the pair of Majorana fermions on the shared edges couple [14] as indicated. The 2π phase-slip permutes the Majorana fermions as shown, leading to the transformation in (2.12).

junctions, which have not been previously studied. In the presence of a charging energy, the phase of each island becomes a quantum rotor. The kinetic energy of the rotor is provided by the charging energy E_c, which depends on the capacitance between an island and the rest of the array, and is described by the following Hamiltonian

$$H_c = 4E_c \sum_j (\hat{n}_j - n_g)^2 \tag{2.8}$$

where $\hat{n}_j \equiv (-i) \cdot \partial/\partial\varphi_j$ is the Cooper pair number operator for the jth island and n_g is the offset charge, which can be tuned by an externally applied electric field. The potential energy of the rotor is provided by the Josephson coupling E_J between adjacent superconducting islands, given by

$$H_J = -E_J \sum_{\langle j,j' \rangle} \cos(\hat{\varphi}_j - \hat{\varphi}_{j'} - a_{jj'}), \tag{2.9}$$

where $a_{jj'} = \varphi_{0,j} - \varphi_{0,j'}$ is externally set up such that the minimum of the Josephson energy corresponds to $\varphi_j = \varphi_{0,j} \mod 2\pi$, with $\varphi_{0,j} = 0, 2\pi/3$ and $-2\pi/3$ for the A, B and C-type islands, respectively.

Combining (2.7), (2.8) and (2.9), the full Hamiltonian for our setup, i.e. an array of superconducting islands on a TI surface, is given by

$$H = H_0 + H_c + H_J. \tag{2.10}$$

We work in the regime $E_J \gg E_c$. Under this condition, low-energy states of the quantum rotor on a given island φ_j consist of small-amplitude fluctuations around each potential minimum $\varphi_{0,j} + 2\pi m$. Moreover, different minima are connected by quantum phase slips, in which the

phase φ tunnels through a high energy barrier to wind by $2\pi n$, with n an integer. The small-amplitude phase fluctuations around a potential minimum correspond to a quantum harmonic oscillator, and thus generate a set of energy levels given by

$$\epsilon_\alpha^0 \approx (\alpha + 1/2)\sqrt{8E_JE_c}. \tag{2.11}$$

with $\alpha \in \mathbb{N}$.

On the other hand, quantum phase slips on a superconducting island strongly couple to the Majorana fermions that reside on the border with its neighbors, previously obtained by holding the phase fixed at $\varphi_{0,j}$. In other words, Majorana fermions enter the low-energy effective theory of (2.10) via quantum phase slips induced by small the charging energy on each superconducting island. This new physics makes our system different from a conventional Cooper pair box. Remarkably, the action of a quantum phase slip involves Majorana fermions in a way that depends periodically on the phase winding number n mod 6. Consider, for example, phase slips at the central superconducting island in Fig. 3. For $n = 1$, a 2π phase slip $\varphi = 0 \to 2\pi$ cyclically permutes the three Majorana fermions bound to vortices in the counterclockwise direction, and the three Majorana fermions bound to anti-vortices in the clockwise direction, i.e.,

$$\varphi = 0 \to 2\pi : \quad \gamma_1 \to \gamma_3, \gamma_3 \to \gamma_5, \gamma_5 \to -\gamma_1$$
$$\gamma_2 \to -\gamma_6, \gamma_4 \to \gamma_2, \gamma_6 \to \gamma_4, \tag{2.12}$$

as shown in Figure 2-4, where $i = 1, ..., 6$ labels the six Majorana fermions at vertices of this island in clockwise order. The physical movement of Majorana fermions induced by phase slips is a unique and attractive advantage of our setup, compared to other setups in which the positions of Majorana fermions are fixed [110, 114, 115, 116]. On the other hand, for $n = 3$, a 6π phase slip takes each Majorana fermion over a full circle and back to its original position, from which it acquires a minus sign [14], i.e.,

$$\varphi = 0 \to 6\pi : \quad \gamma_i \to -\gamma_i. \tag{2.13}$$

Only for $n = 6$ does each Majorana fermion come back to its original position unchanged.

We now add up the contributions of various phase slips to derive an effective Hamiltonian for Majorana fermions as a function of the offset charge n_g for each state of the harmonic oscillator:

$$H_\alpha(n_g) = \epsilon_\alpha^0 + \sum_{n=1}^{6}(t_{\alpha,n}\hat{U}_n e^{i2\pi n n_g} + \text{h.c.}). \tag{2.14}$$

Here ϵ_α^0 is the quantized energy of the harmonic oscillator given by (2.11), which is the same for all internal states of the Majorana fermions. The second term describes quantum phase slips: $t_{\alpha,n}$ denotes the amplitude of the α-th energy level of the harmonic oscillator tunneling between two potential minima that differ by $2\pi n$, while $\hat{U}_n$ is the unitary operator acting on the Majorana

51

fermions due to a $2\pi n$ phase slip. The coupling $t_{\alpha,n}$ depends on the energy barrier in the phase slip event and can be modulated by tuning E_c/E_J; for example, $t_{\alpha,1} \propto e^{-\sqrt{8E_J/E_c}}$ [117]. The offset charge n_g provides an Aharonov-Bohm flux proportional to the winding number n.

The Hamiltonian (2.14) is analogous to the Bloch Hamiltonian that describes the band structure of a particle hopping in a one-dimensional periodic potential, with the offset charge n_g playing the role of crystal momentum. Importantly, the phase particle carries internal degrees of freedom resulting from Majorana fermions $\gamma_1, ..., \gamma_6$ that are unique to our system. A phase slip that moves the phase particle to a different potential minimum also permutes the Majorana fermions as shown in (2.12,2.13), similar to a spinful particle hopping in the presence of a non-Abelian gauge field. These permutations are represented by the unitary operators $\hat{U}_n$ in the effective Hamiltonian (2.14) acting on Majorana fermions. For example, the operator $\hat{U}_1$ that generates the transformation (2.12) is given by:

$$\hat{U}_1 = \frac{1 + \gamma_2\gamma_3}{\sqrt{2}} \cdot \frac{1 + \gamma_4\gamma_5}{\sqrt{2}} \cdot \frac{1 - \gamma_6\gamma_1}{\sqrt{2}} \cdot \frac{1 + \gamma_1\gamma_2}{\sqrt{2}} \cdot \frac{1 + \gamma_3\gamma_4}{\sqrt{2}} \cdot \frac{1 + \gamma_5\gamma_6}{\sqrt{2}}. \tag{2.15}$$

It follows from the addition of phase slips that $\hat{U}_n = (\hat{U}_1)^n$. In particular, the unitary operator $\hat{U}_3$, which takes γ_i to $-\gamma_i$ as shown in (2.13), has a simple form:

$$\hat{U}_3 = -\prod_{i=1}^{6} \gamma_i = i\mathcal{O}, \tag{2.16}$$

where $\mathcal{O}$ is the plaquette operator defined in the Majorana plaquette model (2.2). On the other hand, for $n = 1, 2, 4$ or 5, U_n is a sum of operators $\gamma_i\gamma_j$, $\gamma_i\gamma_j\gamma_k\gamma_l$ and $i\mathcal{O}$.

Substituting the expressions for the U_n's into (2.14), we find that the effective Hamiltonian induced by the small charging energy of a single island takes the following form

$$H_\alpha(n_g) = \epsilon_\alpha^0 + \Delta_\alpha(n_g)\mathcal{O} + V_\alpha(n_g), \tag{2.17}$$

with

$$\Delta_\alpha(n_g) = \sum_{m=1}^{5} t_{\alpha,m}\sin(2\pi m n_g). \tag{2.18}$$

$V_\alpha(n_g)$ includes a constant $t_{\alpha,6}\cos(12\pi n_g)$, as well as Majorana bilinear and quartic operators generated by phase slips with winding number $n \neq 0 \mod 3$. Unlike $\mathcal{O}$, these operators on neighboring islands do not commute. However, by appropriately tuning n_g the contribution of quartic operators to the effective Hamiltonian may be made to vanish, so that the only remaining terms in the Hamiltonian will be the six-Majorana interaction and Majorana bilinear terms. The bilinear term receives no contribution from any $\pm 6\pi m$ phase slip, while $\Delta_\alpha(n_g)$ receives contributions from *every* $\pm 2\pi m$ phase-slip process. Therefore, for the remainder of this chapter, we assume that V can be treated as a perturbation to the Majorana plaquette model

that does not destroy the Z_2 topological order of the gapped phase. We note that an alternative setup without the presence of V has been presented in a recent work [?].

2.2.2 Discussion

In deriving the effective Hamiltonian (2.14), we have implicitly assumed that Majorana fermions are the only low-lying excitations involved in phase slip events, separated by an energy gap from other Andreev bound states in the junctions between islands. This assumption is valid because of the finite size of the islands, which leads to a discrete Andreev bound-state spectrum with a finite gap for all values of the phase. The presence of this gap justifies our derivation of the effective Hamiltonian (2.14) in a controlled manner.

Over the last few years, considerable experimental progress has been made in hybrid TI-superconducting systems. Proximity-induced superconductivity and supercurrents have been observed in a number of TI materials [118, 119, 120, 121, 122, 123, 124]. Low-temperature scanning tunneling microscopy (STM) experiments have found proximity-induced superconducting gap on TI surface states, and the tunneling spectrum of Abrikosov vortices shows a zero-bias conductance peak, which is robust in a range of magnetic field and splits at higher field [96]. This peak has been attributed to the predicted Majorana fermion zero-modes in the vortex cores of superconducting TI surface states. In view of these rapid, unabated advances, we regard the hybrid TI-superconductor system as a very promising material platform for realizing the Majorana plaquette model and studying the exciting physics of Majorana fermions enabled by quantum phase slips.

Besides TIs, a two-dimensional electron gas (2DEG) with spin-orbit coupling (such as InAs) can be driven into a helical state with an odd number of spin-polarized Fermi surfaces by an external Zeeman field, which provides another promising platform for realizing topological superconductivity via proximity effect [125, 126]. In this topological regime, vortices and tri-junctions of a superconducting 2DEG host a single Majorana fermion, similar to the TI surface. Thus our propsed setup for the Majorana plaquette model in Section IIA directly applies to this system as well.

In addition to TIs and 2DEG, (quasi-)one-dimensional semiconductors and metals with strong spin-orbit coupling have become a hotly pursued system for Majorana fermions [89, 90, 91]. Signatures of Majorana fermions were reported in 2012, based on the observation of zero-bias conductance peak in hybrid nanowire-superconductor systems [93, 94]. One can envision a network of nanowires in proximity with Cooper-pair boxes to realize our Majorana plaquette model. In this direction it is worth noting that a new physical system—a nanowire with an epitaxially grown superconductor layer— has been recently introduced to study Andreev bound-states in the presence of charging energy [127].

Many other physical systems for Majorana fermions have been theoretically proposed and experimentally pursued, too numerous to list. Regardless of the particular system, non-local interactions between multiple Majorana fermions emerge from the charging energy of supercon-

ductors via quantum phase slips, and in the universal regime, such interactions are determined by the transformation of Majorana fermions under phase slips, as we have shown in Section IIB.

Finally, we note several previous works related to our Majorana plaquette model and its physical realization. In Ref. [110], Xu and Fu first introduced a model of interacting Majorana fermions that realizes Z_2 topological order. This model involves 4-body and 8-body plaquette interactions on square and octagonal plaquettes in a two-dimensional lattice. Physical realizations of this model were proposed using an array of superconductor islands in proximity with either 2D TI [110], or semiconductor nanowires [128, 129]. The 4-body nonlocal interaction between Majorana fermions comes directly from the charging energy, whereas the 8-body interaction comes from a *high-order* ring-exchange process generated by single-electron tunneling between islands. In comparison, our Majorana plaquette model on the honeycomb lattice has the theoretical novelty of possessing an exact anyon permutation symmetry, and can be realized in a much simpler manner using an array of superconductors on a 3D TI with global phase coherence, with all the required interactions coming directly from the charging energy. We also note a recent work on lattice models of Majorana fermions in Abrikosov vortices on a superconducting TI surface [130], which use different interactions and do not exhibit topological order.

2.3 Majorana Surface Code Operations

In the rest of this chapter, we demonstrate that the Majorana plaquette model finds a natural application as a "Majorana fermion surface code", on which universal quantum computation and error correction may be performed. The main idea of the surface code is to (i) use anyons of the Majorana plaquette model to encode logical qubits, (ii) manipulate anyons to perform gate operations on logical qubits, and (iii) use commuting measurements of the Majorana plaquette operators for error correction. We will describe the detailed implementation of the Majorana surface code, including the creation of logical qubits, error correction, and protocols for logical gate operations required for universal quantum computation.

The surface code architecture [15, 100, 101] is a *measurement-based* scheme for quantum computation. It uses projective measurements of commuting operators—called "stabilizers"—acting on a 2D array of physical qubits to produce a highly-entangled "code state" $|\psi\rangle$. Logical qubits are created by stopping the measurement of certain commuting operators to create "holes". The different possible anyon charges at a hole are the degrees of freedom that define a logical qubit. Logical gates are realized by manipulating and braiding holes via a sequence of measurements.

A key advantage of the surface code is its remarkable capability for *error detection*. The random measurement of an operator in the surface code corresponds to nucleating pairs of anyons, a process that can be reliably measured by tracking the eigenvalues of the commuting stabilizers. Reliable error detection hinges on (i) having a large number of physical qubits for a given encoded logical qubit, and (ii) a sufficiently low error rate for stabilizer measurements [15]. For the previously studied surface code with bosonic physical qubits, it has been estimated

[131, 132] that below a threshold as high as $\sim 1\%$ error-rate per physical qubit operation, scaling the size of the surface code permits an exponential suppression of errors propagated. This error tolerance makes the surface code architecture one of the most realistic approaches to practical, large-scale quantum computation.

Recent practical realizations of the surface code have used superconducting qubits coupled to a microwave transmission line resonator to perform qubit manipulations and measurements [106, 107, 108]. Here, a physical qubit is defined by two energy levels arising from quantization of number/phase fluctuations in a conventional Cooper pair box. The surface code is implemented on a 2D array of physical qubits with the four-qubit interactions of Kitaev's toric code Hamiltonian [19] as the set of commuting stabilizers. The four-qubit stabilizer is measured by performing a sequence of single and two-qubit gates between the four *physical* qubits and additional ancilla qubits [15]. Experiments have demonstrated the remarkable ability to operate these physical gates with fidelity above the threshold required for surface code error correction [106]. Recent experiments have also used error detection to preserve entangled code states on a surface code with a 9×1 [107] and a 2×2 [108] array of stabilizers. It remains to be shown that logical qubits can be successfully encoded and manipulated via logical gates in these surface code arrays.

2.3.1 Implementation

We implement the Majorana surface code on a 2D array of Majorana fermions by performing projective measurements of the Majorana plaquette operators $\{\mathcal{O}_p\}$, which form a complete set of commuting stabilizers. For the remainder of this chapter, we will use 'plaquette operators' and 'stabilizers' interchangeably to refer to $\{\mathcal{O}_p\}$. A practical *physical* system for implementing the Majorana surface code is the superconductor-TI hybrid system introduced in the previous section. We place a array of superconducting islands on the TI surface, which are strongly Josephson coupled. By introducing external circuits or applying fluxes, we engineer the Josephson coupling between islands to achieve the phase configuration in Figure 2-3, leading to a honeycomb lattice of Majorana fermions at tri-junctions.

To perform a projective measurement of the Majorana plaquette operator on a given island, i.e., a single stabilizer, we decrease the Josephson coupling of the island with the rest of the array to activate quantum phase slips from the small but non-zero charging energy on this island. As shown by the effective Hamiltonian in (C.14), these quantum phase slips (partially) lift the degeneracy between states in the eight-dimensional Fock space of the six Majorana fermions. In particular, for every energy level of the harmonic oscillator, there is an energy splitting $\Delta_\alpha(n_g)$ between states of Majorana fermions with $\Gamma = +1$ (even fermion parity) and with $\Gamma = -1$ (odd fermion parity) from (2.18), where Γ is the stabilizer eigenvalue; this is shown schematically in Figure 2-5b. Therefore, the charging energy of the island creates an energy difference between different stabilizer eigenstates. Furthermore, the *energy gap* between the two lowest harmonic oscillator levels on the island is a function of the stabilizer eigenvalue $\Gamma = \pm 1$, and in the limit
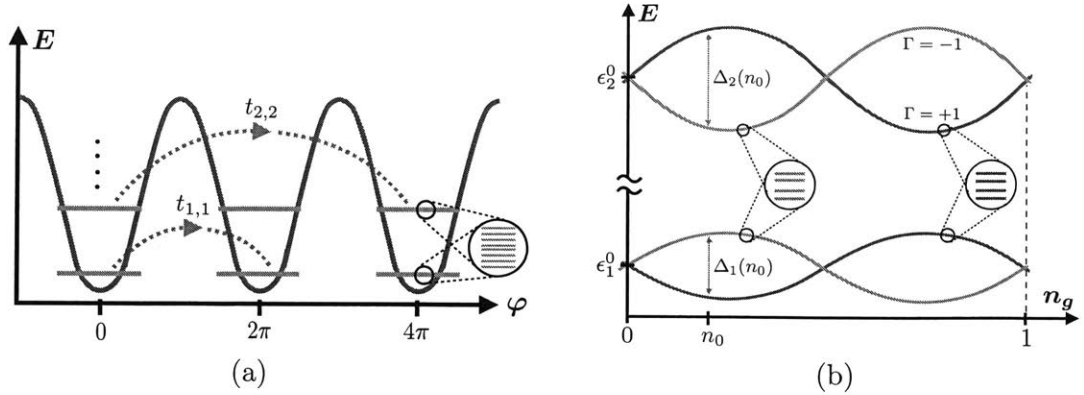
Figure 2-5: (a.) Schematic of the harmonic oscillator energy levels of the effective Hamiltonian (C.14), centered at $\varphi = 2\pi n$, with the 2π and 4π phase-slip amplitudes for the lowest energy levels shown. In (b), we show a schematic plot of the two lowest harmonic oscillator levels as a function of the gate-charge. The energy splittings Δ_1 and Δ_2 are between states with even ($\Gamma = +1$) and odd fermion parity ($\Gamma = -1$) within the first and second harmonic oscillator levels, respectively. Each level within a fixed fermion parity sector is nearly four-fold degenerate.

of negligible interaction V takes the following form:

$$\Delta E_\Gamma(n_g) = \epsilon_0 + [\Delta_2(n_g) - \Delta_1(n_g)]\, \Gamma + \ldots \tag{2.19}$$

where $\epsilon_0 \equiv \epsilon_2^0 - \epsilon_1^0 \approx \sqrt{8E_J E_c}$. The sensitivity of the energy gap to the stabilizer eigenvalue now permits a stabilizer measurement by simply measuring the energy gap. By shining a probe microwave beam on this island, we may measure the phase shift of the transmitted photons to determine the gap between the two harmonic oscillator levels [133, 134].

We now perform these stabilizer measurements on all of the superconducting islands to project onto an eigenstate of the Majorana plaquette Hamiltonian (5.1); this will be our reference "code state". We continue to perform measurements on all hexagonal islands in each cycle of the surface code in order to maintain the state. In subsequent cycles, we may encode logical qubits into the code state and manipulate the qubits via measurement. While projection onto the code state and error correction in the surface code rely exclusively on measuring the six-Majorana plaquette interaction, manipulation of logical qubits also requires measuring nearest-neighbor Majorana bilinears on the hexagonal lattice. This may be done by tuning the phase of neighboring superconducting islands to bring the pair of Majorana fermions on the shared edge sufficiently close together [14], so that the resulting wavefunction overlap further splits the nearly four-fold degeneracy within a single fermion parity sector shown in Figure 2-5b. Again, the Majorana bilinear may be measured by shining a probe beam to measure the energy gap to the next harmonic oscillator level.

Using the commuting six-Majorana operators in our plaquette model to realize a surface code provides unique advantages over the more conventional surface code with bosonic phys-
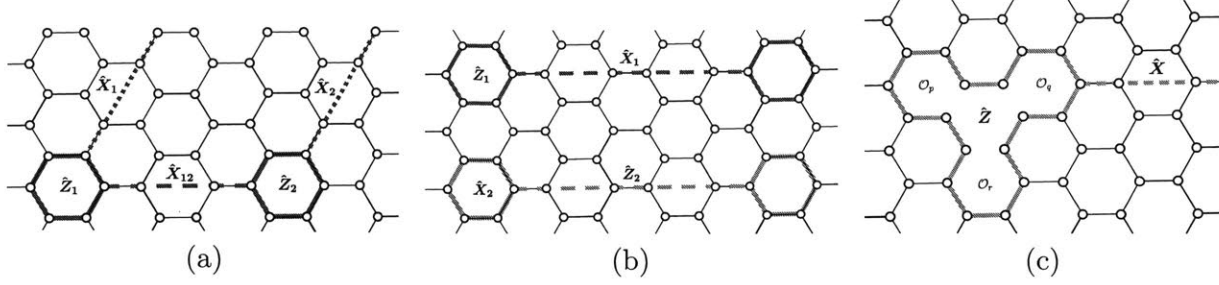
Figure 2-6: Logical qubits in the Majorana surface code. In (a) we stop the measurement of two plaquette operators in subsequent surface code cycles, increasing the ground-state degeneracy by a factor of four. If we take $\hat{Z}_1$ and $\hat{Z}_2$ to be the logical $\hat{Z}$ operators for the two encoded qubits, the corresponding $\hat{X}_1$ and $\hat{X}_2$ operators are given by Wilson lines connecting to the boundary. The two qubits may be coherently manipulated by applying the operator $\hat{X}_{12}$ as shown. In practice, it is simpler to define logical qubits by stopping the measurement of pairs of plaquettes of a single type, with the logical $\hat{X}$ and $\hat{Z}$ defined as shown in (b). We may also consider a logical qubit made of several 'holes', as in (c), to minimize errors during qubit manipulation.

ical qubits. First, while a four-spin stabilizer measurement in the usual surface code requires performing $6-8$ gates/measurements between a set of physical and ancilla qubits [15, 131], stabilizer eigenvalues in the Majorana surface code are obtained via a *single-step measurement* by shining a probe beam. We emphasize that even when measurement is not being performed, the intrinsic charging energy of the islands generates a finite gap $\Delta_1(n_g)$ to creating anyon excitations, and naturally *suppresses* errors at temperatures $k_B T < \Delta_1(n_g)$. We anticipate that the corresponding error tolerance for scalable quantum computation is substantially improved for the Majorana surface code. Second, the Majorana surface code operates with lower overhead than its bosonic counterpart, using three-qubit stabilizers, and requiring no ancilla qubits. Finally, the anyon transmutation required to perform a logical Hadamard gate in the conventional surface code corresponds to a duality transformation that exchanges the star and plaquette toric code operators. This operation is quite difficult to perform on a single logical qubit as it also requires lattice surgery to patch the transformed logical qubit back into the remaining surface code [15, 135]. As lattice symmetries permute anyon sectors in the Majorana plaquette model, anyon transmutation in the Majorana surface code corresponds to a *lattice translation* of the logical qubit, substantially simplifying the Hadamard gate implementation.

2.3.2 Logical qubits and error correction

Logical qubits may be encoded in the surface code by ceasing the measurement of the plaquette operator on a hexagonal superconducting island in a surface code cycle, while continuing measurements on all other plaquettes. In theory, we could stop measuring a single plaquette and define a two-level system, with the $\hat{Z}$ and $\hat{X}$ operators of the logical qubit defined by the plaquette operator and a Wilson line connecting the plaquette to the boundary, respectively. A pair of such qubits on the A-type plaquettes is shown in Figure 2-6a, where the solid and dashed lines

correspond to products of Majorana fermions that define the indicated logical operators. The two qubits shown may also be coherently manipulated by acting with the Wilson line operator connecting the two plaquettes, denoted $\hat{X}_{12}$.

In practice, however, it is difficult to manipulate qubits with an operator that connects to a distant boundary, so it is simpler to encode a logical qubit by stopping the stabilizer measurement on two well-separated plaquettes of the same type. We choose to only manipulate two of the four resulting degrees of freedom by defining $\hat{Z} \equiv \mathcal{O}_p$ and $\hat{X} \equiv W_{pq}$, the Wilson line operator connecting the two plaquettes. We use the opposite convention to define the logical $\hat{Z}$ and $\hat{X}$ operators for a qubit on the adjacent B plaquettes; an example of such logical qubits is shown in Figure 2-6b. We note that when such a qubit is created, it is automatically initialized to an eigenstate of the plaquette operator, with eigenvalue given by the measurement performed in the previous surface code cycle. As a result, logical qubits of type A (B) are initialized to an eigenstate of the $\hat{Z}$ ($\hat{X}$) logical operator.

To reduce errors during qubit manipulation, we may define a qubit by ceasing measurement of multiple adjacent plaquettes as shown in Figure 2-6b. In this particular case, the logical operator $\hat{X}$ is still a Wilson line connecting to another set of distant 'holes'. However, the logical Z is defined as $\hat{Z} \equiv \mathcal{O}_p \otimes \mathcal{O}_q \otimes \mathcal{O}_r$. For the remainder of our discussion, we will consider logical qubits with only a single plaquette operator used to define the logical $\hat{Z}$; the generalization to larger qubits is straightforward.

Errors may occur during qubit manipulation, including (1) single-qubit errors due to the unintended measurement of a local operator involving an even number of Majorana fermions and (2) measurement errors. Single-qubit error correction may be performed on logical qubits by constantly measuring the remaining plaquette eigenvalues during surface code cycles. Since only *pairs* of plaquettes may be flipped simultaneously by a random measurement, corresponding to the nucleation of a pair of anyons of a single type, detecting the change of an odd number of plaquette eigenvalues in a single surface code cycle will generally signal the presence of a random measurement performed on a nearby logical qubit. More precisely, when a stabilizer eigenvalue changes in a surface code cycle, it is efficient to store the location of that stabilizer, and wait several code cycles, accumulating a spacetime diagram of stabilizer errors as additional errors occur [131, 132, 105]. After sufficiently many code cycles, the spacetime diagram may be used to determine the most likely configuration of Wilson lines that could have generated those errors [104, 15] using a minimum-weight perfect matching algorithm [136, 137]. Errors may be subsequently corrected by software when performing logical qubit manipulations and readouts [15]. Random measurement errors involve incorrectly registering the eigenvalue of a plaquette operator; these are naturally corrected by performing multiple surface code cycles to verify the accuracy of a measurement.

2.3.3 Logical gate implementations

The Majorana surface code may be used for universal quantum computation by implementing CNOT, T, and Hadamard gates on logical qubits; this has been extensively studied in the context of the surface code architecture with underlying bosonic degrees of freedom [135, 15]. Here, we describe the implementations of these gates in our realization of quantum computation with a Majorana surface code. Our gate implementations follow the spirit of the implementations presented in [15].

All gates in the Majorana surface code are implemented on logical qubits via a sequence of measurements. Let $\hat{U}$ be the desired unitary we wish to perform on the quantum state of several logical qubits, defined by the logical operators $\{\hat{X}_i\}$ and $\{\hat{Z}_i\}$. It is convenient to keep track of the transformation of the logical state by monitoring the transformation of logical operators $\hat{X}_i \to \hat{U}\hat{X}_i\hat{U}^\dagger$, $\hat{Z}_i \to \hat{U}\hat{Z}_i\hat{U}^\dagger$. In practice, performing the appropriate sequence of measurements will yield the transformation W, such that:

$$\hat{U}\hat{X}_i\hat{U}^\dagger = \pm\hat{W}\hat{X}_i\hat{W}^\dagger \tag{2.20}$$

$$\hat{U}\hat{Z}_i\hat{U}^\dagger = \pm\hat{W}\hat{Z}_i\hat{W}^\dagger \tag{2.21}$$

where the signs depend on the outcomes of specific measurements performed. These measurement outcomes are stored in a software and used to correctly interpret the readout of a logical qubit. In what follows, we will often demonstrate our gate implementations in an "operator picture", where a set of operators in the surface code $\hat{o}_1, \ldots, \hat{o}_n$ and $\hat{p}_1, \ldots, \hat{p}_m$ with eigenvalues ± 1 are measured in an appropriate sequence. This implements a logical gate via the desired transformations:

$$\hat{Z} \to \hat{Z} \otimes \prod_{j=1}^{n} \hat{o}_j = \hat{U}\hat{Z}\hat{U}^\dagger \tag{2.22}$$

$$\hat{X} \to \hat{X} \otimes \prod_{j=1}^{m} \hat{p}_j = \hat{U}\hat{X}\hat{U}^\dagger. \tag{2.23}$$

In practice, the measured outcomes for the $\{\hat{o}_i\}$ and $\{\hat{p}_j\}$ operators will be stored by software and used to obtain the above transformations during logical qubit readout.

CNOT gate: A CNOT gate takes two qubits – a "control" and a "target" – and flips the value of the target qubit based on the value of the control, and returns the control unchanged. The action of a CNOT takes the following form in the basis of two-qubit states:

$$\hat{C} = \begin{pmatrix} 1 & 0 & 0 & 0 \\ 0 & 1 & 0 & 0 \\ 0 & 0 & 0 & 1 \\ 0 & 0 & 1 & 0 \end{pmatrix} \tag{2.24}$$
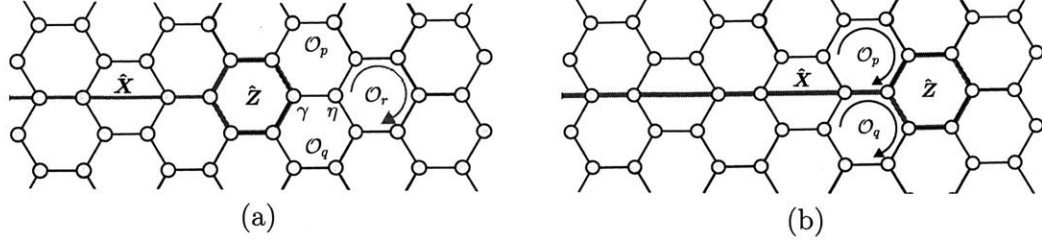
Figure 2-7: We may move a logical qubit defined by $\hat{X}$ and $\hat{Z}$ operators along a given sublattice. We first multiply the logical $\hat{Z}$ by $\hat{\mathcal{O}}_r$ and turn $\hat{\mathcal{O}}_p$ and $\hat{\mathcal{O}}_q$ into four-Majorana operators. After measuring $i\gamma\eta$ in the next code cycle, we extend the logical $\hat{X} \to \hat{X} \otimes i\gamma\eta$. Finally, we begin measuring $\hat{Z}$ in the next surface code cycle and restore $\hat{\mathcal{O}}_p$ and $\hat{\mathcal{O}}_q$ to six-Majorana operators.

A CNOT gate may be implemented by braiding logical qubits in the Majorana surface code. In the simplest case, a CNOT between two logical qubits of different types is implemented through a single braiding operation that produces an overall sign if the hexagonal ends of both qubits contain an anyon, due to the π mutual statistics, demonstrated in Section I. In the following section, we first describe the procedure to move a logical qubit along a given type of plaquette before discussing the braiding procedure required to produce a CNOT gate.

Consider the A-type logical qubit shown in Figure 2-7. To move the qubit one unit to the right, we perform the following sequence of measurements. We begin by multiplying the $\hat{Z}$ logical operator by the eigenvalue of the adjacent r plaquette operator to perform the transformation:

$$\hat{Z} \to \hat{Z}' \equiv \hat{Z} \otimes \hat{\mathcal{O}}_r. \tag{2.25}$$

As the r plaquette is being continuously measured, its eigenvalue $\mathcal{O}_r = \pm 1$ is known from the previous surface code cycle. In the next cycle, we stop measuring $\hat{\mathcal{O}}_r$ and measure the Majorana bilinear $i\gamma\eta$. We then multiply the $\hat{X}$ operator by the measurement outcome, affecting the transformation

$$\hat{X} \to \hat{X}' \equiv \hat{X} \otimes i\gamma\eta. \tag{2.26}$$

In the final surface code cycle, we begin measuring the original $\hat{Z}$ stabilizer and continue to include the measurement of the $\hat{Z}$ stabilizer in all subsequent surface code cycles. Furthermore, we redefine the logical operator $\hat{Z}'$ as

$$\hat{Z}' \to \hat{Z}'' \equiv \hat{Z}' \otimes \hat{Z}. \tag{2.27}$$

The initial qubit configuration and final outcome are depicted schematically in Figure 2-7. This sequence of measurements has shifted the A-type qubit by moving its hexagonal end one unit to the right, and may generally be used to move an A- or B-type logical qubit within the A or B plaquettes, respectively.

We may now braid pairs of logical qubits to perform a CNOT gate in the Majorana surface
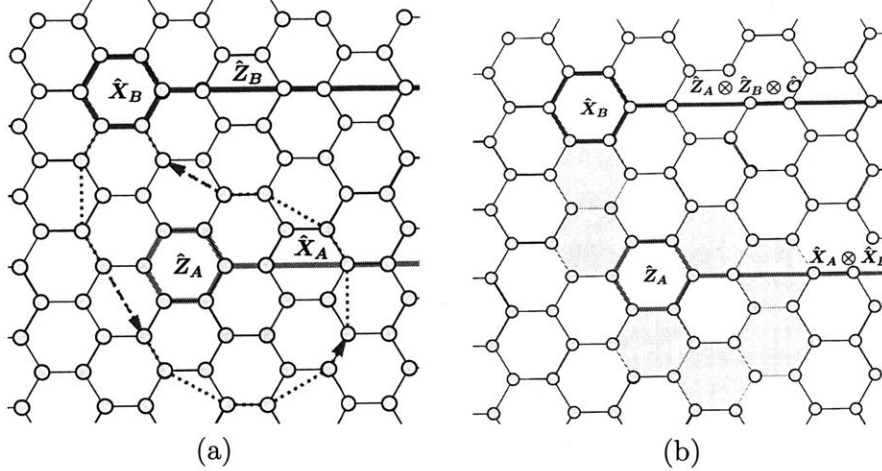
Figure 2-8: **CNOT Gate**. Braiding two logical qubits to perform a logical CNOT. In (a), a possible trajectory for braiding the first qubit around the second is indicated by the dotted line. Since the two qubits live on distinct sublattices, the braiding procedure induces the transformation $\hat{X}_A \to \hat{X}_A \otimes \hat{X}_B$ and $\hat{Z}_B \to \hat{Z}_A \otimes \hat{Z}_B \otimes \hat{O}$, where $\hat{O}$ is the product of the colored plaquettes shown. This performs a CNOT transformation on the braided qubit.

code. The simplest CNOT that we may realize is between two distinct types of qubits, taking the A qubit as the control, as shown in Figure 2-8. Since the qubits are distinct, braiding the B-type qubit – with logical operators $\hat{X}_B$ and $\hat{Z}_B$ – along a closed path ℓ enclosing the second qubit (i) multiplies the Wilson line of the B-type qubit by the anyon charge enclosed by ℓ and (ii) multiplies the Wilson line of the A qubit by the anyon charge of the B qubit. This results in the transformation:

$$\hat{X}_A \to \hat{X}_A \otimes \hat{X}_B \qquad \hat{Z}_B \to \hat{Z}_A \otimes \hat{Z}_B \otimes \prod_{p \in \ell} \hat{O}_p \qquad (2.28)$$

where $\{\hat{O}_p\}$ are A and C-type plaquette operators enclosed by the braiding trajectory, as shown in Figure 2-8. Since the eigenvalues of the enclosed plaquette operators are known from the previous surface code cycle, we may implement the logical CNOT ($\hat{Z}_A \to \hat{Z}_A$, $\hat{Z}_B \to \hat{Z}_A \otimes \hat{Z}_B$) by multiplying the transformed $\hat{Z}_B$ by an appropriate sign. In summary, the simplest braiding process between an A and a B logical qubit implements a CNOT on the B qubit, with the A qubit as the control.

A CNOT between two logical qubits of the *same* type may also be performed by appropriately braiding pairs of distinct types of logical qubits. In this case, we will take one qubit as the control by convention and store the outcome of the CNOT gate in a third ancilla qubit. First, consider performing a CNOT gate on two A-type qubits. To implement the CNOT, we prepare two additional ancilla qubits; the first is an A qubit prepared in the state $|\varphi\rangle \equiv [|+_z\rangle + |-_z\rangle]/\sqrt{2}$, while the second is a B qubit prepared in the state $|+_x\rangle$, with $|\pm_z\rangle$ and $|\pm_x\rangle$ the eigenstates of the logical Z and X operators, respectively. Both ancilla qubits are prepared by measuring a

+1 eigenvalue for the Wilson line joining the pair of plaquettes of the appropriate qubit. For the A (B) qubit, this projects onto an eigenstate of the logical X (Z) operator, and produces the desired ancilla states.

We now represent a complete basis of the four-qubit states as $|z_B, z_c, z_t, z_{\text{out}}\rangle$, referring to the eigenvalues of the logical Z operators of the B ancilla, the control, the target and the ancilla A qubits, respectively. We start out with an initial state $|\psi_{\text{init}}\rangle$ of the form:

$$|\psi_{\text{init}}\rangle \equiv \frac{1}{\sqrt{2}}\Big[|+, z_c, z_t, +\rangle + |+, z_c, z_t, -\rangle \Big] \tag{2.29}$$

Next, we braid the B ancilla qubit around all three remaining qubits as shown in Figure 2-9a. Up to an overall sign determined by the eigenvalues of plaquette operators enclosed by the braiding trajectory that are known from previous surface code cycles, this braiding implements the transformation $\hat{Z}_B \rightarrow \hat{Z}_B \otimes \hat{Z}_c \otimes \hat{Z}_t \otimes \hat{Z}_{\text{out}}$ on the logical Z of the ancilla qubit, where $\hat{Z}_c$, $\hat{Z}_t$ and $\hat{Z}_{\text{out}}$ are the logical Z operators for the control, target, and ancilla A-type qubits, respectively. The final state we obtain is then of the form:

$$|\psi_{\text{final}}\rangle = \frac{1}{\sqrt{2}}\Big[|z_c z_t, z_c, z_t, +\rangle + |-z_c z_t, z_c, z_t, -\rangle \Big] \tag{2.30}$$

This braiding process is convenient, as a measurement of the state of the B qubit can determine whether the the state of the A *ancilla* contains the correct outcome of the CNOT operation. If we now measure the logical Z of the B qubit and obtain $\hat{Z}_B = +1$ then we project onto a state with $z_c z_t = z_{\text{out}}$. In this case, the A ancilla qubit contains the correct outcome of the CNOT between the other A qubits. If $\hat{Z}_B = -1$, however, then $z_c z_t = -z_{\text{out}}$ and the A ancilla contains the opposite of the correct CNOT outcome. In this case, we may act with $\hat{X}_{\text{out}}$ on the A ancilla qubit in the surface code software [15] to obtain the desired final state.

A similar process may be used to perform logical CNOT's between two B qubits; now, we prepare an A ancilla qubit and a B ancilla qubit in the states shown in Figure 2-9b. After braiding the ancilla A qubit around the control, target, and ancilla B qubits, if we measure $\hat{X}_A = +1$, then the B ancilla contains the desired outcome of the CNOT operation. Again, by convention, we take the control qubit to be the first one enclosed by the braiding trajectory, as shown in Figure 2-9b.

Hadamard gate: The Hadamard is a single-qubit gate taking the matrix form:

$$\hat{H} = \frac{1}{\sqrt{2}}\begin{pmatrix} 1 & 1 \\ 1 & -1 \end{pmatrix} \tag{2.31}$$

The action of a Hadamard is to exchange the logical $\hat{X}$ and $\hat{Z}$ operators so that $\hat{H}\hat{X}\hat{H}^\dagger = \hat{Z}$ and $\hat{H}\hat{Z}\hat{H}^\dagger = \hat{X}$. As the logical $\hat{X}$ and $\hat{Z}$ are defined oppositely on different types of qubits, a Hadamard operation in the bosonic surface code corresponds to an electric/magnetic duality transformation that interchanges star and plaquette operators in the toric code. In the
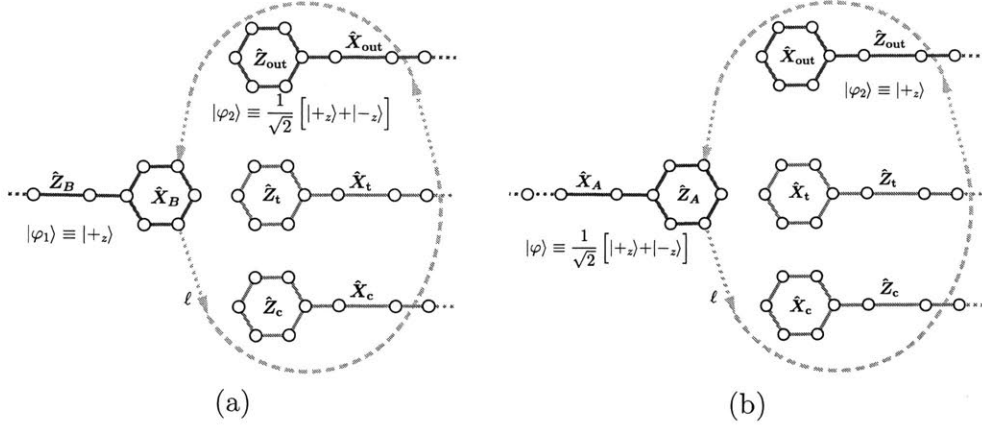
Figure 2-9: Braiding processes that implement the transformation (a) $\hat{Z}_a \rightarrow \hat{Z}_a \otimes \hat{Z}_c \otimes \hat{Z}_t \otimes \hat{Z}_{\text{out}}$ up to an overall sign, as determined by the product of the remaining plaquette operators enclosed by the path ℓ, and (b) $\hat{Z}_{\text{out}} \rightarrow \hat{Z}_{\text{out}} \otimes \hat{Z}_A$, $\hat{Z}_t \rightarrow \hat{Z}_t \otimes \hat{Z}_A$, $\hat{Z}_c \rightarrow \hat{Z}_c \otimes \hat{Z}_A$. The two braids are used to realize CNOT gates between two (a) A-type and (b) B-type logical qubits, respectively. By convention, we take the lowest qubit enclosed by the braiding trajectory to be the control for the logical CNOT.

ordinary surface code, such a transformation is quite difficult to implement, requiring a series of Hadamards on physical qubits enclosing the logical qubit so as to interchange the $\hat{X}$ and $\hat{Z}$ stabilizers, followed by physical swap gates in order to correctly patch the transformed logical qubit back into the remaining surface code array [135]. As lattice symmetries permute the anyons in the Majorana plaquette model, however, the logical Hadamard may be realized in the Majorana surface code by simply moving a logical qubit between *distinct* plaquettes.

We implement the logical Hadamard by the procedure shown in Figure 2-10. Consider an A-type logical qubit. We multiply the logical $\hat{X}$ operator of the qubit, defined by the Wilson line in Figure 2-10a, by the product of the adjacent plaquette operators $\{\hat{\mathcal{O}}_{\mu_k}\}$ extending between the hexagonal ends of the qubit. The eigenvalues of these plaquette operators are known from previous surface code cycles. This operation implements the transformation:

$$\hat{X} \rightarrow \hat{Z}' \equiv \hat{X} \otimes \prod_k \hat{\mathcal{O}}_{\mu_k}. \tag{2.32}$$

At the same time, we multiply the logical $\hat{Z}$ by the adjacent plaquette operator $\hat{\mathcal{O}}_p$, shown in Figure 2-10a, that borders the logical qubit above:

$$\hat{Z} \rightarrow \hat{X}' \equiv \hat{Z} \otimes \hat{\mathcal{O}}_p. \tag{2.33}$$

In subsequent surface code cycles, we stop measuring the eigenvalue of $\hat{\mathcal{O}}_p$. We implement a similar transformation on the other hexagonal end of the logical qubit, by stopping the measurement of the plaquette operator above the other qubit 'hole'. The end result, after performing these operations, is shown in Figure 2-10b. The solid and dashed blue lines indicate the prod-
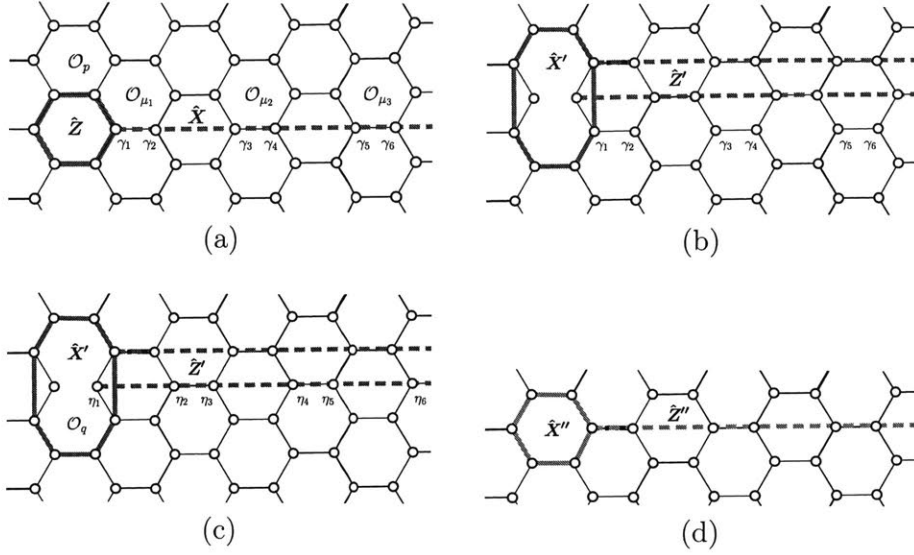
Figure 2-10: **Hadamard gate**. A logical Hadamard is performed by transferring a qubit between distinct sublattices, so that the logical $\hat{X}$ and $\hat{Z}$ operators are exchanged. We do this by taking the qubit in (a) and multiplying by logical $\hat{X}$ by the plaquette operators $\{\hat{\mathcal{O}}_{\mu_k}\}$ and the logical $\hat{Z}$ by $\hat{\mathcal{O}}_p$ and ceasing measurement of the fermion parity of plaquette p, yielding the operators shown in (b). Next, we measure the product $(i\eta_1\eta_2)(i\eta_3\eta_4)\cdots$ and and $\hat{\mathcal{O}}_q$ and multiply with $\hat{Z}'$ and $\hat{X}'$, respectively. The final result is shown in (d).

ucts of the Majorana fermions on the appropriate sites that define the $\hat{X}'$ and $\hat{Z}'$ operators, respectively.

In the next surface code cycle, we measure the product $(i\eta_1\eta_2)(i\eta_3\eta_4)\cdots$ of the Majorana fermions along the lower 'string' that defines the $\hat{Z}'$ operator; this measurement commutes with $\hat{X}'$ since the two operators do not overlap, as shown in Figure 2-10c. Afterwards, we measure $\hat{\mathcal{O}}_q$, as well as the plaquette operator $\hat{\mathcal{O}}_h$ for the other 'hole' of the original logical qubit. Then, we may perform the following transformations on the logical $\hat{X}'$ and $\hat{Z}'$ operators:

$$\hat{X}' \to \hat{X}'' \equiv \hat{X}' \otimes \hat{\mathcal{O}}_q \tag{2.34}$$

$$\hat{Z}' \to \hat{Z}'' \equiv \hat{Z}' \otimes \prod_\ell (i\eta_{2\ell-1}\eta_{2\ell}). \tag{2.35}$$

This yields the logical qubit shown in Figure 2-10d. In subsequent surface code cycles, we continue measuring the eigenvalues of $\hat{\mathcal{O}}_q$ and $\hat{\mathcal{O}}_h$. Since the logical $\hat{Z}$ and $\hat{X}$ operators are defined differently on the A and B-type plaquettes, our procedure for transforming our A qubit into a B qubit implements a logical Hadamard gate. An identical protocol may be used to perform a Hadamard on a logical B qubit.

S and T-gates: Finally, we implement the logical S- and T-gates, described by the following

64

single-qubit operations:

$$\hat{S} = \begin{pmatrix} 1 & 0 \\ 0 & i \end{pmatrix} \qquad \hat{T} = \begin{pmatrix} 1 & 0 \\ 0 & e^{i\pi/4} \end{pmatrix} \tag{2.36}$$

As demonstrated in [15], it is possible to realize these gates by performing a series of logical Hadamard and CNOT gates between the logical qubit and an appropriate logical ancilla qubit. Here, we first discuss the S- and T-gate implementations, given the appropriate ancilla qubit, before outline a procedure for creating these logical ancillas in the surface code.

To implement an S-gate, we prepare a logical ancilla in the state

$$|\varphi_S\rangle \equiv \frac{1}{\sqrt{2}}\Big[\, |+_z\rangle + i\, |-_z\rangle \,\Big] \tag{2.37}$$

Then, if $|\Psi\rangle$ is the state of the logical qubit of interest, the following sequence of logical Hadamard and CNOT gates implements the transformation $|\Psi\rangle \to \hat{S}\,|\Psi\rangle$ [15]:
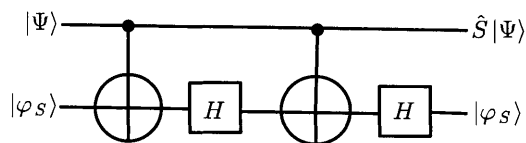
To perform a T-gate, we first prepare a logical ancilla in the state

$$|\varphi_T\rangle \equiv \frac{1}{\sqrt{2}}\Big[\, |+_z\rangle + e^{i\pi/4}\, |-_z\rangle \,\Big]. \tag{2.38}$$

The T-gate is then implemented via a probabilistic circuit. We perform a CNOT between the ancilla and the logical qubit of interest, and then measure the logical $\hat{Z}$ of the qubit. Depending on the measurement outcome, we implement an S-gate as shown below: If the measurement
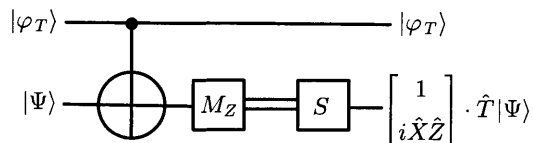
outcome $M_Z = +1$, then we obtain the correct output $\hat{T}\,|\Psi\rangle$; otherwise, if $M_Z = -1$, then we have performed the transformation $|\Psi\rangle \to \hat{X}\hat{T}^{\dagger}\,|\Psi\rangle$. In this case, we implement an S-gate on the logical qubit and obtain the final state $i\hat{X}\hat{Z}\hat{T}\,|\Psi\rangle$. The action of the operator $i\hat{X}\hat{Z}$ may be undone in the surface code software to implement a pure T-gate on the logical qubit [15].

To realize the above implementations, we may prepare logical ancilla qubits in the states $|\varphi_T\rangle$ and $|\varphi_S\rangle$ as follows. First, we create a "short qubit" [15] by ceasing the fermion parity measurement on two adjacent plaquettes p, q belonging to the same sublattice, as shown in Figure 2-11a. For this qubit, let $\hat{X} \equiv \hat{\mathcal{O}}_p$ and $\hat{Z} \equiv i\gamma\eta$. The qubit is initialized to a state $|\Psi_\pm\rangle$ such that $\hat{X}\,|\Psi_\pm\rangle = \pm\,|\Psi\rangle$. In a basis of eigenstates of the logical $\hat{Z}$, the qubit state takes the
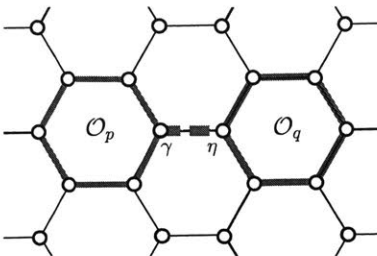
Figure 2-11: **S- and T-gate Ancilla Preparation.** We create the $|\varphi_S\rangle$ and $|\varphi_T\rangle$ ancilla states, needed to realize logical S- and T-gates by preparing the "short qubit" [15] shown above. We cease stabilizer measurements on two adjacent plaquettes p and q. In the next surface code cycle, we perform a rotation of the two-level system defined by $i\gamma\eta$. Finally, we enlargen the logical qubit by extending one end of the qubit, to guarantee stability against noise.

form $|\Psi_\pm\rangle = (|+_z\rangle \pm |-_z\rangle)/\sqrt{2}$. Now, we assume that the two-level system formed by the pair of Majorana fermions γ and η can be manipulated by performing a rotation

$$\hat{R}(\theta) = \begin{pmatrix} 1 & 0 \\ 0 & e^{i\theta} \end{pmatrix} \tag{2.39}$$

that acts in the basis of $|\pm_z\rangle$ states. This may be implemented by using the phase of the adjacent superconducting islands to tune the coupling between the Majorana zero modes [138]. To prepare the state $|\varphi_S\rangle$, we perform the rotation $\hat{R}(\pm\pi/2)|\Psi_\pm\rangle$ in the next surface code cycle, while to prepare $|\varphi_T\rangle$, we perform the operation $\hat{R}((2\pi \pm \pi)/4)|\Psi_\pm\rangle$. Afterwards, to guarantee the stability of the qubit against noise generated by the environment, we increase the length of the logical $\hat{X}$ operator by extending one end of the logical qubit, as discussed in detail previously and shown schematically in Figure 2-7. In practice, a high-fidelity implementation of the S- and T-gates requires that the "short qubits" are put through a distillation circuit, as discussed in [15], which may be implemented using a sequence of logical CNOT gates with other ancilla logical qubits.

We have presented a two-dimensional model of interacting Majorana fermions that realizes a novel type of Z_2 topological order with a microscopic S_3 anyon symmetry. The required multi-fermion interactions in the plaquette model are naturally generated by phase-slips in an array of phase-locked s-wave superconducting islands on a TI surface. Based on this physical realization, we propose the Majorana surface code and provide the necessary measurement protocols and gate implementations for universal quantum computation. The Majorana surface code provides substantially increased error tolerance, reduced overhead, and simpler logical gate implementations over a surface code with bosonic physical qubits. We are optimistic that the Majorana fermion surface code will be physically implemented, and may provide an advantageous platform for fault-tolerant quantum computation.

Chapter 3

Quantum Information Processing with Majorana Zero Modes

The previous chapter introduced a concrete proposal for universal quantum computation using Majorana zero modes in an array of topological superconductor islands. To complement this long-term goal, we propose realistic steps towards quantum information processing with Majorana zero modes that may be addressed in on-going experiments. Following theoretical proposals, over the last few years transport and scanning tunneling microscopy experiments have reported the observation of zero-bias conductance peak as a signature of Majorana zero modes in various material platforms including nanowires [93], atomic chains [95] and topological insulators [96, 139], proximitized by s-wave superconductors. These results suggest the existence of Majorana zero modes, and encourage research towards demonstrating their topological properties. Among these, non-Abelian statistics is widely regarded as the "holy grail" for topological phases of matter and for topological quantum computation.

Theoretical proposals for detecting the non-Abelian statistics of Majoranas have mostly relied on braiding, i.e. moving Majoranas around each other via a sequence of operations. For example, by changing the phase of Josephson junctions, Majorana zero modes localized in Josephson vortices can be braided in an array of superconducting islands on a topological insulator [14]. By tuning the gate voltage, Majoranas in proximitized nanowires can be braided in a T-junction [140, 141]. Detecting non-Abelian statistics further requires measuring the state of Majoranas before and after braiding. Both the motion and measurement of Majoranas are yet to be experimentally achieved. Furthermore, physically moving Majoranas in nanowire networks suffers from dangerous thermal errors that are very difficult to correct [142]. These errors may be avoidable in other proposals that selectively tune couplings between Majoranas to implement braiding transformations [143, 116, 144].

We address practical goals for quantum computation with Majorana zero modes in this chapter. We introduce a new scheme for (i) detecting the non-Abelian statistics of Majorana zero modes and (ii) implementing braiding operations, without any physical braiding, which is

entirely based on projective measurements, as opposed to unitary evolution. In our scheme, a topological qubit encoded in any pair of *well-separated* Majoranas is read out from the transmission phase shift in electron teleportation through the topological superconductor that hosts these Majoranas [99]. Electron teleportation is a remarkable mesoscopic transport phenomenon enabled by the fractional nature of Majorana zero modes and the charging energy of the superconductor. Here we use electron teleportation to directly measure and manipulate Majorana qubits without moving, hybridizing or destroying Majorana zero modes. Importantly, thanks to the spatial separation of Majorana zero modes, teleportation-based Majorana qubit readout is inherently error-free.

In our scheme for "braiding without braiding", the unitary transformation that would be generated by physically exchanging a pair of Majoranas is realized by performing a sequence of projective measurements of Majorana bilinear operators. The theoretical basis for using projective measurements to implement quantum gates was provided in Ref. [145, 27]. Within the framework of non-Abelian topological order, replacing anyon braiding by topological charge measurements was proposed by Bonderson, Freedman and Nayak [146]. On the other hand, electron teleportation provides an ideal way of measuring Majorana qubits in *mesoscopic* topological systems [99], where the charging energy required for teleportation comes from the long-range Coulomb interaction. As a result, the physics of teleportation lies beyond theory of topological order for systems with short-range interactions and in the thermodynamic limit. By combining teleportation-based measurement and measurement-based braiding, our work unveils a novel and practical approach to quantum information processing with well-separated, stationary Majorana zero modes.

Our work is especially timely in view of a recent groundbreaking experiment on epitaxially grown InAs/Al superconducting nanowires [147], which are theoretically predicted to host Majorana end modes under an external magnetic field [125, 90, 91]. Due to charging effects in the Coulomb blockade regime, transport through the nanowire at zero magnetic field is dominated by Cooper pair tunneling, leading to zero-bias conductance oscillations with the gate voltage that are charge-$2e$ periodic. However, above a critical field and in the presence of a superconducting gap, the conductance oscillations become charge-e periodic. The observed charge-e transport in a superconducting state supports the theoretically predicted scenario of electron teleportation via Majorana modes [99, 115, 148]. Another distinctive feature of teleportation is that single-electron transport through the superconducting island is phase coherent [99]. This important property forms the basis for topological qubit readout in this chapter. To detect the phase coherence requires an electron interferometer, which is currently under experimental pursuit [149]. Given these exciting developments, we believe teleportation-based braiding without braiding is a practical scheme for detecting the non-Abelian statistics of Majorana zero modes, and offers a promising prospect for robust quantum information processing.

Our teleportation-based scheme for implementing projective measurements and performing "braiding without braiding" on stationary and spatially-separated Majorana zero modes has

significant advantages over other schemes based on physically moving Majoranas to implement logical gates or to perform qubit readout. For braiding to be feasible, Majoranas must be moved sufficiently slowly to obey an adiabaticity condition [141], which is especially stringent in disordered nanowires without a hard spectral gap [150, 151]. Qubit readout and gate operation in our proposal are not limited by this constraint. Moreover, in the process of moving Majoranas, dangerous thermal errors on the topological qubit may be accumulated, which are extremely difficult (if not impossible) to de-code and correct [152]. Finally, teleportation-based measurement of Majorana qubits has advantages over proposed readout schemes based on charge sensing [141] which can only be performed on pairs of Majorana zero modes that are spatially adjacent.

After completion of this work, other proposals for storing and manipulating Majorana qubits in nanowire networks have been introduced [153, 154], which also uses electron teleportation to measure the fermion parity of well-separated Majorana zero modes. These proposals further propose measurement-based gate implementation of the Clifford group [154, 153], which goes beyond the scope of this work. We note, however, that the detrimental effects of error processes such as quasiparticle poisoning have yet to be properly addressed.

This chapter is organized as follows. We begin by reviewing the phenomenon of phase-coherent electron teleportation through Majorana zero modes. We then describe two teleportation based setups – the Majorana interferometer and the Majorana SQUID – for measuring a topological qubit encoded in a pair of well-separated Majorana zero modes, and for detecting their non-Abelian statistics. Next, we present a general protocol for implementing braiding transformations on Majorana zero modes exclusively through projective measurements. Finally, we provide a concrete experimental realization of our proposal using proximitized nanowires. Our general scheme of teleportation-based braiding without braiding is applicable to any Majorana platform, provided that the topological superconductor hosting the Majoranas has a finite charging energy.

3.1 Conceptual Basis

In this section we lay out the theoretical basis of teleportation-based measurement of a topological qubit encoded in a pair of spatially separated Majorana zero modes. We first elaborate on the transmission phase shift in electron teleportation via a pair of Majoranas and its dependence on the state of the topological qubit, as pointed out in Ref. [99]. Next, we propose two ways of detecting this phase shift, or equivalently reading out the topological qubit, by measuring the conductance in an electron interferometer or the persistent current in a closed loop. We then explicitly show the change of the teleportation phase shift in the process of physically exchanging two Majorana zero modes. The difference in the phase shift—a physical observable measured by interferometry—before and after the braiding directly proves the system has evolved into a new state, thus demonstrating the non-Abelian statistics of Majorana zero modes.

3.1.1 Teleportation-Based Measurement of a Topological Qubit

Let us consider a mesocopic topological superconductor island hosting a number of well-separated Majorana zero modes that have negligible wavefunction hybridization. Each Majorana zero mode of interest is tunnel coupled to a normal metal lead, and the tunnel couplings can be turned on and off by gates. The superconducting island is capacitively coupled to a nearby gate. We assume that the charging energy E_c is smaller than the superconducting gap Δ, but larger than the tunnel coupling to the leads, as defined by Eq.(3.6) below.

In the absence of a tunnel coupling to leads, the ground state energy of the island depends on the total number of electrons N through the charging energy:

$$E(N) = E_c(N - n_g)^2, \tag{3.1}$$

where the offset charge n_g is continuously tunable by the gate voltage. Due to the presence of Majorana zero modes, the superconducting island can accommodate an even and an odd number of electrons on equal ground without paying the energy cost of the superconducting gap. Thus N takes both even and odd integer values. Throughout this chapter, we assume that the island is in the Coulomb blockade regime away from the charge degeneracy point, so that the total charge of the island is fixed, denoted by $N = N_0$. Under this condition, the island has $2^{M/2-1}$ degenerate ground states, where M (an even integer) is the number of Majorana zero modes present. These degenerate ground states form a topologically protected Hilbert space, which we use to encode quantum information. By detuning the island far away from charge degeneracy, the topological qubits are protected against quasiparticle poisoning from outside the island at low temperature.

A complete basis for this 2^{M-1}-dimensional Hilbert space is given by the common eigenstates of a set of nonoverlapping Majorana bilinear operators, e.g., $(i\gamma_1\gamma_2, i\gamma_3\gamma_4, ..., i\gamma_{M-1}\gamma_M)$. A Majorana bilinear operator $i\gamma_a\gamma_b$ has two eigenstates $|\pm\rangle_{ab}$, defined by

$$i\gamma_a\gamma_b|\pm\rangle_{ab} = \pm|\pm\rangle_{ab}. \tag{3.2}$$

Thus, measuring the topological qubit in this basis amounts to measuring the eigenvalue of $i\gamma_a\gamma_b$. Any way of partitioning Majoranas into pairs defines a corresponding basis for the topological qubit, and different bases are related by unitary transformations known as F-symbols, which are determined by the fusion rules for the Majoranas. It is thus desirable to be able to measure the eigenvalue of *any* Majorana bilinear operator, so that the topological qubit can be measured in any basis.

We now describe a teleportation-based protocol to measure the eigenvalue of any Majorana bilinear $i\gamma_a\gamma_b$ by coupling the Majorana island to lead a and to lead b. The bare tunneling

$$G = g_0 + g_1 \cos\left[\frac{e(\Phi - \Phi_c)}{\hbar}\right] i\gamma_1\gamma_2 \qquad\qquad G = g_0 + g_1 \cos\left[\frac{e(\Phi - \Phi_c)}{\hbar}\right] \psi_1\psi_2\gamma_1\gamma_2$$

(a)   (b)
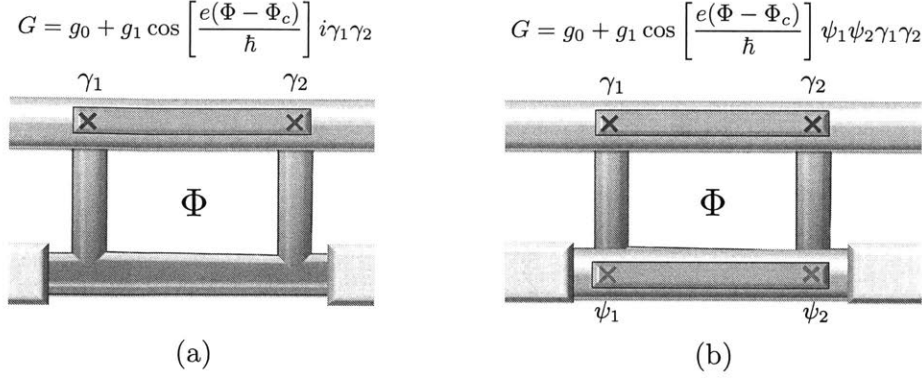
Figure 3-1: **Majorana Interferometer** – Two electron interferometry setups to measure the topological qubit formed by Majorana zero modes γ_1 and γ_2. In both interferometers, one path goes through the topological qubit while the other path goes through (a) a normal metal with sufficiently long phase coherence length (blue) and (b) a second Majorana island initialized in a definite parity state $i\psi_1\psi_2 = \pm 1$.

Hamiltonian is given by

$$H_T^0 = \sum_{j=a,b} t_j c_j^\dagger(0) f(\mathbf{r}_j) + \text{h.c.} \tag{3.3}$$

where $c_j(0)$ is the electron operator at the end of lead j, and $f(\mathbf{r}_j)$ is the electron operator in the island at the tunneling location $\mathbf{r}_j$, where the Majorana zero mode γ_j is located. Next, we expand $f(\mathbf{r}_j)$ in terms of quasiparticle operators in the superconducting island:

$$f^\dagger(\mathbf{r}_j) = \xi_j^*(\mathbf{r}) e^{i\theta/2} \gamma_j + \cdots \tag{3.4}$$

Here $\xi_j(\mathbf{r})$ is the wavefunction associated with the Majorana mode operator γ_j, defined by

$$\gamma_j = \int d\mathbf{r} \left[\xi_j(\mathbf{r}) e^{-i\theta/2} f^\dagger(\mathbf{r}) + \xi_j^*(\mathbf{r}) e^{i\theta/2} f(\mathbf{r})\right]. \tag{3.5}$$

Here, θ is the phase operator of the superconductor, which is conjugate to the electron number operator N and satisfies the commutation relation $[\theta, N] = 2i$. In the operator expansion (3.4) we have neglected all quasiparticles above the superconducting gap which are irrelevant to the low energy physics of our interest, as well as Majorana zero modes at other locations whose amplitudes at $\mathbf{r}_j$ are exponentially small. Thus, as shown by (3.4), in the low-energy Hilbert space the electron creation operator $f^\dagger(\mathbf{r}_j)$ is represented as a product of the Majorana mode operator γ_j and the charge-raising operator $e^{i\theta/2}$ which increases the charge of the island by $1e$. Physically speaking, Eq. (3.4) describes the charge-statistics separation of an electron after entering a topological superconductor: the charge of the electron is spread out over the entire superconductor, while its Fermi statistics is retained by a localized Majorana fermion that is charge neutral.

Substituting (3.4) into the bare Hamiltonian (3.3) yields an effective tunneling Hamiltonian

$$H_T = \sum_{j=a,b} \lambda_j c_j^\dagger(0) \gamma_j e^{-i\theta/2} + \text{h.c.}, \quad \text{with } \lambda_j = t_j \xi_j(\mathbf{r}_j)$$

We define the tunnel coupling Γ as

$$\Gamma = \sum_{j=a,b} 2\pi\rho\lambda_j^2, \tag{3.6}$$

where ρ is the density of states in the leads. Assuming $\Gamma \ll E_\pm$ where $E_\pm \equiv E(N_0 \pm 1) - E(N_0)$ is the energy difference between the charge states $N = N_0$ and $N = N_0 \pm 1$, transmission through the island is dominated by a second-order process, where a single electron tunnels into the island from one lead and a single electron exits from the island to another lead. Therefore, from second-order perturbation in H_T, we obtain an effective coupling between a Majorana island in the off-resonance Coulomb blockade regime and the leads

$$
\begin{aligned}
H_{ab} &= -\lambda_a^* \lambda_b c_b^\dagger(0) c_a(0) \bigg[\frac{\langle N_0 | \gamma_b e^{-i\theta/2} | N_0 + 1 \rangle \langle N_0 + 1 | \gamma_a e^{i\theta/2} | N_0 \rangle}{E(N_0 + 1) - E(N_0)} \\
&\quad + \frac{\langle N_0 | \gamma_a e^{i\theta/2} | N_0 - 1 \rangle \langle N_0 - 1 | \gamma_b e^{-i\theta/2} | N_0 \rangle}{E(N_0 - 1) - E(N_0)} \bigg] + \text{h.c.} \\
&= \gamma_a \gamma_b \left[T_{ab} c_b^\dagger(0) c_a(0) - T_{ab}^* c_a^\dagger(0) c_b(0) \right],
\end{aligned}
\tag{3.7}
$$

where $T_{ab} \equiv \lambda_a^* \lambda_b \left(\frac{1}{E_+} + \frac{1}{E_-} \right)$ is the effective single electron tunneling between lead a and b, mediated by a pair of Majorana zero modes γ_a, γ_b. Due to this entanglement of Majorana degrees of freedom with electron tunneling between two leads, H_{ab} enables a direct projective measurement of the Majorana bilinear $i\gamma_a\gamma_b$, even when γ_a and γ_b are far apart in the superconductor island, as we show below.

Let us first consider the case that the Majorana island is initialized to be an eigenstate of $i\gamma_a\gamma_b$, either $|+\rangle_{ab}$ or $|-\rangle_{ab}$. It follows from (3.7) that the single electron tunneling amplitude from lead a to b, which is mediated by γ_a and γ_b, is equal to $-iT_{ab}$ for the Majorana qubit state $|+\rangle_{ab}$, and $+iT_{ab}$ for the state $|-\rangle_{ab}$. Therefore, the two Majorana qubit states $|\pm\rangle_{ab}$ are distinguishable by the π difference in the transmission phase shift in electron teleportation via a pair of Majorana zero modes [99].

To measure the teleportation phase shift requires quantum interference. We now propose two phase measurement schemes for Majorana qubit readout. The first scheme is based on a conductance measurement in a two-path electron interferometer, with one path going through the Majorana island and the other path serving as a reference. The reference path may be a normal metal with a sufficiently long phase coherence length [99], or a second Majorana island in a definite parity state [110, 155], as shown in Fig. 3-1. The total conductance G then contains a term proportional to $(i\gamma_a\gamma_b)$ due to the interference between the two paths, i.e.,

$$I \sim \varepsilon_1 (i\gamma_1\gamma_2) \frac{e}{\hbar} \sin\left[\frac{e(\Phi - \Phi_c)}{\hbar}\right]$$

$$\gamma_1 \qquad \gamma_2$$

$$I \sim \varepsilon_2 (\psi_1\psi_2\gamma_1\gamma_2) \frac{e}{\hbar} \sin\left[\frac{e(\Phi - \Phi_c)}{\hbar}\right]$$

$$\gamma_1 \qquad \gamma_2$$

$$\Phi \qquad\qquad \Phi$$

$$\psi_1 \qquad \psi_2$$

(a) (b)
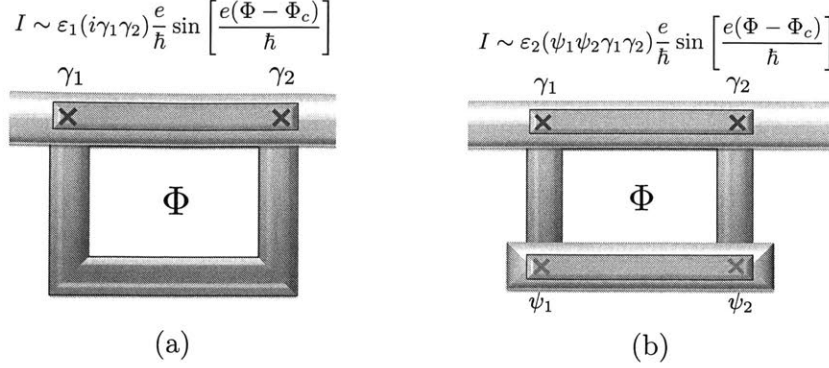
Figure 3-2: **Majorana SQUID** – When the two Majorana zero modes γ_1 and γ_2 are connected by a bridge outside the island to form a closed loop, with the bridge being (a) a normal metal with sufficiently long phase coherence length or (b) a reference Majorana island in a definite parity state $i\psi_1\psi_2 = \pm 1$, the topological qubit defined by $i\gamma_1\gamma_2 = \pm 1$ may be read out by measuring the persistent current I in the ground state, which is a h/e-periodic function of the applied flux Φ.

$G(\Phi) = g_0 + ig(\Phi)\gamma_a\gamma_b$, where g depends periodically on the external magnetic flux Φ enclosed by the two interfering paths, with h/e-periodicity. Since the conductance takes different values for the qubit state $|\pm\rangle_{ab}$, the conductance measurement in such Majorana interferometer provides a projective measurement of the topological qubit in the basis $|\pm\rangle_{ab}$.

The second scheme for qubit readout is based on measuring the persistent current in a closed loop. This loop can be made by connecting Majorana zero modes on the island to the ends of a normal metal bridge (see Fig. 3-2a), or to a reference Majorana island in a definite qubit state (see Fig. 3-2b). Due to the phase coherence of electron motion around the loop, the energy of the closed system depends periodically on the external magnetic flux Φ through the loop with h/e periodicity,

$$E = E_0 + i\varepsilon\gamma_a\gamma_b \cos\left[\frac{e(\Phi - \Phi_c)}{\hbar}\right], \tag{3.8}$$

where Φ_c and ε depend on details of the setup such as tunnel couplings between the island and the normal metal bridge. Eq.(3.8) implies the presence of a persistent circulating current in the loop

$$I = \frac{\partial E}{\partial \Phi} = (i\gamma_a\gamma_b) \frac{e\varepsilon}{\hbar} \sin\left[\frac{e(\Phi - \Phi_c)}{\hbar}\right]. \tag{3.9}$$

This circulating current flows in opposite directions for the two Majorana qubit states $|\pm\rangle_{ab}$. Thus the Majorana qubit is faithfully transferred to the state of the persistent current, which can then be read out by inductive coupling the system to a SQUID loop.

We now estimate the magnitude of the persistent current in a Majorana SQUID by treating the transmission through a Majorana island as single electron hopping across a weak link, as

described by the effective Hamiltonian (3.7). Details of our calculation are presented in the Appendix A.1. When the Majorana SQUID is formed by a single island connected to a normal metal bridge, we find that the magnitude of the persistent current at zero temperature is given by

$$I_0 \sim \frac{e\Gamma}{\hbar} \delta \left(\frac{1}{E_+} + \frac{1}{E_-} \right) \tag{3.10}$$

as explicitly calculated in the Appendix A.1. Here, Γ is the tunnel coupling between the island and the normal metal defined in (3.6), and δ is the single-particle level spacing in the metal, which is inversely proportional to the length of the bridge. An order-of-magnitude estimate based on experimental parameters in Ref. [147, 127, 148] yields $I_0 \sim 10$ nA.

When the Majorana SQUID consists of two islands connected by two normal metal bridges, we determine the persistent current by modeling the bridges as mediating a direct electron tunneling between the Majorana islands. In this case, we consider the Hamiltonian $H = H_T + H_c$ for the full system, where

$$H_c = \sum_{i=1,2} E_c^{(i)} (N_i - n_g^{(i)})^2 \tag{3.11}$$

describes the charging energy for each of the Majorana islands ($i = 1, 2$). Here, $E_c^{(i)}$, N_i and $n_g^{(i)}$ are the charging energies, total charge, and gate charges, respectively, for island i. For simplicity, we let $E_c^{(1)} = E_c^{(2)} = E_c$ for the remainder of our calculation. Furthermore, as shown in Sec. IA, electron tunneling between the two Majorana islands is described at low energies by an effective Hamiltonian in terms of the Majorana operators, as given by

$$
\begin{aligned}
H_t = {}& it_1 \psi_1 \gamma_1 \, e^{i(\theta_1 - \theta_2)/2} + \text{h.c.} \\
& + it_2 e^{ie\Phi/\hbar} \psi_2 \gamma_2 \, e^{i(\theta_2 - \theta_1)/2} + \text{h.c.}
\end{aligned}
\tag{3.12}
$$

with $\theta_{1,2}$ the superconducting phases on each Majorana island and Φ, the applied flux through the ring.

In the presence of a large charging energy $E_c \gg t_{1,2}$, the effective Hamiltonian for the system is, to lowest order in perturbation theory, given by

$$H_{\text{eff}} = \frac{2|t_1 t_2|}{E_+ + E_-} \cos \left[\frac{e(\Phi - \Phi_c)}{\hbar} \right] \psi_1 \psi_2 \gamma_1 \gamma_2, \tag{3.13}$$

where the constant Φ_c provides an overall shift and is present when $t_{1,2}$ are complex. The magnitude of the persistent current is then given by

$$I_0 \sim \frac{e}{\hbar} \left(\frac{|t_1 t_2|}{E_+ + E_-} \right) \tag{3.14}$$

In the Appendix A.1, we also model the persistent current in a Majorana SQUID with two Majorana islands as single electron hopping in a ring with two weak links and determine the magnitude of the persistent current.

3.1.2 Detecting Non-Abelian Statistics from the Teleportation Phase Shift

In this section we explicitly demonstrate the change of teleportation phase shift due to braiding Majorana zero modes in a two-dimensional topological superconductor. Here, Majorana braiding is realized by adiabatically exchanging two identical vortices, which host Majorana zero modes in their cores [86]. Since the teleportation phase shift is a physical observable that can be measured by interferometry, its change before and after braiding implies a change in the quantum state of the system, thus providing direct proof for non-Abelian statistics.

Before proceeding, we first clarify what we mean by non-Abelian statistics of Majorana-carrying vortices in a superconductor. We assume that the superconductor is well described by a Bogoliubov–de Gennes (BdG) Hamiltonian with a pairing potential $\Delta(\mathbf{r}) = |\Delta(\mathbf{r})|e^{i\theta(\mathbf{r})}$ that is a complex function of position. We assume that apart from the overall phase θ, the pairing potential configuration $\Delta(\mathbf{r})$ is non-dynamical and externally set up. On the other hand, we take the overall superconducting phase θ as a quantum mechanical variable, which is conjugate to the total number of electrons N. Throughout this chapter, we take N to be fixed due to the large charging energy, so that θ is fluctuating.

In this setting, Majorana zero modes are not deconfined anyons but a type of "twist defect" [112] associated with vortices, the point-like singularities in $\Delta(\mathbf{r})$. A vortex centered at $\mathbf{R}$ corresponds to a $\pm 2\pi$ winding of the phase $\theta(\mathbf{r})$ around $\mathbf{R}$. As we adiabatically exchange two vortices, $\Delta(\mathbf{r})$ varies slowly. To define non-Abelian statistics, it is required that the full function $\Delta(\mathbf{r})$ returns to its original configuration after the vortex exchange. The evolution of the system into a new quantum state after this process is a defining feature of the non-Abelian statistics of Majorana zero modes bound to vortex cores.

As a warm-up, consider two well-separated vortices centered at $\mathbf{R}_1$ and $\mathbf{R}_2$, and denote the corresponding Majorana zero modes localized in the vortex cores by γ_1 and γ_2. We connect γ_1 and γ_2 by a normal metal bridge to form an interferometer as discussed in Sec. IA, and consider how the teleportation phase shift evolves as a third vortex moves around the vortex at $\mathbf{R}_2$ in a full circle (see Fig. 3-3a). For any given vortex configuration, the wavefunction associated with any Majorana zero mode $\xi_j(\mathbf{r})$, obtained by solving the BdG Hamiltonian, is defined up to an overall choice of sign. Since the Majorana zero mode operator γ_j is defined from $\xi_j(\mathbf{r})$ via Eq. (3.5), γ_j is *not gauge-invariant* as emphasized in Ref. [156]. Nonetheless, this choice of sign for the wavefunctions $\xi_{1,2}(\mathbf{r})$ does *not* affect any physical observables, which necessarily correspond to gauge-invariant operators such as $\xi_j(\mathbf{r})\gamma_j$.

For convenience, we now choose the signs of these wavefunctions such that $\xi_{1,2}(\mathbf{r})$ vary continuously with the moving position of the third vortex. The eigenvalue of the Majorana bilinear operator $i\gamma_1\gamma_2$, taking two possible values ± 1, must stay constant during the braiding
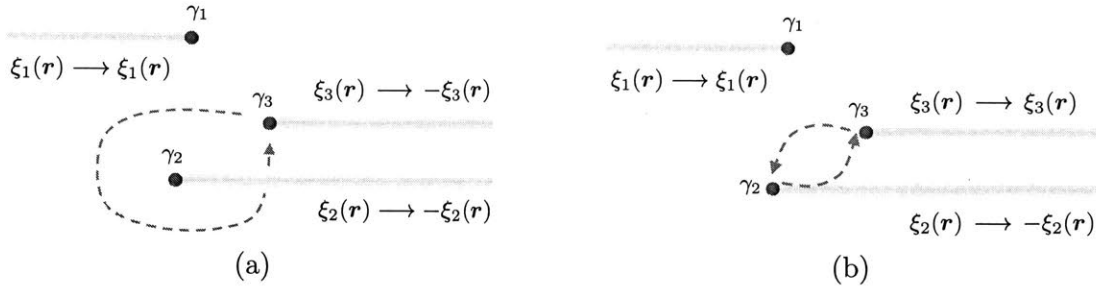
Figure 3-3: **Teleportation Phase-Shift** – Braiding (a) or exchanging (b) Majorana zero modes induces a transformation on the wavefunctions as indicated. The shaded lines shown above are physical regions where the superconducting phase rapidly advances by 2π. The sign change in the transmission amplitude of electron teleportation, due to the "branch cuts" sweeping through the Majorana zero modes [16], provides a signature of their non-Abelian statistics.

process, as expected from continuity. As a result, the teleportation amplitude, whose expression (3.7) contains the product $\xi_1(\mathbf{R}_1)\xi_2(\mathbf{R}_2)\gamma_1\gamma_2$, also varies continuously. As shown by Ivanov [16], after the third vortex returns to its original position and the original vortex configuration is restored, the wavefunction $\xi_1(\mathbf{r})$ comes back to itself while $\xi_2(\mathbf{r})$ and $\xi_3(\mathbf{r})$ change sign, as shown in Fig. 3-3a. Consequently, the phase shift in electron teleportation via Majorana zero modes γ_1 and γ_2 changes by π before and after the third vortex circles around γ_2. This quantized change of a physical observable signals a change in the quantum state of the system induced by braiding.

The teleportation phase can also detect the change in the state of the system when two vortices are *exchanged*, as shown in Fig. 3-3b. We require that the local configurations of the pairing potential near the vortex centers $\mathbf{R}_2$ and $\mathbf{R}_3$ are identical, so that the wavefunctions of the Majorana zero modes γ_2 and γ_3 are related by translation, i.e. $\xi_2(\mathbf{r} - \mathbf{R}_2) = \xi_3(\mathbf{r} - \mathbf{R}_3)$. After exchanging vortices 2 and 3 in the manner shown in Fig. 3-3b, the original vortex configuration $\Delta(\mathbf{r})$ is restored and the Majorana wavefunctions transform as $\xi_2(\mathbf{r}) \longrightarrow -\xi_2(\mathbf{r})$, and $\xi_3(\mathbf{r}) \longrightarrow \xi_3(\mathbf{r})$. To demonstrate the braiding-induced change in the quantum state of the system, we connect γ_2 and a reference Majorana zero mode γ_1 by a normal metal bridge to form an interferometer, and monitor the evolution of the teleportation phase shift in the process of exchanging γ_2 and γ_3, while keeping one end of the bridge attached to the moving Majorana γ_2. The initial teleportation amplitude from $\mathbf{R}_1$ to $\mathbf{R}_2$ is given by the product $\xi_1(\mathbf{R}_1)\xi_2(\mathbf{R}_2)\gamma_1\gamma_2$. After braiding, this interferometer measures the teleportation amplitude from $\mathbf{R}_1$ to $\mathbf{R}_3$, given by $\xi_1(\mathbf{R}_1)\xi_3(\mathbf{R}_3)\gamma_1\gamma_2$. This result should be compared with the teleportation amplitude from $\mathbf{R}_1$ to $\mathbf{R}_3$ before braiding, given by $\xi_1(\mathbf{R}_1)\xi_3(\mathbf{R}_3)\gamma_1\gamma_3$ and measurable by an interferometer containing γ_1 and γ_3. This comparison shows that braiding γ_2 and γ_3 has the effect of the transformation $\gamma_3 \to \gamma_2$. Repeating the same analysis for the teleportation amplitude from $\mathbf{R}_1$ to $\mathbf{R}_2$ shows that same braiding process also has the effect of the transformation $\gamma_2 \to -\gamma_3$. Our analysis based on electron teleportation thus reproduces the "Ivanov rule" for Majorana

braiding [16]

$$\gamma_2 \to -\gamma_3, \gamma_3 \to \gamma_2. \tag{3.15}$$

It is worth noting that the above braiding transformation (3.15) *per se* is non-gauge-invariant, as it is expressed in terms of Majorana operators that suffer from a Z_2 sign ambiguity. Only after the sign convention for the zero mode wavefunction $\xi_{2,3}$ is specified, as we did previously by choosing $\xi_2(\mathbf{r} - \mathbf{R}_2) = \xi_3(\mathbf{r} - \mathbf{R}_3)$, do the Majorana operators $\gamma_{1,2}$ become well-defined, so that the braiding transformation (3.15) becomes meaningful.

Our analysis, as presented, demonstrates that the braiding-induced change in the teleportation phase shift is a physical observable described by a gauge invariant operator involving $\xi_a^* \xi_b \gamma_a \gamma_b$ and $\xi_a \xi_b^* \gamma_a \gamma_b$. Thus the change is teleportation phase shift is a *direct* and *measurable* consequence of the non-Abelian statistics of Majorana zero modes.

3.2 Measurement-Based Braiding

We now describe the theoretical protocol for performing a braiding transformation on a collection of Majorana zero modes exclusively through a sequence of projective measurements, without needing to move the zero modes; such a measurement-based approach was originally described in Ref. [146] in the general context of quantum information processing with anyons. We subsequently describe a teleportation-based measurement protocol for realizing this proposal. Consider the schematic setup shown in Fig. 3-4a; Majorana zero modes γ_1, γ_2, γ_3, and γ_4 are used to encode two logical qubits, while χ_1 and χ_2 will serve, for our purposes, as a single ancilla qubit. We prepare the ancilla qubit in the state $i\chi_1\chi_2 = +1$ so that the initial state of the system is given by

$$|\psi_i\rangle = |\phi\rangle \otimes |i\chi_1\chi_2 = +1\rangle \tag{3.16}$$

with $|\phi\rangle$, the logical two-qubit state of the four Majoranas $\{\gamma_i\}$ that we wish to manipulate.

Our measurement-based braiding protocol is based on the fact that projective measurements of Majorana bilinear operators

$$\hat{P}_{\gamma_n\chi_m}^{(\pm)} \equiv \frac{1 \pm i\gamma_n\chi_m}{2}, \tag{3.17}$$

may be used to implement a unitary braiding transformation up to an overall normalization factor. Specifically, observe the mathematical identity

$$\hat{P}_{\chi_1\chi_2}^{(+)} \hat{P}_{\chi_1\gamma_3}^{(+)} \hat{P}_{\gamma_2\chi_1}^{(+)} |\psi_i\rangle = \frac{1}{2^{3/2}} \hat{U}_{23} |\psi_i\rangle \tag{3.18}$$

77

$\gamma_1 \quad \gamma_2 \quad \chi_1 \quad \chi_2 \quad \gamma_3 \quad \gamma_4$

$i\chi_1\chi_2 = +1$

$|\psi_i\rangle \sim |\phi\rangle \otimes |i\chi_1\chi_2 = +1\rangle$

Measurements

I. $i\gamma_2\chi_1 = +1$

II. $i\chi_1\gamma_3 = +1$

III. $i\chi_1\chi_2 = +1$

$|\psi_f\rangle \sim \hat{U}_{23}|\phi\rangle \otimes |i\chi_1\chi_2 = +1\rangle$

(a)

Measurement j — Outcome = -1 (undesirable) — Measurement $j-1$

Outcome = $+1$ (desirable)

Outcome = ± 1

Measurement $j+1$ — Outcome = -1 (undesirable) — $\cdots$

Outcome = $+1$ (desirable)

(b)
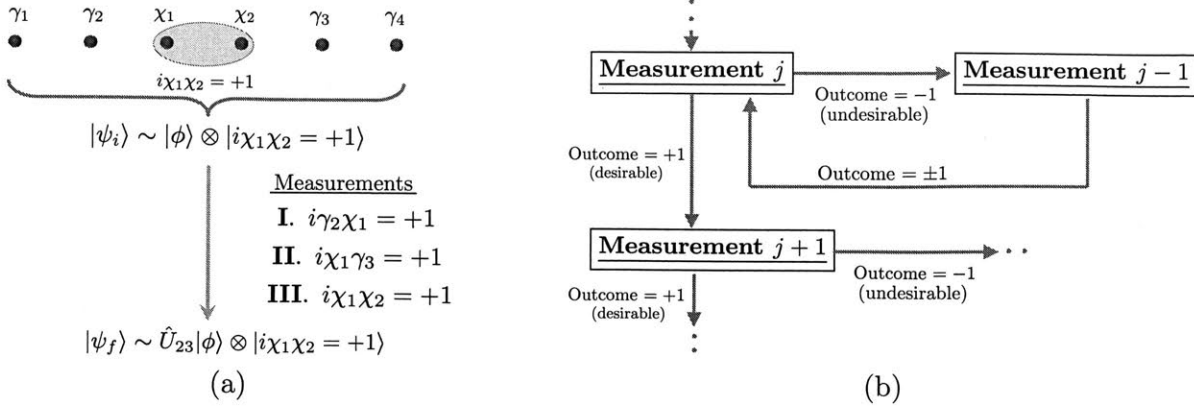
Figure 3-4: **Measurement-Based Braiding** — In (a), we depict the initial state $|\psi_i\rangle$, with Majorana zero modes χ_1 and χ_2 initialized in the state $i\chi_1\chi_2 = +1$. Performing the indicated sequence of measurements is equivalent to braiding Majorana fermions γ_2 and γ_3, up to a normalization factor. If a measurement yields an undesirable outcome, the previous measurement step may be repeated, as indicated in the decision tree in (b), to recover the state before the undesirable measurement was performed.

where the operator

$$\hat{U}_{23} \equiv \frac{1 + \gamma_2\gamma_3}{\sqrt{2}} \tag{3.19}$$

implements the unitary braiding transformation (3.15). The measurements that must be performed to realize this braiding operation, starting from the state $|\psi_i\rangle$, are summarized in Fig. 3-4a.

Successfully performing a measurement-based braiding transformation crucially relies on the outcomes of the measurements that are performed. If a measurement yields an undesirable outcome, however, it is still possible to obtain the desired final state by performing an appropriate sequence of operations. As an example, assume that the first measurement yields the undesirable result that $i\gamma_2\chi_1 = -1$ so that subsequently, the state of the system is given by $|\varphi\rangle \equiv P_{\gamma_2\chi_1}^{(-)}|\psi_i\rangle$. We may recover the state of the system *before* the undesirable measurement, $|\psi_i\rangle$, by measuring the bilinear $i\chi_1\chi_2$. If we find that $i\chi_1\chi_2 = +1$, then we recover the initial state

$$P_{\chi_1\chi_2}^{(+)}|\varphi\rangle = \frac{1}{2}|\psi_i\rangle \tag{3.20}$$

up to a change in normalization, and we may now re-do the measurement of the bilinear $i\gamma_2\chi_1$. More generally, in order to recover the state $|\psi_i\rangle$, we must alternate measurements of the bilinears $i\chi_1\chi_2$ and $i\gamma_2\chi_1$ until we obtain the measurement outcome $i\chi_1\chi_2 = +1$. Observe that

$$P_{\chi_1\chi_2}^{(+)} P_{\gamma_2\chi_1}^{(s_n)} P_{\chi_1\chi_2}^{(-)} \cdots P_{\gamma_2\chi_1}^{(s_1)} P_{\chi_1\chi_2}^{(-)} |\varphi\rangle = -\frac{s_n}{2^n}|\psi_i\rangle \tag{3.21}$$

where $s_i = \pm 1$.

A similar protocol may be used to recover from any undesirable measurement outcome. As summarized in the "decision tree" in Fig. 3-4b, when measurement step j is undesirable, we alternate between measurement steps $j - 1$ and j; this cycle is repeated until measurement step j yields the desired outcome. The number of steps required to recover from an undesirable measurement only changes the normalization of the final state, as can be seen from Eq. (3.21).

We have assumed in our analysis that undesirable measurements only arise due to the inherently probabilistic nature of the measurement-based braiding protocol. However, an undetected error event (e.g. quasiparticle poisoning) that occurs during the measurement procedure can also lead to an undesirable final state. For Majorana zero modes in proximitized nanowires, quasiparticle poisoning from external normal leads may be suppressed by the charging energy of the wire; however, this will not suppress poisoning of Majorana qubits due to the presence of quasiparticles at finite temperature *within* the nanowire, an important issue which has not been addressed. A scheme for quantum error correction with Majorana zero-modes will the subject of a forthcoming work [4].

3.3 Experimental Realization

We now propose a teleportation-based scheme for realizing measurement-based braiding; our proposal is summarized in Fig. 3-5. Consider a superconducting nanowire; gate voltages may be applied along the length of the nanowire to introduce an interface between the topological and trivial superconducting regions, which localizes a Majorana zero mode. In our setup, we apply gate voltages so that six Majorana zero modes appear ($\gamma_1, \gamma_2, \gamma_3, \gamma_4, \chi_1$ and χ_2) at points along the wire. The distance between the Majoranas is assumed to be sufficiently large, so that hybridization between adjacent Majoranas may be neglected. We initialize χ_1 and χ_2 in the state $i\chi_1\chi_2 = +1$ by nucleating the two Majorana zero modes in a topologically trivial region of the nanowire where the total fermion parity is fixed.

Parallel to the existing nanowire in our setup, we now place either (i) a normal metal strip or (ii) a single, proximitized nanowire with gate voltages applied appropriately so that the gated region is topological and hosts two Majorana zero modes (ψ_1 and ψ_2) at its two ends. In both setups, four metal bridges are used to connect the existing nanowire to the normal metal or the second nanowire. In the following section, we will describe the implementation of setup (ii). A similar protocol may be used to implement setup (i), involving the same sequence of interferometric or flux-based measurements, as long as the metal strip has a sufficiently long phase coherence length.

To implement our "braiding without braiding" protocol using setup (ii), we will tune gate voltages to re-position ψ_1 and ψ_2 along the length of the second nanowire; hence we will refer to this nanowire as the "Majorana bus". We initialize the Majorana zero modes in the bus in the state $i\psi_1\psi_2 = +1$. The Majorana bus and the remaining Majoranas in our setup are coupled together by four metallic bridges, and each coupling can be tuned on or off, as indi-
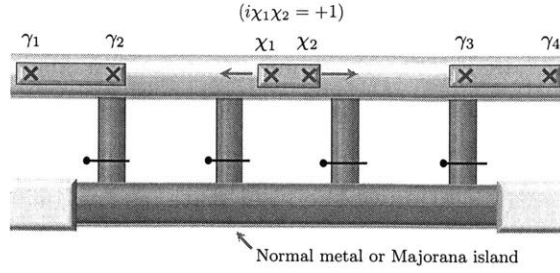
(a) Initialization
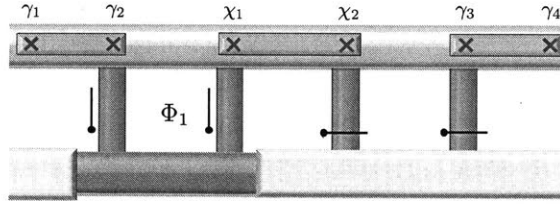
(b) Measurement I $(i\gamma_2\chi_1 = +1)$
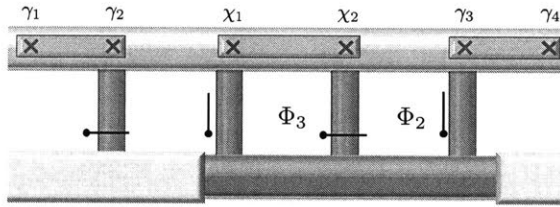
(c) Measurement II $(i\chi_1\gamma_3 = +1)$
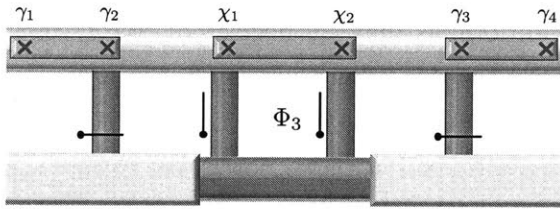
(d) Measurement III $(i\chi_1\chi_2 = +1)$

Figure 3-5: **Experimental Realization**— Protocol for teleportation-based braiding without braiding is illustrated in a nanowire-based Majorana platform. A nanowire hosts six Majorana zero modes at the interface between topological and trivial superconducting regions. $\gamma_1, ..., \gamma_4$ are used as topological qubits and χ_1, χ_2 as an ancilla qubit. The green strip can be either a normal metal with a long phase coherence length or a Majorana island in a definite parity state (a Majorana bus). We begin by initializing the the ancilla qubit in (a), before performing measurements of the appropriate Majorana bilinears in the top nanowire. The coupling between the topological superconductor wire to the normal metal or Majorana bus through the metallic strips may be turned on and off, as indicated schematically by the "switches". Fluxes may be applied through appropriate loops for topological qubit readout via conductance or persistent current measurement.

cated schematically by the "switches" in Fig. 3-5. Each lead is chosen to be shorter than the phase coherence length of the metal, to allow for Majorana qubit readout based on electron teleportation and intereference.

We may perform projective measurements of Majorana bilinears in the top nanowire using the interference of electron trajectories through our setup. This can be achieved by measuring the persistent current in a closed loop, or by measuring the two-terminal conductance across the Majorana bus. To implement either measurement procedure, we first align the Majorana bus so that ψ_1 and ψ_2 are across from the pair Majorana zero modes that we wish to measure, respectively. By turning on the switches on the metallic strips, we introduce electron tunneling between aligned Majorana zero modes on the bus and on the top wire. In the presence of a large charging energy on both the bus and the wire, the effective Hamiltonian describing the full system is given by Eq.(3.13); it depends periodically on the flux through the loop Φ and on the eigenvalue of the Majorana bilinear operator in the top wire. A flux- or conductance-based readout of the Majorana bilinear may then be performed, as detailed in the following section.

3.3.1   Measurement Procedures

To perform a flux-based measurement one of the Majorana bilinears, we tune gate voltages in the Majorana bus so that ψ_1 and ψ_2 are across from the Majorana zero modes in the top row that we wish to measure. For concreteness, consider a measurement of $i\gamma_2\chi_1$, as shown in Fig. 3-5b. After aligning the Majorana bus, we turn off the couplings in the last two metallic strips; this is indicated schematically by the closed and open switches in Fig. 3-5a. Furthermore, we insert a flux Φ_1 through the loop formed by ψ_1, ψ_2, χ_1 and γ_2, as shown.

In the presence of a charging energy that removes the degeneracy between even and odd charge-states on both the Majorana bus and on the top nanowires, the Hamiltonian for the system is $H = H_t + H_c$ – with

$$H_t = it_1\psi_1\gamma_2\, e^{i(\theta_1-\theta_2)/2} + it_2 e^{ie\Phi/\hbar}\psi_2\chi_1\, e^{i(\theta_2-\theta_1)/2} + \text{h.c.}$$

describing the coupling between the Majorana bus to γ_2 and χ_1 through the metallic strips, while H_c is the charging energy on the nanowire and Majorana bus, as given previously in Eq. (3.11). A measurement of the persistent current may be used to determine the Majorana bilinear $i\gamma_2\chi_1$ as detailed in Sec. IIA.

To perform a conductance measurement, we may introduce a weak tunnel coupling between the Majorana bus and two external leads. A similar protocol for measuring stabilizer operators for the Majorana fermion surface code [155, 1, 2, 157] has also been proposed [155, 157]. The tunneling Hamiltonian takes the form

$$H_T = t_L c_L^\dagger \psi_1 e^{-i\theta_1/2} + t_R c_R^\dagger \psi_2 e^{-i\theta_1/2} + \text{h.c.} \tag{3.22}$$

where $t_{L,R}$ are the tunnel couplings to the left and right leads. Here, $e^{\pm i\theta_1/2}$ is the charge-e

81

raising (lowering) operator on the bus, while $c_L^\dagger$ and $c_R^\dagger$ are the electron creation operators in the left and right lead, respectively.

When the charging energy is large, we may derive an effective Hamiltonian that takes the form $H_{\text{eff}} = H_0 + H_1$ to lowest order, where

$$H_0 = \frac{2|t_1 t_2|}{E_+ + E_-} \cos\left[\frac{e(\Phi_1 - \Phi_c)}{\hbar}\right] \psi_1 \psi_2 \gamma_2 \chi_1 \tag{3.23}$$

and

$$\begin{aligned} H_1 = t_L^* t_R &\left(\frac{1}{E_+} + \frac{1}{E_-}\right) \psi_1 \psi_2 c_R^\dagger c_L \\ &+ 2|t_1 t_2| t_L^* t_R \left[\frac{1}{(E_+)^3} + \frac{1}{(E_-)^3}\right] \cos\left[\frac{e(\Phi - \Phi_c)}{\hbar}\right] (i\gamma_2 \chi_1) c_R^\dagger c_L + \text{h.c.} \end{aligned} \tag{3.24}$$

The tunneling conductance depends sensitively on the measured value of the bilinear $i\gamma_2 \chi_1$ and is determined to be

$$G = g_0 + \frac{2\pi e^2}{\hbar} g_1 \cos\left[\frac{e(\Phi_1 - \Phi_c)}{\hbar}\right] \psi_1 \psi_2 \gamma_2 \chi_1. \tag{3.25}$$

Here g_0 is a constant contribution to the conductance that is independent of the measurement outcome, while

$$g_1 = 4|t_L|^2 |t_R|^2 |t_1 t_2| \left[\frac{1}{(E_+)^3} + \frac{1}{(E_-)^3}\right] \left[\frac{1}{E_+} + \frac{1}{E_-}\right] \rho_L \rho_R$$

with $\rho_{L,R}$, the density of states in the left and right leads, respectively.

Chapter 4

Small Fermionic Quantum Codes

Qubits for quantum information processing are mostly built from bosonic degrees of freedom, so that the two basis states of a physical qubit have the same fermion parity. Recently, there has been a growing effort towards storing quantum information in fermion states, so that a qubit is encoded in the fermion occupation number ($n = 0, 1$) or equivalently, the fermion parity $(-1)^n = \pm 1$. Fermion qubits may be constructed from localized sub-gap states in a superconductor [158, 159, 160, 161]. A remarkable recent experiment [162] has demonstrated the coherent manipulation of Andreev states in a superconducting weak link.

In addition to providing a new implementation of a quantum computer, using fermions as the carriers of quantum information necessitates a new computational model, as Fermi statistics forbids a mapping of local quantum gates acting on fermions to local gates acting on bosons [163]. For the same reason, quantum error correction – which is essential for fault-tolerant quantum computation – is different in systems of fermions and of bosons. Quantum error correction in Fermi systems has received attention only recently [109, 1, 142, 152].

An important factor limiting the performance of quantum information processing with fermion qubits is quasiparticle poisoning, whereby a single electron tunnels between states that store information and unknown states in the environment, thereby changing the fermion parity of the encoded qubit, and resulting in an error. Various experiments indicate that the quasiparticle density in a gapped superconductor far exceeds its value in thermal equilibrium [164, 165], and the origin of the excess quasiparticles is not well understood. Fermion parity flips due to quasiparticle poisoning have been directly observed in continuous, real-time measurements on spin-degenerate Andreev bound states in superconducting atomic contacts [162]. DC transport measurements on spin-polarized subgap states in proximitized semiconductor nanowires have inferred possible parity lifetimes up to 10 ms [127, 166]. To extend the lifetime of fermion qubits requires finding reliable ways of correcting both parity-conserving and parity-violating errors.

In addition to Andreev bound-states, spatially-separated zero-energy Majorana fermions (Majorana zero modes) [84, 86] have received recent attention as carriers of quantum information. These fractional degrees of freedom are predicted to exist in topological superconductors. Following theoretical proposals, recent experiments have observed evidence for Majorana

fermions in proximitized nanowires [167, 147, 93], atomic chains [95] and topological insulators [139]. A variety of different approaches to quantum information processing with Majorana fermions have been proposed [84, 109, 1, 2, 155, 157, 168, 3, 169, 154]. The original work of Kitaev [84] proposed storing one qubit in the fermion parity of a pair of spatially separated Majorana zero modes $\gamma_{1,2}$, which together form a complex fermion $f^\dagger = \gamma_1 + i\gamma_2$. However, unlike ordinary complex fermions, the parity operator in Majorana qubits ($i\gamma_1\gamma_2$) is a non-local operator whose eigenvalue cannot be inferred from local measurements. It is thus expected that error processes involving multiple Majorana fermions are suppressed exponentially in their spatial separation. However, this separation does *not* offer protection against quasiparticle poisoning, which is a local process that involves individual Majorana fermions independently [98, 170]. Therefore, quasiparticle poisoning presents a serious challenge for the long-term prospects of quantum information processing with both complex and Majorana fermions.

Recent interest in error correction in Fermi systems has led to a new and more robust approach to Majorana-based quantum computation, in which qubits are encoded in a collection of Majorana fermions [1, 109]; the added redundancy is advantageous for error correction. In Majorana fermion "surface codes" [1, 155], measurements of commuting operators ("stabilizers") in a two-dimensional array of Majorana fermions are used for active error correction and measurement-based quantum computation. A family of Majorana fermion codes has also been constructed from a restricted set of Pauli stabilizer codes for bosonic qubits [109]. In previous studies of fermion codes, however, fermion parity conservation has often been assumed and as a result, the issue of correcting fermion-parity violating errors has not been addressed.

In this chapter, we introduce efficient fermion error-correcting codes that can correct for quasiparticle poisoning errors as well as other error processes. These codes are inherently "fermionic" in the sense that they cannot be mapped onto a bosonic code through local unitary transformations. Error detection and correction, as in the stabilizer formalism [171], is implemented through the projective measurement of a set of commuting multi-fermion operators, or stabilizers, that do not disturb the encoded qubit. An essential feature of our codes that enables error correction is that the encoded qubit can only be determined by measuring a multi-fermion operator, in contrast to the standard encoding of a qubit in a fermion bilinear [84].

This chapter is organized as follows. In Sec. I, we derive a fundamental lower bound on the number of physical fermion qubits N required to encode k logical qubits, such that the smallest logical operator on an encoded qubit is a d-body operator. We refer to such fermion code as $[[N, k, d]]_f$ code. In Sec. II, we introduce the $[[6, 1, 3]]_f$ code, which is the *shortest* fermion quantum error-correcting code that encodes one logical qubit. This code corrects quasiparticle poisoning errors as well as certain parity-conserving errors, and is thus applicable to systems of Majorana fermions and of ordinary fermions. In Sec. III, we demonstrate that any fermion code may be constructed from a restricted class of *classical* binary error-correcting codes. This correspondence allows us to introduce large families of non-degenerate fermion codes, which we discuss at length. We introduce a family of translationally-invariant codes, including codes with

only four-body stabilizer operators. We present another family of codes in which logical qubit states have the same global fermion parity, thus permitting a simpler implementation of logical operations.

In Sec. IV, we reveal the significant advantages of error-correction in Majorana fermion systems, as compared to systems of bosons or ordinary fermions. Provided that Majorana fermions are well separated, the dominant error source is quasiparticle poisoning. Interestingly, we find that in a sufficiently large system, error correction is possible when the poisoning probability is below a threshold ($\sim 10\%$) or *above* an upper limit ($\sim 90\%$). The remarkable feasibility of error correction in a very noisy environment stems from the fact that poisoning the same Majorana fermion twice recovers the qubit, so that error-correction in the Majorana platform is quasi-classical. In Sec. V, we conclude by discussing the physical implementation of Majorana fermion error-correcting codes with four-body operators.

4.1 Fermion Error-Correcting Codes

We would like to identify efficient error-correcting codes for N microscopic fermions that stabilize qubits encoded in the fermion parity. Any complex fermion creation/annihilation operator can be expressed in terms of real (Majorana) fermion operators $\{\gamma_n\}$, which satisfy the anti-commutation relation $\{\gamma_n, \gamma_m\} = 2\delta_{nm}$. In this chapter, we consider a wide class of fermion error-correcting codes, where stabilizers $\mathcal{O}_n$ are products of an even number of Majorana fermion operators, hereafter referred to as "Majorana stabilizers". These stabilizers mutually commute ($[\mathcal{O}_n, \mathcal{O}_m] = 0$), square to the identity ($\mathcal{O}_n^2 = +1$), and commute with the total fermion parity $\Gamma \equiv i^N \gamma_1 \gamma_2 \cdots \gamma_{2N}$.

The unintentional action of the environment on the system, such as quasiparticle poisoning, can lead to decoherence. These errors are represented by the action of t-body operators on the code state. For example, a local fermion-parity flip corresponds to acting a single fermion operator on the qubits, hence $t = 1$. In general, a "weight-t error" is correctable if it is has a unique syndrome, i.e. if the error is *uniquely* identifiable through measurements of stabilizers, i.e. the operator acting on the physical qubits in a correctable error process anti-commutes with a unique set of stabilizer operators. The resulting stabilizer eigenvalue flips are the "syndrome". Such a code, where each correctable error has a unique syndrome, is referred to as "non-degenerate", and we will restrict our attention to such codes for important reasons that we elaborate at the end of this section. Any fermion code in the remainder of our discussion is assumed to be non-degenerate, unless otherwise specified.

We refer to any fermion error-correcting code as an $[[N, k, d]]_f$ code if k qubits are encoded in N complex fermions or $2N$ Majorana fermions, such that a d-body Majorana operator is the smallest logical operator acting on the encoded states, i.e. d is the "code distance". If t is the maximum weight of a correctable error in a non-degenerate $[[N, k, d]]_f$ code, then the code distance $d \geq 2t+1$. A weight-1 error corresponds to an elementary quasiparticle poisoning event,

as represented by a Majorana operator γ_j, which anti-commutes with the parity $\{\gamma_j, \Gamma\} = 0$. In this language, the Kitaev Majorana chain (with stabilizers $\mathcal{O}_n = i\gamma_{2n}\gamma_{2n+1}$) is an $[[N, 1, 1]]_f$ code, while four Majorana fermions with a single stabilizer ($\mathcal{O} \equiv \gamma_1\gamma_2\gamma_3\gamma_4$) define a $[[2, 1, 2]]_f$ fermion code. Importantly, neither code can recover from quasiparticle poisoning events.

We begin by formulating general conditions for fermion error-correcting codes with Majorana stabilizers. First, an $[[N, k, d]]_f$ code must have exactly $N - k$ independent stabilizers to guarantee that the space of states satisfying $\mathcal{O}_n |\Psi\rangle = |\Psi\rangle$ is 2^k-fold degenerate, which is used to encode k logical qubits. Second, error correction on the encoded qubits requires constructing a mapping between operators whose action on the system generates errors and the $2^{N-k} - 1$ stabilizer configurations describing states that result from the occurrence of errors. For example, consider codes that are capable of correcting all elementary fermion-parity flip errors, as represented by single Majorana operators $\gamma_1, \ldots, \gamma_{2N}$. Clearly, it is possible to have a unique syndrome for each of these $2N$ error processes only if $2^{N-k} - 1 \geq 2N$. More generally, a non-degenerate $[[N, k, d]]_f$ code exists, that can correct errors of weight less than t only if

$$2^{N-k} \geq \sum_{m=0}^{t} \binom{2N}{m}.$$

(4.1)

Bounds similar to (4.1) may also be derived for *degenerate* fermion codes, for which two or more distinct, correctable errors have the same syndrome. Such codes are of interest, as they would appear to be more efficient than non-degenerate codes. We observe, however, that there are no fermion codes that are degenerate for weight-1 errors. In such a code, at least two weight-1 operators (say γ_n and γ_m) would have the same syndrome. These errors would only be correctable if $i\gamma_n\gamma_m = +1$ in the codespace, making γ_n and γ_m "ancilla" degrees of freedom that can then be removed entirely from the code. This argument demonstrates that any fermion code encoding one or more qubits must be non-degenerate for elementary quasiparticle poisoning (weight-1) errors. Degenerate fermion codes that can correct for weight-2 errors, may also be of interest to correct for both de-phasing and quasiparticle poisoning in a system of complex fermions. Such codes only improve on the bound (4.1) for non-degenerate fermion codes within a limited range of N, and the existence of these degenerate codes is not clear. Therefore, we choose to focus our attention on non-degenerate codes for the remainder of this chapter.

We conclude this section by observing that any Pauli stabilizer code may be trivially used to construct a fermion code, by representing each Pauli spin by four Majorana fermions with fixed fermion parity [44, 109]. From any $[[N, k, d]]$ Pauli stabilizer code (encoding k qubits in N microscopic spins, with code distance d), one may construct a $[[2N, k, 2d]]_f$ code which can correct weight-1 errors, by making the replacement $X_n \to i\chi_n^{(x)}\gamma_n$, $Y_n \to i\chi_n^{(y)}\gamma_n$, and $Z_n \to i\chi_n^{(z)}\gamma_n$ for each Pauli spin, and by adding the stabilizer $D_n \equiv i\chi_n^x\chi_n^y\chi_n^z\gamma_n$ at each site to the code [44]. Here, $\chi_n^{(x,y,z)}$ and γ_n are Majorana fermion operators. This mapping yields a class of fermion error-correcting codes that can correct for *at most* weight-1 errors, and these codes are often not very efficient. We shall soon present more efficient fermion codes, which

cannot be mapped onto a bosonic code in this manner.

4.2   The Shortest Fermion Code

In the following section, we introduce and study certain families of fermion error-correcting codes. We begin by introducing the shortest fermion code $[[6,1,3]]_f$, which encodes a single logical qubit and corrects for elementary fermion-parity flip errors. We thoroughly describe two operational modes for this error-correcting code in systems of either well-separated Majorana fermions or ordinary complex fermions.

Our $[[6,1,3]]_f$ code is defined by the following stabilizers

$$\mathcal{O}_1 = \gamma_1\gamma_2\gamma_3\gamma_4 \qquad \mathcal{O}_2 = \gamma_3\gamma_4\gamma_5\gamma_6 \qquad \mathcal{O}_3 = \gamma_7\gamma_8\gamma_9\gamma_{10}$$
$$\mathcal{O}_4 = \gamma_9\gamma_{10}\gamma_{11}\gamma_{12} \qquad \mathcal{O}_5 = i\gamma_2\gamma_4\gamma_6\gamma_8\gamma_{10}\gamma_{12} \tag{4.2}$$

This code encodes a single fermion logical qubit, which can be represented by two logical Majorana fermion operators $\Gamma_{1,2}$. The fermion parity of this logical qubit, $i\Gamma_1\Gamma_2$, is given by the total fermion parity of the system:

$$i\Gamma_1\Gamma_2 = \prod_{n=1}^{12} \gamma_n, \tag{4.3}$$

and the logical parity flip operators $\Gamma_{1,2}$ are given by

$$\Gamma_1 = \gamma_1\gamma_3\gamma_5, \qquad\qquad \Gamma_2 = \gamma_2\gamma_4\gamma_6\gamma_7\gamma_8\gamma_9\gamma_{10}\gamma_{11}\gamma_{12}. \tag{4.4}$$

These logical parity flip operators commute with all stabilizers.

Each elementary quasiparticle poisoning process anti-commutes with a unique combination of stabilizers, as indicated in the table below:

γ_1	$\mathcal{O}_1$	γ_7	$\mathcal{O}_3$
γ_2	$\mathcal{O}_1, \mathcal{O}_5$	γ_8	$\mathcal{O}_3, \mathcal{O}_5$
γ_3	$\mathcal{O}_1, \mathcal{O}_2$	γ_9	$\mathcal{O}_3, \mathcal{O}_4$
γ_4	$\mathcal{O}_1, \mathcal{O}_2, \mathcal{O}_5$	γ_{10}	$\mathcal{O}_3, \mathcal{O}_4, \mathcal{O}_5$
γ_5	$\mathcal{O}_2$	γ_{11}	$\mathcal{O}_4$
γ_6	$\mathcal{O}_2, \mathcal{O}_5$	γ_{12}	$\mathcal{O}_4, \mathcal{O}_5$

so that the code is non-degenerate for all weight-1 errors. This may be used to decode and correct for poisoning events in the system that result bit-flip errors on the encoded qubit, by performing constant projective measurements of the commuting stabilizers.

In a system consisiting of well-separated Majorana fermions, dominant error processes are local quasiparticle poisoning events involving single Majorana fermions. In contrast, for a system

87

of *complex* fermions denoted by c_j, there can also be dephasing errors resulting from uninten-tional coupling of local fermion density $c_j^\dagger c_j$ to the environment. Our $[[6, 1, 3]]_f$ code also serves as an error-correcting code for *complex* fermions, after pairing the twelve Majorana fermions into six complex fermions as follows

$$c_1 \equiv \frac{1}{2}(\gamma_1 + i\gamma_{12}) \tag{4.5}$$

and

$$c_n \equiv \frac{1}{2}(\gamma_n + i\gamma_{n+5}) \quad \text{for } n = 2, \dots, 6 \tag{4.6}$$

With the above identification, each of the local fermion parity operators $P_n \equiv 2c_n^\dagger c_n - 1$ anti-commutes with a unique combination of stablizers, as summarized in the following table:

P_1	$\mathcal{O}_1, \mathcal{O}_4, \mathcal{O}_5$	P_2	$\mathcal{O}_1, \mathcal{O}_3, \mathcal{O}_5$
P_3	$\mathcal{O}_1, \mathcal{O}_2, \mathcal{O}_3, \mathcal{O}_5$	P_4	$\mathcal{O}_1, \mathcal{O}_3, \mathcal{O}_4, \mathcal{O}_5$
P_5	$\mathcal{O}_2, \mathcal{O}_3, \mathcal{O}_4, \mathcal{O}_5$	P_6	$\mathcal{O}_2, \mathcal{O}_4, \mathcal{O}_5$

Consider a de-phasing error, which takes the general form of a unitary operator $U_n(\delta\tau) = e^{i\delta\tau \sum_n t_n c_n^\dagger c_n}$ acting on the system. For sufficiently short measurement times $\delta\tau$, we expand the unitary to linear order $U_n(\delta\tau) = 1 + i\delta\tau \sum_n t_n c_n^\dagger c_n + O(\delta\tau^2)$ and only consider *on-site* de-phasing. After the action of $U_n(\delta\tau)$ on the system, a measurement of the stabilizers will either project onto the original state of the system, or onto the state $P_n |\Psi\rangle$ up to an overall phase. Since each P_n has a unique syndrome, the de-phasing error may be uniquely determined and de-coded. Bit-flip errors generated by elementary quasi-particle poisoning processes may also be decoded in this setup, as shown in the previous section.

4.3   General Framework

We now introduce a general framework that allows us to systematically construct a large range of fermion codes, by revealing a remarkable connection between fermion codes with Majorana stabilizers and certain classical error-correcting codes, which allows for a systematic and efficient way to search for fermion codes. This provides one of the main results of this chapter, and is presented in Sec. IIIA. Based on this framework, we obtain two representative families of fermion error-correcting codes, which have larger code distance and can correct for higher-weight errors.

4.3.1   Constructing Fermion Codes from Classical Error Correcting Codes

We now present a systematic construction of fermion codes, by relating them to certain *classical* error-correcting codes, and reducing the search for fermion codes to a well-defined mathematical problem. The starting point for our construction is a representation of Majorana stabilizers as

binary vectors. Any product of Majorana fermion operators may be represented, up to an overall phase factor, as

$$\mathcal{O}_i \sim \prod_{n=1}^{2N} (\gamma_n)^{v_n^{(i)}} \tag{4.7}$$

where $\boldsymbol{v}^{(i)} \equiv (v_1^{(i)}, v_2^{(i)}, \ldots, v_{2N}^{(i)})$ is a *binary* vector, i.e. a vector over the finite field $\mathbb{F}_2 = \{0, 1\}$, which is equipped with both Z_2 addition and Z_2 multiplication. The product of operators $\mathcal{O}_i \mathcal{O}_j$ is represented as vector addition $\boldsymbol{v}^{(i)} + \boldsymbol{v}^{(j)}$. An operator $\mathcal{O}_j$ commutes with the total fermion parity if and only if the corresponding binary vector is self-orthogonal

$$\boldsymbol{v}^{(j)} \cdot (\boldsymbol{v}^{(j)})^T = 0, \tag{4.8}$$

and any pair of such operators mutually commute $[\mathcal{O}_i, \mathcal{O}_j] = 0$ if and only if

$$\boldsymbol{v}^{(i)} \cdot (\boldsymbol{v}^{(j)})^T = 0. \tag{4.9}$$

In this notation, we may compactly specify any fermion error-correcting code by a binary "stabilizer matrix"

$$S \equiv \begin{pmatrix} \boldsymbol{v}^{(1)} \\ \vdots \\ \boldsymbol{v}^{(m)} \end{pmatrix} \tag{4.10}$$

satisfying

$$S \cdot S^T = 0. \tag{4.11}$$

While (4.11) is a necessary and sufficient condition for having independent, commuting stabilizers, the resulting fermion code may be unable to correct for any errors. The distance of the fermion code is precisely the weight of the lowest-weight, binary vector $\boldsymbol{v}$ that satisfies $S \cdot \boldsymbol{v}^T = 0$, as $\boldsymbol{v}$ then corresponds to the smallest operator that commutes with all of the stabilizers and acts non-trivially on the codespace.

A binary matrix satisfying (4.11) specifies a so-called "weakly self-dual" binary *classical* error-correcting code [172]. In a classical code, a bit-string, as specified by a binary vector $\boldsymbol{w} = (w_1, w_2, \ldots)$, may be encoded by multiplying by the *generator matrix*

$$G = \begin{pmatrix} \boldsymbol{v}^{(1)} \\ \vdots \\ \boldsymbol{v}^{(m)} \end{pmatrix} \tag{4.12}$$

of the classical code, i.e. $\boldsymbol{w}^T \to \boldsymbol{w}^T \cdot G$. The space of valid encoded bit-strings is referred to

N	f(x)	Code
7	$1 + x + x^2 + x^4$	$[[7,1,3]]_f$
14	$1 + x + x^4 + x^5 + x^6 + x^7$	$[[7,0,4]]_f$
15	$1 + x + x^2 + x^3 + x^5 + x^7 + x^8 + x^{11}$	$[[15,7,3]]_f$
21	$1 + x^6 + x^9 + x^{12}$ $1 + x + x^3 + x^6 + x^7 + x^{10} + x^{13} + x^{15}$ $1 + x + x^3 + x^5 + x^9 + x^{10} + x^{11} + x^{12}$	$[[21,3,3]]_f$ $[[21,9,3]]_f$ $[[21,3,5]]_f$
23	$1 + x + x^2 + x^3 + x^4 + x^7 + x^{10} + x^{12}$	$[[23,1,7]]_f$
28	$1 + x^4 + x^8 + x^{16}$ $1 + x + x^3 + x^4 + x^5 + x^7 + x^8 + x^9 + x^{11} + x^{16} + x^{19}$ $1 + x^2 + x^8 + x^{10} + x^{12} + x^{14}$ $1 + x^2 + x^4 + x^7 + x^8 + x^9 + x^{11} + x^{15}$ $1 + x + x^2 + x^3 + x^4 + x^5 + x^7 + x^{10} + x^{11} + x^{12} + x^{15} + x^{16}$ $1 + x + x^2 + x^5 + x^8 + x^9 + x^{10} + x^{12} + x^{14} + x^{17}$ $1 + x^3 + x^5 + x^6 + x^8 + x^{11} + x^{12} + x^{13} + x^{14} + x^{15} + x^{17} + x^{18}$ $1 + x + x^3 + x^4 + x^5 + x^7 + x^8 + x^9 + x^{11} + x^{16} + x^{17} + x^{19}$	$[[14,2,3]]_f$ $[[14,5,3]]_f$ $[[14,0,4]]_f$ $[[14,1,4]]_f$ $[[14,2,4]]_f$ $[[14,3,4]]_f$ $[[14,4,4]]_f$ $[[14,5,3]]_f$
30	$1 + x + x^2 + x^5 + x^9 + x^{10} + x^{11} + x^{12} + x^{14} + x^{15}$ $1 + x^2 + x^3 + x^4 + x^5 + x^7 + x^8 + x^{11} + x^{16} + x^{19}$ $1 + x^2 + x^4 + x^5 + x^6 + x^7 + x^9 + x^{11} + x^{12} + x^{17}$ $1 + x + x^4 + x^5 + x^{10} + x^{11} + x^{12} + x^{13} + \displaystyle\sum_{n=16}^{21} x^n$ $1 + x^3 + x^5 + x^6 + x^9 + x^{13} + x^{14} + x^{16}$ $1 + x + x^2 + x^6 + x^7 + x^9 + x^{11} + x^{12} + x^{16} + x^{17} + x^{19} + x^{20}$ $1 + x + x^2 + x^3 + x^4 + x^8 + x^9 + x^{10} + x^{11} + x^{13} + x^{17} + x^{18}$ $1 + x^2 + x^4 + x^6 + x^{10} + x^{14} + x^{16} + x^{22}$	$[[15,0,6]]_f$ $[[15,4,4]]_f$ $[[15,2,6]]_f$ $[[15,6,4]]_f$ $[[15,1,6]]_f$ $[[15,5,3]]_f$ $[[15,3,5]]_f$ $[[15,7,3]]_f$

Table 4.1: **Translationally-Invariant Fermion Codes:** A list of the weakly self-dual (binary) classical codes of size $N \leq 30$ with distance $d \geq 3$, and the corresponding fermion codes that they give rise to, using the mapping presented in the main text. When N is odd, we may obtain a fermion code in a variety of ways, as discussed in Sec. IIID. The fermion codes presented in the table for odd N are obtained from two copies of the classical code, so that the resulting system has an even number of Majorana fermions, and describes a physical Hilbert space.

as the *codespace* $\mathcal{C} \equiv \mathrm{span}(\boldsymbol{v}^{(1)}, \ldots, \boldsymbol{v}^{(m)})$, and any bit-string in the codespace is referred to as a codeword. A *parity-check matrix* H, which projects onto the space orthogonal to $\mathcal{C}$, may be used to decode errors of sufficiently small weight on the encoded bit-string, since $H \cdot \boldsymbol{v} = 0$ if and only if $\boldsymbol{v}$ is a valid codeword (i.e. $\boldsymbol{v} \in \mathcal{C}$). We may also construct the *dual* code $\mathcal{C}^{\perp}$, with generator matrix H and parity-check matrix G. The condition $G \cdot G^T = 0$ implies that $\mathcal{C} \subseteq \mathcal{C}^{\perp}$, which defines a "weakly self-dual" classical code.

The relation we have derived allows us to view the generator matrix G of any weakly self-dual classical code as the stabilizer matrix S of a fermion code. Let the weakly self-dual code have code parameters $[2N, k, d]$, where the classical code distance d is precisely the minimum weight of a codeword, while the classical code dimension $k = \dim(\mathcal{C})$. Our construction yields

the following mapping to a fermion code

$$[2N, k, d] \longrightarrow [[N, N-k, d^\perp]]_f \tag{4.13}$$

where $d^\perp$ is the code distance of the dual code $\mathcal{C}^\perp$. If the weakly self-dual code $\mathcal{C}$ involves an odd number of bits, then we can employ various schemes to construct a fermion code, which we elaborate on in Sec. IIID.

4.3.2 Cyclic Fermion Codes

We now construct representative families of fermion codes with code distance $d \geq 3$ by taking advantage of our mapping to weakly self-dual classical codes. The first family includes all fermion codes with one-dimensional translational symmetry. These codes are obtained from a subset of "cyclic" codes in classical coding theory [172]. The second family describes an infinite set of codes with increasing distance, where all of the encoded qubits have the same global fermion parity. This property would theoretically permit a simpler practical implementation of the logical operators in the code.

We may construct one-dimensional, translationally-invariant fermion codes through the following procedure, which we prove in Sec. 4.5. Consider the polynomial ring $\mathbb{F}_2[x]$, i.e. the set of polynomials in x with coefficients in the field $\mathbb{F}_2$. We now

I. Factorize $x^N - 1$ as $x^N - 1 = f(x)g(x)$

II. Check that $\widetilde{f}(x) \equiv x^{\deg(g)}g(x^{-1})$ divides $f(x)$, where $\deg(g)$ is the degree of $g(x)$.

The first condition provides a well-known way to generate translationally-invariant (cyclic) classical error-correcting codes [172], while the additional second condition yields the subset of these codes which are weakly self-dual, as we demonstrate in Sec. 4.5. If a polynomial $f(x)$ satisfies both conditions, then it may be used to define a translationally-invariant fermion code as follows. From the polynomial $f(x)$, which we write as

$$f(x) = \sum_{m=0}^{N-1} f_m x^m \tag{4.14}$$

we extract the vector $\boldsymbol{f} = (f_0, \ldots, f_{N-1})$, which we may take to be the binary vector representation of a Majorana stabilizer. In this way, any polynomial of the form (4.14) represents a Majorana operator acting on a system of N Majorana fermions. Similar techniques have been successfully applied to find Majorana stabilizer codes in two and three spatial dimensions [6].

If N is even, we take the polynomials

$$f(x), \ x f(x), \ x^2 f(x), \ \ldots, \ x^{N-\deg(f)} f(x) \tag{4.15}$$

91

to define the $[N - \deg(f)]$ stabilizers of a fermion code with N microscopic Majorana fermions. These stabilizers are all independent of each other, by construction, while the condition (II) guarantees that all of the stabilizers commute with each other and with the fermion parity. In practice, $f(x)$ is precisely the so-called "generator polynomial" [172] of a weakly self-dual, binary cyclic classical code, which we have then used to define a fermion code. If N is odd, we may take two disjoint copies of the classical code to define the resulting fermion code, which now has $2N$ Majorana fermions. In this case, the fermion code is defined by the stabilizers

$$f(x), \; x f(x), \; x^2 f(x), \; \ldots, \; x^{N-\deg(f)} f(x),$$
$$x^N f(x), \; x^{N+1} f(x), \; \ldots, \; x^{2N-\deg(f)} f(x) \tag{4.16}$$

Translationally-invariant fermion codes with code distance $d \geq 3$ that are obtained from weakly self-dual cyclic codes of size $N \leq 30$ via our construction, are indicated in Table I. Many of these codes can correct for higher-weight errors, beyond the simplest quasiparticle poisoning events. For example, the $[[15, 1, 6]]_f$ code has code-distance $d = 6$ and can correct for any weight-2 fermionic error. From the polynomial $f(x)$ indicated in Table I, we observe that the fermion code is defined by stabilizers $\mathcal{O}_1, \mathcal{O}_2, \ldots, \mathcal{O}_{14}$ where

$$\mathcal{O}_i \equiv \gamma_i \gamma_{i+3} \gamma_{i+5} \gamma_{i+6} \gamma_{i+9} \gamma_{i+13} \gamma_{i+14} \gamma_{i+16} \tag{4.17}$$

This code may be used either for well-separated Majorana fermions or for complex fermions, to correct elementary de-phasing or quasiparticle poisoning errors. As another example, the $[[23, 1, 7]]_f$ code, which is based on the well-known classical Golay code, has stabilizers $\mathcal{O}_1, \mathcal{O}_2, \ldots, \mathcal{O}_{11}$, $\mathcal{O}_{23}, \mathcal{O}_{24}, \ldots, \mathcal{O}_{33}$ where

$$\mathcal{O}_i \equiv \gamma_i \gamma_{i+1} \gamma_{i+2} \gamma_{i+3} \gamma_{i+4} \gamma_{i+7} \gamma_{i+10} \gamma_{i+12} \tag{4.18}$$

and can correct for any weight-3 fermionic error.

4.3.3 Fermion Codes with Fixed Global Fermion Parity in the Codespace

More complex families of fermion error-correcting codes with increasing code distance may also be constructed by searching for other weakly self-dual classical codes. We now review the code parameters for one such family of fermion codes, which has the important advantage that the global fermion parity is fixed in the codespace, so that all of the encoded qubits have the same global parity. In practice, this would make practical implementation of these codes more feasible, since all logical operators on the encoded qubits simply measure the parity of some subset of the Majorana fermions in the code. The explicit construction of the stabilizers for these codes is provided in Sec. 4.6. This family of fermion codes has code parameters

$$\left[\left[2^{m-1}, \; 2^{m-1} - B(r, m), \; 2^{r+1} \right] \right]_f \tag{4.19}$$

Classical (Weakly Self-Dual)	Fermion Code

$$[2N, k, d] \longrightarrow [[N, N-k, d^\perp]]_f$$

$$[2N-1, k, d] \xrightarrow{\text{Concatenation}} [[2N-1, 2N-1-k, d^\perp]]_f$$

$$[2N-1, k, d] \xrightarrow{+\gamma_{2N}} [[N, N-k, d^\perp]]_f^* \quad \frac{\text{Complex Fermions}}{\text{(no q.p.p errors)}}$$
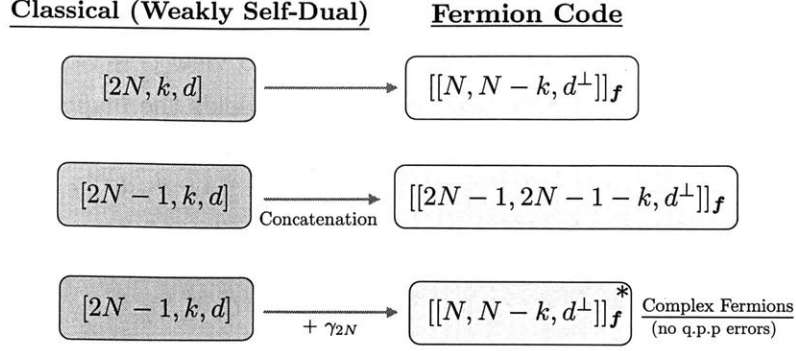
Figure 4-1: **Code Mappings:** A summary of the mappings between classical (weakly self-dual) error-correcting codes, and various fermion codes. When the number of bits in the classical code is even, the generator matrix of the code may be taken to be the stabilizer matrix S of the fermion code. When the number of bits is odd, one can concatenate two such codes, or add a single Majorana so as to describe a physical Hilbert space. The latter case is useful in platforms with complex fermions where quasiparticle poisoning is suppressed, and the indicated code distance assumes that parity-violating processes are forbidden.

with $m \geq 2r + 1$ and

$$B(r, m) \equiv \sum_{j=0}^{r} \binom{m}{j}. \tag{4.20}$$

We refer to this family as the $\mathrm{RM}_f(r, m)$ codes as these codes are obtained from a subset of the well-known Reed-Muller classical error-correcting codes. Any member of this family can *at least* correct for elementary quasiparticle poisoning errors.

A simple example of a code in this family is $\mathrm{RM}_f(1, 4) = [[8, 3, 4]]_f$, whose stabilizers may be written as eight-Majorana operators, in the form

$$\mathcal{O}_1 \equiv \prod_{m=1}^{8} \gamma_{2m} \qquad \mathcal{O}_2 \equiv \prod_{m=1}^{8} \gamma_{2m-1} \qquad \mathcal{O}_3 \equiv \prod_{m=1}^{8} \gamma_m \tag{4.21}$$

$$\mathcal{O}_4 \equiv \prod_{m=1}^{4} \gamma_m \gamma_{m+9} \qquad \mathcal{O}_5 \equiv \prod_{m=1}^{2} \gamma_m \gamma_{m+4} \gamma_{m+8} \gamma_{m+12} \tag{4.22}$$

Observe that the global fermion parity $\Gamma = \mathcal{O}_1 \mathcal{O}_2$, so that all of the encoded states have parity $\Gamma = +1$.

4.3.4 Fermion Codes and Code Concatenation

We now present, in formal terms, the more general schemes for constructing fermion codes from weakly self-dual classical error correcting codes with an *odd* number of bits, i.e. with code parameters $[2N+1, k, d]$ and generator matrix G. In this case, the simplest way to construct a

fermion code in order to guarantee that the resulting code has an even number of Majorana zero modes, and thus describes a physical Hilbert space, is to view $G \oplus G$ as the stabilizer matrix for a fermion code. This "code concatenation" protocol yields the mapping

$$[2N - 1, k, d] \quad \longrightarrow \quad [[2N - 1, 2N - 1 - k, d^{\perp}]]_f \tag{4.23}$$

and is reminiscent of the well-known Calderbank-Shor-Steane (CSS) construction [173, 174], in which two classical error correcting codes $C_{1,2}$ satisfying $C_1 \subseteq C_2$, may be used to construct a Pauli stabilizer code. The mapping (4.23) is equivalent to the statement that a weakly self-dual CSS code may be used to construct a fermion code by replacing X_i, $Z_i \rightarrow \gamma_i$ [109]. This construction may also be generalized by "concatenating" two different weakly self-dual classical codes, each with an odd number of bits, to produce a new fermion code.

A second protocol – which is useful as a method for constructing codes in platforms with complex fermions in which de-phasing is the primary source of error – involves taking G to be the stabilizer matrix for a code in a platform of $2N$ Majorana fermions. Since the classical code involves $2N - 1$ bits, none of the stabilizers in the fermion code act on the last Majorana fermion (γ_{2N}). As a result, while not all elementary quasiparticle poisoning errors are detectable, higher-weight errors can still be corrected, a feature which may be useful in platforms where de-phasing is the primary error source and quasiparticle poisoning is suppressed. We emphasize that both of the above protocols are only needed in the construction of a fermion code when the classical code involves an odd number of bits.

4.3.5 Error Correction in Bosonic and Fermionic Codes

We conclude our discussion of fermion codes by highlighting the important differences between error correction in Bose and Fermi systems, as well as the advantages of error correction in fermionic platforms where quasiparticle poisoning is the dominant error-source. As we have emphasized, there Fermi statistics generically forbids a local unitary mapping between fermionic and bosonic systems. In contrast, a non-local unitary transformation on a Bose system will not give rise to a fermion error-correcting code, since local errors in the fermion system will be non-local in the Bose system and will be un-correctable. An example of this phenomenon is given by the celebrated 5-qubit code, which encodes a single logical qubit in the state of five spins, and can correct for single-qubit errors.

The stabilizers for the $[[5, 1, 3]]$ (five-qubit) code are given by

$$\mathcal{O}_i \equiv \sigma_i^x \sigma_{i+1}^z \sigma_{i+2}^z \sigma_{i+3}^x \quad (i = 1, \dots, 4) \tag{4.24}$$

with "periodic boundary conditions", i.e. so that $\hat{\sigma}_{i+5} = \hat{\sigma}_i$. All operators commute and square to the identity. The Pauli operators for the encoded qubit are given by $\hat{Z} \equiv \prod_{i=1}^5 \sigma_i^z$, $\hat{X} \equiv \prod_{i=1}^5 \sigma_i^x$. Since the code distance is $d = 3$, and the code can correct for single-qubit errors, after performing a non-local unitary (Jordan-Wigner) transformation, local fermion operators

that represent distinct quasi-particle poisoning events – which correspond to string operators of the spins – may have identical syndromes. Performing a Jordan-Wigner transformation of the 5-qubit code, $\sigma_n^z = -i\gamma_{2n-1}\gamma_{2n}$, $\sigma_n^x = \gamma_{2n-1}\prod_{m=1}^{n-1}(-i\gamma_{2m-1}\gamma_{2m})$, naturally yields a stabilizer code for Majorana fermions, where the commuting operators now stabilize the fermion parity of the entire system. We observe, for example, that after this transformation

$$\gamma_2 = \sigma_1^y \qquad \gamma_7 = \sigma_1^z\sigma_2^z\sigma_3^z\sigma_4^x \tag{4.25}$$

Therefore, within the ground-state subspace of the 5-qubit code, both of these single-Majorana operators have identical syndromes since $\gamma_7\,|\Psi_{\mathrm{gs}}\rangle = \gamma_7\,\mathcal{O}_1\,|\Psi_{\mathrm{gs}}\rangle = i\gamma_2\,|\Psi_{\mathrm{gs}}\rangle$. More generally, the action of the operators γ_n and γ_{n+5} are indistinguishable through measurements of the stabilizer operators. Therefore, the fermion code obtained from a non-local unitary transformation on the 5-qubit code cannot correct for quasiparticle poisoning errors.

Our approach to fermion codes highlights an important advantage of error correction in Majorana platforms, where quasiparticle poisoning is the dominant error source. Our inequality for non-degenerate Majorana stabilizer codes (4.1) is the fermionic counterpart of the quantum Hamming bound for Pauli stabilizer codes [175, 171]. The asymptotic limit of the Hamming bound for large N [173] highlights an important advantage of error-correction in the Majorana platform. Let p be the probability per site that an elementary quasiparticle poisoning error occurs within a time $\Delta\tau$. The probability p gives the *typical* fraction of Majorana fermions that have experienced a quasiparticle poisoning event in this time interval; in other words, an error of weight $2Np$ will have typically occurred in time $\Delta\tau$. Assuming that our code only needs to correct for typical error configurations, the inequality (4.1) simplifies, and its behavior for large N is given by

$$\epsilon \leq 1 - 2\,H(p) \tag{4.26}$$

where $\epsilon \equiv k/N$ is the *code efficiency* and $H(p)$ is the binary entropy function $H(p) \equiv -p\log_2(p) - (1-p)\log_2(1-p)$. Error-correction appears to possible in a fermion code even when the poisoning probability p is *large*, as the code efficiency $\epsilon > 0$ when $|p - \frac{1}{2}| > c$ with $c \approx 0.39$. This reflects the fact that the number of typical configurations for quasiparticle poisoning in a fermion system decrease as the error probability $p \to 1$. In contrast, the entropy of error configurations grows much faster in Pauli stabilizer codes, since there are three single-qubit errors per site, giving rise to a probability threshold p_c above which error correction is impossible.

4.4   Physical Implementation of Fermion Codes

Fermion codes with sufficiently few-body interactions may admit a convenient physical implementation in platforms with Majorana zero modes. As demonstrated in [99] a striking signature of Majorana fermions in a mesoscopic superconducting island is the presence of phase-coherent

(a) Measurement of $\mathcal{O}_1$ and $\mathcal{O}_2$ (b) Measurement of $\mathcal{O}_3$
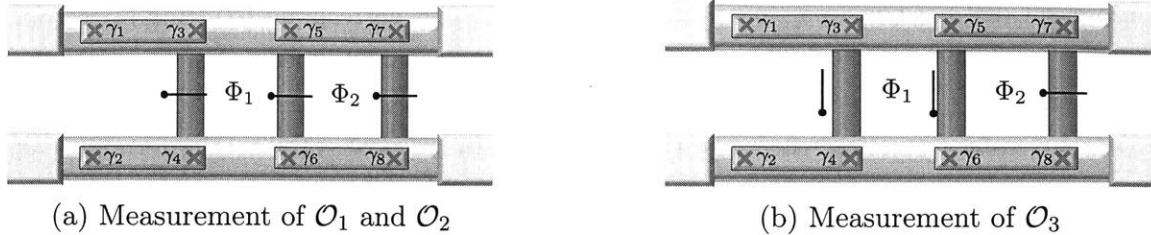
Figure 4-2: **Implementation of the $[[4, 0, 4]]_f$ Code:** Gate voltages are applied on two proximitized nanowires so that 6 well-separated Majorana fermions appear. Metal bridges (shown in blue) couple the nanowires, with voltages applied to tune the couplings "on" or "off" as indicated by the switches in the figures. Each wire has a large charging energy. In (a), the two-terminal conductance using the leads (shown in yellow) may be used to measure $\mathcal{O}_1$ and $\mathcal{O}_2$, while in (b) a measurement of the persistent current flowing in a loop enclosing flux Φ_1 measures $\mathcal{O}_3$. A similar protocol involving a flux Φ_2 may be used to measure $\mathcal{O}_4$.

single-electron transport (termed "teleportation"). Measurements of the transmission phase-shift of electron "teleportation" through Majorana zero modes – by measuring the conductance in an electron interferometer or the persistent current in a closed loop – may be used to perform projective measurements of two-body and four-body Majorana operators [3].

In this section, we present a physical implementation of the simplest fermion code derived from weakly self-dual Reed-Muller codes in Sec. IIC, $\mathrm{RM}_f(1, 3) = [[4, 0, 4]]_f$ code, which is defined by the stabilizers

$$\mathcal{O}_1 \equiv \gamma_1 \gamma_3 \gamma_5 \gamma_7 \qquad \mathcal{O}_2 \equiv \gamma_2 \gamma_4 \gamma_6 \gamma_8 \tag{4.27}$$

$$\mathcal{O}_3 \equiv \gamma_3 \gamma_4 \gamma_5 \gamma_6 \qquad \mathcal{O}_4 \equiv \gamma_5 \gamma_6 \gamma_7 \gamma_8 \tag{4.28}$$

While the codespace encodes no qubits, this code can correct for any elementary quasiparticle poisoning errors; as a result, its physical implementation may be useful to study quasiparticle poisoning times in a platform of Majorana zero modes. Our physical implementation may be extended to implement other fermion codes with sufficiently few-body interactions, such as the translationally-invariant $[[7, 1, 3]]_f$ code, which only involves quartic interactions, and is the fermionic counterpart to the well-known Steane code [176].

The physical implementation of the $[[4, 0, 4]]_f$ code involves using two parallel semicoductor nanowires with spin-orbit coupling, and proximitized by s-wave superconductors, as shown in Fig. 4-2. In the presence of a large Zeeman field, it is well-known that the proximitized nanowire goes into a topological superconducting regime, which localizes Majorana zero modes at the interface with a trivial superconductor. In the setup shown in Fig. 4-2, gate voltages may be applied along the length of the nanowires to create alternating interfaces between topological and trivial p-wave superconducting segments that host Majorana zero modes, in order to realize the configuration of twelve Majorana fermions shown. The Majoranas are well-separated so that hybridization between adjacent zero modes may be neglected. Furthermore, normal metal

bridges (shown in blue) are placed between the two nanowires and between the lower nanowire to introduce a coupling between the appropriate Majorana zero modes, which may be tuned by applying voltages along the bridges. Finally, we assume that the total charge on each nanowire segment is fixed by taking the charging energy E_C to be large on each nanowire..

Due to the large charging energy on each nanowire, the quartic Majorana operators $\mathcal{O}_1$ and $\mathcal{O}_2$ in the $[[4, 0, 4]]_f$ code may be measured by applying fluxes through elementary loops formed by the nanowires and the metal bridges in our setup and measuring the persistent current, which depends sensitively on the stabilizer eigenvalue (e.g. $I \sim \epsilon(e/\hbar)\sin[e\Phi_1/\hbar]\mathcal{O}_1$). Projective measurements of the other two quartic operators may be performed by measuring the two-terminal conductance through leads attached to the ends of the two nanowires – shown in yellow in Fig. 4-2 – which is sensitive to the eigenvalue of the appropriate quartic operator. As an example, for the measurement of the $\mathcal{O}_3$ in Fig. 4-2b, the two-terminal conductance $G = g_0 + g_1\mathcal{O}_3$ [3, 155]. Intricate details of the persistent-current and conductance-based measurements of Majorana operators are provided in Ref. [3].

4.5   Weakly Self-Dual Cyclic Codes

The codespace $\mathcal{C}$ of a cyclic code on N bits is identified with an *ideal* I in the quotient ring $R = \mathbb{F}_2[x]/\langle x^N - 1\rangle$ [172] where $\mathbb{F}_2[x]$ is the polynomial ring over the finite field $\mathbb{F}_2$, while

$$\langle x^N - 1\rangle \equiv \left\{ h(x)\,(x^N - 1) \,|\, h(x) \in \mathbb{F}_2[x] \right\} \tag{4.29}$$

is the ideal generated by $x^N - 1$. An ideal I is a collection of elements $\{g_i\}$ in the ring R satisfying the property that $\sum_i r_i g_i \in I$ where $r_i \in R$; that is, I is an additive subgroup of R that is invariant under multiplication by any element of R.

To construct the generator matrix for any weakly self-dual cyclic code, we first observe that R is a principal ideal ring, i.e. any ideal $I \subseteq R$ is generated by a single polynomial $f(x) \in I$, which is the lowest-degree, monic polynomial contained in the ideal. We may prove this by contradiction. Let $h(x) \in I$, so that $h(x) = q(x)f(x) + r(x)$ where the remainder satisfies $\deg(r) < \deg(f)$. Since $h(x) \in I$, we must have $r(x) \in I$, in which case $\deg(r) \geq \deg(f)$ since $f(x)$ is the lowest-degree monic polynomial in I. Therefore, $r(x) = 0$ and $f(x)$ divides any $h(x) \in I$. We conclude that $I = \langle f(x)\rangle$. Furthermore, the generator $f(x)$ of any ideal in R must divide $x^N - 1$. We may again prove this by contradiction. Let $q(x)f(x) + r(x) = x^N - 1$ for some appropriate choice of $q(x)$ and $r(x)$. Here, the remainder $r(x) \neq 0$ iff $\deg(r) < \deg(f)$. As a result, $r(x) = q(x)f(x) \bmod x^N - 1$, so that $r(x) \in I$. Using the fact that $f(x)$ has minimal degree in I, we conclude that $\deg(r) > \deg(f)$, so that $r(x) = 0$. Then $f(x)$ divides $x^N - 1$.

Therefore, the generator of any ideal $I \subseteq R$ may be constructed by factorizing $x^N - 1 = f(x)g(x)$. Since $f(x)$ is a monic polynomial of degree-d, $g(x)$ must be also be monic, of degree

$(N-d)$. If we write

$$f(x) = \sum_{m=0}^{d} f_m x^m \qquad g(x) = \sum_{m=0}^{N-d} g_m x^m \tag{4.30}$$

then the condition $x^N - 1 = f(x)g(x)$ is equivalent to the matrix equation $F \cdot G^T = 0$ where

$$F = \begin{pmatrix} f_0 & f_1 & f_2 & \cdots & f_d & 0 & 0 & \cdots \\ 0 & f_0 & f_1 & \cdots & f_{d-1} & f_d & 0 & \cdots \\ \vdots & & \ddots & \ddots & & \ddots & \ddots & \\ 0 & 0 & \cdots & f_0 & f_1 & \cdots & f_{d-1} & f_d \end{pmatrix} \tag{4.31}$$

$$G = \begin{pmatrix} g_{N-d} & g_{N-d-1} & \cdots & \cdots & g_0 & 0 & 0 & \cdots \\ 0 & g_{N-d} & \cdots & \cdots & g_1 & g_0 & 0 & \cdots \\ \vdots & & \ddots & & & & \ddots & \\ 0 & 0 & \cdots & g_{N-d} & \cdots & \cdots & g_1 & g_0 \end{pmatrix}$$

We observe that, by construction both G and F have full row-rank. Therefore, if we take F to be the generator matrix of the classical cyclic code $\mathcal{C}$, then G must be the parity-check matrix. Alternatively, G is the generator matrix of the dual code $\mathcal{C}^\perp$, with generator polynomial

$$\widetilde{f}(x) \equiv x^{N-d} g(x^{-1}) \tag{4.32}$$

The code $\mathcal{C}$ is weakly self-dual iff $\mathcal{C} \subseteq \mathcal{C}^\perp$. This can only be the case if $\langle f(x) \rangle \subseteq \langle \widetilde{f}(x) \rangle$ in which case, $\widetilde{f}(x)$ must divide $f(x)$.

To summarize, we may factorize $x^N - 1 = f(x)g(x)$ and then check that $\widetilde{f}(x)$, as defined in (4.32), divides $f(x)$. In this case, the matrix F may be taken to be the binary *stabilizer matrix* for the fermion code. Since $F^T F = 0$ by construction, all of the operators in the code commute with each other and with the total fermion parity.

4.6 $\mathrm{RM}_f(r, m)$ from Reed Muller Codes

As we have already seen, a convenient way to construct a binary matrix S satisfying $S \cdot S^T = 0$, is to construct the rows of S from orthogonal basis vectors for a binary vector space. A particularly convenient choice, which yields a class of fermion codes where the total fermion parity is fixed in the codespace is given by classical Reed-Muller codes $\mathrm{RM}(r, m)$ [172], which are constructed from the vector space of polynomials of degree-r in m binary variables. The $\mathbb{F}_2$ dimension of

98

this space is precisely

$$k_{\mathrm{RM}} = \sum_{j=0}^{r} \binom{m}{j}. \tag{4.33}$$

The Reed-Muller codes are known to be weakly self-dual [172] when $m \geq 2r + 1$.

The microscopic expressions for the stabilizers in the corresponding fermion error-correcting code are obtained by representing each monomial of degree less than $(r + 1)$ as a binary vector. We begin by representing the variable x_k as a binary vector $\boldsymbol{v}^{(k)} \in (\mathbb{F}_2)^{2^m}$ with an alternating sequence of 2^{m-k} ones and zeros, i.e.

$$x_k \longrightarrow \boldsymbol{v}^{(k)} \equiv (\underbrace{1, \ldots, 1}_{2^{m-k} \text{ times}}, \underbrace{0, \ldots, 0}_{2^{m-k} \text{ times}}, \underbrace{1, \ldots, 1}_{2^{m-k} \text{ times}}, \ldots)$$

while 1 is represented as $1 \longrightarrow \boldsymbol{v}^{(0)} \equiv (\underbrace{1, \ldots, 1}_{2^m \text{ times}})$. Monomials are represented by taking vector products, i.e.

$$x_j x_k \longrightarrow \boldsymbol{v}^{(j,k)} \equiv \boldsymbol{v}^{(j)} \star \boldsymbol{v}^{(k)} \tag{4.34}$$

where

$$\boldsymbol{v}^{(j)} \star \boldsymbol{v}^{(k)} \equiv \left(v_1^{(j)} v_1^{(k)}, \ v_2^{(j)} v_2^{(k)}, \ldots, v_{2^m}^{(j)} v_{2^m}^{(k)} \right) \tag{4.35}$$

In this way, we may represent all of the monomials that form the basis elements of the vector space of polynomials of degree-r in m binary variables, as binary vectors. These vectors are then used to construct the rows of the generator matrix of the Reed-Muller code [172], which may then be taken to be the stabilizer matrix of a fermion code when $m \geq 2r + 1$. As an example, the matrix of stabilizers for the $[[4, 0, 4]]_f$ code, as obtained from this construction, is precisely the generator matrix for $\mathrm{RM}(1, 3)$ and is given by

$$S_{[[4,0,4]]_f} = \begin{pmatrix} 1 & 1 & 1 & 1 & 1 & 1 & 1 & 1 \\ 1 & 1 & 1 & 1 & 0 & 0 & 0 & 0 \\ 1 & 1 & 0 & 0 & 1 & 1 & 0 & 0 \\ 1 & 0 & 1 & 0 & 1 & 0 & 1 & 0 \end{pmatrix} \tag{4.36}$$

Appropriately adding rows of this matrix yields a more convenient choice of stabilizers for this code, involving only quartic Majorana operators. These stabilizers may be explicitly written as

$$\mathcal{O}_1 \equiv \gamma_1 \gamma_3 \gamma_5 \gamma_7 \qquad \mathcal{O}_2 \equiv \gamma_2 \gamma_4 \gamma_6 \gamma_8 \tag{4.37}$$

$$\mathcal{O}_3 \equiv \gamma_3 \gamma_4 \gamma_5 \gamma_6 \qquad \mathcal{O}_4 \equiv \gamma_5 \gamma_6 \gamma_7 \gamma_8. \tag{4.38}$$

as presented in the main text. Similarly, the matrix of stabilizers for $\mathrm{RM}_f(1,4) = [[8,3,4]]_f$ is given by

$$S_{[[8,3,4]]_f} = (\boldsymbol{v}^{(0)}, \boldsymbol{v}^{(1)}, \boldsymbol{v}^{(2)}, \boldsymbol{v}^{(3)}, \boldsymbol{v}^{(4)})^T \tag{4.39}$$

Yet another example is given by $\mathrm{RM}_f(2,5) = [[16,0,8]]_f$ with stabilizer matrix $S_{[[16,0,8]]_f} = (\boldsymbol{v}^{(0)}, \boldsymbol{v}^{(1)}, \boldsymbol{v}^{(2)}, \boldsymbol{v}^{(3)}, \boldsymbol{v}^{(4)}, \boldsymbol{v}^{(5)}, \boldsymbol{v}^{(1,2)}, \boldsymbol{v}^{(1,3)}, \boldsymbol{v}^{(1,4)}, \boldsymbol{v}^{(1,5)}, \boldsymbol{v}^{(2,3)}, \boldsymbol{v}^{(2,4)}, \boldsymbol{v}^{(2,5)}, \boldsymbol{v}^{(3,4)}, \boldsymbol{v}^{(3,5)}, \boldsymbol{v}^{(4,5)})^T$. More generally, the generator matrix for an $\mathrm{RM}(r,m)$ code with $m \geq 2r + 1$ corresponds to a fermion code with parameters given in (4.19). The code distance d is precisely the Hamming distance for the dual code to $\mathrm{RM}(r,m)$ code which is the code $\mathrm{RM}(m - r - 1, m)$.

Part II

Fracton Topological Order

Haah's code provides a remarkable example of an exotic quantum phase in an exactly solvable model. As reviewed in Chapter 1, the ground-state of this model exhibits a sub-extensive degeneracy on the torus, and distinct ground-states cannot be distinguished by local observables. Related to this sub-extensive "topological" degeneracy is the existence of gapped excitations that are strictly localized in space, a feature which lies beyond the paradigm of topological quantum field theory. In this section, we systematically construct solvable models of interacting spins and fermions in three spatial dimensions, that describe stable, gapped phases of matter with immobile, point-like topological excitations, reminiscent of Haah's code. We term the gapped excitations, which are immobile due to the intricate patterns of entanglement in the ground-state, "fractons". We introduce a generalization of conventional lattice gauge theory that describes fracton topological phases and as a consequence, we obtain a duality between fracton topological order and interacting systems with global symmetries along sub-systems (e.g. planar symmetries). We also propose solvable models in which fractons carry a protected internal degeneracy, and behave as a natural generalization of non-Abelian anyons in a three-dimensional quantum system. We provide a self-contained description of the algebraic techniques used to study these exactly solvable models. This section is based on Ref. [5, 6, 7, 8].

Chapter 5

New Kinds of Topological Quantum Order

In this chapter, we introduce a class of translationally-invariant, solvable Hamiltonians of interacting Majorana fermions that exhibit a new kind of fermion topological quantum order. These models have extensive topological degeneracy and a hierarchy of topological excitations that are only free to move within sub-manifolds of the full lattice. In one particular Hamiltonian in $d = 3$ spatial dimensions, the fundamental excitations are strictly localized, while composites of these excitations are free to move along one- and two-dimensional surfaces. The fundamental excitations are termed "fractons", as they behave as fractions of a mobile particle. Due to its fermionic nature, the topological order in our model enables an electron to break up into these immobile fractons; this appears to be the ultimate form of electron "fractionalization" in three dimensions.

To systematically search for these models, compute their ground-state degeneracy on a d-dimensional torus and study their excitations, we introduce a purely algebraic description of commuting Majorana Hamiltonians. We demonstrate that on a d-dimensional lattice with a two-site basis and a single interaction term per unit cell, such a Hamiltonian *generically* exhibits extensive topological degeneracy. We emphasize that each of our models may be written in terms of complex fermions by choosing appropriate pairings of Majorana fermions over the entire lattice. Our models also admit a *local* mapping to a boson model with identical topological degeneracy and a similar dimensional hierarchy of excitations, after projecting out half of the Hilbert space. We note that one of our models has similar phenomenology to a spin model studied in ref. [177, 178].

Our approach to studying ideal Majorana Hamiltonians provides a novel geometric framework for topological order, beyond topological quantum field theory. Remarkably, a commuting Majorana Hamiltonian on a torus specifies an algebraic variety – defined as the common zeros of a collection of polynomials over a finite field – that encodes all physical properties of the topologically-ordered state. While a TQFT assigns a ground-state sector to an isotopy class

of smooth, closed curves on a manifold, our models associate ground-state sectors with curves based on finer equivalence relations, resulting in extensive topological degeneracy in dimensions $d \geq 3$. We emphasize that our models are distinct from the exotic phase realized by Haah's code [46] and related models [179], due to the presence of mobile topological excitations that are composites of fractons. As a related matter, separating a set of isolated fractons "optimally" only requires creating a finite number of mobile excitations during intermediate steps. Unlike Haah's code, this energy barrier is independent of the distance of separation.

Universal features of our interacting Majorana models clearly demonstrate that they are in distinct phases from non-interacting stacks of lower dimensional systems. We consider one of our Hamiltonians – the Majorana checkerboard model – as a concrete example. First, in a non-interacting stack of lower-dimensional systems, *all* point-like topological excitations necessarily appear at the ends of string-like operators (Wilson lines). In contrast, the immobile fracton excitation in the checkerboard model appears in isolation at the corners of membrane-like operators, which cannot be made smaller. (An argument of Ref. [109] can be adapted here.) This feature alone *rigorously* establishes this model as distinct from any stack of lower-dimensional systems. Second, the topological ground-state degeneracy D for the Majorana checkerboard model on an $L \times L \times L$ torus satisfies $\log_2 D = 3L - 3$, for any L. The universal, sub-leading correction to $\log_2 D$ is a unique signature of this exotic phase that is impossible to obtain using a stack of lower-dimensional systems that respect the same lattice symmetries of our model; if it were a stack of lower-dimensional systems, $\log D$ must be simply doubled as the system size is doubled. We emphasize that both of the above features are independent of energetics. Even the low-energy effective theory of a stacked system with a similar excitation spectrum would still be describing an identifiably distinct quantum phase of matter, as these universal properties would be different. For similar reasons, the remaining Majorana models identified in this chapter may not be obtained by a stacking procedure.

5.1 Overview

Due to the length of this chapter, we begin with a detailed summary of our findings. We consider exactly solvable Hamiltonians of interacting Majorana fermions that realize exotic forms of topological order. On a d-dimensional lattice with a basis, these Hamiltonians will be the sum of a single type of local operator over all lattice sites

$$H = -\sum_m \mathcal{O}_m \tag{5.1}$$

so that all operators mutually commute and square to the identity, i.e.,

$$[\mathcal{O}_m, \mathcal{O}_n] = 0, \qquad (\mathcal{O}_n)^2 = +1. \tag{5.2}$$
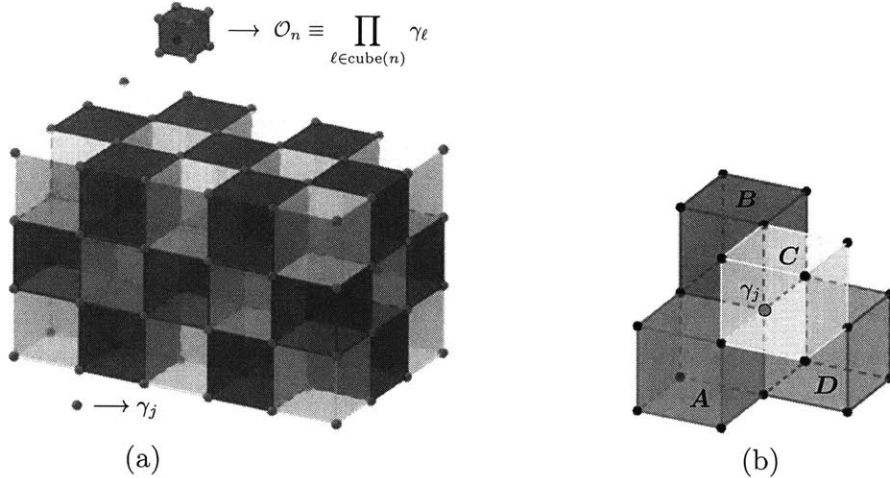
Figure 5-1: **Majorana Checkerboard Model:** The Majorana checkerboard model is defined on a cubic lattice, as in (a), with a single Majorana fermion per lattice site (colored red). The operator $\mathcal{O}_n$ is the product of the 8 Majorana fermions at the vertices of a cube. The Hamiltonian is a sum of these local operators over every *other* cube (colored blue) in a checkerboard pattern. As any pair of operators either share exactly one edge or none, all operators mutually commute. We choose to label the cubic operators A, B, C, and D as shown in (b). Acting with a single Majorana operator γ_j creates these four excitations.

The operator $\mathcal{O}_n$ is required to be a product of an even number of Majorana fermions, so that the fermion parity of the entire system is conserved. A ground state $|\Psi\rangle$ of (5.1) will satisfy the constraint that

$$\mathcal{O}_m |\Psi\rangle = |\Psi\rangle, \tag{5.3}$$

for all m.

In Section 5.2, we introduce a purely algebraic approach to systematically search for and study topological order in commuting Majorana Hamiltonians (5.1). A similar approach has been used previously to study topological order in commuting Pauli Hamiltonians [47]. We represent the operator $\mathcal{O}$ appearing in (5.1) as a set of Laurent polynomials over the field $\mathbb{F}_2$, which consists of two elements $\{0, 1\}$ with $\mathbb{Z}_2$ addition and multiplication. We derive a mathematical condition for a set of such polynomials to represent a commuting Majorana Hamiltonian with topological order. This polynomial representation enables us to analytically determine the topological ground state degeneracy on a d-dimensional torus and deduce properties of topological excitations using algebraic methods.

Using this polynomial approach, we demonstrate the following results. First, a topologically-ordered commuting Majorana Hamiltonian on a lattice with a two-site basis may be entirely specified by a single polynomial over $\mathbb{F}_2$. The ground state degeneracy for such a Hamiltonian on a d-dimensional torus of size L, which we denote by D_0, will *generally* take the

asymptotic form:

$$\log_2 D_0 = c\, L^{d-2} + O(L^{d-3}) \tag{5.4}$$

for some constant c. We perform an exhaustive analysis and discover a class of commuting Majorana fermion models on a three-dimensional lattice with a two-site basis, which exhibit *extensive* topological degeneracy of the form (5.4) with $d = 3$.

Remarkably, despite being translationally invariant, our models admit fundamental point-like excitations that are strictly localized in space, and cannot move without paying a finite energy cost to create additional excitations. Composites of these fundamental excitations, however, are *topological* excitations that are free to move within sub-manifolds of the d-dimensional lattice. We term these fundamental excitations that behave as fractions of mobile particles, "fractons." Furthermore, we refer to bound states of fractons that can only move freely along an n-dimensional manifold as "dimension-n" particles. In particular, a dimension-2 particle can be an anyon with well-defined fractional statistics.

To motivate further study of ideal Majorana Hamiltonians, we now describe in detail the phenomenology of fracton excitations and their composites in the simplest of our models, the Majorana checkerboard model. As shown in Figure 5-1(a), here the operator $\mathcal{O}_n$ is the product of the eight Majorana fermions at the vertices of a cube. The Hamiltonian is simply the sum of these operators over a face-centered-cubic (fcc) array of cubes, forming a three-dimensional checkerboard. Since adjacent cubes share a common edge with two vertices, operators $\mathcal{O}_n$ on different cubes are mutually commuting, and their common eigenstate defines the ground state. For convenience in later analysis, we choose to identify four species of cube operators – A, B, C, and D – as shown in Figure 5-1(b).

A fundamental excitation in the Majorana checkerboard model is obtained when the eigenvalue of a cube operator $\mathcal{O}_n$ is flipped. The product of $\mathcal{O}_n$ over all cubes of a single type (A, B, C, or D) is equal to the fermion parity Γ of the entire system and is fixed.

$$\Gamma = \prod_{p \in A} \mathcal{O}_p = \prod_{p \in B} \mathcal{O}_p = \prod_{p \in C} \mathcal{O}_p = \prod_{p \in D} \mathcal{O}_p, \tag{5.5}$$

Therefore, a single cube-flip excitation cannot be created alone, and is a topological excitation. Remarkably, the fundamental cube excitation in this model is completely *immobile*, as we observe through the following physical argument. In the checkerboard model, acting on the ground-state with a single Majorana fermion flips the eigenvalues of four adjacent cube operators, as shown in Figure 5-1(b). This four-cube excitation may trivially move by acting with a Majorana bilinear. If the fundamental cube excitation were mobile, then it would be possible to move it in any arbitrary direction, as the cube operator itself preserves all lattice symmetries. In this case, the cube excitation would have well-defined (fermion or boson) statistics, and a four-cube bound-state could never be a *fermion*. Therefore, it must be the case that the fundamental cube excitation is frozen. A rigorous proof of the immobility of the fundamental excitation is given

Excitation	Type	Statistics	Operator
$ABCD$	Majorana	Fermion	γ
$AA, BB,$ CC, DD	Dim.-2 Anyon	Boson	Pair of Adjacent Wilson Lines
AB, AC, AD, BC, BD, CD	Dim.-1 Particle	——	Single Wilson Line
A, B, C, D	Fracton	——	Membrane

Table 5.1: Hierarchy of excitations in the Majorana checkerboard model. The fundamental cube excitation is a fracton, while two-fracton bound-states can behave as particles that are either free to move along one- or two-dimensional surfaces. The operator that creates each type of excitation is indicated.

in Section 5.4 using the polynomial representation of the ideal Majorana Hamiltonian.

We now analyze the fracton bound-states in the Majorana checkerboard model in detail, along with the mutual statistics of the excitations. Using the labeling of the cube operators shown in Figure 5-1(b), we find the hierarchy of quasiparticles shown in Table 5.1 in the Majorana checkerboard model. The fundamental fracton excitation appears at the *corners* of membrane-like operators and may only be created in groups of four. Two-fracton bound-states can form dimension-1 particles or dimension-2 anyons. Remarkably, a dimension-2 anyon has π mutual statistics with a fracton lying in its plane of motion. As a result, while the fracton is immobile, its presence may be detected by a braiding experiment. Furthermore, the exact location of a single fracton within a finite volume V may be determined by braiding dimension-2 anyons in the three mutually orthogonal planes around the boundary ∂V. In this way, the exact quasiparticle content within V is effectively encoded "holographically", and may be determined by $\sim O(\ell)$ braiding experiments, where ℓ is the linear size of a box bounding V. We now proceed to explore the hierarchy of excitations in detail.

Dimension-1 Particle: The dimension-1 particle may be created by acting with a single Wilson line operator, defined by the product of the Majorana operators along a straight path ℓ. Up to an overall pre-factor of $\pm 1, \pm i$, we write the Wilson line operator as

$$\hat{W}_\ell \propto \prod_{n \in \ell} \gamma_n. \tag{5.6}$$

As shown in Figure 5-2(a), the straight Wilson line anti-commutes with two cube operators at
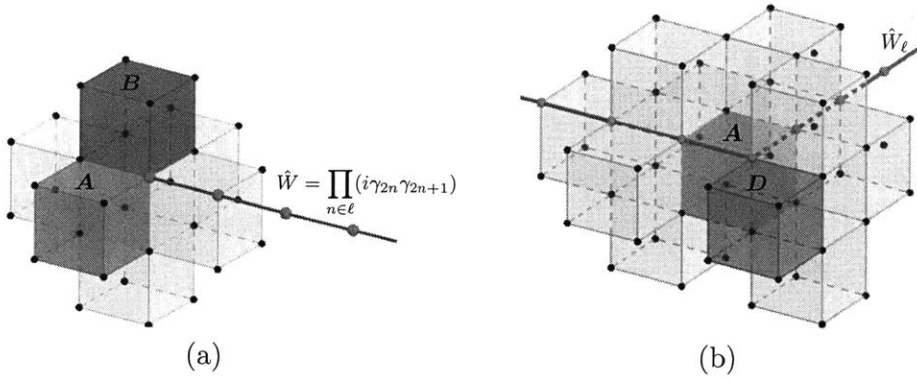
Figure 5-2: **Dimension-1 Particle**: Excitations (colored) may be created by acting with Wilson line operators. In (a), a straight Wilson line creates pairs of dimension-1 particles at the endpoints. The dimension-1 particle may hop freely in the direction of the Wilson line, by acting with Majorana bilinear terms. Remarkably, the dimension-1 particle cannot hop in any other direction without creating additional excitations. Introducing a "corner" in the Wilson line, as in (b), creates an additional topological excitation localized at the corner.

each of its endpoints; the two cube excitations at a given endpoint are of different types. As a result, $\hat{W}_\ell$ creates pairs of excitations of the form AB, AC, AD, BC, BD, or CD. Remarkably, these two-fracton bound-states are only free to move along a line, by simply extending the Wilson line operator $\hat{W}_\ell$ by acting with a Majorana bilinear along the path ℓ. If we try to move this two-fracton bound-state in a plane, we must introduce a corner in the Wilson line, which localizes an additional *topological* excitation at the corner, as shown in Figure 5-2(b); the excitation cannot be removed by the action of any local operator. As the pattern of excitations produced by a Wilson line $\hat{W}_\ell$ is sensitive to the *geometry* of ℓ, the two-fracton bound-states AB, AC, AD, BC, BD, and CD are restricted to move along a line and behave as dimension-1 particles. We emphasize that they cannot move in a higher-dimensional space without creating additional cube excitations.

Dimension-2 Anyon: Acting with a pair of adjacent Wilson lines $\hat{W}_\ell^{(1)}$ and $\hat{W}_{\ell'}^{(2)}$ along parallel paths ℓ and ℓ', respectively, also creates a pair of two-fracton bound-states localized at the ends, as shown in Figure 5-3(a). At each end of the path, however, the operator $\hat{W}_\ell^{(1)}\hat{W}_{\ell'}^{(2)}$ now creates pairs of cube excitations of the *same* type (AA, BB, CC or DD). These two-fracton bound-states, where each fracton is of the same type, are allowed to move freely in the two-dimensional plane orthogonal to the shortest line segment connecting the two paths ℓ and ℓ' without creating additional excitations; this is shown in Figure 5-3(b). We note that detailed geometric features of a *single* Wilson line, such as the presence of sharp corners, determine the pattern of excitations created from the ground-state. However, when acting with an appropriate *pair* of adjacent Wilson lines, the excitations created at the sharp corners may be annihilated. Therefore, a pair of adjacent Wilson lines may be deformed in the plane with no energy cost. We conclude that the AA, BB, CC and DD two-fracton bound-states are dimension-2 anyons.

108
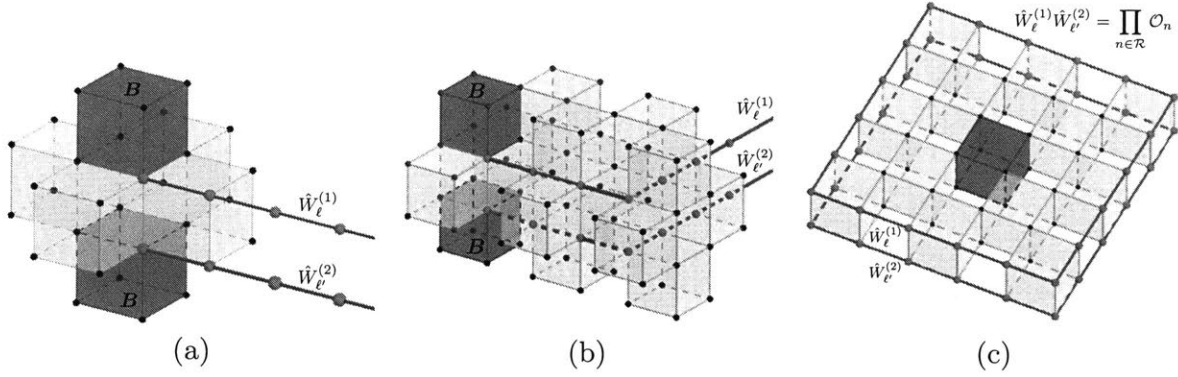
Figure 5-3: **Dimension-2 Anyon**: Acting with two adjacent Wilson line operators $\hat{W}_1$ and $\hat{W}_2$ creates pairs of excitations at the endpoints of the same type (*AA*, *BB*, *CC* or *DD*). These two-fracton excitations are free to move in a two-dimensional plane orthogonal to the shortest line segment connecting the pair of Wilson lines. Furthermore, in (b) we may detect a fracton (colored blue) by braiding a dimension-2 anyon around a closed loop enclosing the fracton. As the braiding operator, a pair of closed Wilson line operators $\hat{W}_1\hat{W}_2$, is equal to the product of the enclosed cube operators as shown above. Therefore, the braiding produces an overall minus sign if an odd number of fractons are enclosed.

Braiding a dimension-2 anyon around a closed loop in the plane is equivalent to acting with the product of cube operators within the two-dimensional region enclosed by the loop; this is shown for a particular choice of loop in Figure 5-3(c). As a result, braiding a dimension-2 anyon around a closed loop enclosing a single fracton in the plane produces an overall minus sign. The ability to detect a fracton with a dimension-2 anyon produces non-trivial mutual statistics between the dimension-2 anyon and other particles in the excitation spectrum of the Majorana checkerboard model. First, a dimension-2 anyon has π mutual statistics with any dimension-1 particle in the same plane, as braiding the dimension-2 anyon in a closed loop will only detect one of the two fractons that make up the dimension-1 particle. Furthermore, the dimension-2 anyon has π mutual statistics with dimension-2 anyons that are free to move in adjacent, parallel planes.

Fractons and Membrane Operators: Acting with Majorana operators on a flat, two-dimensional membrane Σ creates fracton excitations at the *corners* of the boundary of Σ, as shown in Figure 5-4. We write the membrane operator up to an overall pre-factor of $\pm 1, \pm i$ as

$$\hat{\mathcal{M}} \propto \prod_{n \in \Sigma} \gamma_n. \tag{5.7}$$

For a rectangular membrane in the x-y plane, the boundary $\partial\Sigma$ is a closed, rectangular loop with dimensions ℓ_x and ℓ_y. We note that if ℓ_x and ℓ_y are both even, then the fracton excitations created at the corners of $\partial\Sigma$ will all be of the same type. Alternatively, if ℓ_x is odd and ℓ_y is even, then the pairs of fracton excitations separated in the y-direction will be of the same type, while fractons separated in the x-direction will be distinct.

109
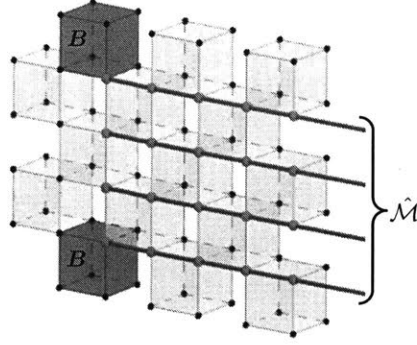
Figure 5-4: **Membrane Operator & Fracton Excitations**: Acting with a product of Majorana operators on a surface Σ creates localized excitations at the corners of the boundary $\partial\Sigma$ as shown above.

Extensive Topological Degeneracy: Using the algebraic representation of the Majorana checkerboard model, we compute its ground-state degeneracy D_0 to be

$$\log_2 D_0 = 3L - 3 \tag{5.8}$$

on an $L \times L \times L$ three-torus, with periodic boundary conditions imposed in the x, y, and z directions, with each cube having unit side length. Pairs of string-like Wilson loop operators wrapping non-trivial cycles of the torus – corresponding to tunneling dimension-2 anyons – distinguish the ground-state sectors. As the number of distinct dimension-2 anyons grows linearly with system size, the ground-state degeneracy is necessarily extensive.

We emphasize that the algebraic approach allows us to systematically search for topologically ordered, ideal Majorana Hamiltonians, rigorously characterize the nature of excitations, and calculate the ground-state degeneracy in a wide range of Majorana models using techniques in algebraic geometry. As a result, the next two sections of this chapter introduce and focus on the polynomial representation of ideal Majorana Hamiltonians and draw broad conclusions based on this representation. In Section 5.3, we present the 6 distinct three-dimensional Majorana models with nearest-neighbor interactions that are topologically-ordered. In particular, one of our models, which may naturally be written in terms of complex fermions on an fcc lattice, has a fundamental excitation that may only freely move along a line in the (1,1,1) direction.

We conclude, in Section 5.4, with a proof of the presence of fractons in the Majorana checkerboard model, and briefly outline the phenomenology of excitations in the remaining models.

5.2 Topological Order in Commuting Majorana Hamiltonians

In this section, we introduce a representation of the operators in the ideal Majorana Hamiltonian (5.1) as a vector of Laurent polynomials over the finite field $\mathbb{F}_2$. The algebraic representation provides an important starting point for studying and classifying Majorana Hamiltonians. We

demonstrate that the following conditions, that

1. All operators in the ideal Hamiltonian mutually commute, and

2. Degenerate ground-states of the Hamiltonian are locally indistinguishable

may be phrased entirely in the polynomial representation. The ground-state degeneracy of an ideal Majorana Hamiltonian (5.1) on the torus can be computed as the dimension of a quotient ring [47].

We demonstrate that an ideal Majorana Hamiltonian obeying (i) and (ii) on a lattice with a two-site basis and a single interaction term per unit cell may be specified by a *single* polynomial over $\mathbb{F}_2$. We use this result to systematically search for and characterize commuting Majorana Hamiltonians. In $d = 3$ dimensions, we find 6 distinct, non-trivial models with nearest-neighbor interactions, extensive topological degeneracy, and a dimensional hierarchy of excitations.

5.2.1 Algebraic Representation

To study commuting Majorana Hamiltonians, we represent the operator $\mathcal{O}$ appearing in Eq. (5.1) as a polynomial over the field $\mathbb{F}_2$. A similar mapping has been introduced in the context of Pauli Hamiltonians [47]. Consider a d-dimensional lattice with translation operators $\{t_1, \ldots, t_d\}$ and an n-site unit cell. We restrict n to be an *even* integer so that there is a well-defined number of complex fermions per lattice site. We label the Majorana fermions within the unit cell at the origin as γ_j for $j = 1, 2, \ldots, n$. All other Majorana fermions on the lattice are obtained by acting with translation operators.

Any Hermitian operator acting on this lattice may be written as a sum of products of Majorana operators. Formally, we may write a $\mathcal{O}$ as

$$\mathcal{O} = \prod_{j=1}^{n} \prod_{\{n_i\}} \left(t_1^{n_1} \cdots t_d^{n_d} \cdot \gamma_j \right)^{c_j(n_1, \ldots, n_d)} \tag{5.9}$$

with $n_i \in \mathbb{Z}$ and $c_j(n_1, \ldots, n_d) \in \{0, 1\}$. For simplicity, we have omitted the prefactor $\pm 1, \pm i$ in the expression for $\mathcal{O}$, which plays no role in our analysis. We introduce a purely algebraic representation of this operator by noting that any product of translation operators may be written as a monomial, e.g. $t_1^{n_1} \cdots t_d^{n_d} \Longleftrightarrow x_1^{n_1} \cdots x_d^{n_d}$. In this way, the action of the translation group is naturally represented by monomial multiplication.

Recall that distinct Majorana fermions anti-commute and that each Majorana operator squares to the identity. Therefore at each site within a unit cell, the identity $\mathbb{1}$ and γ under multiplication form the group $\mathbb{Z}_2$, with the two operators represented by the group elements 0 and 1, respectively. In this representation, the operator equality $\gamma^2 = \mathbb{1}$ maps to the $\mathbb{Z}_2$ group addition $1 + 1 = 0$. This simple algebra of Majorana fermions allows us to write any product of Majorana operators as the *sum* of monomials – representing the location of each Majorana operator via the action of the translation group – with $\mathbb{Z}_2$ coefficients. As an example, consider

111

a lattice with a single site per unit cell, and the Majorana operator γ at the origin. A Majorana bilinear admits the following polynomial representation:

$$\gamma \cdot \left(t_1^{m_1} t_2^{m_2} \cdots t_d^{m_d} \cdot \gamma \right) \iff 1 + x_1^{m_1} x_2^{m_2} \cdots x_d^{m_d}. \tag{5.10}$$

In this notation, operator multiplication corresponds to polynomial addition with $\mathbb{Z}_2$ coefficients.

For the general case of a unit cell with n sites, we represent a product of Majorana operators as a *vector* of polynomials over $\mathbb{F}_2$, with the j-th entry of the vector representing the action of the translation group on γ_j, the j-th Majorana fermions in the unit cell at the origin. For example, the operator (5.9) may be written as

$$S(x_1, ..., x_d) = \sum_{\{n_i\}} x_1^{n_1} \cdots x_d^{n_d} \begin{pmatrix} c_1(n_1, ..., n_d) \\ c_2(n_1, ..., n_d) \\ \vdots \\ c_{2n}(n_1, ..., n_d) \end{pmatrix} \tag{5.11}$$

Adopting the terminology in Ref. [47], we refer to S as the "stabilizer map" for the remainder of this chapter.

To illustrate the algebraic representation of operators in commuting Majorana Hamiltonians, we present a concrete example. Consider the Majorana plaquette model in Ref. [1], which is defined on a two-dimensional honeycomb lattice with one Majorana fermion per site and a Hamiltonian of the form (5.1) where $\mathcal{O}_p$ is the product of the six Majorana fermions at the vertex of a hexagonal plaquette p. We show a single hexagonal plaquette on the lattice in Figure 5-5(a), along with the Majorana fermions γ_a and γ_b within the two-site unit cell. The corresponding stabilizer map $S(x, y)$ for the six-Majorana operator is given by:

$$S(x, y) = \begin{pmatrix} 1 + x + y \\ 1 + x + x\bar{y} \end{pmatrix}. \tag{5.12}$$

Here, we adopt the notation that $\bar{y} \equiv y^{-1}$, $\bar{x} \equiv x^{-1}$. As shown in Ref. [1], this Hamiltonian exhibits a novel form of $\mathbb{Z}_2$ topological order with fermion parity-graded excitations and exact anyon permutation symmetries.

Next, we consider the action of an arbitrary operator W on the ground state $|\Psi\rangle$ of the commuting Majorana Hamiltonian. When W anticommutes with an operator $\mathcal{O}_n$ in the Hamiltonian, it flips its eigenvalue and thus creates an excitation. We use a polynomial to record the locations of all excitations in the state $W |\Psi\rangle$; each location is labeled by the translation vector connecting it to the origin. Specifically, for a Hamiltonian with stabilizer map $S(x_1, \cdots, x_d)$ and an arbitrary operator W with a polynomial representation $P(W)$ of the form (5.11), we define the "excitation map" $E(x_1, \ldots, x_d)$ so that $E(x_1, \ldots, x_d) \cdot P(W) \in \mathbb{F}_2[x_1^{\pm 1}, \cdots, x_d^{\pm 1}]$ describes the excitations created by W. In the Supplemental Material [?], we demonstrate that E is
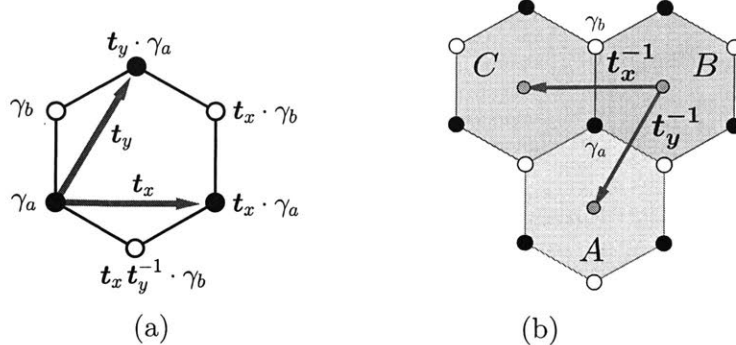
Figure 5-5: The Majorana plaquette model, as studied in [1]. Consider a honeycomb lattice with a single Majorana fermion on each lattice site. We define an operator $\mathcal{O}_p$ as the product of the six Majorana fermions on the vertices of a hexagonal plaquette p, as shown in (a). The colored plaquettes in (b) correspond to the three distinct bosonic excitations ($A, B,$ or C) that may each be created in pairs by acting with Wilson line operators.

simply given from the stabilizer map as follows:

$$E(x_1, \ldots, x_d) = \overline{S(x_1, \cdots, x_d)} \tag{5.13}$$

where $\overline{S(x_1, \ldots, x_d)} \equiv [S(\overline{x_1}, \ldots, \overline{x_d})]^T$.

As an example, the excitation map for the Majorana plaquette model is given by $E(x, y) = (1 + \bar{x} + \bar{y}, \ 1 + \bar{x} + \bar{x}y)$. Below, we show the action of the operator γ_a at the origin in the Majorana plaquette model, which creates three adjacent excitations as specified by the red points. The locations of the excitations are obtained by performing the matrix multiplication of E with the polynomial representation $\begin{pmatrix} 1 \\ 0 \end{pmatrix}$ of γ_a:

$$E(x, y) \cdot \begin{pmatrix} 1 \\ 0 \end{pmatrix} = 1 + \bar{x} + \bar{y}. \tag{5.14}$$

Therefore, the action of γ_a may be represented by the polynomial $1 + \bar{x} + \bar{y}$, labeling the locations of the flipped plaquettes; here, the plaquette operator corresponding to the origin (i.e. the location "1") is to the right of γ_a, as can be seen from its polynomial representation (5.12). A dictionary that summarizes the relationship between Majorana operators and polynomials is given in Table 5.2.

5.2.2 Topological Order and Ground-State Degeneracy in the Algebraic Representation

The polynomial representation of Majorana operators serves as a starting point for constructing commuting Majorana Hamiltonians that exhibit topological orders. As we demonstrate in the Supplemental Material [?], for a translationally invariant Majorana Hamiltonian with a sin-

gle operator per lattice site, *all* operators mutually commute *if and only if* its stabilizer map $S(x_1, \cdots, x_d)$ satisfies the condition

$$\overline{S(x_1, \ldots, x_d)} \cdot S(x_1, \ldots, x_d) = 0. \tag{5.15}$$

More generally, if the Hamiltonian contains multiple operators per lattice site $\{\mathcal{O}^{(i)}\}$, then we may define a set of stabilizer maps for each type of operator $\{S_i\}$, so that the condition $\overline{S_i(x_1, \ldots, x_d)} \cdot S_j(x_1, \ldots, x_d) = 0$ for all i, j, guarantees that all terms in the Hamiltonian commute.

We next formulate a necessary and sufficient algebraic condition for topological order in commuting Majorana Hamiltonians, which requires that any degenerate ground-states of a topologically-ordered Hamiltonian cannot be distinguished by local operators. The local indistinguishability is equivalent to the condition that, for any *local* operator M_i

$$\Pi_{\mathrm{GS}} \, M_i \, \Pi_{\mathrm{GS}} = c(M_i) \, \Pi_{\mathrm{GS}} \tag{5.16}$$

where Π_{GS} is the projector onto a ground-state sector and $c(M_i)$ is a constant that *only* depends on the operator. For our case, consider an operator M_I that is the product of Majorana operators, and $P(M_i)$, the polynomial representation of M_i. If M_i anti-commutes with *any* term in the Hamiltonian, then M_i creates excitations when acting on the ground-state, and we have $\Pi_{\mathrm{GS}} \, M_i \, \Pi_{\mathrm{GS}} = 0$. If M_i commutes with the Hamiltonian, then $P(M_i) \in \ker E$, as M_i creates no excitations. In this case, the condition $\Pi_{\mathrm{GS}} \, M_i \, \Pi_{\mathrm{GS}} = c(M_i)\Pi_{\mathrm{GS}}$ is guaranteed if M_i may be written as a product of operators already appearing in the Hamiltonian. More generally, any local operator M that commutes with the Hamiltonian then takes the form:

$$M = \sum_i M_i \tag{5.17}$$

where each term M_i is the product of operators already appearing in the Hamiltonian. This condition is necessary for distinct ground-state sectors to be locally indistinguishable.

In our polynomial representation, we enforce the condition (5.16) by requiring that the stabilizer and excitation maps satisfy the following condition on an infinite lattice

$$\ker E \cong \operatorname{im} S. \tag{5.18}$$

Recall that the image of S is the set of all polynomial linear combinations of $S(x_1, \ldots, x_d)$, taking the form of

$$\sum_{\{n_i\}} x_1^{n_1} \cdots x_d^{n_d} S(x_1, \ldots, x_d), \tag{5.19}$$

and representing all operators that can be written as a product of the commuting operators

114

Operator	Polynomial
Majorana Fermion γ_j $[j = 1, \ldots, n$ for each site in the unit cell$]$	Vector over $\mathbb{F}_2$ $\vec{e}_j$ $[n$-dimensional unit vector with j^{th} entry equal to $1]$
Translation $t_1^{n_1} t_2^{n_2} \cdots t_d^{n_d} \gamma_j$	Monomial Multiplication $x_1^{n_1} x_2^{n_2} \cdots x_d^{n_d} \vec{e}_j$
Multiplication $\gamma_j \cdot t_k^n \gamma_\ell$	Addition in $\mathbb{F}_2[x_1, \cdots, x_d]$ $\vec{e}_j + (x_k)^n \vec{e}_\ell$

Table 5.2: Summary of the polynomial representation of Majorana operators. An arbitrary operator in d spatial dimensions, written as the product of Majorana fermions, may be represented as a vector with entries in the Laurent polynomial ring $\mathbb{F}_2[x_1^{\pm 1}, \cdots, x_d^{\pm 1}]$.

appearing in the Hamiltonian. On the other hand, the kernel of the excitation map E is the set of all operators that do not create any excitation when acting on the ground state. The above algebraic condition (5.18) for topological order is thus equivalent to the statement that *any* operator that creates no excitations on a ground state on an infinite lattice is necessarily a product of operators $\{\mathcal{O}_n\}$ already appearing the Hamiltonian. In other words, there are no non-trivial, locally conserved quantities, and any degenerate ground-states of the Hamiltonian are locally indistinguishable. In summary, imposing the commutativity (5.15) and local indistinguishability (5.18) conditions on a stabilizer map produces an ideal Majorana Hamiltonian with topological order.

We may compute the ground-state degeneracy of an ideal Majorana Hamiltonian in the polynomial representation via constraint-counting. A lattice with $2M$ Majorana fermions defines a 2^M-dimensional Hilbert space. On the torus, however, fixing the eigenvalues of the commuting operators in the ideal Majorana Hamiltonian only imposes $M - k$ multiplicatively independent constraints, since the product of certain operators appearing in the Hamiltonian will yield the identity. The ground-state degeneracy is simply given by the space of states satisfying the constraints, which is precisely $2^M/2^{M-k} = 2^k$. As each ideal Majorana Hamiltonian in this chapter consists of exactly one term for each pair of Majorana modes, we see that k is directly equal to the number of constraints on the commuting operators appearing in the Hamiltonian.

For example, in the Majorana plaquette model, we may group the plaquette operators $\{\mathcal{O}_p\}$

115

into three types (A, B, and C) as shown in Figure 5-5(b). On the torus, the product of the A, B, and C-type operators is identical and equal to the total fermion parity [1]. This yields the following two independent constraints:

$$\prod_{p \in A} \hat{\mathcal{O}}_p \prod_{p \in B} \hat{\mathcal{O}}_p = \prod_{p \in B} \hat{\mathcal{O}}_p \prod_{p \in C} \hat{\mathcal{O}}_p = 1, \tag{5.20}$$

and produces a 2^2-fold degenerate ground-state on the torus. These constraints may be compactly represented using polynomials labeling the locations of the A, B and C-type plaquettes. For example, the collection of all A plaquettes is captured by the polynomial

$$p_A = (1 + xy + x^2 y^2) \left(\sum_{n=0}^{L-1} x^{3n} \right) \left(\sum_{m=0}^{L-1} y^{3m} \right). \tag{5.21}$$

It is straightforward to expand p_A to verify that the exponents of the non-zero terms describe the positions of A plaquettes. Here, L specifies the periodic boundary conditions in the x and y directions, so that $x^L = 1$, $y^L = 1$. Similarly, the collections of all plaquettes in B and C are encoded in $y p_A$ and $\bar{x} y p_A$, respectively. The constraints (5.20) arise from the fact that $(p_A + y p_A) S = 0$, using Eq. (5.12) and the boundary conditions.

In terms of the stabilizer map, any multiplicative constraint on the operators in the ideal Majorana Hamiltonian on the torus is in one-to-one correspondence with a solution p of the equation $p \cdot S = 0$, so that the polynomial p is an element of the kernel of S. Therefore, the number of independent relations is given by

$$k = \dim_{\mathbb{F}_2}[\ker(S)]. \tag{5.22}$$

We rewrite the expression (5.22) in a more convenient form for calculations that will also allow us to make general statements about the scaling behavior of the ground-state degeneracy with system size for an ideal Majorana Hamiltonian of the form (5.1). As proven in Corollary 4.5 in Ref. [47], Eq. (5.22) is equivalent to the dimension of the following quotient ring:

$$k = \log_2 D = \dim_{\mathbb{F}_2} \left(\frac{\mathbb{F}_2[x_1, \cdots, x_d]}{I(S) + \mathfrak{b}_L} \right). \tag{5.23}$$

Here, $I(S)$ the *ideal* generated by the stabilizer map; if $S^T = (s_1, \ldots, s_{2n})$ then $I(S)$ is the space of polynomials in $\mathbb{F}_2[x_1^{\pm 1}, \ldots, x_d^{\pm 1}]$ obtained as a linear combination of $\{s_i\}$:

$$I(S) \equiv \left\{ p = \sum_{i=1}^{2n} c_i s_i \;\middle|\; c_i \in \mathbb{F}_2[x_1^{\pm 1}, \ldots, x_d^{\pm 1}] \right\}. \tag{5.24}$$

We will denote the ideal generated by a set $\{s_1, \ldots, s_n\}$ by $\langle s_1, \ldots, s_n \rangle$. Furthermore, we define the ideal $\mathfrak{b}_L \equiv \langle x_1^L - 1, \ldots, x_d^L - 1 \rangle$. As the quotient space identifies the zero element

Algebraic Expression	Physical Interpretation
$\overline{S(x_1,..,x_d)} \cdot S(x_1,..,x_d) = 0$	Commutativity condition, that all operators $\{\mathcal{O}_n\}$ appearing in the Hamiltonian mutually commute.
$\mathrm{im}(S)$	Set of operators that may be written as the product of commuting operators $\{\mathcal{O}_n\}$ in the Hamiltonian.
$\ker(E)$	Set of operators that create no excitations when acting on the ground-state $\lvert\Psi\rangle$.
$k = \dim_{\mathbb{F}_2}[\ker(S)]$	The number of independent relations among the commuting operators in the Hamiltonian on a torus. The ground state degeneracy $D = 2^k$.
$p \in \mathbb{F}_2[x_1^{\pm},\ldots,x_d^{\pm}]$	Configuration of excitations, specified by the locations of operators $\{\mathcal{O}_n\}$ with eigenvalue -1.
$q \in I(S)$	A configuration of excitations that may be created by acting with an operator on the ground-state $\lvert\Psi\rangle$.

Table 5.3: Dictionary of various algebraic quantities and their physical interpretation in the context of a commuting Majorana Hamiltonian.

in $\mathbb{F}_2[x_1^{\pm 1},\ldots,x_d^{\pm 1}]$ with the generators of $I(S) + \mathfrak{b}_L$, we observe that the ideal $\mathfrak{b}_L$ is used to enforce the periodic boundary conditions on a d-dimensional torus with side-length L.

We emphasize that the ideal $I(S)$ is the space of excitations that can be created through the action of any operator on the ground-state. Therefore, the expression (5.23) may be physically interpreted as counting certain superselection sectors of the ideal Majorana Hamiltonian. Any $p \in \mathbb{F}_2[x_1^{\pm 1},\cdots,x_d^{\pm 1}]$ corresponds to a virtual eigenstate of the Hamiltonian with excitations at the locations specified by the polynomial p. Certain states, however, cannot be created by acting with an operator on a ground-state $\lvert\Psi\rangle$ due to the k constraints on the commuting operators. For example, in the Majorana plaquette model, it is impossible to obtain a state with a single plaquette excitation by acting on the ground-state, since the products of A, B and C plaquettes must satisfy (5.20). As $I(S)/(I(S) \cap \mathfrak{b}_L)$ is the set of excitations that can be created by the action of operators on the ground-state for a finite system, the quotient space $\left(\mathbb{F}_2[x_1^{\pm 1},\cdots,x_d^{\pm 1}]/\mathfrak{b}_L\right)/\left(I(S)/(I(S) \cap \mathfrak{b}_L)\right) = \mathbb{F}_2[x_1,\cdots,x_d]/\left(\mathfrak{b}_L + I(S)\right)$ is the set of virtual

eigenstates of the Hamiltonian that cannot be deformed into each other through the action of any local operator. For the Majorana plaquette model, this quotient space is

$$\frac{\mathbb{F}_2[x,y]}{\langle 1 + x + y,\ x + y + xy,\ x^L - 1,\ y^L - 1 \rangle} \cong \mathbb{F}_2^2 \tag{5.25}$$

when $L \bmod 3 = 0$ so that there are an equal number of A, B, and C plaquettes. In this case, the trivial vacuum (0) and a state with a single plaquette excitation (1) on A, B, or C correspond to the four superselection sectors in the quotient ring.

The expression for the ground-state degeneracy (5.23) is convenient as the dimension of a quotient ring may be computed using algebraic techniques. Most often, we will determine a Gröbner basis for the ideal $I(S) + \mathfrak{b}_L$ in order to determine membership in the quotient ring. For a polynomial ring R, we may define a total monomial ordering (e.g. lexicographic order with $x_1 \succ x_2 \succ \ldots \succ x_d$); we denote the leading monomial in a polynomial $h \in R$ as $\mathrm{LM}(h)$ with respect to this ordering. Given an ideal $I = \langle s_1, \cdots, s_n \rangle$ of a polynomial ring, there exists a canonical choice of generators for the ideal, known as the Gröbner basis $\{g_1, \cdots, g_n\}$, with the property that for any $f \in I$, $\mathrm{LM}(f) \in \langle \mathrm{LM}(g_1), \ldots, \mathrm{LM}(g_n) \rangle$, i.e. any element of the ideal has a leading term contained in the ideal generated by the leading terms of the Gröbner basis. As a result, the dimension of the quotient ring $\dim[R/I]$ is merely given by the number of monomials that are smaller (in the monomial ordering) than all of the leading terms in the Gröbner basis. This is because any polynomial $p \in R$ may be reduced by the Gröbner basis until the leading term of the reduced polynomial satisfies $\mathrm{LM}(p_{\mathrm{red}}) < \mathrm{LM}(g_i)$ for all $i = 1, \ldots, n$. Therefore, each monomial m satisfying $m < \mathrm{LM}(g_i)$ for all i corresponds to a unique representative of the quotient ring R/I.

We note that calculations of the ground-state degeneracy for any commuting Majorana Hamiltonians presented in this chapter are done by determining a Gröbner basis for the ideal $I(S) + \mathfrak{b}_L$. In this way, the calculation of the degeneracy reduces to counting points in an algebraic set.

5.2.3 Unitary and Stable Equivalence

The polynomial representation of the ideal Majorana Hamiltonian contains built-in redundancies, since we may re-define the unit cell or translation operators on the d-dimensional lattice. For the stabilizer map, the translation corresponds to multiplication of any entry of $S(x_1, \ldots, x_d)$ by a monomial. In this way, a stabilizer map $S(x_1, \ldots, x_d)$ is only defined up to monomial multiplication on each of its entries. Furthermore, for an ideal Majorana Hamiltonian with longer-range interactions, we may always enlarge the unit cell. As our focus will be on Majorana models with nearest-neighbor interactions, we neglect this redundancy in the stabilizer map.

Equivalence relations, given by local unitary transformations on ideal Majorana Hamiltonians, may also be considered in the polynomial language. For instance, two ideal Majorana Hamiltonians, defined by stabilizer maps $S(x_1, \ldots, x_d)$ and $S'(x_1, \ldots, x_d)$ are *unitar-*

ily equivalent if there exists a matrix U such that $S'(x_1, \ldots, x_d) = U \cdot S(x_1, \ldots, x_d)$ where $U \in O(n; \mathbb{F}_2)$, an orthogonal matrix over $\mathbb{F}_2$ satisfying $U^T U = 1$. This guarantees that if $\overline{S(x_1, \ldots, x_d)} \cdot S(x_1, \ldots, x_d) = 0$, then $\overline{S'(x_1, \ldots, x_d)} \cdot S'(x_1, \ldots, x_d) = 0$ as well. Finally, we take two stabilizer maps to be *stably* equivalent if we can obtain one from the other by attaching a trivial (dimerized) set of Majorana fermions. This is expressed as $S(x_1, \ldots, x_d)^T \sim S(x_1, \ldots, x_d)^T \oplus (0, \cdots, 0, 1, 1)$.

5.3 Extensive Topological Degeneracy in $d \geq 3$

Using the commutativity (5.15) and local indistinguishability (5.18) conditions, and the built-in redundancy in the polynomial description, we demonstrate in the Supplemental Material [?], that an ideal Majorana Hamiltonian defined on a d-dimensional lattice with a two-site basis is topologically-ordered if the stabilizer map may be written in the following form, after multiplying each entry by appropriate monomials:

$$S = \begin{pmatrix} f(x_1, \cdots, x_d) \\ \overline{f(x_1, \cdots, x_d)} \end{pmatrix} \tag{5.26}$$

where $f(x_1, \cdots, x_d) \in \mathbb{F}_2[x_1^{\pm 1}, \cdots, x_d^{\pm 1}]$ and f and $\bar{f}$ are co-prime, i.e., f and $\bar{f}$ have no common polynomial factors. As a result, a topologically-ordered, ideal Majorana Hamiltonian with a two-site basis may be specified by a single polynomial. For example, the stabilizer map for the Majorana plaquette model takes the form $S^T = (f(x, y), x \cdot \overline{f(x, y)})$ with $f(x, y) = 1 + x + y$.

The dimension of the quotient ring (5.23) scales as the dimension of the space of the zeros of the ideal $I(S)$ over the field extension $\mathbb{F}_{2^m}$ when $L = 2^m - 1$. As a result, for an ideal Majorana Hamiltonian (5.1) with a two-site unit cell, the space of solutions to

$$f(x_1, \ldots, x_d) = 0, \qquad \overline{f(x_1, \ldots, x_d)} = 0 \tag{5.27}$$

generally defines an $(d - 2)$-dimensional variety, so that the ground-state degeneracy scales on the d-dimensional torus with side-length L as $\log_2 D = cL^{d-2} + \cdots$ for some constant c. We emphasize that this produces a class of ideal Majorana models with extensive topological degeneracy in $d = 3$ dimensions. Remarkably, while our models have a two-dimensional Hilbert space and a single interaction term per lattice site, this only constrains the full Hilbert space up to extensive topological degeneracy.

We have exhaustively searched for distinct, ideal Majorana Hamiltonians with a two-site basis and nearest-neighbor interactions in $d = 2$ and $d = 3$ spatial dimensions. This is straightforward as the orthogonal group $O(2; \mathbb{F}_2) = \{\mathbb{1}_{2 \times 2}, \sigma^x\}$ so that the space of local unitary transformations between these ideal Majorana Hamiltonians is trivial. In $d = 2$ spatial dimensions,
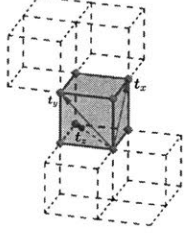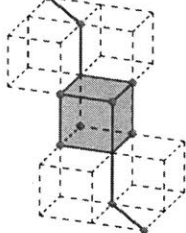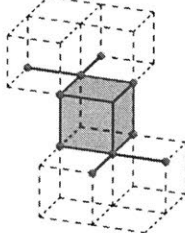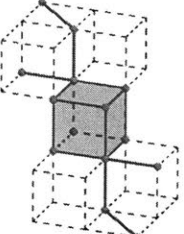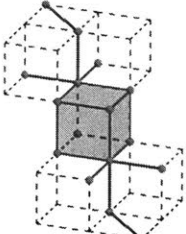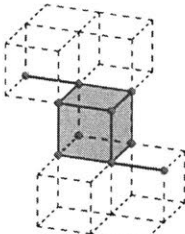
	$f_1(x,y,z)$	$f_2(x,y,z)$	$f_3(x,y,z)$
f	$1+x+y+z$	$1+z+xy$ $+yz+xz$	$1+x+y$ $+yz+xz$
$\mathcal{O}$			
$\log_2 D$	$3L-2$	$6L-6\ (L=3n)$ $0\ (L\neq 3n)$	$4L/3\ (L=6\cdot 2^n)$ $8L/5\ (L=5\cdot 2^n)$ $\vdots$
	$f_4(x,y,z)$	$f_5(x,y,z)$	$f_6(x,y,z)$
f	$1+y+z$ $+xy+yz+xz$	$1+x+y+z$ $+xy+yz+xz$	$1+x+y$ $+z+yz$
$\mathcal{O}$			
$\log_2 D$	$4L-4\ (L=2n)$ $2L-1\ (L=2n+1)$	$2L-2\ (L=2^{2n+1}-1)$ $2L-4\ (L=2^{2n}-1)$ $\vdots$	$4L/3\ (L=6\cdot 2^n)$ $8L/5\ (L=5\cdot 2^n)$ $\vdots$

Table 5.4: We find 7 distinct, topologically-ordered ideal Majorana Hamiltonians with nearest-neighbor interactions on a lattice with a two-site unit cell in $d=3$ spatial dimensions. The first model $f_0(x,y,z)=1+y+z$ (not shown) is a trivial stack of two-dimensional Majorana plaquette models, considered in Ref. [1]. For the remaining 6 models, the action of the elementary operator $\mathcal{O}$ appearing in the ideal Majorana Hamiltonian is shown above as the product of the Majorana fermions on the indicated red dots. In the depiction of the Majorana checkerboard model $f_1(x,y,z)$, we have also shown the choice of translation vectors $\{\boldsymbol{t}_x,\boldsymbol{t}_y,\boldsymbol{t}_z\}$ on the lattice, originating from one of the sites within the unit cell; to compute the ground-state degeneracy on an $L\times L\times L$ torus, we impose periodic boundary conditions by requiring that $\boldsymbol{t}_x^L=\boldsymbol{t}_y^L=\boldsymbol{t}_z^L=1$. The topological ground-state degeneracy (D) of each of these models is extensive. For models $f_3(x,y,z)$, $f_5(x,y,z)$, and $f_6(x,y,z)$, the ground-state degeneracy on the three-torus is a highly sensitive function of system size, and only the maximum value of the degeneracy is shown for the indicated choices of L.

the only such Hamiltonian is the Majorana plaquette model with

$$f(x,y) = 1 + x + y. \tag{5.28}$$

In $d = 3$ dimensions, however, we find 7 distinct Majorana models with a two-site basis and nearest-neighbor interactions. The first model has the polynomial representation $f_0(x,y,z) = 1 + y + z$ and is a trivial stack of two-dimensional Majorana plaquette models. The polynomial representations of the remaining models, along with their ground-state degeneracies on a torus of side-length L are shown in Table 5.4. For simplicity, we have imposed periodic boundary conditions by requiring that $t_x^L = t_y^L = t_z^L = 1$ for the translation vectors $\{t_x, t_y, t_z\}$ shown in the representation of the Majorana checkerboard model $f_1(x,y,z) = 1 + x + y + z$ in Table 5.4. Each of the models shown exhibits extensive topological degeneracy and admits at least one topological excitation that is free to move in a sub-manifold of the full lattice.

5.4 Fracton Excitations and Dimension-n Anyons

A remarkable feature of these Majorana models is the presence of fundamental excitations that are either perfectly immobile or only free to move in a sub-manifold of the lattice; attempting to move these excitations by acting with any local operator will necessarily create additional excitations. A bound-state of these immobile excitations, however, forms a particle that can freely move along a higher-dimensional sub-manifold.

The existence of a fracton fundamental excitation may be shown rigorously in the polynomial representation of the Majorana models. An element $p \in I(S)$ of the ideal defined by the stabilizer map corresponds to a set of excitations that may be created by acting on the ground-state. The fundamental excitation is mobile if and only if it is possible to create an isolated pair of such excitations. Therefore, an ideal Majorana model admits fracton excitations if the stabilizer ideal contains no binomial terms, i.e.

$$1 + x_1^{n_1} x_2^{n_2} \cdots x_d^{n_d} \notin I(S) \tag{5.29}$$

for any $n_i \in \mathbb{Z}$.

We now apply the polynomial criterion for fracton excitations to the Majorana checkerboard model and to the model $f_5(x,y,z) = 1 + x + y + z + xy + yz + xz$, both shown in Table 5.4.

5.4.1 Fractons in the Majorana Checkerboard Model

We consider the Majorana checkerboard model, specified by the single polynomial $f(x,y,z) = 1 + x + y + z$, so that the stabilizer map is given by $S = \left(f(x,y,z), \overline{f(x,y,z)} \right)^T$. We wish to prove that the ideal generated by the stabilizer map $I(S)$ contains no binomial terms, so that the fundamental cube excitation is a fracton. This may be shown by considering the zero-locus

of the ideal, i.e., the solutions to the zeros of the generators of the ideal:

$$1 + x + y + z = 0 \tag{5.30}$$

$$xyz + xy + yz + xz = 0. \tag{5.31}$$

A polynomial p belong to $I(S)$ only if p vanishes on the zero-locus of the ideal. Note that solutions to (5.30) take the form $(x, y, z) = (1, \alpha, \alpha)$, $(\alpha, 1, \alpha)$ or $(\alpha, \alpha, 1)$, where α is an arbitrary element in the extension of $\mathbb{F}_2$. However, we see that the binomial $1 + x^n y^m z^\ell$ vanishes on this space of solutions only if $n = m = \ell = 0$, in which case the binomial is zero. Therefore, we conclude that

$$1 + x^n y^m z^\ell \notin I(S). \tag{5.32}$$

As a result, there is no way to create the fundamental cube excitation in the Majorana checkerboard model in pairs. Therefore, the cube excitation is an immobile fracton; a single cube excitation cannot be moved without creating additional excitations.

5.4.2 Dimension-1 Fundamental Excitations in $f_5(x, y, z)$

Now, we consider the isotropic model $f_5(x, y, z) = 1 + x + y + z + xy + yz + xz$, with stabilizer map defined by $S(x, y, z) = \left(f_5(x, y, z),\, xyz \cdot \overline{f_5(x, y, z)} \right)$. From the excitation map $E(x, y, z) \equiv \overline{S(x, y, z)}$, we find that the Majorana bilinear along the $(1,1,1)$ direction creates a pair of fundamental excitations:

$$E(x, y, z) \cdot \begin{pmatrix} 1 \\ 1 \end{pmatrix} = 1 + \overline{xyz}. \tag{5.33}$$

Therefore, the fundamental excitation in this model is clearly not a fracton. We now demonstrate that the fundamental excitation may *only* hop freely along the $(1,1,1)$ direction, without creating additional excitations. Consider the variety $V(I)$ defined by the stabilizer ideal $I(S) = \langle 1 + x + y + z + xy + yz + xz,\ xyz + x + y + z + xy + yz + xz \rangle$, i.e. the zero-locus of the generators of the ideal over an extension of $\mathbb{F}_2$. The following is a point on the variety:

$$(x, y, z) = \left(t,\, \frac{1}{1+t},\, \frac{t+1}{t} \right) \tag{5.34}$$

with t in an extension of $\mathbb{F}_2$. As a result, if $1 + x^n y^m \in I(S)$, we must have from (5.34) that $t^n = (1 + t)^m$ for infinitely many t. This can only be true if $n = m = 0$. As a result, the fundamental excitation cannot hop freely in the xy-plane. As the generators of the ideal are symmetric under exchanging any pair of variables (e.g. $x \longleftrightarrow y$), we conclude that $1 + y^n z^m$, $1 + x^n z^m \in I(S)$ only if $n = m = 0$, so that the fundamental excitation cannot freely hop in the

yz- or *xz*-planes. From these results, we are led to the conclusion that

$$1 + x^n y^m z^\ell \notin I(S) \tag{5.35}$$

when n, m and ℓ are distinct. Therefore, we have shown that the fundamental excitation in the model defined by $f_5(x, y, z)$ is restricted to hop along the $(1,1,1)$ direction of the cubic lattice without creating additional excitations.

5.5   Polynomial Representations of Majorana Hamiltonians

In this section, we prove a statement presented in the main text, that in a commuting Majorana Hamiltonian, of the general form

$$H = -\sum_m \left[\mathcal{O}_m^{(1)} + \mathcal{O}_m^{(2)} + \cdots + \mathcal{O}_m^{(N)} \right] \tag{5.36}$$

two Majorana operators $\mathcal{O}_n^{(i)}$ and $\mathcal{O}_m^{(j)}$ commute over all lattice sites (i.e. $[\mathcal{O}_n^{(i)}, \mathcal{O}_m^{(j)}] = 0$ for any n, m) if and only if their respective stabilizer maps S_i and S_j satisfy $\bar{S}_i \cdot S_j = 0$. Furthermore, we show that the excitation map $E_i = \bar{S}_i$ may be constructed for each operator in the Hamiltonian, so that, given the polynomial representation P of some operator, the quantity $E_i \cdot P$ yields a polynomial encoding the pattern of excitations created by that operator when acting on the ground-state.

Consider a *d*-dimensional lattice with translation group $\Lambda \cong \mathbb{Z}^d$, and a single Majorana fermion per lattice site. At a given site, the identity operator $\mathbb{1}$ and the Majorana fermion γ form the group $\mathbb{Z}_2 \cong \mathbb{Z}/2\mathbb{Z}$ under multiplication since

$$\mathbb{1} \times \gamma = \gamma \times \mathbb{1} = \gamma \tag{5.37}$$

$$\mathbb{1} \times \mathbb{1} = \gamma \times \gamma = \mathbb{1}. \tag{5.38}$$

We refer to this as the 'Majorana group' $\mathcal{M}$ at a given lattice site. The group $\mathcal{M}$ naturally forms a vector space over the finite field $\mathbb{F}_2$ since for some $\alpha \in \mathbb{Z}_2$ and $m \in \mathcal{M}$ we may define the $\mathbb{Z}_2$ action $\alpha \cdot m \equiv m^\alpha \in \mathcal{M}$. Furthermore, any element of the translation group $g \in \Lambda$ has a natural action on $\mathcal{M}$ by multiplication. For instance, let $c, d \in \mathbb{Z}_2$, so that we may represent the action of g on the operator $(\gamma)^c$ simply as $g \cdot c \in \mathbb{F}_2$. A more general operator, for instance $(g \cdot \gamma)^c \otimes (h \cdot \gamma)^d$ may be written as $g \cdot c + h \cdot d \in \mathbb{F}_2$.

Now, we consider a *d*-dimensional lattice with an *n*-site basis so that each site again contains a single Majorana fermion; n is restricted to be an *even* integer so that we may have a well-defined number of *complex* fermions per lattice site. We represent each of the n Majorana fermions at a given lattice site as γ_j, with $j = 1, \ldots, n$. Recall that distinct Majorana fermions anti-commute. Let $g \in \Lambda \cong \mathbb{Z}^d$ be an element of the lattice translation group. From the natural action of the translation group on the Majorana fermions, we may write any two Hermitian

operators $\mathcal{O}_1$ and $\mathcal{O}_2$ up to overall factors of $\pm i$ as

$$\mathcal{O}_1 \equiv \prod_{g \in \Lambda} \left[\prod_{j=1}^{n} (g \cdot \gamma_j)^{c_j(g)} \right] \qquad \mathcal{O}_2 \equiv \prod_{g \in \Lambda} \left[\prod_{j=1}^{n} (g \cdot \gamma_j)^{d_j(g)} \right] \tag{5.39}$$

with the coefficients $c_j(g)$, $d_j(g) \in \mathbb{Z}_2$. On physical grounds, we require that each operator is the product of an *even* number of Majorana fermions so that the total fermion parity is conserved. This is equivalent to the condition that

$$\sum_{g \in \Lambda} \sum_{j=1}^{n} c_j(g) = \sum_{g \in \Lambda} \sum_{j=1}^{n} d_j(g) = 0 \in \mathbb{F}_2 \tag{5.40}$$

Two operators commuting with the total fermion parity commute if and only if they have overlapping support on an even number of Majorana fermions. As a result, the operators $\mathcal{O}_1$ and $h \cdot \mathcal{O}_2$ commute for some $h \in \Lambda$ if

$$\sum_{g \in \Lambda} \sum_{j=1}^{n} c_j(g) \, d_j(h^{-1}g) = 0. \tag{5.41}$$

The condition (5.41) may be simply imposed by representing the operators $\mathcal{O}_1$ and $\mathcal{O}_2$ as

$$S_1 \equiv \sum_{g \in \Lambda} g \cdot \begin{pmatrix} c_1(g) \\ c_2(g) \\ \vdots \\ c_n(g) \end{pmatrix} \qquad S_2 \equiv \sum_{g \in \Lambda} g \cdot \begin{pmatrix} d_1(g) \\ d_2(g) \\ \vdots \\ d_n(g) \end{pmatrix} \tag{5.42}$$

respectively. We further define $\bar{\sigma}_i$ by combining the antipode map $g \to g^{-1}$ with transposition of the S_i vector. For example,

$$\overline{S_1} = \sum_{g \in \Lambda} g^{-1} \cdot \begin{pmatrix} c_1(g) & c_2(g) & \cdots & c_n(g) \end{pmatrix} \tag{5.43}$$

Now, we demonstrate the following statement: $\overline{S_2} \cdot S_1 = 0$ if and only if $[\mathcal{O}_1, \, \ell \cdot \mathcal{O}_2] = 0 \; \forall \; \ell \in \Lambda$.

We demonstrate this by explicit calculation. First note that:

$$\overline{S_2} \cdot S_1 = \sum_{g,h \in \Lambda} \sum_{j=1}^{n} h^{-1} g \cdot c_j(g) \, d_j(h) = \sum_{\ell \in \Lambda} \ell \left[\sum_{g \in \Lambda} \sum_{j=1}^{n} c_j(g) \, d_j(\ell^{-1}g) \right] \tag{5.44}$$

We now observe that $\overline{S_2} \cdot S_1 = 0$ if and only if the quantity in brackets vanishes $\forall \; \ell \in \Lambda$. However, this is precisely the condition (5.41) required so that $[\mathcal{O}_1, \, \ell \cdot \mathcal{O}_2] = 0$. This completes the proof.

A natural consequence of this proposition is the following. Consider N types of operators

at each lattice site, and a Hamiltonian of the form:

$$H = -\sum_m \left[\mathcal{O}_m^{(1)} + \mathcal{O}_m^{(2)} + \cdots + \mathcal{O}_m^{(N)} \right] \tag{5.45}$$

where the sum is over all lattice sites. We may now represent each operator $\mathcal{O}^{(i)}$ at a particular lattice site by a stabilizer map S_i. Then, all of the operators appearing in the Hamiltonian *mutually commute* (i.e. $[\mathcal{O}_n^{(i)}, \mathcal{O}_m^{(j)}] = 0 \; \forall \; i, j, m, n$) if and only if

$$\overline{S_i} \cdot S_j = 0 \tag{5.46}$$

for any pair i, j.

From the stabilizer map, we may determine how the action of an arbitrary operator $\mathcal{O}$ on the ground-state creates a pattern of excitations. Let S be the stabilizer map for an ideal Majorana Hamiltonian with a single operator per lattice site and an n-site unit cell. Furthermore, let P be the polynomial representation of some operator $\mathcal{O}$. We represent S and P as

$$S \equiv \sum_{g \in \Lambda} g \cdot \begin{pmatrix} c_1(g) \\ c_2(g) \\ \vdots \\ c_n(g) \end{pmatrix} \qquad P \equiv \sum_{g \in \Lambda} g \cdot \begin{pmatrix} d_1(g) \\ d_2(g) \\ \vdots \\ d_n(g) \end{pmatrix} \tag{5.47}$$

respectively. Recall that the condition (5.41) determines whether the operator $\mathcal{O}$ commutes with a given stabilizer appearing in the Hamiltonian. Whenever, $\mathcal{O}$ anti-commutes with a stabilizer operator, it creates an excitation at the location of the stabilizer. The pattern of excitations created by $\mathcal{O}$ is then specified by the expression

$$\sum_{h \in \Lambda} h^{-1} \left[\sum_{g \in \Lambda} \sum_{j=1}^n c_j(g) \, d_j(h^{-1}g) \right] = \sum_{h, g \in \Lambda} \sum_{j=1}^n h \, g^{-1} c_j(g) \, d_j(h)$$

$$= \sum_{j=1}^n \left[\sum_{g \in \Lambda} g^{-1} c_j(g) \sum_{h \in \Lambda} h \, d_j(h) \right] = \bar{S} \cdot P \tag{5.48}$$

Therefore, we define the *excitation map*

$$E \equiv \overline{S} \tag{5.49}$$

so that $E \cdot P$ yields a polynomial representation of the pattern of excitations created by the operator $\mathcal{O}$ when acting on the ground-state.

5.6   Stabilizer Maps for Ideal Majorana Hamiltonians with a Two-Site Basis

We now prove the following statement: a topologically-ordered, ideal Majorana Hamiltonian with a two-site basis and a single operator per lattice site, is specified by a stabilizer map is of the form:

$$S = \begin{pmatrix} f(x_1, \ldots, x_d) \\[2ex] \overline{f(x_1, \ldots, x_d)} \end{pmatrix} \tag{5.50}$$

with $f(x_1, \ldots, x_d) \in R \equiv \mathbb{F}_2[x_1, \ldots, x_d]$. Note that S is uniquely defined only up to monomial multiplication on each of its entries.

We demonstrate this as follows. For an ideal Majorana Hamiltonian with a two-site basis, let the stabilizer map be of the form $S^T = (f, g)$ with $f, g \in R$. Recall that the excitation map is given by $E = (\bar{f}, \bar{g})$. We require on an open lattice that $\ker(E) \cong \operatorname{im}(S)$, so that any degenerate ground-states of the Hamiltonian are locally indistinguishable. Note that $\ker(E)$ and $\operatorname{im}(S)$ are defined as

$$\ker(E) \equiv \left\{ \begin{pmatrix} \alpha \\ \beta \end{pmatrix} \in R^2 \,\middle|\, \alpha\bar{f} = \beta\bar{g} \right\} \qquad \operatorname{im}(S) \equiv \left\{ \begin{pmatrix} c \cdot f \\ c \cdot g \end{pmatrix} \,\middle|\, c \in R \right\} \tag{5.51}$$

Let g and f take the form $g = hg'$ and $f = hf'$, for some $h \in R$, so that $\gcd(f, g) = h$, and so that $\gcd(g', f') = 1$. In this case, we observe that

$$\begin{pmatrix} \overline{g'} \\[1ex] \overline{f'} \end{pmatrix} \in \ker(E) \tag{5.52}$$

If this element is generated by $\operatorname{im}(S)$, it must be the case that

$$\begin{pmatrix} \overline{g'} \\[1ex] \overline{f'} \end{pmatrix} = c \begin{pmatrix} f \\ g \end{pmatrix} = c \cdot h \begin{pmatrix} f' \\ g' \end{pmatrix} \tag{5.53}$$

for some $c \in R$. However, this equation is only satisfied if $c \cdot h \cdot \overline{c \cdot h} = 1$, which implies that both c and h must be monomials. As S is only uniquely defined up to monomial multiplication on its entries, we may restrict the remainder of our analysis to stabilizer maps $S = (f, g)^T$ with f and g co-prime so that $\gcd(f, g) = 1$.

Since f and g are co-prime, the condition $\alpha\bar{f} = \beta\bar{g}$ for a vector $(\alpha, \beta)^T$ to be in $\ker(E)$ is satisfied only if $\alpha = c \cdot \bar{g}$ and $\beta = c \cdot \bar{f}$ for some $c \in R$. Now consider that in order for

$\mathrm{im}(S) \cong \ker(E)$ on an open surface, we must have that

$$d \cdot \begin{pmatrix} f \\ g \end{pmatrix} = \begin{pmatrix} c \cdot \bar{g} \\ c \cdot \bar{f} \end{pmatrix}. \tag{5.54}$$

for some $d \in R$. This is indeed satisfied if $c = d$, so that $f = \bar{g}$. Now, we have that the most general form of the stabilizer map (up to monomial multiplication on each entry) is $S = (f, \bar{f})^T$ for some $f \in R$ such that $\gcd(f, \bar{f}) = 1$. The commutativity condition $\bar{S} \cdot S = 0$ is trivially satisfied. This completes the proof.

Chapter 6

Fracton Phases from Duality: A Unified Framework

A remarkable property of the phases of matter introduced in the previous chapter is the existence of point-like fractional excitations ("fractons") [6], which can only be created at the corners of membrane- or fractal-like operators, unlike anyons that are created at the ends of Wilson lines. The creation of anyons at the two ends of a Wilson line immediately implies that anyons can move by repeated application of a local, line-like operator. In contrast, the absence of any operator that can create a pair of fractons implies that a single fracton cannot move without creating additional excitations, i.e. fractons are fundamentally *immobile*. The possible fracton topological orders in solvable models can be grouped into two categories: found:

Type I fracton phases, such as the Chamon-Bravyi-Leemhuis-Terhal (CBLT) model [178, 109] and the Majorana cubic model [6], have fracton excitations appearing at the corners of *membrane* operators; composites of fractons form topological excitations that are only mobile within lower-dimensional subsystems.

Type II fracton phases, such as Haah's code [46] and related models [179], have fracton excitations that appear at the corners of *fractal* operators [1]. All topological excitations are strictly localized and there are no mobile topological quasiparticles.

Fracton topological order [46, 178, 109, 179, 6] provides an exciting development in the search for new quantum phases of matter, for new schemes for quantum information processing [181], and in the investigation of glassy dynamics in interacting quantum systems [182]. Fractons enable new forms of electron fractionalization [6], and provide an alternative to Fermi or Bose statistics in three dimensions. Fractons may be used to build a robust, finite-temperature quantum memory, as theoretically demonstrated for Haah's code [46, 48]. The innately slow dynamics of fractons provides an intriguing connection with quantum glasses, many-body localization, and a new testing ground for the postulates of quantum statistical mechanics.

---

[1] Other models *without* any immobile excitations, but with fractal operators, have been studied [180].

Research on fracton topological phases is in its early stages and has been based on studies of specific lattice models. It is thus highly desirable to find a more unified theoretical framework for fracton topological order. In this work, we demonstrate that fracton topological phases can be obtained as the quantum dual of d-dimensional systems that possess "subsystem symmetries", namely a set of symmetries associated with subsystems of dimension $2 \leq d_s < d$. Specifically, we establish an exact duality relating both type-I and type-II fracton topological orders to symmetry-breaking order in quantum systems with subsystem symmetries along planes and fractals, respectively. This duality between fracton topological order and subsystem symmetry-breaking, hereafter referred to as the "F-S" duality, is naturally obtained from a generalized lattice gauge theory which we introduce. Instead of placing a gauge field on links between neighboring sites as in a standard lattice gauge theory, we introduce a new field to mediate *multi-body* interactions between matter fields on a cluster of neighboring sites. This yields an interacting quantum system with a generalized Gauss' law that characterizes the fracton topological phase.

Before describing our construction in generality, we present a concrete example that yields a new class of type-I fracton topological phases. Consider a model of Ising spins at the sites of a three-dimensional cubic lattice, whose Hamiltonian (H_{plaq}) is defined to be a sum of four-spin interactions at each plaquette, as shown in Table 6.1. This classical "plaquette Ising model" is invariant under a spin-flip $\tau \to -\tau$ along any xy, yz or xz-plane of the cubic lattice. The plaquette Ising model has a rich history of study, attracting interest as a model for the statistical mechanics of smooth surfaces, and as a lattice regularization of string theory [183, 184, 185, 186, 187, 188].

We introduce a generalized lattice gauge theory to construct the quantum dual of the plaquette Ising model in a transverse field. This generalizes Wegner's duality [189] between the d-dimensional transverse-field Ising model and Ising lattice gauge theory [34]. Wegner's duality is motivated by the observation that a configuration of Ising spins may be specified by the locations of the *domain walls* between symmetry-breaking states of the Ising model. As a result, a dual representation of the Ising matter is given by Ising "domain wall" fields on the links of the lattice. Furthermore, since domain walls form closed, $(d-1)$-dimensional surfaces, physical states in the domain wall Hilbert space must satisfy a local "zero-flux" condition, that the lattice curl of the domain wall spins vanishes around each plaquette. In this way, the d-dimensional transverse-field Ising model is dual to $\mathbb{Z}_2$ lattice gauge theory.

Our duality between fracton topological order and subsystem symmetry-breaking is obtained by a similar observation. A configuration of Ising spins may, equivalently, be specified by the eigenvalue of each *interaction term* in the Hamiltonian[2]. For example, to obtain the dual of the plaquette Ising model, we are naturally led to introduce the Ising fields $\{\sigma\}$ at the center of each plaquette. Physically, the σ field labels the presence or absence of a domain wall between the

---

[2]More precisely, a configuration of Ising spins may be specified exactly by the eigenvalues of interaction terms in the Hamiltonian, only up to spin-flips performed along subsystems that leave all of the interaction terms invariant.
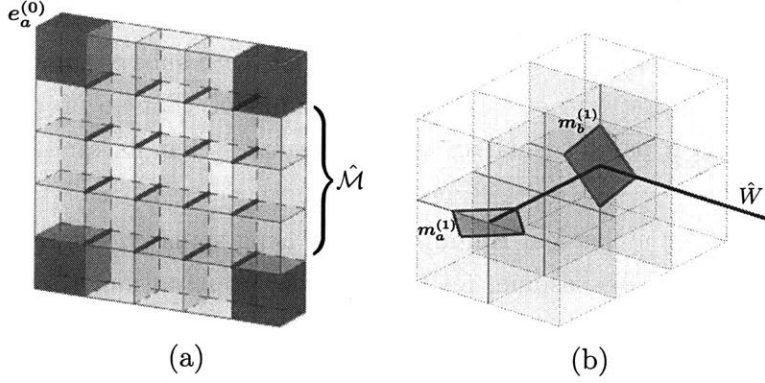
Figure 6-1: The fundamental excitations of the X-cube model are shown in (a) and (b). Acting on the ground- state of the X-cube model with a product of σ^z operators along the colored red links that lie within a flat, rectangular region $\mathcal{M}$ generates four fracton cube excitations ($e_a^{(0)}$) at the corners of the region. A straight Wilson line of σ^x operators acting on the blue links in (b) isolates a pair of quasiparticles ($m_a^{(1)}$ or $m_b^{(1)}$) at the ends, that are only free to move along the line. Attempting to move these quasiparticles in any other direction by introducing a corner in the Wilson line, creates a topological excitation at the corner as shown in (b).

subsystem symmetry-breaking ground-states of the plaquette Ising Hamiltonian. While domain walls in the ordinary Ising model form closed surfaces, the σ fields in our model must satisfy more exotic local constraints due to the geometry of the plaquette interactions to ensure a one-to-one correspondence with the physical space of domain walls in H_{plaq}.

As we demonstrate below, the quantum dual of the plaquette Ising Hamiltonian, in terms of the σ fields, exhibits fracton topological order. The resulting fracton Hamiltonian has a solvable limit, analogous to the deconfined phase of a conventional gauge theory, which is given by a Hamiltonian for the Ising fields (σ), now placed at the links of the dual cubic lattice. As shown in Table 6.1, this fracton Hamiltonian consists of two types of terms: (1) a twelve-spin σ^x interaction for the spins surrounding a dual cube and (2) four-spin σ^z-interactions at each vertex of the dual cubic lattice that are aligned along the xy, yz and xz-planes. The cubic and cross-like geometries of the interactions motivate the name "X-cube" model. The ground-state is topologically-ordered, as the ground-states are locally indistinguishable, and one of the fundamental excitations – obtained by flipping the eigenvalue of the cubic interaction term – is a fracton. This can be seen by observing that there is no local operator that can create a single pair of cube excitations. For example, the operator σ_n^z creates four cube excitations when acting on the ground-state. Repeated application of σ_n^z over a membrane separates the four cube excitations to each *corner* as shown in Figure 6-1a. Therefore, a single cube excitation is fundamentally immobile, and cannot move without creating additional cube excitations. Pairs of cube excitations, however, can be moved by sequentially applying a local, membrane-like operator.

The quasiparticle content of the X-cube model is summarized in Table 6.1, along with other fracton phases such as Haah's code, the CBLT model, and a new spin model which we

introduce and term the "checkerboard model". All of these phases are obtained by applying our generalized lattice gauge theory prescription to spin models with subsystem symmetries. As we will demonstrate, a simple property of the classical spin model, that no product of interaction terms acts exclusively on a pair of isolated spins, guarantees that its quantum dual exhibits fracton topological order.

More generally, consider a classical Hamiltonian for Ising spins (τ_i) at the sites of a three-dimensional Bravais lattice. We assume, for simplicity of presentation, that there is a single spin at each lattice site; the case where the unit cell is larger is explained in the Appendix. The Hamiltonian consists of ℓ types of interactions at each lattice site i, and may be written in the form:

$$H_0 = -t \sum_i \left(\mathcal{O}_i^{(1)}[\tau] + \cdots + \mathcal{O}_i^{(\ell)}[\tau] \right). \tag{6.1}$$

with the constant $t > 0$. We demonstrate that a classical spin Hamiltonian (6.1) satisfying certain simple properties may be used to build a topologically-ordered, quantum system with fracton excitations. First, we require that the spin Hamiltonian (6.1) has a *subsystem symmetry* under which the spin-flip transformation $\tau \to -\tau$ along non-local subsystems of the lattice – i.e. subsystems that scale with the system size – leaves H_0 invariant. We further require that H_0 has no *local* symmetries. In this sense, a subsystem symmetry is "intermediate" between local and global symmetries [190, 191]. For the remainder of this work, we will refer to the plaquette Ising model (H_{plaq}) and the tetrahedral Ising Hamiltonian (H_{tetr}) as concrete examples. As shown in Table 6.1, the Hamiltonian H_{tetr} is defined on the face- centered cubic (fcc) lattice and consists of nearest-neighbor four-spin interactions that form elementary tetrahedra. The tetrahedral Ising model has two interaction terms per site on the fcc lattice. Both the tetrahedral and plaquette Ising models have a subsystem symmetry, as they are invariant under spin-flips along orthogonal planes (xy, yz or xz).

An important consequence of the subsystem symmetry of the spin Hamiltonian H_0 is that the resulting ground-state has sub-extensive *classical* degeneracy D, taking the form $\log D \sim O(L)$ on the length-L three-torus. Since the degeneracy is classical in nature, each ground-state may be distinguished by a local order parameter. Transitioning between ground-states, however, requires performing a spin-flip along a subsystem. While a local perturbation can lift the classical degeneracy, no local operator can connect distinct ground-states.

6.1 Generalized Lattice Gauge Theory and the *F-S* Duality

We now build a quantum Hamiltonian with fracton topological order by promoting the subsystem symmetry of the spin system (6.1) to a local symmetry. We begin by adding a transverse field at each lattice site to allow the classical spins to exhibit quantum fluctuations. Next, we introduce additional Ising spins ($\sigma_{i,a}$) at the center of each multi-spin interaction appearing in
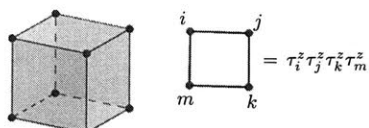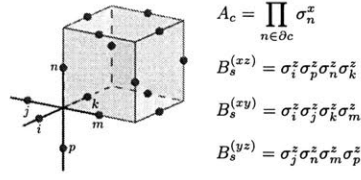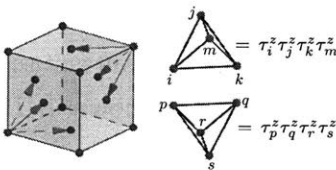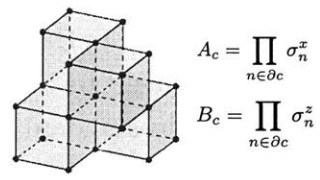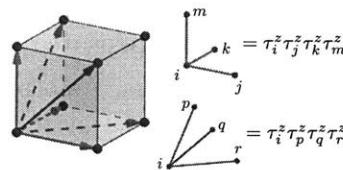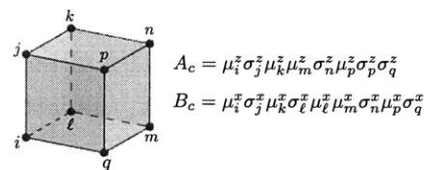
Symmetry Breaking	Symmetry	Fracton Topological Phase
$= \tau_i^z \tau_j^z \tau_k^z \tau_m^z$ **Plaquette Ising Model**	Planar	$A_c = \prod_{n \in \partial c} \sigma_n^x$ $B_s^{(xz)} = \sigma_i^z \sigma_p^z \sigma_n^z \sigma_k^z$ $B_s^{(xy)} = \sigma_i^z \sigma_j^z \sigma_k^z \sigma_m^z$ $B_s^{(yz)} = \sigma_j^z \sigma_n^z \sigma_m^z \sigma_p^z$ **X-Cube Model** [Type I : $e_a^{(0)}, m_a^{(1)}, m_b^{(1)}$]
$= \tau_i^z \tau_j^z \tau_k^z \tau_m^z$ $= \tau_p^z \tau_q^z \tau_r^z \tau_s^z$ **Tetrahedral Ising Model**	Planar	$A_c = \prod_{n \in \partial c} \sigma_n^x$ $B_c = \prod_{n \in \partial c} \sigma_n^z$ **Checkerboard Model** [Type I : $e_a^{(0)}, m_a^{(0)}$]
$k = \tau_i^z \tau_j^z \tau_k^z \tau_m^z$ $= \tau_i^z \tau_p^z \tau_q^z \tau_r^z$ **Fractal Ising Model**	Fractal	$A_c = \mu_i^z \sigma_j^z \mu_k^z \mu_m^z \sigma_n^z \mu_p^z \sigma_p^z \sigma_q^z$ $B_c = \mu_i^x \sigma_j^x \mu_k^x \sigma_\ell^x \mu_\ell^x \mu_m^x \sigma_n^x \mu_p^x \sigma_q^x$ **Haah's Code** [Type II : $e_a^{(0)}, m_a^{(0)}$]

Table 6.1: Representative examples of fracton topological orders built from classical spin systems with the indicated subsystem symmetries. In the plaquette Ising model, spins lie on the sites of a cubic lattice, and the Hamiltonian is a sum of four-spin interactions at the face of each cube. In the tetrahedral Ising model, spins on an fcc lattice participate in four-spin interactions coupling neighboring spins that form a tetrahedron, as indicated. Finally, the fractal Ising model consists of two types of four-spin interactions, and has a fractal symmetry; the Hamiltonian is invariant under a spin-flip along a three-dimensional Sierpinski triangle, as elaborated in later sections. The X-cube, checkerboard, and Haah's code fracton models, are solvable limits of fracton phases that are obtained by "gauging" the subsystem symmetry of these spin models. The X-cube model is represented by placing spins on links of the cubic lattice, and the Hamiltonian is a sum of a twelve-spin σ^x-operator at each cube and the indicated planar, four-spin σ^z-operators. The checkerboard model is a sum of eight-spin σ^x- and σ^z- interactions over cubes arranged on an fcc lattice. Only the fundamental excitation types are indicated, with the notation $e_a^{(j)}$ ($m_a^{(j)}$) to refer to a dimension-j excitation – i.e. an excitation that is only free to move within a dimension-j subsystem without creating additional excitations.

H_0; these spins appear at the sites of a lattice with an ℓ-site basis. We introduce a minimal coupling H_c between the σ spins and the Ising matter fields, by coupling each σ to its corresponding multi-spin interaction:

$$H_c \equiv -t \sum_i \left(\sigma^z_{i,1} \mathcal{O}^{(1)}_i[\tau^z] + \cdots + \sigma^z_{i,\ell} \mathcal{O}^{(\ell)}_i[\tau^z] \right). \tag{6.2}$$

After this minimal coupling, the Hamiltonian describing σ and the Ising matter fields is

$$H = H_c - h \sum_i \tau^x_i. \tag{6.3}$$

We refer to σ as the *nexus field*, as each σ is placed at the center of an elementary multi-spin interaction of the classical spin Hamiltonian. We will soon observe that the nexus field provides a natural generalization of a gauge field in a conventional lattice gauge theory. In contrast to our construction, applying the standard gauging procedure to any of the spin models shown in Table 6.1 by introducing a gauge field on the links of the cubic lattice would result in a Hamiltonian with conventional $\mathbb{Z}_2$ topological order. Our procedure is also distinct from discretizations of "higher-form" gauge theories, in which interactions between $(n-1)$-form matter fields are mediated by an n-form gauge field [192, 193].

The subsystem symmetry of the classical spin system (6.1) has now been promoted to a local spin- flip symmetry of the Hamiltonian (6.3). While τ^x_n – the generator of a single spin-flip – anti-commutes with several multi-spin interactions in (6.1), this can be compensated by acting with the nexus field $\sigma^x_{j,a}$ on the lattice sites associated with these interactions. As a result, the operator

$$G_i = \tau^x_i A_i \tag{6.4}$$

where

$$A_i \equiv \prod_{(j,a) \in P(i)} \sigma^x_{j,a} \tag{6.5}$$

generates a local symmetry of the Hamiltonian ($[G_i, H] = 0$). The set $P(i)$ specifies the locations of multi-spin interactions that anti-commute with τ^x_i.

We proceed to add all other interaction terms involving the nexus field and the Ising spins that are consistent with this local spin-flip symmetry. To lowest-order, we include a transverse field for the matter and nexus fields:

$$H = -t \sum_{i,a} \sigma^z_{i,a} \mathcal{O}^{(a)}_i[\tau^z] - h \sum_i \tau^x_i - J \sum_{i,a} \sigma^x_{i,a} \tag{6.6}$$

Since the operator G_i generates a local symmetry of the Hamiltonian, we may impose the

134

condition $G_i |\Psi\rangle = |\Psi\rangle$ on the Hilbert space, which amounts to a generalized Gauss's law. In analogy with conventional gauge theory, we will refer to A_i as the *nexus charge* operator. As an example, the nexus charge operator in the X-code model is given by the product of σ^z on twelve spins sitting at the links surrounding a cube, as shown in Table 6.1.

Since the generalized Gauss's law condition commutes with the spin-nexus Hamiltonian (6.6), it is possible to choose a "gauge" that completely eliminates the Ising matter fields, and yields a Hamiltonian exclusively for the nexus spins. First, we impose the generalized Gauss's law $\tau_i^x |\Psi\rangle = A_i |\Psi\rangle$ to obtain a Hamiltonian acting within the constrained Hilbert space

$$H = -t\sum_{i,a} \sigma_{i,a}^z \mathcal{O}_i^{(a)}[\tau^z] - h\sum_i A_i - J\sum_{i,a} \sigma_{i,a}^x \tag{6.7}$$

Since each τ_i^z operator commutes with the Hamiltonian, we may restrict our attention to states in the constrained Hilbert space that satisfy $\tau_i^z = +1$. This yields the gauge-fixed Hamiltonian

$$H = -t\sum_{i,a} \sigma_{i,a}^z - h\sum_i A_i - J\sum_{i,a} \sigma_{i,a}^x \tag{6.8}$$

When $t/h \ll 1$, it is convenient to identify an effective Hamiltonian that takes the form

$$H_{\text{eff}} = -K\sum_{i,k} B_i^{(k)} - h\sum_i A_i - J\sum_{i,a} \sigma_{i,a}^x \tag{6.9}$$

where we have introduced operators $B_i^{(k)}$ at each lattice site i. These operators are determined in perturbation theory by computing the simplest product of σ^z terms near a given lattice site that commute with the nexus charge $[B_i^{(k)}, A_j] = 0$. As an example the $B_i^{(k)}$ operators obtained by applying this construction to the plaquette Ising model are shown in Table 6.1.

Our proposal bears resemblance to the construction of a conventional lattice gauge theory. First, the Hamiltonian for $\mathbb{Z}_2$ gauge theory is recovered from the general form of the Hamiltonian for the Ising matter and nexus fields (6.6) if the matter fields couple through nearest-neighbor two-body interactions, so that $\mathcal{O}_i^{(a)} = \tau_i^z \tau_{i_a}^z$ where i_a is nearest-neighbor to site i. This is in contrast to the multi-body interactions that are present in our models with subsystem symmetry. In the gauge-fixed Hamiltonian (6.8), A_i then becomes the familiar $\mathbb{Z}_2$ charge operator, while the operator B_n, appearing in the effective Hamiltonian H_{eff}, precisely measures the $\mathbb{Z}_2$ flux through an elementary plaquette.

Within our construction, the $B_i^{(k)}$ operators provide the natural generalization of the flux in a lattice gauge theory. As the excitation obtained by flipping the eigenvalue of a $B_i^{(k)}$ operator is often point-like, we will refer to the excitation as a "generalized monopole". While the flux is always a line-like excitation in a three-dimensional Abelian lattice gauge theory, the behavior of the "generalized monopole" can be quite varied. As an example, the generalized monopole is a fracton in both the checkerboard spin model and in Haah's code, but is free to move along a line without creating additional excitations in the X-cube model. We refer to such an excitation

135

H_{spin}	H_{nexus}	Explanation
$\mathcal{O}_i^{(a)}$	$\sigma_{i,a}^z$	A classical configuration of Ising spins (τ) may be specified by spins (σ) placed at the centers of each of the interaction terms $\mathcal{O}_i^{(a)}$ for the Ising matter.
τ_i^x	A_i	The dual representation of τ_i^x is given by the nexus charge A_i, defined as the product of σ_i^x terms that correspond to the interactions flipped by τ_i^x.
$\displaystyle\prod_{(i,a)\in Q(j)} \mathcal{O}_i^{(a)} = 1$	$B_j^{(1)}\,\lvert\Psi\rangle = \lvert\Psi\rangle$	A local product of interactions for the Ising matter fields that yields the identity corresponds to a constraint on the dual Hilbert space. The constraint restricts the Hilbert space of $\{\sigma\}$ to that of *domain wall* configurations in the ordered phase of H_0.
$\displaystyle\widetilde{W} \equiv \prod_{(i,a)\in\Sigma} \mathcal{O}_i^{(a)}$	$\displaystyle W \equiv \prod_{(i,a)\in\Sigma} \sigma_{i,a}^z$	A product of σ^z operators is dual to a product of interaction terms for the matter fields. As a result, the nexus charge is a fracton only if there is no product of interaction terms that can create an isolated pair of spin-flips.

Table 6.2: Correspondence between operators in the Hilbert spaces of the Ising matter fields and the nexus spins, obtained from the *F-S* duality.
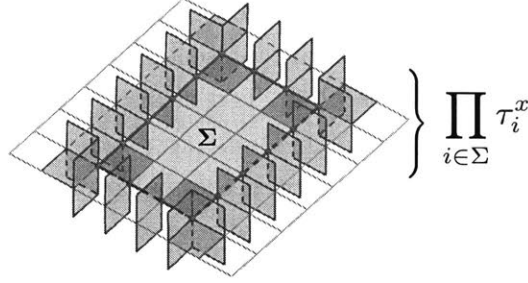
Figure 6-2: A "domain wall" in the ground-state of the plaquette Ising model (H_{plaq}) is depicted, by coloring the plaquette interactions that have been flipped by the action of a spin-flip transformation along a planar region Σ. The F-S duality implies that the ground-state for the X-code fracton phase is given by an equal superposition of a dual representation of these domain-walls.

as a dimension-1 quasiparticle [6], as the excitation is only mobile along a line. As shown in Figure 6-1b, a straight Wilson line can create an isolated pair of the generalized monopole excitations in the X-cube model, which can only move along the line without creating additional excitations. Within type-I fracton topological order, composites of the fracton charge excitations that are mobile in two dimensions can have non-trivial mutual statistics with the generalized monopole. This is true in both the checkerboard and X-cube models, where an anyon formed from a composite of two fracton charges has π-statistics with a generalized monopole in its plane of motion.

We now consider the generalized lattice gauge theory (6.8) when $J = 0$, so that the nexus field (defined in the σ^z-basis) has no dynamics. The resulting Hamiltonian

$$H_{\mathrm{nexus}} = -t \sum_{i,a} \sigma_{i,a}^z - h \sum_i A_i \tag{6.10}$$

has a local symmetry, as the $B_i^{(k)}$ operators commute with each term in (6.10). We refer to the emergent local constraints on the Hilbert space

$$B_i^{(k)} |\Psi\rangle = |\Psi\rangle \tag{6.11}$$

as the generalized "flatness" condition, analogous to a flat connection in a continuum gauge theory, as these constraints are obtained in the limit that there is zero "flux" of the nexus field.

Our construction of a generalized lattice gauge theory implies that the quantum dual of the Ising matter in the presence of a transverse field:

$$H_{\mathrm{spin}} = -t \sum_{i,a} \mathcal{O}_i^{(a)}[\tau^z] - h \sum_i \tau_i^x. \tag{6.12}$$

is precisely given by the nexus Hamiltonian (6.10), combined with the generalized flatness condition (6.11).

Without appealing to the generalized lattice gauge theory, the duality can be obtained directly from the Hamiltonian H_{spin}. A dual representation is constructed by placing the nexus spins at the centers of the interactions $\mathcal{O}_i^{(a)}$. The nexus spins are now interpreted as domain wall variables for the ordered phase $(t/h \gg 1)$ of the spin model H_{spin}. The nexus spins must satisfy local constraints due to the geometry of the multi-spin interactions $\mathcal{O}_i^{(a)}[\tau]$ in order to correspond to the physical space of domain walls between ground-states of H_0. These local constraints are precisely given by the generalized flatness condition (6.11). As an example, the generalized monopole operators $B_i^{(k)}$ for the plaquette Ising model are obtained by noting that the product of four plaquette interactions that wrap a cube is equal to the identity. Our F-S duality implies a map between local operators in the Hilbert spaces of the Ising matter and nexus fields, as summarized in Table 6.2. As an example, a domain wall in the ground-state of the plaquette Ising model is shown in Figure 6-2.

The duality constructed above is physically intuitive, but it is also useful to have a more direct correspondence. Here we explain unitary transformations from the Hilbert spaces for spin models to constrained Hilbert spaces for nexus fields. The unitary transformation does not always preserve locality but does preserve the locality of operators that appear in Hamiltonians under interest. The simplest example would be the one-dimensional transverse field Ising model.

6.2 Fracton Topological Order

We now invoke the F-S duality to demonstrate that the commuting Hamiltonian

$$H_{\text{fracton}} = -\sum_{i,k} B_i^{(k)} - \sum_i A_i \qquad (6.13)$$

exhibits fracton topological order. We argue that (i) the spectrum of H_{fracton} has sub-extensive topological degeneracy and that (ii) the nexus charge is fundamentally immobile. We provide rigorous proofs of these statements in the Appendix using techniques in commutative algebra and elementary algebraic geometry, which provide effective mathematical tools to study the subsystem symmetries of classical spin models, as well as the ground-state degeneracy and excitation spectrum of fracton topological phases. An algebraic representation of a classical Ising system defines an algebraic variety over the field of characteristic 2 ($\mathbb{F}_2$), defined by $\mathbb{Z}_2$ addition and multiplication [47]. Two conditions on this variety, as derived in the Appendix from the Buchsbaum-Eisenbud criterion [194, 195] for the exactness of a complex of free modules, guarantee that the quantum dual exhibits fracton topological order.

We begin by using the F-S duality to demonstrate that the sub-extensive degeneracy of the classical, $h = 0$ ground-state of H_{spin} implies that the Hamiltonian H_{fracton} has sub-extensive *topological* ground-state degeneracy on the torus. Recall that a product of τ_i^x operators along an appropriate subsystem Σ generates a symmetry of the Hamiltonian H_{spin}. When $t/h \gg 1$, the ground-state exhibits classical, sub-extensive degeneracy since there are $O(L)$ independent sub-

systems along which a spin-flip commutes with all of the interaction terms $\mathcal{O}_i^{(a)}$. The plaquette Ising model, for example, commutes with the product of τ_i^x along a plane, and the ground-state has sub-extensive, classical degeneracy since there are $O(L)$ independent planes along which a spin-flip may be performed.

From the operator dictionary for the F-S duality, the dual representation of this spin-flip operator is given by a product of nexus charges A_i along the same subsystem Σ. Furthermore, each interaction term $\mathcal{O}_i^{(a)}$ is dual to a single-spin operator $\sigma_{i,a}^z$. Since the F-S duality preserves the commutation relations between operators, we conclude that due to the subsystem symmetry of H_{spin}, the operators in the dual theory satisfy:

$$\left[\sigma_{i,a}^z, \prod_{i \in \Sigma} A_i\right] = 0 \tag{6.14}$$

for all i, a. This commutation relation can only be satisfied if the product of nexus charges along Σ yields the identity, so that $\prod_{i \in \Sigma} A_i = 1$. This relation implies that not all of the nexus charge operators are independent on the torus. Each of the $O(L)$ independent subsystems associated with the subsystem symmetry of H_{spin} reduces the number of independent nexus charge operators by one. We denote the total number of such independent subsystems by k_A.

In the ground-state of the fracton Hamiltonian, the 2^N-dimensional Hilbert space of N nexus spins is constrained by the M nexus charge and monopole operators that appear in the Hamiltonian. However, only $M - k$ of the operators are independent on the torus, where $k = k_A + k_B$ is the number of "dependency relations" on both the nexus charge and monopole operators. The topological ground-state degeneracy on the torus is given by $D = 2^{k+(N-M)}$. When the number of interactions appearing in H_{fracton} is identical to the total number of nexus spins ($N = M$), as is the case for all of the fracton models considered in this work, the topological degeneracy is precisely $D = 2^k$. In this case, the sub-extensive degeneracy of the $h = 0$ ground-state of the spin model H_{spin} provides a lower bound on the topological degeneracy of H_{fracton}. For example, the checkerboard spin model has topological ground-state degeneracy $\log_2 D = 6L - 6$ on the length-L three-torus, as we compute in the Appendix, while the tetrahedral Ising model only has classical degeneracy $\log_2 D_c \sim O(3L)$ since the model has subsystem symmetries along three orthogonal planes.

In addition to the sub-extensive, topological degeneracy of H_{fracton}, we also wish to show that that there is no degeneracy in the spectrum of Hamiltonian due to the presence of *local* observables. In the absence of local observables, the local reduced density matrix will be identical for any degenerate states in the spectrum of the Hamiltonian, and the topological degeneracy, as computed by constraint-counting, will be stable to local perturbations [196]. As we demonstrate in the Appendix, the ground-states of H_{fracton} are guaranteed to be locally indistinguishable, provided that the classical spin system H_0 has no lower-dimensional symmetries along subsystems of dimension $d_s < 2$ (e.g. line-like symmetries). We prove this by using an algebraic representation of H_{fracton} and also argue this as a consequence of the F-S duality.

$$W \equiv \prod_{(i,a)\in\Sigma} \sigma^z_{i,a} \qquad\qquad \widetilde{W} \equiv \prod_{(i,a)\in\Sigma} \mathcal{O}^{(a)}_i[\tau^z]$$

$$O = \mathcal{O}^{(a)}_i[\tau^z]$$

$$\Sigma \qquad\qquad\qquad \Sigma$$

$$W|\Psi_{gs}\rangle \qquad\qquad\qquad \widetilde{W}|\Psi_{para}\rangle$$

(a) (b)

$$\sigma^z_{i,a} \qquad \prod_{(i,a)\in\Gamma}\sigma^z_{i,a} \qquad\qquad \prod_{(i,a)\in\Gamma}\mathcal{O}^{(a)}_i[\tau^z] = \tau^z_m \tau^z_n \tau^z_p \tau^z_q$$

$$\Gamma \qquad\qquad \tau^z_m \quad \tau^z_n \qquad \tau^z_q \quad \tau^z_p$$

(c) (d)
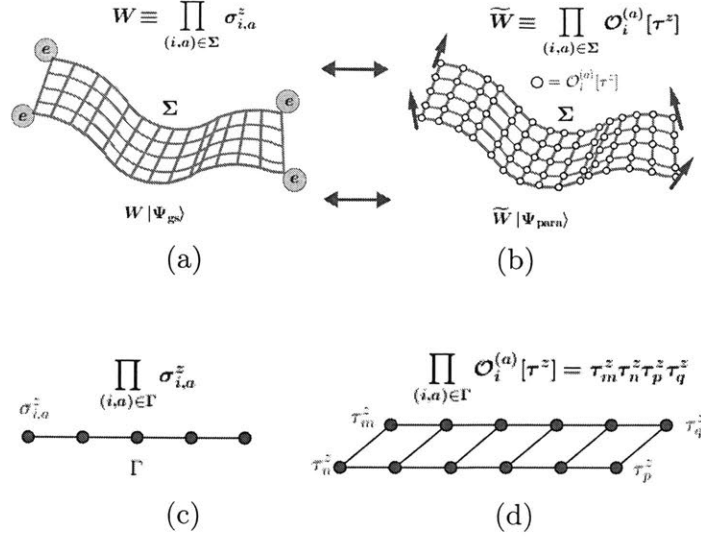
Figure 6-3: The nexus charge is a fracton only if there is no operator W that can create an isolated pair of excitations when acting on the ground-state of H_{fracton}, as in (a). Equivalently, a dual representation of the operator, given as a product of the interaction terms in the quantum dual as shown in (b), cannot create an isolated pair of spin-flips when acting on the paramagnetic state $|\Psi_{\text{para}}\rangle \equiv |\rightarrow \cdots \rightarrow\rangle$. An example is given in (c) and (d); a straight Wilson line acting on the ground-state of $H_{\text{X-Cube}}$ in (c) admits a dual representation as a product of four-spin plaquette interactions along a line, as shown in (d). No product of interaction terms in the plaquette Ising model can produce an isolated pair of spin-flips. As a result, the nexus charge in $H_{\text{X-Cube}}$ must be a fracton.

Having demonstrated that H_{fracton} exhibits sub-extensive topological degeneracy and that the degenerate ground-states are locally indistinguishable, we now demonstrate that the nexus charge is indeed a fracton excitation, provided that the spin model (6.12) satisfies a simple condition. Consider acting on the ground-state of H_{fracton} with the operator

$$W \equiv \prod_{(i,a)\in\Sigma} \sigma^z_{i,a} \tag{6.15}$$

where Σ is some subset of the lattice. The operator W will create nexus charge excitations by anti-commuting with a collection of A_i operators. Invoking the F-S duality, we observe that the pattern of excitations created by W is precisely given by the location of spin-flips created by the dual operator $\widetilde{W} \equiv \prod_{(i,a)\in\Sigma} \mathcal{O}^{(a)}_i[\tau^z]$ when acting on the paramagnetic state $|\Psi_{\text{para}}\rangle \equiv |\rightarrow \cdots \rightarrow\rangle$. The spectrum of H_{fracton} contains fractons only if there is *no operator* of the form $\widetilde{W}$ that can create a single pair of spin-flip excitations. If such an operator did exist, then it would be possible to move a single nexus charge without any energy cost and the charge would be mobile.

Our condition for the existence of fracton excitations is simple to demonstrate for the plaquette Ising and tetrahedral Ising Hamiltonians. Here, it is evident that any product of the four-spin interactions shown in Table 6.1 creates *at least* four spin-flip excitations when act-

ing on the paramagnetic state $|\tilde{\Psi}\rangle$. Therefore, the nexus charge for each of the corresponding H_{fracton} Hamiltonians is a fracton. In fact, if any Ising Hamiltonian H_0 has a subsystem symmetry along three orthogonal planes, and two or more independent interactions per lattice site, then the quantum dual will always exhibit fracton topological order, as we demonstrate in the Appendix. All Type-I fracton topological phases that have been discovered thus far fit into this framework.

We now summarize the precise conditions on the classical spin system H_0, as derived in the Appendix using the algebraic representation of the classical spin system, that guarantee that H_{fracton} exhibits fracton topological order:

1. H_{spin} contains more than one independent interaction term per lattice site

2. No product of the interaction terms $(\mathcal{O}_i^{(a)})$ can generate an isolated pair of spin-flips

6.3   Phase Diagram

We discuss the phase diagram of the spin-nexus Hamiltonian (6.6). In the limit $t \ll h$, the nexus field decouples from the Ising matter; τ_i^x is set to 1, and the effective Hamiltonian for the nexus field is

$$H_{t \ll h} = -\tilde{t} \sum_{i,k} B_i^{(k)} - J \sum_i \sigma_i^x. \tag{6.16}$$

The generalized Gauss' law becomes $A_i = 1$. Here, $\tilde{t}$ is some power of t as $B_i^{(k)}$ is obtained from perturbation theory. When $J \ll \tilde{t}$, the nexus field forms a fracton phase that is described by Hamiltonian H_{fracton}. The topologically-ordered fracton phase and the Ising paramagnet survive up to a finite t/h and J/h, as both phases are gapped and stable to perturbations [196].

Confinement: From the topologically-ordered fracton phase, we may proceed in two directions. First, we consider increasing J/h while keeping $t/h \ll 1$, a constant. Above a critical value $(J/h) \geq (J/h)_*$, the ground-state will be a condensate of nexus flux excitations and the fracton topological order will be destroyed. The nature of the transition between the fracton phase and the trivial (confined) phase is currently unknown.

'Higgs' Phase: We now consider the region of the phase diagram where $t \gg h$, keeping $J \ll h$ at a fixed constant. Here, the matter fields enter an ordered state with $\langle \sigma_i^z \mathcal{O}_i^{(a)}[\tau^z] \rangle = 1$. This may be seen as the analog of a 'Higgs' phase, as the Ising order gives the nexus field a mass $m \sim O(t)$ that destroys the fracton topological phase. The ground-state in this region of the phase diagram is non-degenerate, even though the ordered phase of the pure spin model (6.12) has sub-extensive degeneracy. We may demonstrate this by observing that in the gauge-fixed Hamiltonian (6.8), increasing t/h destroys the fracton topological order by condensing the nexus charge, and produces a non-degenerate ground-state. We also observe from H_{eff} that the confined and Higgs regions of the spin-nexus phase diagram are smoothly connected, as in the
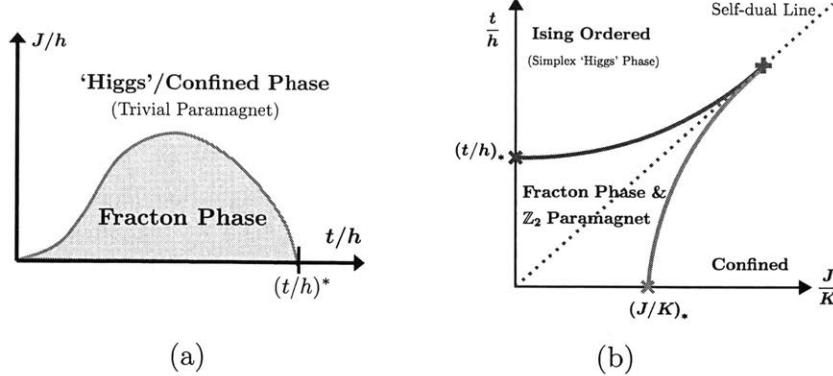
Figure 6-4: Schematic phase diagram of (a) the spin-nexus Hamiltonian (6.6). The 'Higgs' phase for the nexus field is smoothly connected to the phase reached by condensing the nexus charge. The checkerboard model coupled to Ising matter fields admits an additional *self-duality* under the exchange of the nexus charge and flux; as a result, the phase diagram is as shown in (b).

Ising lattice gauge theory. We summarize our schematic phase diagram in Fig. B-1a.

In passing, we observe that the checkerboard fracton Hamiltonian in Table 6.1 in the presence of two transverse fields $H = -K \sum_c B_c - h \sum_c A_c - \sum_{i,j} (J \sigma_{i,a}^x + t \sigma_{i,a}^z)$ has a symmetry under $\sigma^z \leftrightarrow \sigma^x$. This implies that the phase diagram should be symmetric under $K \leftrightarrow h$ and $J \leftrightarrow t$. The confinement and 'Higgs' transition must be dual to each other, and the line of phase transitions must meet at a self-dual point of the phase diagram. It is unknown whether any of the indicated phase transitions in Fig. B-1 are continuous.

6.4   Outlook

Translationally-invariant, commuting Hamiltonians built from interacting qubits [47] and fermions [6] admit a convenient algebraic representation as a collection of polynomials over a finite field. The translation group of the lattice is $\mathbb{Z}^D$, whose group algebra happens to be the polynomial algebra. The polynomials conveniently keep track of the support of various operators. Remarkably, this algebraic characterization of the Hamiltonian terms enable us to decide whether the given Hamiltonians is commuting, degenerate, topologically ordered, and the nature of the excitations [6, 47]. Also, it gives a unique method to calculate the ground-state degeneracy of our exotic models. In the context of our nexus theory, the polynomial representation has a natural physical interpretation, as it precisely specifies the generalized Gauss' law G_n that defines the spin-nexus Hamiltonian (6.6). In this way, the polynomial representation encodes the local symmetry that defines a fracton topological phase. We elaborate on these method in the appendix, which we aim to be pedagogical.

With the identification of a generalized Gauss's law that characterizes a fracton topological phase, our work provides an important step towards searching for material realizations of fracton topological order. Such a local conservation law can, in principle, appear in physical systems such as frustrated magnets, where our generalized gauge theory can emerge as an effective

description at low energies, leading to fracton topological order.

6.5 Algebraic Construction of a Fracton Hamiltonian

Commutative algebra and elementary algebraic geometry provide an indispensable machinery for demonstrating the results summarized in the main text. Starting from a purely algebraic representation of commuting Pauli Hamiltonians, as originally introduced in Ref. [47], we demonstrate that certain classical spin systems with subsystem symmetry may be used to construct a commuting Hamiltonian with fracton topological order. Only the data contained in the classical spin model is required as input to generate the topologically-ordered fracton Hamiltonian. This map between a classical spin system and a topologically-ordered Hamiltonian may be used to construct a wide variety of topological orders, ranging from conventional $\mathbb{Z}_N$ gauge theory to the type-I and type-II fracton topological orders presented in the main text. Our presentation of this correspondence in this section, while mathematically inclined, is self-contained and includes a rigorous and precise statement of the results summarized in the main text.

Given a translationally-invariant Pauli Hamiltonian (also called stabilizer or additive code Hamiltonian) it is possible to write a purely algebraic representation of the Hamiltonian, known as the stabilizer map [47]. For a Hamiltonian defined on a d-dimensional lattice with an ℓ-site basis, and containing m distinct operators per lattice site, the stabilizer map will be a $2\ell \times m$ matrix of Laurent polynomials over the finite field $\mathbb{F}_2$. The prescription to obtain the stabilizer matrix is as follows. Given a Pauli operator (a tensor product of Pauli matrices), write it as a product of two Pauli operators, where one entirely consists of σ^x and the other of σ^z, using $\sigma^y = i\sigma^x\sigma^z$. Select a reference site s_0. Relative to s_0, an arbitrary site where a Pauli matrix acts on will be given by an integer displacement vector, e.g., (a, b, c) in three dimensions, and one writes it as $x^a y^b z^c$. Thus, every nontrivial factor σ^x or σ^z gives a monomial $x^a y^b z^c$. Collect all monomials corresponding to σ^z that act on a-th spins in the unit cell, and combine them with $+$. This give a Laurent polynomial that goes into a-th component in a column vector. The sum of monomials corresponding to σ^x goes into $(a + \ell)$-th component. This way, one obtains a column vector of Laurent polynomials associated with the Pauli operator. For each type of term in the Hamiltonian, repeat the process to obtain a collection of column vectors, that is a matrix. Note that the overall sign of the Pauli operator is dismissed. We denote by $p(O)$ the Laurent polynomial vector corresponding to the Pauli operator O.

From the stabilizer map S, we may then define the *excitation map* E, defined so that $E \cdot p(\mathcal{O})$ yields the pattern of excitations created by $\mathcal{O}$ when acting on the ground-state of the stabilizer Hamiltonian. As shown in [47], the excitation map is given by $E \equiv S^\dagger \lambda_\ell$ with $S^\dagger \equiv (\overline{S})^T$ and where

$$\lambda_\ell \equiv \begin{pmatrix} 0 & \mathbf{1}_{\ell \times \ell} \\ \mathbf{1}_{\ell \times \ell} & 0 \end{pmatrix}. \tag{6.17}$$

143

Here, $\overline{S}$ indicates that each monomial in the stabilizer map has been inverted, e.g. for the polynomial $f(x, y, z)$ we have $\overline{f(x, y, z)} = f(\overline{x}, \overline{y}, \overline{z})$ with $\overline{x} \equiv x^{-1}$, $\overline{y} \equiv y^{-1}$, $\overline{z} \equiv z^{-1}$. The following are necessary conditions for the stabilizer map to correspond to a topologically-ordered stabilizer Hamiltonian. First, all terms in the Hamiltonian commute if and only if $S^\dagger \lambda_\ell S = E \cdot S = 0$ [47]. Second, we require that any degenerate ground-states on the torus are locally indistinguishable, so that the degeneracy is topological in nature. This is guaranteed if, on an infinite system, $\ker E = \operatorname{im} S$. This means that any local operator commuting with the stabilizer Hamiltonian is always a product of operators already appearing in the Hamiltonian.

Consider the classical spin Hamiltonian H_0, defined on a Bravais lattice with a single spin per lattice site. The stabilizer map for this classical spin Hamiltonian takes the form

$$S_c \equiv \begin{pmatrix} f_1 & f_2 & \cdots & f_n \\ 0 & 0 & \cdots & 0 \end{pmatrix} \tag{6.18}$$

As the Hamiltonian is classical and contains only τ^z-type terms, the second row in the stabilizer map is identically zero.

As an example, consider the plaquette Ising model. There are three plaquette terms depending on their orientation. The plaquette in the xy-plane couples spins at $(0, 0, 0)$, $(1, 0, 0)$, $(0, 1, 0)$, and $(1, 1, 0)$ by τ^z operators. The position coordiantes are translated into the monomials as 1, x, y, xy, respectively, and thus the the plaquette term is mapped to $1 + x + y + xy$. Likewise, the plaquette term in yz-plane is represented by $1 + y + z + yz$, and that in zx-plane is by $1 + x + z + xz$. The stabilizer map is

$$S_{\text{plaq}} = \begin{pmatrix} 1 + x + y + xy & 1 + y + z + yz & 1 + x + z + xz \\ 0 & 0 & 0 \end{pmatrix}. \tag{6.19}$$

Below, we will often omit the zero rows, which will not cause any confusion when it is clear from the context whether the operator is of σ^z or σ^x type.

We now summarize our main results using algebraic language. Given the stabilizer map of the form S_c for a classical spin Hamiltonian in d spatial dimensions, consider the *ideal* $I(S_c) \equiv \langle f_1, \ldots, f_n \rangle$, defined as the set of all linear combinations of the polynomials f_1, ..., f_n in the stabilizer map:

$$I(S_c) \equiv \left\{ \sum_{i=1}^{n} c_i f_i \;\middle|\; c_i \in \mathbb{F}_2[x_1^\pm, \ldots, x_d^\pm] \right\}. \tag{6.20}$$

If the ideal $I(S_c)$ constructed from the stabilizer map satisfies the following conditions, then the quantum dual obtained by our prescription in the main text exhibits fracton topological order.

1. Co-dimension Condition: The stabilizer ideal must have a sufficiently large co-dimension

144

(height)

$$\text{codim}\, I(S_c) \geq 2. \tag{6.21}$$

Physically, this means that the classical spin Hamiltonian must have at least two independent interactions per lattice site. This condition alone ensures that the quantum dual of the classical model with transversal field is topologically ordered.

2. **Fracton Condition:** The stabilizer ideal $I(S_c) \equiv \langle f_1, \ldots, f_n \rangle$ does not contain binomial terms,

$$1 + x_1^{n_1} \cdots x_d^{n_d} \notin I(S_c) \tag{6.22}$$

for all $n_1, \ldots, n_d > 0$. Physically, this guarantees that, in the topologically-ordered Hamiltonian built from the algebraic data in the classical spin model, the elementary topological excitations are immobile.

3. **Planar symmetries imply the fracton condition:** Planar symmetries on xy, yz, and zx planes imply $f_i(1,1,z) = 0$, $f_i(x,1,1) = 0$, and $f_i(1,y,1) = 0$ for all i, respectively. The latter conditions combined imply the fracton condition.

If the first two conditions are satisfied, then we may build a commuting Hamiltonian with fracton topological order from the data in the classical stabilizer map S_c. The topological ground-state degeneracy of this Hamiltonian will take the general form $\log_2 D \sim c_1 L^{d-2}$ on the length-L torus.

6.5.1 Symmetries

An operator $\mathcal{O}$, given by a product of τ^x terms, generates a subsystem symmetry if $\mathcal{O}$ commutes with the classical Hamiltonian H_0. In the polynomial representation, the non-local operator $\mathcal{O}$ is expressed by a formal infinite sum $h(\mathcal{O}) = \sum_{\vec{s}} x^{s_1} y^{s_2} z^{s_3}$ where $\vec{s}$ ranges over all spins where $\mathcal{O}$ acts on by τ^x. The commutativity of $\mathcal{O}$ with the Hamiltonian is equivalent to the requirement that $\mathcal{O}$ does not create any excitations when acting on the ground-state. This is the case if and only if the image of $h(\mathcal{O})$ under the excitation map $E = S^\dagger \lambda_1$ is zero: $E\, h(\mathcal{O}) = 0$, or equivalently, $h(\bar{x}, \bar{y}, \bar{z})S = 0$.

As an example, consider an operator O_{xy} that flips all spins on an xy-plane. The polynomial representation reads

$$h_{xy} = \sum_{n,m \in \mathbb{Z}} x^n y^m = \overline{h_{xy}}. \tag{6.23}$$

This formal infinite series has a property that $x h_{xy} = h_{xy} = y h_{xy}$, which is just another expression of the fact that O_{xy} is translation invariant within the xy-plane. Consequently, for

145

any Laurent polynomial $f(x, y, z)$ we have $f(x, y, z)h_{xy} = f(1, 1, z)h_{xy}$. We observe that this is a symmetry of the plaquette Ising model, whose stabilizer map is found in (6.19), since

$$h_{xy} \cdot (1 + x + y + xy) = h_{xy} \cdot (1 + 1 + 1 + 1) = 0,$$
$$h_{xy} \cdot (1 + y + z + yz) = h_{xy} \cdot (1 + 1 + z + z) = 0,$$
$$h_{xy} \cdot (1 + x + z + xz) = h_{xy} \cdot (1 + 1 + z + z) = 0.$$

Due to the translation invariance of the model, the operator O_{xy} at any xy-plane is a symmetry. In the polynomial representation, the operator O_{xy} at $z = c$-plane is expressed as $z^c h_{xy}$ and the above equation is trivially satisfied. We leave it to readers to verify that similar operators on yz- and zx-planes are symmetries of the plaquette Ising model.

6.5.2 F-S duality

Recall that the local symmetry operator $G_i = \tau_i^x A_i$ was defined by $A_i = \prod_{a \in P(i)} \sigma_{i,a}^x$ where $P(i)$ is the set of all classical interaction terms $\mathcal{O}_i^{(a)}$ that anti-commutes with τ_i^x. In the polynomial formulation, $P(i)$ is exactly the image of $p(\tau_i^x)$ (the polynomials representing τ_i^x, which is a unit vector) under the excitation map $S_c^\dagger \lambda_1$. This means that the polynomial representation of the operator A_i is the conjugate transpose of the first row of S_c.

The "flatness" constraint operator B_k is obtained by considering the nontrivial local product of $\mathcal{O}_i^{(a)}$ that becomes the identity. Since the identity is a zero vector in the polynomial representation, Each B_k operator corresponds to a nontrivial relation

$$\sum_{a=1}^{\ell} b_a p(O_i^{(a)}) = 0 \tag{6.24}$$

where $p(\mathcal{O}_i^{(a)}) = (S_c)_a$ is the polynomial representing the τ^z-type classical interaction term. The collection of vectors b in the relation is the kernel of the matrix S_c. There are finitely many *generators* $G^{(k)}$ of $\ker S_c$, where $G^{(k)} \in \mathbb{F}_2[x^\pm, y^\pm, z^\pm]^\ell$. (The fact that there are only finitely many generators is a property of the ring $\mathbb{F}_2[x^\pm, y^\pm, z^\pm]$ being Noetherian.) These generators are nothing but the polynomial representation of B_k.

For the plaquette Ising model, $\ker S_{\text{plaq}}$ has two generators

$$G^{(1)} = (1 + z, 1 + x, 0)^T \tag{6.25}$$
$$G^{(2)} = (0, 1 + x, 1 + y)^T. \tag{6.26}$$

Each generator encodes the product of the appropriate plaquette interactions at each cube that yield the identity, as shown in Fig. 6-5.

Summarizing, given a classical Hamiltonian represented by a row matrix S_c of Laurent polynomials, we have obtained a quantum model whose Hamiltonian terms corresponds to the
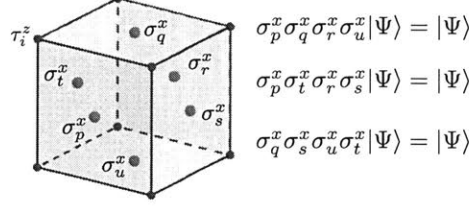
Figure 6-5: Dual representation of the plaquette Ising model in the presence of a transverse field. We place nexus spins at the center of each four-spin plaquette interaction, so that $\sigma_p^x \equiv \prod_{i \in \partial p} \tau_i^z$. The product of four adjacent four-spin interactions that wrap around the cube is equal to the identity (e.g. the product of plaquette interactions p, q, r and u). In the dual representation, this leads to the indicated constraints at each cube. Only two of the three constraints are independent.

columns of the following stabilizer map.

$$S_f = S_c^\dagger \oplus G = \begin{pmatrix} S_c^\dagger & 0 \\ 0 & G \end{pmatrix} \tag{6.27}$$

where $G = \begin{pmatrix} G^{(1)} & \cdots & G^{(m)} \end{pmatrix}$ is a matrix enumerating generators of $\ker S_c$ in its columns. The excitation map is then

$$E_f = S_f^\dagger \lambda_\ell = \begin{pmatrix} 0 & S_c \\ G^\dagger & 0 \end{pmatrix}. \tag{6.28}$$

Physically, this Hamiltonian is defined on a Bravais lattice with an ℓ-site basis. At each lattice site, the Hamiltonian has a single "σ^x-type" (nexus charge) interaction and m "σ^z-type" (nexus flux) interactions.

A wide range of conventional and fracton topological orders are described by stabilizer maps of the form $S_f = S_c^\dagger \oplus G$. Physically, this means that these topologically ordered states are built by "gauging" the symmetry of a classical spin system, which can be easily read off from the stabilizer map S_f for the topologically ordered state.

First, the stabilizer map built from the plaquette Ising model (see (6.19)) is given as

$$S_{\text{X-Cube}} = \begin{pmatrix} 1 + \bar{x} + \bar{y} + \overline{xy} & 0 & 0 \\ 1 + \bar{y} + \bar{z} + \overline{yz} & 0 & 0 \\ 1 + \bar{x} + \bar{z} + \overline{xz} & 0 & 0 \\ 0 & 1 + z & 0 \\ 0 & 1 + x & 1 + x \\ 0 & 0 & 1 + y \end{pmatrix} \tag{6.29}$$

This stabilizer map corresponds to the topologically ordered "X-Cube" fracton Hamiltonian presented in the main text. Second, all commuting Hamiltonians for $\mathbb{Z}_N$ topological order

in two- and three-dimensions are described by stabilizer maps of this form. The stabilizer Hamiltonian for three-dimensional $\mathbb{Z}_2$ topological order is given by

$$
S_{\mathbb{Z}_2} = \begin{pmatrix}
1 + \bar{x} & 0 & 0 & 0 \\
1 + \bar{y} & 0 & 0 & 0 \\
1 + \bar{z} & 0 & 0 & 0 \\
0 & 1 + y & 1 + z & 0 \\
0 & 1 + x & 0 & 1 + z \\
0 & 0 & 1 + x & 1 + y
\end{pmatrix}. \tag{6.30}
$$

Furthermore, the Haah's code, a topologically ordered state with *only* immobile topological excitations is described by the stabilizer map

$$
S_{\text{Haah}} = \begin{pmatrix}
1 + \bar{x}\bar{y} + \bar{y}\bar{z} + \bar{x}\bar{z} & 0 \\
1 + \bar{x} + \bar{y} + \bar{z} & 0 \\
0 & 1 + x + y + z \\
0 & 1 + xy + yz + xz
\end{pmatrix}. \tag{6.31}
$$

We may immediately read off the classical spin systems whose symmetries have been "gauged" to obtain these topologically ordered states, since the stabilizer map S_f contains the *classical* excitation map $E_c = S_c^\dagger \lambda_1$. For example, from the stabilizer map for 3D $\mathbb{Z}_2$ topological order, we identify the stabilizer map

$$
S_{\text{Ising}} = (1 + x, 1 + y, 1 + z) \tag{6.32}
$$

which precisely describes the classical 3D Ising model on the simple cubic lattice. A more exotic example is given by the classical spin system

$$
S_{\text{fractal}} = (\underbrace{1 + xy + yz + xz}_{f}, \underbrace{1 + x + y + z}_{g}) \tag{6.33}
$$

which is used to build Haah's code. A schematic representation of this classical spin Hamiltonian is shown in Fig. 6-6 as a sum of two types of four-spin interactions at each cube on the three-dimensional cubic lattice. The precise subsystem symmetry in this classical spin model is highly sensitive to the boundary conditions imposed on the system. For simplicity, we consider the length-L three-torus with $L = 2^n$ for positive integers n. Using the fact that $f^{2^n}, g^{2^n} \in \mathfrak{b}_L = (x^L + 1, y^L + 1, z^L + 1)$, we find a symmetry generator

$$
h = f^{2^n - 1} g^{2^n - 1}. \tag{6.34}
$$

This symmetry generator, which corresponds to a spin-flip transformation on a fractal configuration on the three-dimensional cubic lattice that resembles a Sierpinski triangle, is quite different

$$\mathcal{O}_i^{(1)}[\tau] = \tau_i^z \tau_j^z \tau_k^z \tau_\ell^z \qquad \mathcal{O}_i^{(2)}[\tau] = \tau_i^z \tau_m^z \tau_n^z \tau_p^z$$
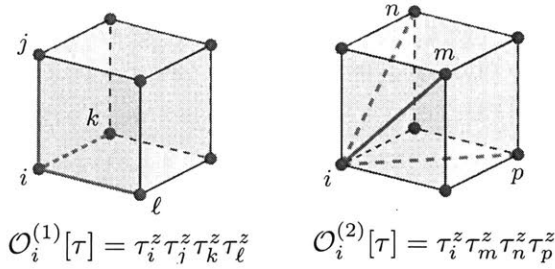
Figure 6-6: The classical spin model defined on the cubic lattice with fractal subsystem symmetry that corresponds to Haah's code. The spin model may be conveniently written as a sum of two types of four-spin interactions at each cube, as indicated above.

from the planar symmetry for the plaquette Ising model. It is this *fractal* subsystem symmetry that is "gauged" to obtain the corresponding topologically-ordered state, known as Haah's code [46].

6.5.3 The Codimension Condition Implies Topological Order

The codimension of an ideal of polynomials f_i is the codimension of the algebraic variety (zero-locus) defined by the system of polynomial equations $f_i = 0$. The variety may be neither smooth nor connected. One has to look at the component of the largest geometric dimension and take the difference of that dimension from the ambient dimension, in order to obtain the correct codimension. For instance, the codimension of $((x-1)(y-1), (x-1)(z-1))$ is 1 since the zero-locus contains a plane $x = 1$ in three-dimensional space, whereas the codimension of $(z-1, y-1)$ is 2 since the zero-locus is the line given by $z = 1 = y$. Although this codimension criterion can never be met in one spatial dimension, the codimension criterion is fairly mild in higher dimensions. For example, it is satisfied by the standard Ising model with nearest neighbor interaction on two or higher dimensional lattices, and the ideal $I(S_c)$ has codimension that is equal to the spatial dimension, the maximum possible value. In fact, the exotic topological phases that we investigate exploits this mild requirement, and all our examples have the property that $I(S_c)$ has codimension exactly two, saturating the inequality in the criterion $\mathrm{codim}\, I(S_c) \geq 2$.

We now return to the stabilizer map $S_f = E_c \oplus G$ and show that S_f indeed corresponds to a topologically ordered and commuting Hamiltonian. First, $S_c \cdot G = 0$ implies that $G^\dagger \cdot S_c^\dagger = 0$, and hence $E_f \cdot S_f = 0$; the Hamiltonian corresponding to the stabilizer map S_f consists of all commuting terms. In addition, we have $\ker S_c = \mathrm{Im}\, G$ by definition. As a result, the local indistinguishability condition for any degenerate ground-states of the stabilizer Hamiltonian on the torus, given by $\ker E_f = \mathrm{Im}\, S_f$, is satisfied if and only if $\ker G^\dagger = \mathrm{Im}\, S_c^\dagger$. Said differently, the complex

$$0 \to R^1 \xrightarrow{S_c^\dagger} R^\ell \xrightarrow{G^\dagger} R^m \tag{6.35}$$

149

where R^n is a free module of rank n over the Laurent polynomial ring $R = \mathbb{F}_2[x^\pm, y^\pm, z^\pm]$, must be exact. The equivalent condition for this to be true is our condition $\mathrm{codim}\, I(S_c) \geq 2$. The proof of this is purely algebraic, and a general reader might want to skip the rest of this subsection.

A criterion for the exactness of a complex of free modules is provided by the following [195, 194]:

Theorem [Buchsbaum-Eisenbud] *A chain complex of free modules over* $R = \mathbb{F}_2[x^\pm, y^\pm, z^\pm]$

$$0 \to F_n \xrightarrow{\phi_n} F_{n-1} \xrightarrow{\phi_{n-1}} \cdots F_2 \xrightarrow{\phi_2} F_1 \xrightarrow{\phi_1} F_0 \tag{6.36}$$

is exact if and only if

- $\mathrm{rank}(F_i) = \mathrm{rank}(\phi_i) + \mathrm{rank}(\phi_{i+1})$ *for* $i = 1, \ldots, n$ *and*

- $\mathrm{codim}\, I(\phi_i) \geq i$ *for* $i = 1, \ldots, n$.

Here, $I(\phi_i)$ *is the* k*-th determinantal ideal* $I_k(\phi_i)$ *with the largest* k *such that* $I_k(\phi_i) \neq 0$.

The k-th determinantal ideal is one that generated by all determinants of $k \times k$ submatrices. It is important that the complex is terminated with 0 at the left end. (The original theorem is more general than we state here, and is given in terms of *depth* of the determinantal ideal. In general, the codimension only upper bounds the depth, and the two notions are not equal. However, our Laurent polynomial ring is sufficiently nice, i.e., Cohen-Macaulay, that the two quantities are equal for any ideal; our ring is obtained from a polynomial ring over a field followed by localization by a single element xyz.)

We apply the Buchsbaum-Eisenbud criterion to our complex (6.35). Since $\ker S_c = \mathrm{Im}\, G$, we know by the theorem that $\mathrm{rank}\, S_c + \mathrm{rank}\, G = \ell$ and $\mathrm{codim}\, I(G) \geq 2$. Since the conjugation is an automorphism of R, the rank is invariant under conjugate transpose. This implies that $\mathrm{rank}\, S_c^\dagger + \mathrm{rank}\, G^\dagger = \ell$ and $\mathrm{codim}\, I(G^\dagger) \geq 2$. Since $S_c^\dagger$ has one column, we have $\mathrm{rank}\, S_c^\dagger = 1$. These implies the first condition. All we need is the second condition, $\mathrm{codim}\, I(G^\dagger) \geq 1$ and $\mathrm{codim}\, I(S_c^\dagger) \geq 2$. The former is already shown, and the latter is exactly our requirement.

An example of a classical spin system that *violates* our codimension condition is given by the stabilizer map $S_c = (f, g)$, with $f = 1 + x$ and $g = 1 + x + y + z + xy + yz + xz + xyz$. This classical spin system has a *linear* subsystem symmetry as the symmetry generator

$$h_x = \sum_{n \in \mathbb{Z}} x^n \tag{6.37}$$

satisfies $h_x f = 0 = h_x g$. We see that $\mathrm{codim}\, I(S_c) = 1$, since the zero-locus of the polynomials f and g contains a plane given by $x = 1$. Therefore, the stabilizer map $S_f = S_c^\dagger \oplus G$ for this classical spin model corresponds to a commuting Hamiltonian with degeneracy due to *local* observables (order parameter) and does not exhibit topological order.

150

While we have provided an algebraic condition on the classical spin model that guarantees that the dual Hamiltonian with stabilizer map S_f, has no local observables, we may also argue for the local indistinguishability of the ground-states using the F-S duality. Ground-states of the Hamiltonian H_{fracton}, using the notation presented in the main text, satisfy $B_i^{(k)} |\Psi\rangle = A_i |\Psi\rangle = |\Psi\rangle$, and will be locally indistinguishable if any local operator that commutes with H_{fracton} can be written as a product of nexus charges A_i or generalized monopole operators $B_i^{(k)}$. Recall that the generalized monopole operators are defined as the set of all local, σ^z-type operators that commute with the nexus charges. Therefore, by construction, the only σ^z-type operators that commute with H_{fracton} are products of $B_i^{(k)}$.

We now invoke the F-S duality to argue that any local, σ^x-type operator that commutes with H_{fracton} can be written as a product of nexus charges, provided that the classical spin model H_0 has no lower-dimensional ($d_s < 2$) subsystem symmetries. Assume that such a σ^x-type operator $\mathcal{O}_X$ does exist, that can distinguish the ground-states of H_{fracton}. Since this operator commutes with all of the generalized monopole operators, $\mathcal{O}_X$ corresponds to a valid domain wall configuration that can be created by acting on the ground-state of the spin model H_0. Therefore, we may invoke the F-S duality to construct a dual representation of $\mathcal{O}_X$ in terms of the Ising matter fields. Since $\mathcal{O}_X$ is a σ^x-type operator that cannot be written as a local product of nexus charges, however, its dual representation $\widetilde{\mathcal{O}_X}$ will be given by a *non-local* product of τ_i^x operators. Physically, this duality implies that performing spin-flips along a this non-local by acting with $\widetilde{\mathcal{O}_X}$ on the classical ground-state of H_0 will flip a local set of interaction terms $\mathcal{O}_i^{(a)}$ at a point at the boundary of the region, as specified by the support of the operator $\mathcal{O}_X$. By taking products of the $\mathcal{O}_X$ operators, it is possible to reduce the dimension d_s along which the dual operator $\widetilde{\mathcal{O}_X}$ has support to $d_s < 2$. However, this immediately implies that on the torus, the classical spin system H_0 has a subsystem symmetry along a region that is of smaller dimension than a plane. Therefore, by requiring that H_0 has no lower-dimensional $d_s < 2$ subsystem symmetries, we guarantee the local indistinguishability of the ground-states of H_{fracton}.

6.5.4 The Fracton Condition

We now consider the excitation map E_f for the commuting, topologically-ordered Hamiltonian built from the data contained in the classical spin model. We show that the topological excitations of this model are *fractons* if and only if the stabilizer ideal $I(S_c) \equiv \langle f_1, \ldots, f_n \rangle$ contains no binomial terms (the fracton condition above). From the excitation map E_f (6.28), we observe that one of the excitations (the nexus charge) lives on the sites of the lattice. An operator $\mathcal{O}$ that is a product of σ^z terms, when acting on the ground-state, generates a pattern of nexus charge excitations. The possible nexus charge configurations by finitely supported operators are in one-to-one correspondence with the image of the excitation map; this is the defining property of the excitation map. The submatrix of the excitation map that is responsible for the nexus charge consists of one row, which is the same as S_c, and therefore the image is equal to the

$I(S_c)$.

A topological excitation is a *fracton* if it is impossible to create an isolated pair of such excitations from the ground-state. Hence, the stabilizer Hamiltonian S_f exhibits fracton topological order if and only if $I(S_c)$ contains no binomial terms

$$1 + x^{n_1} \cdots x^{n_d} \notin I(S_c) \tag{6.38}$$

for all n_1, ..., $n_d \in \mathbb{Z}$. This is a condition on the classical spin Hamiltonian that no product of any interactions $h^{(i)}[\tau]$ can simply be a product of a *pair* τ^z terms. For example, the classical Ising model, with nearest-neighbor spin-spin interactions, trivially violates this condition in any dimension. It is not always obvious to test whether an ideal contains a binomial. We explain one test technique with examples shortly.

The fracton condition cannot be satisfied if the codimension of $I(S_c)$ is equal to the spatial dimension, the maximum value [47]. In the latter is true, then any point-like excitation appears at the tip of some string like operator, which can be freely bent in the system, and it behaves as an ordinary particle.

6.5.5 Classical Spin Models with Planar subsystem Symmetry

In this section, we show that applying our construction to classical spin models with spin-flip symmetries along planes always yields a fracton topological phase. Consider a stabilizer map $S_c = (f_1, \ldots, f_n)$ for a classical spin Hamiltonian, where $f_1, \ldots, f_n$ are Laurent polynomials. As we have shown in Appendix 6.5.1, the symmetry generators

$$
\begin{aligned}
h_{xy} &= \sum_{n,m \in \mathbb{Z}} x^n y^m, \\
h_{yz} &= \sum_{n,m \in \mathbb{Z}} y^n z^m, \\
h_{xz} &= \sum_{n,m \in \mathbb{Z}} x^n z^m
\end{aligned}
\tag{6.39}
$$

satisfy

$$
\begin{aligned}
h_{xy} f_i &= 0 \\
h_{yz} f_i &= 0 \\
h_{xz} f_i &= 0
\end{aligned}
$$

for all $i = 1, \ldots, n$. We also have seen that $h_{xy} g(x, y, z) = g(1, 1, z)$, etc., for any Laurent polynomial g. The symmetry condition then implies that the polynomials $f_i(1, 1, t)$, $f_i(1, t, 1)$, $f_i(t, 1, 1)$ are identically zero for all i. That is, $(1, 1, t)$, etc., are roots of the polynomials f_i. Geometrically, this means that the variety defined by $f_i(x, y, z) = 0$ contains three lines

152

parametrized by $t \mapsto (1, 1, t), (1, t, 1), (t, 1, 1)$.

We can use this observation to show the fracton condition. Suppose on the contrary that the ideal $I(S_c)$ contains a binomial term.

$$1 + x^a y^b z^c \in I(S_c). \tag{6.40}$$

Since any member of the ideal is a linear combination of generators, we have

$$1 + x^a y^b z^c = \sum_i g_i(x, y, z) f_i(x, y, z). \tag{6.41}$$

Let us substitute x, y, z with the solution $(1, 1, t)$:

$$1 + t^c = \sum_i g_i(1, 1, t) f_i(1, 1, t) = 0. \tag{6.42}$$

Since this has to be true as a polynomial in t, we deduce that $c = 0$. Likewise, the solution $(1, t, 1)$ implies $b = 0$, and $(t, 1, 1)$ implies $a = 0$. Therefore, our binomial was actually $1 + x^0 y^0 z^0 = 0$, and the ideal $I(S_c)$ does not contain any binomial.

It has to be noted that the fracton condition (the absence of binomial) alone does not imply that the F-S dual of the classical spin model is topologically ordered; the codimension condition should be checked separately. If the initial classical model had line-like symmetries, then we would have solutions of form e.g. $(t_1, t_2, 1)$. This has a codimension 1, and the hence $\mathrm{codim}\, I(S_c) \leq 1$, and the F-S dual would not be topologically ordered.

We conclude that for any classical spin system with spin-flip symmetries along all three orthogonal planes and no "lower dimensional" symmetries, our construction for gauging this symmetry will give rise to a fracton topological phase.

Let us demonstrate that the nexus charge in the "X-Cube" Hamiltonian is a fracton excitation using the above technique. Recall that $I(S_c) = \langle 1 + x + y + xy, 1 + y + z + yz, 1 + x + z + xz \rangle$ for the plaquette Ising model. The symmetry generators h_{xy}, h_{yz}, h_{xz} of (6.39) is indeed the symmetries of the X-Cube model, and therefore $I(S_c)$ does not contain any binomial. By solving the equation $1 + x + y + xy = 0$, $1 + y + z + yz = 0$, and $1 + x + z + xz = 0$, we see that $(1, 1, t), (1, t, 1)$, and $(t, 1, 1)$ are the only solutions, which are lines of geometric dimension 1, and therefore the codimension of $I(S_c)$ is equal to 2. Therefore, X-Cube model has fracton (immobile) topological excitations. This derivation provides a formal proof of the simple physical statement that no product of the four-spin interactions in the classical plaquette Ising model can act exclusively on an isolated pair of spins.

We can adapt the above argument to construct another spin model with fracton topological order. Consider the classical spin system

$$S_c = (1 + x + z + x\overline{z},\ 1 + x + y + x\overline{y}) \tag{6.43}$$

153

Observe that $f_1 = 1 + x + z + x\overline{z} = \overline{z}(1+z)(x+z)$ and $f_2 = 1 + x + y + x\overline{y} = \overline{y}(1+y)(x+y)$. Thus we identify the three planar symmetries of this classical spin model

$$h_1 = \sum_{n,m \in \mathbb{Z}} x^n y^m, \tag{6.44}$$

$$h_2 = \sum_{n,m \in \mathbb{Z}} (x+z)^n (x+y)^m, \tag{6.45}$$

$$h_3 = \sum_{n,m \in \mathbb{Z}} x^n (x+z)^m. \tag{6.46}$$

It is routine to check that $h_i f_j = 0$. Since $f_1(x,y,z)$ and $f_2(x,y,z)$ do not have any common factor, the ideal $I(S_c) = \langle f_1, f_2 \rangle$ has codimension 2, satisfying our codimension condition. The set of relations between f_1 and f_2 (the kernel of S_c), is generated by $G = (1 + \overline{x} + \overline{y} + \overline{x}y, 1 + \overline{x} + \overline{z} + \overline{x}z)^T$. Through our F-S duality, we obtain a stabilizer map

$$S_{\text{CBLT}} = \begin{pmatrix} 1 + x + z + x\overline{z} & 0 \\ 1 + x + y + x\overline{y} & 0 \\ 0 & 1 + \overline{x} + \overline{y} + \overline{x}y \\ 0 & 1 + \overline{x} + \overline{z} + \overline{x}z \end{pmatrix}, \tag{6.47}$$

which corresponds to a stabilizer Hamiltonian with fracton topological order. In fact, this stabilizer map has an extra property that $f_1 \overline{f_2} + \overline{f_1} f_2 = 0$, which allow us to consider a simpler stabilizer map

$$S_{\text{CBLT}} = S_c^T = \begin{pmatrix} 1 + x + z + x\overline{z} \\ 1 + x + y + x\overline{y} \end{pmatrix} \tag{6.48}$$

corresponding to a fracton phase with "half" of the topological degeneracy. This stabilizer map is precisely the CBLT model [178, 177], which has a single type of fracton excitation, and degeneracy D given by $\log_2 D = 8L$ [177, 47] on the length-L three-torus. The CBLT model is conveniently represented on the face-centered cubic (fcc) lattice as shown in Figure 6-7a.

6.5.6 Classical Spin Models with an m-Site Unit Cell

So far we have assumed that a classical spin model had a single spin per Bravais lattice site. When the unit cell has m spins ($m \geq 1$), our duality construction and criteria for topological order directly carry over. However, the fracton condition and its relation to planar symmetries require some extra attention.

The stabilizer map S_c for the classical spin (τ^z) system is an $m \times \ell$ matrix of Laurent polynomials (omitting the lower half-block representing τ^x), where ℓ is the number of interactions

$$h_i^{(1)}[\tau] = \tau_i^z \tau_j^z \tau_k^z \tau_\ell^z \qquad h_i^{(2)}[\tau] = \tau_i^z \tau_m^z \tau_k^z \tau_n^z$$

CBLT Model

(a)   (b)
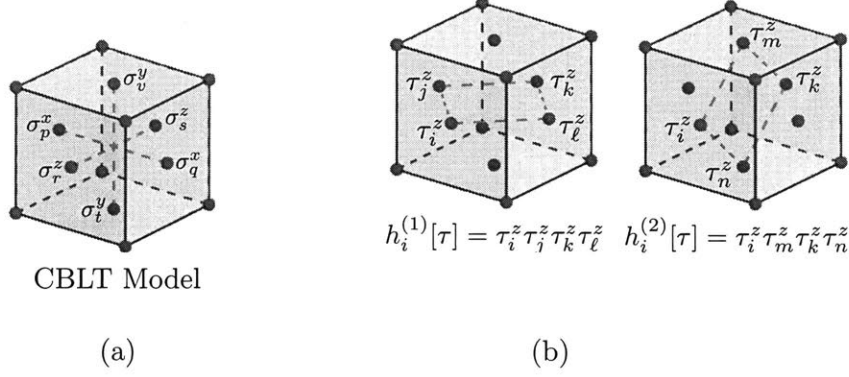
Figure 6-7: The (a) CBLT model represented on an fcc lattice. The model consists of a single, six-spin interaction term per lattice site. This model may be constructed from the interacting spin model shown in (b) on the fcc lattice, with two four-spin interactions per lattice site.

per unit cell.

$$S_c = \begin{pmatrix} f_1^{(1)} & f_2^{(1)} & \cdots & f_\ell^{(1)} \\ f_1^{(2)} & f_2^{(2)} & \cdots & f_\ell^{(2)} \\ \vdots & \vdots & \ddots & \\ f_1^{(m)} & f_2^{(m)} & \cdots & f_\ell^{(m)} \end{pmatrix} \tag{6.49}$$

Our generalized gauge theory prescription produces a (quantum) stabilizer Hamiltonian described by $S_f \equiv S_c^\dagger \oplus G$ where $S_c^\dagger = (\overline{S_c})^T$ and G is a matrix of the generators of $\ker S_c$. The matrix G is nonzero if and only if $k = \operatorname{rank} S_c < \ell$. This condition is satisfied when S_c is a row matrix and there are two or more interactions per spin, as is the case in all the examples in this paper with a single site per unit cell. The Buchsbaum-Eisenbud criterion for exact sequence can be applied, and, if $G \neq 0$, we see that the only nontrivial condition is that $\operatorname{codim} I(S_c) \geq 2$ where $I(S_c) = I_k(S_c)$ is the k-th determinantal ideal with the largest k such that $I_k(S_c)$ is nonzero. Summarizing, the topological order is realized in S_f if and only if

- $k = \operatorname{rank} S_c < \ell$, and

- $\operatorname{codim} I_k(S_c) \geq 2$.

We now assume that the classical system has planar subsystem symmetry. The three independent generators of spin-flip transformations along orthogonal planes are denoted h_{xy}, h_{yz} and h_{xz}. The classical system on a lattice with an m-site basis has planar subsystem symmetry if and only if

$$h_j \cdot \sum_{i=1}^m f_k^{(i)}(x, y, z) = 0 \tag{6.50}$$

for all $j = xy, yz, zx$ and $k = 1, \ldots, \ell$. As before, this implies that

$$\sum_{i=1}^{m} f_k^{(i)}(1,1,t) = 0, \quad \sum_{i=1}^{m} f_k^{(i)}(1,t,1) = 0, \quad \sum_{i=1}^{m} f_k^{(i)}(t,1,1) = 0.$$

Suppose the nexus charge exists for the moment. The condition that the nexus charges, the excitation of $S_c^\dagger$ terms in S_f, are all fractons is that $\operatorname{Im} S_c$ does not contain any two-term element of form

$$\begin{pmatrix} \vdots \\ 0 \\ 1 + x^a y^b z^c \\ 0 \\ \vdots \end{pmatrix}.$$

If there is such a two-term element, then

$$\begin{pmatrix} \vdots \\ 0 \\ 1 + x^a y^b z^c \\ 0 \\ \vdots \end{pmatrix} = \begin{pmatrix} \vdots \\ \sum_{k=1}^{\ell} f_k^{(i-1)}(x,y,z) g_k(x,y,z) \\ \sum_{k=1}^{\ell} f_k^{(i)}(x,y,z) g_k(x,y,z) \\ \sum_{k=1}^{\ell} f_k^{(i+1)}(x,y,z) g_k(x,y,z) \\ \vdots \end{pmatrix}.$$

Summing all the components, we get

$$1 + x^a y^b z^c = \sum_{k,i} f_k^{(i)} g_k(x,y,z). \tag{6.51}$$

Evaluating the polynomial at $(1,1,t)$, etc., we conclude that $a = b = c = 0$. Therefore, we conclude that there is no two-term element.

The existence of the nexus charge might seem mundane, but we do not know whether this is true even assuming the various conditions we have discussed. It is however known that in three spatial dimensions any topologically ordered stabilizer Hamiltonian has a point-like excitation [47]. This implies that either the nexus charge sector or the nexus flux sector admits isolated point-like excitations. If this point-like excitation happens to be a nexus charge, then the symmetry of the classical side implies that this charge is immobile (fracton). We note that when the unit cell consists of a single spin in the classical side ($m = 1$), the existence of the nexus charge was immediate since $\operatorname{coker} S_c$ is a torsion module. We conclude this section by

summarizing our discussion: given an aribitrary classical spin model with planar symmetries, with the number of interaction terms per Bravais lattice site is greater than the size of the unit cell, any nexus charge, if exists, is a fracton.

6.6 Degeneracy of the Checkerboard and X-Cube Models

Here, we derive the ground-state degeneracy of the checkerboard and X-cube model, constructed from the tetrahedral Ising and plaquette Ising models, respectively.

Let us briefly review the properties of the checkerboard model. Consider a three-dimensional cubic lattice of spin-1/2 degrees of freedom. Each spin sits at the vertex of a cube, with the cubes arranged in a checkerboard configuration, so that any pair of neighboring cubes overlap on exactly two spins as shown in Table 6.1. We define the Hamiltonian

$$H_0 = -\sum_c \prod_{n \in \partial c} \sigma_n^x - \sum_c \prod_{n \in \partial c} \sigma_n^z. \tag{6.52}$$

where each product is taken over the eight spins sitting at the vertex of cube c, while the sum is taken over cubes in the checkerboard configuration. The topological excitations in this model are similar to that of the Majorana cubic model [6]. The fundamental fracton excitation may be isolated at the corners of a membrane operator, given by the product of spin operators along a flat, two-dimensional surface. Composites of fracton excitations, however, are topological excitations that are free to move along one- and two-dimensional subsystems without any energy cost. Wilson line operators, given by the product of spin operators along *straight* lines, create pairs of fracton excitations at each end; these composite excitations are "dimension-1" particles, which are only free to move along the Wilson line. A pair of parallel Wilson lines in adjacent layers, however, maybe used to create excitations that are free to move within the plane. These topological excitations are *anyons* with well-defined mutual and self-statistics.

The stabilizer map for the checkerboard model is given by the expression

$$S_{\text{check}} = \begin{pmatrix} f & 0 \\ \overline{f} & 0 \\ 0 & \overline{f} \\ 0 & f \end{pmatrix} \tag{6.53}$$

where $f = 1 + x + y + z \in \mathbb{F}_2[x^{\pm}, y^{\pm}, z^{\pm}]$.

For a topologically ordered stabilizer Hamiltonian with the stabilizer map S and excitation map $E = S^{\dagger}\lambda_{\ell}$, the ground state degeneracy D on a length-L torus is given by

$$2\log_2 D = \dim_{\mathbb{F}_2} \ker E / \operatorname{Im} S \quad \text{over} \quad \mathbb{F}_2[x, y, z]/\langle x^L + 1, y^L + 1, z^L + 1 \rangle. \tag{6.54}$$

If the number of spins in the unit cell, ℓ, is equal to the number of interaction types (the number

157

of columns in S), then

$$\log_2 D = \dim_{\mathbb{F}_2} \operatorname{coker} S^\dagger. \tag{6.55}$$

This is applicable for all examples in this paper, except for the $\mathbb{Z}_2$ gauge theory in three-dimensions. In our examples where $S^\dagger = S_c \oplus G^\dagger$ is block-diagonal, the formula further decomposes as

$$\log_2 D = \dim_{\mathbb{F}_2} \operatorname{coker} S_c + \dim_{\mathbb{F}_2} \operatorname{coker} G^\dagger. \tag{6.56}$$

Since the checkerboard stabilizer map has an extra structure that $S_c = G^\dagger$, the degeneracy calculation reduces to that of

$$\log_2 D_{\text{check}} = 2 \dim_{\mathbb{F}_2} \frac{\mathbb{F}_2[x, y, z]/\langle x^L + 1,\ y^L + 1,\ z^L + 1\rangle}{\langle 1 + x + y + z,\ xyz + xy + yz + zx\rangle}.$$

This was calculated in Ref. [6], and the answer is $\log_2 D_{\text{check}} = 6L - 6$.

The X-Cube model has different blocks in $S^\dagger_{\text{X-Cube}}$. Here we calculate the degeneracy of $H_{\text{X-Cube}}$ for odd L only. One component reads

$$\frac{\mathbb{F}_2[x, y, z]/\langle x^L + 1,\ y^L + 1,\ z^L + 1\rangle}{\langle(1 + x)(1 + y),\ (1 + y)(1 + z),\ (1 + x)(1 + z)\rangle}. \tag{6.57}$$

One may extend the coefficient field to the algebraic closure $\mathbb{F}$, and since L is odd, $x^L + 1 = 0$ has L distinct roots, one of which is $x = 1$. Localizing at the maximal ideal $\langle x + t, y + 1, z + 1\rangle$, we see that the factor ring becomes just $\mathbb{F}$ of dimension 1. Using the cyclic symmetry $x \to y \to z \to x$, we see that the factor ring has dimension $3(L - 1) + 1 = 3L - 2$. The other component is

$$\frac{(\mathbb{F}[x, y, z]/\langle x^L + 1,\ y^L + 1,\ z^L + 1\rangle)^2}{\begin{pmatrix} z + 1 & 1 + x & 0 \\ 0 & 1 + x & 1 + y \end{pmatrix}} \tag{6.58}$$

The second determinantal ideal of the matrix in the denominator is the same as $I(S_c)$, so we only have to consider localization at points $(1, 1, t)$, $(1, t, 1)$, and $(t, 1, 1)$. Localization at $(1, 1, t \neq 1)$ amounts to evaluating the matrix at that point due to the boundary conditions, and the factor module becomes $\mathbb{F}^1$. At $(1, 1, 1)$, the matrix becomes zero, and the factor module becomes $\mathbb{F}^2$. Hence, the factor ring has dimension $3(L - 1) + 2 = 3L - 1$. The degeneracy $D_{\text{X-Cube}}$ is thus given by

$$\log_2 D_{\text{X-Cube}} = 6L - 3 \text{ for odd } L. \tag{6.59}$$

158

Chapter 7

Coupled Layer Construction

In the previous chapter, we demonstrated that gapped fracton topological phases may be understood through a generalization of conventional lattice gauge theory for interacting quantum systems that have an extensive set of global symmetries (e.g. planar symmetries) [7]. As a consequence, fracton topological phases may be obtained as the quantum dual of these interacting systems, and this relationship may be used to search for new fracton phases, and to find exotic, interacting systems with fractal symmetries such as the dual of Haah's code [7, 197]. This relationship provides a generalization of the well-known Wegner duality in (2+1)-dimensions that relates symmetry-breaking phase transitions to the confinement transition of conventional lattice gauge theories [189]. Recently, certain gapless phases that have charge excitations with reduced mobility have also been found in "higher-rank" $U(1)$ gauge theories [198].

In this chapter, we introduce a new construction of a fracton topological phase introduced in Ref. [7] which yields an intriguing connection between two-dimensional topological order and exotic three-dimensional topological phases that have excitations with reduced mobility. The starting point for our construction is an isotropic configuration of inter-penetrating, two-dimensional (2D) toric codes [19]. We demonstrate that condensing appropriate excitations in the layered system – termed "composite excitations" – can lead to (i) three-dimensional Z_2 topological order, (ii) a fracton topological order known as the "X-cube" phase [7], whose phenomenology we thoroughly review, or (iii) a topologically trivial paramagnetic state. Condensing composite excitations effectively binds the charges or fluxes of the two-dimensional toric codes, resulting in an emergent topological excitation with reduced mobility. Our proposal also gives rise to a "loop-gas" picture for the ground-state wavefunction of fracton topological phases, as well as a simple understanding of the origin of the immobile excitations, which opens a possible route for constructing other exotic, three-dimensional topological orders.

We present a natural generalization of this procedure that yields a new, Z_N analog of the X-cube phase, before turning our attention to the rich phase structure of this microscopic model. Our results are summarized in the schematic phase diagrams in Appendix B. Of importance is a lattice duality between certain phase transition(s) into the fracton topological phase and a confinement transition in a conventional (3+1)-d Z_N gauge theory driven by the condensation
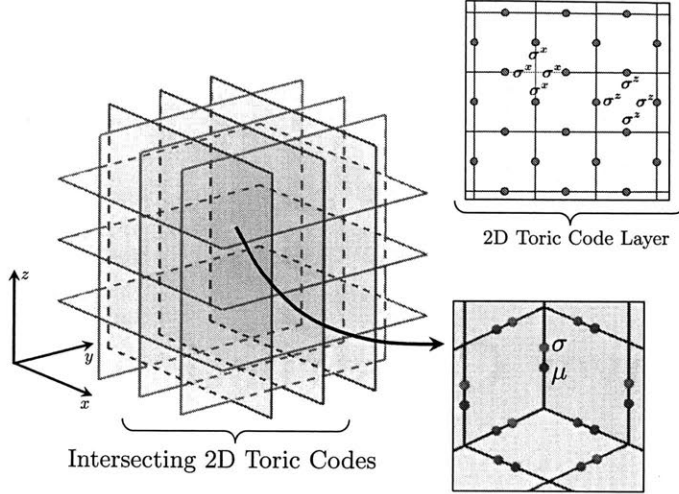
Figure 7-1: **Intersecting Layers of 2D Toric Codes**: A stack of two-dimensional, square-lattice toric codes in the xy (green), yz (red) and xz (blue) directions, which intersect at sites. The resulting three-dimensional cubic lattice has two spins per *link* (σ, μ) as shown. A single layer of the square-lattice toric code is shown as well, with the "star" and "plaquette" operators defined as shown.

of Z_N flux loops. We discuss this duality and the consequences for the phase diagram of the coupled layer system, in Appendix B, where we also present a solvable projector model in which the transition from the fracton topological phase to a trivial confined phase is first order, though this behavior may be non-generic.

7.1 Isotropic Layer Construction

We begin by introducing the microscopic model for our layer construction, before analyzing its rich phase structure and the emergence of fracton topological order. Consider a single layer of the two-dimensional (2D) toric code on the square lattice [19], which describes the zero-correlation length limit of the deconfined phase of two-dimensional Z_2 gauge theory. The Z_2 gauge field lies on the links of the square lattice, and at each lattice site and plaquette, there are four-spin operators that measure the Z_2 charge and flux, respectively (the so-called "star" and "plaquette" operators), as shown in the inset in Fig. 7-1. We take as our convention that a star operator is given as the product of the x-component of the Pauli spins, while a plaquette operator involves a product of the z-component.

We now place L copies of the square-lattice toric code in the xy, yz, and xz planes, respectively; any three mutually orthogonal planes intersect at a single site of the 2D square lattice. As shown schematically in Fig. 7-1, this intersecting, three-dimensional arrangement of the toric codes forms a three-dimensional (3D) cubic lattice with L^3 sites and *two* spins per link. The 2D Z_2 charge operators lie at the sites of the cubic lattice while the Z_2 flux operators lie at plaquettes. Initially, different copies of the 2D toric codes are completely decoupled, and the

Hamiltonian for the full system in terms of the two species of spins (σ and μ) at each link may be written in the form

$$H_0 = -J \sum_{r} \sum_{j=xy, yz, xz} \left[A_r^{(j)} + B_r^{(j)} \right] \tag{7.1}$$

where the sum is over the sites r on the cubic lattice. Here, $A_r^{(j)}$ is the four-spin star operator at site r which measures the Z_2 charge along the copy of the square-lattice toric code that is oriented along the jth plane (with $j = xy$, yz, or xz). We associate three plaquette operators $B_r^{(j)}$ with each site of the cubic lattice, which measure the elementary Z_2 flux through an elementary plaquette oriented in the jth plane. All of the operators in H_{toric} mutually commute, and the ground-state may be written exactly as an equal-amplitude superposition of closed electric-charge loops within each plane. The topological degeneracy D is simply $\log_2 D = 6L$ after imposing periodic boundary conditions. The topologically-degenerate ground-states are locally indistinguishable, so that the 2D Z_2 topological order of the decoupled toric codes is stable in the presence of weak perturbations [196].

We now add an interaction

$$H_1 = -h \sum_{\langle r, r' \rangle} \sigma_{rr'}^z \mu_{rr'}^z - t \sum_{\langle r, r' \rangle} \sigma_{rr'}^x \mu_{rr'}^x \tag{7.2}$$

which couples the two spins on each link of the cubic lattice. We begin by analyzing the phase diagram of the Hamiltonian

$$H = H_0 + H_1. \tag{7.3}$$

The ground-state of (8.1) will have the same topological order as a decoupled set of $3L$ toric codes when $t, h \ll J$. We refer to this as the "decoupled phase" for the remainder of this chapter. In addition, however, we will demonstrate that this Hamiltonian realizes (i) a (3+1)-d Z_2 topological phase and (ii) a fracton topological phase, along with (iii) a trivial paramagnet which corresponds to a confined limit of the two topological phases.

7.1.1 Z_2 Topological Order from Composite Charge Condensation

Starting from the decoupled phase, we now increase h, while keeping J and t fixed, which eventually leads to a $(3 + 1)$-dimensional Z_2 topological phase. Before demonstrating this explicitly with the microscopic Hamiltonian (8.1), we obtain intuition for this result by studying how the ground-state wavefunction changes as h is increased. When acting on the decoupled toric codes, the operator $\sigma_{ss'}^z \mu_{ss'}^z$ creates four electric charge excitations in the orthogonal layers that meet at the link connecting sites s and s'. Increasing h leads to the condensation of this excitation, which we refer to as the *composite electric charge*.
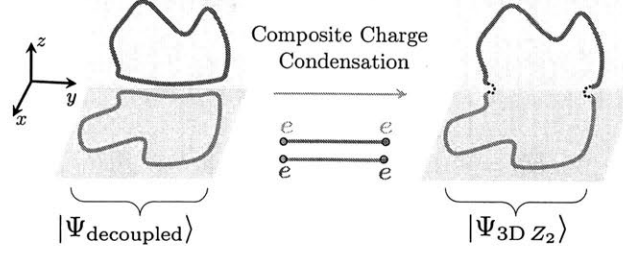
Figure 7-2: **Compostite Charge Condensation & "Gluing" Loops**: Condensing the composite charge excitation "glues" electric charge loops in adjacent, orthogonal layers. The resulting wavefunction is that of the 3D Z_2 topological phase, as described in Sec. I.

Condensing the composite electric charge "glues" the planar electric charge loops in the wavefunction for the decoupled toric codes ($|\Psi_{\text{decoupled}}\rangle$). As shown in Fig. 7-2, adding a composite electric charge has the effect of "cutting open" two electric charge loops in orthogonal layers that appear in a loop configuration in the state $|\Psi_{\text{decoupled}}\rangle$. This "cut" loop configuration is to be interpreted as a single, three-dimensional loop of the *emergent* electric charge $A_s^{(xy)} A_s^{(yz)} A_s^{(xz)}$, which remains well-defined in the condensed phase, and the resulting loop superposition is precisely the wavefunction for the 3D Z_2 topological phase. As we will soon show, composite charge condensation also has the effect of binding the 2D Z_2 fluxes into flux loops. In this way, the 3D electric charge inherits its bosonic self-statistics and π-mutual statistics with flux loops from the 2D Z_2 phase.

We now derive this result from the microscopic Hamiltonian (8.1). When $h \gg J, t$, we let $\sigma_{rr'}^z \mu_{rr'}^z = +1$ and define a single spin degree of freedom for every link of the cubic lattice as

$$\tau_{rr'}^z \equiv \sigma_{rr'}^z \qquad \tau_{rr'}^x \equiv \sigma_{rr'}^x \mu_{rr'}^x \tag{7.4}$$

In terms of this spin, we obtain an effective Hamiltonian in perturbation theory

$$H_{\text{eff}}^{(1)} = -\widetilde{J} \sum_r \widetilde{A}_r - J \sum_p B_p - t \sum_{\langle r, r' \rangle} \tau_{rr'}^x \tag{7.5}$$

where the coupling $\widetilde{J} \sim O(J^3/h^2)$. Here, the operator

$$\widetilde{A}_r \equiv A_r^{(xy)} A_r^{(yz)} A_r^{(xz)} = \prod_{r' \in \text{star}(r)} \tau_{rr'}^x \tag{7.6}$$

is precisely the six-spin operator that measures the Z_2 charge in a (3+1)-dimensional Z_2 topological phase, while

$$B_p \equiv \prod_{r, r' \in \partial p} \tau_{rr'}^z \tag{7.7}$$

162

is the four-spin operator measuring the flux through plaquette p on the cubic lattice. When $t = 0$, the effective Hamiltonian $H_{\text{eff}}^{(1)}$ is precisely that of the 3D toric code [199]. Furthermore, increasing t eventually leads to condensation of the Z_2 flux loops, resulting in a trivial, confined phase. As advertised, the 2D Z_2 fluxes are confined, while a bound-state of the Z_2 fluxes survives as a topological excitation, which becomes the flux loop of the three-dimensional Z_2 topological phase. Condensing a composite excitation has led to the emergence of a new topological excitation whose mobility is restricted.

7.1.2 Fracton Topological Order from Composite Flux Loop Condensation

While composite charge condensation leads to three-dimensional Z_2 topological order, condensing a bound-state of the Z_2 fluxes in adjacent layers – a *composite flux loop* – yields the so-called "X-cube" fracton topological phase, as originally introduced and studied in Ref. [7] using an exactly solvable, commuting Hamiltonian. We first review the phenomenology of the X-cube fracton topological phase before demonstrating that this phase emerges within our layer construction. A detailed description of this fracton phase is provided in Ref. [7].

Phenomenology of the X-cube Phase

The X-cube phase is a gapped topological phase that was introduced in Ref. [7], by studying the dual description of the plaquette Ising model, an interacting spin system with an extensive set of planar spin-flip symmetries; the finite-temperature behavior of this system has been studied previously [183, 184, 185, 186]. While the plaquette Ising model exhibits only symmetry-breaking or paramagnetic phases at zero temperature, its dual description is far more exotic, describing the "confinement" transition of a fracton topological phase. The solvable Hamiltonian for this fracton phase, termed the X-cube model, due to the geometry of the multi-spin interactions [7], was shown to have a topological ground-state degeneracy $\log_2 D = 6L - 3$ on the length-L three-torus, along with exotic topological excitations whose mobility is severely restricted. Since the degenerate ground-states are locally indistinguishable, this degeneracy is stable to perturbations, so that the X-cube model [7] describes a stable, gapped phase of matter.

The X-cube phase has two types of gapped, topological excitations. The first are point-like, immobile excitations (the "fractons") which are created by acting on the ground-state with an operator supported on a flat, rectangular region. The fracton excitations are created at the *corners* of this membrane and may only be created in groups of four. No local operator can move a single fracton without creating other excitations in the system. While individual fracton excitations are immobile, a *pair* of fractons are mobile within a plane and have bosonic self-statistics. In the X-cube fracton phase, there is a second type of point-like topological excitation, referred to as a "dimension-1 quasiparticle", which may only move along straight lines without creating additional excitations. Pairs of fractons which are mobile within planes exhibit π mutual statistics with dim.-1 quasiparticles contained within their plane of motion.

163
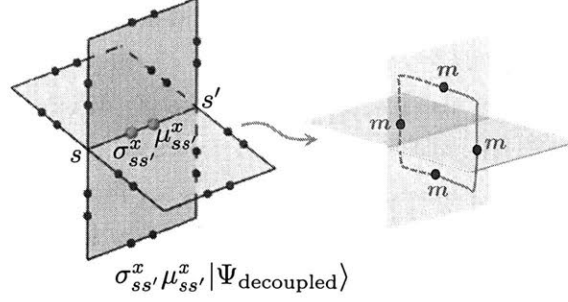
$$\sigma^x_{ss'}\mu^x_{ss'}|\Psi_{\text{decoupled}}\rangle$$

Figure 7-3: **Composite Flux Loop Condensation**: The operator $\sigma^x_{ss'}\mu^x_{ss'}$, when acting on the decoupled layers of the toric codes, creates four flux excitations in orthogonal planes, as shown. Condensing this composite flux leads to the "X-cube" fracton topological phase, with fracton operator $\mathcal{O}_c$ as given in the main text, and shown in Fig. 7-5.

Isotropic Layer Construction

To observe the emergence of the X-cube phase in our layer construction, we start from the decoupled phase of the Hamiltonian (8.1) and increase t, while keeping J and h fixed. Acting with the operator $\sigma^x_{rr'}\mu^x_{rr'}$ on the ground-state of the decoupled planes of toric codes creates four Z_2 fluxes in orthogonal layers, which form a closed loop on the dual lattice as shown in Fig. 7-3a. We refer to this excitation as a *composite flux loop*.

The X-cube fracton phase emerges after condensation of this composite flux loop. When $t \gg J, h$, we let $\sigma^x_{rr'}\mu^x_{rr'} = +1$ and define an effective spin degree of freedom for every link of the cubic lattice as $\tau^x_{rr'} \equiv \sigma^x_{rr'}$, $\tau^z_{rr'} \equiv \sigma^z_{rr'}\mu^z_{rr'}$. We then obtain an effective Hamiltonian in perturbation theory as

$$H^{(2)}_{\text{eff}} = H_{\text{X-cube}} - h \sum_{\langle r, r' \rangle} \tau^z_{rr'} \tag{7.8}$$

where

$$H_{\text{X-cube}} = -J \sum_{r,j} A^{(j)}_r - K \sum_r \mathcal{O}_r \tag{7.9}$$

with $K \sim O(J^6/t^5)$. Here, $A^{(j)}_r$ is a four-spin operator for the spins along the four links emanating from site r that lie in the jth plane:

$$A^{(j)}_r = \prod_{s \in \text{plane}_j(r)} \tau^x_{rs} \tag{7.10}$$

164
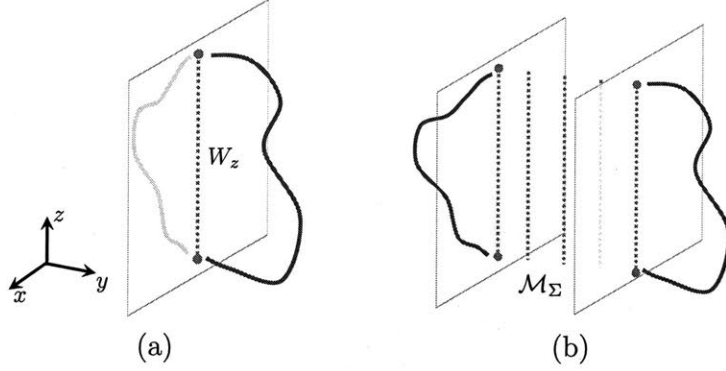
Figure 7-4: **Loop-Gas Representation**: Acting on the X-cube ground-state with (a) a straight, line-like operator W_z creates a pair of Z_2 flux excitations at the ends. This operator "cuts" open a closed loop configuration in the fracton ground-state; alternatively, this operator adds two open strings at its endpoints, when acting on an empty region. For the indicated loop configuration, acting with (b) a membrane operator $\mathcal{M}_\Sigma$ yields two separated, open strings of composite flux. An isolated string endpoint cannot be moved on its own, or else it would be possible to generate a configuration of broken loops that violate the global constraints explained in Sec. IIB. These isolated excitations are the immobile fractons.

while the operator $\mathcal{O}_r$, given by

$$
\begin{aligned}
\mathcal{O}_r &\equiv B_r^{(xy)} B_r^{(yz)} B_r^{(xz)} B_{r+\hat{x}}^{(yz)} B_{r+\hat{y}}^{(xz)} B_{r+\hat{z}}^{(xy)} \\
&= \prod_{r,r' \in \text{cube}(r)} \tau_{rr'}^z
\end{aligned}
\tag{7.11}
$$

is precisely the product of the twelve τ^z spins surrounding an elementary cube as shown in Fig. 7-5. The Hamiltonian $H_{\text{X-cube}}$ is precisely the commuting Hamiltonian that describes the "fixed-point" properties of the X-cube fracton phase, as introduced in Ref. [7]. The ground-state at the solvable point satisfies $\mathcal{O}_r |\Psi\rangle = A_r^{(j)} |\Psi\rangle = |\Psi\rangle$ for all r, j. Excitations may be created by acting with string or membrane operators to violate these constraints. The operators $\mathcal{O}_r$ and $A_r^{(j)}$ measure the Z_2 "charge" of the fracton and dimension-1 excitations (i.e. the presence or absence of an excitation), respectively.

Loop Gas Wavefunction, Excitations and Degeneracy

Our layer construction provides insight into the origin of the exotic topological excitations and sub-extensive ground-state degeneracy of the X-cube phase. First, the ground-state wavefunction of the X-cube fracton phase may be written as a superposition of composite flux loop excitations of the layered 2D toric codes; heuristically

$$
|\Psi_{\text{X-cube}}\rangle \sim \sum_{\mathcal{C}} |\mathcal{C}\rangle
\tag{7.12}
$$

165

with $\mathcal{C}$, a configuration of loops on the dual lattice. Excitations may be obtained at the endpoints of "broken" composite flux loops. We note, however, that while any closed loop configuration is permissible in the ground-state, the manner in which these loops may be broken is highly constrained. First, a composite flux loop that has broken at a single point is precisely a 2D Z_2 flux excitation of the underlying toric codes. Since these excitations must appear in pairs, the composite flux loops can only be broken at *pairs* of points along xy, yz or xz planes. As an example, acting on the ground-state with $W_z = \prod_{r,r'} \tau^x_{rr'}$, a string operator along a line in the z-direction, has the effect of cutting composite flux loops at two points, as shown in Fig. 7-4a, and the resulting pair of 2D Z_2 fluxes may move within a plane. This operator creates the mobile anyon excitations in the X-cube phase, which clearly inherit their "topological" properties (i.e. self-statistics and mutual statistics with the dimension-1 quasiparticle), from the 2D Z_2 fluxes in the toric code.

An isolated string endpoint is precisely the fracton excitation of the X-cube model, and may be obtained by spatially separating the broken endpoints of composite flux loops. An isolated string endpoint cannot be moved on its own without creating additional excitations, for if such an endpoint were mobile, then it would be possible to smoothly deform a configuration of open strings into one which violates the previously-derived constraint. The immobile, isolated endpoints then describe the fracton excitations of the X-cube phase. In practice, acting on the ground-state with a flat membrane operator $\mathcal{M}_\Sigma = \prod_{r,r'\in\Sigma} \tau^x_{rr'}$ will localize these excitations at the corners of Σ, as shown in Fig. 7-4b. In the decoupled toric codes, this operator creates a sequence of 2D Z_2 fluxes in parallel layers. After condensing the composite flux loops, however, only the ends of this layered excitation carry an energy cost, since the bulk of this excitation is locally indistinguishable from a composite flux loop.

The topological degeneracy of the X-cube fracton topological phase – which was previously obtained [7] by counting independent constraints on the operators $\mathcal{O}_r$, $A_r^{(j)}$ on the three-torus using an algebraic representation of the solvable Hamiltonian [46, 47] – may now be understood by counting the number of topological sectors of the decoupled, two-dimensional toric codes that are made equivalent after condensation of the composite flux loop. A discussion of this counting is presented in the Supplemental Material [?].

7.1.3 Z_N X-cube Topological Phase

The spirit of our proposal motivates the construction of new, three-dimensional topological orders, by appropriately condensing "loop" objects in an array of two-dimensional topological phases. An extended discussion of new topological phases that may be built in this manner is the subject of forthcoming work [?]. Here, we discuss the simplest generalization of our construction, involving an array of two-dimensional Z_N toric codes [19] in the same configuration as shown in Fig. 7-1, which gives rise to a Z_N generalization of the X-cube model. After arranging the Z_N toric codes in a three-dimensional array, each link of the three-dimensional cubic lattice now has two Z_N qudit degrees of freedom, denoted $X_{rr'}$, $Z_{rr'}$ and $\widetilde{X}_{rr'}$, $\widetilde{Z}_{rr'}$ respectively, and satisfying

$$A^{(xy)} \sim \mathbf{X}_q^\dagger \mathbf{X}_u \mathbf{X}_s \mathbf{X}_v^\dagger$$
$$A^{(yz)} \sim \mathbf{X}_q^\dagger \mathbf{X}_p \mathbf{X}_s \mathbf{X}_r^\dagger$$
$$A^{(xz)} \sim \mathbf{X}_p^\dagger \mathbf{X}_u \mathbf{X}_r \mathbf{X}_v^\dagger$$
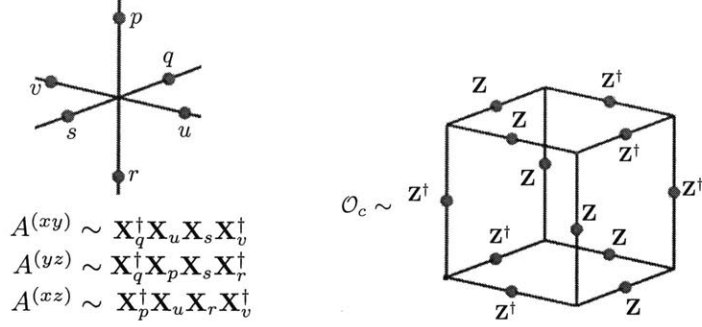
Figure 7-5: The Z_N X-cube Model: Shown are the commuting operators that appear in the solvable Hamiltonian for the Z_N X-cube model $H = -K \sum_c (\mathcal{O}_c + \mathcal{O}_c^\dagger) - J \sum_{r,j} (A_r^{(j)} + A_r^{(j)\dagger})$. The Z_2 case discussed in Sec. IB, is obtained by replacing $\mathbf{Z}, \mathbf{Z}^\dagger \to \tau^z$ and $\mathbf{X}, \mathbf{X}^\dagger \to \tau^x$.

the algebra $XZ = \omega ZX$, $\widetilde{X}\widetilde{Z} = \omega \widetilde{Z}\widetilde{X}$ with $\omega = e^{2\pi i/N}$. We now consider the Hamiltonian

$$H' = H_0' + H_1' \tag{7.13}$$

where H_0 describes the de-coupled layers of Z_N toric codes

$$H_0' = -J \sum_r \sum_{j=xy,yz,xz} \left[A_r^{(j)} + B_r^{(j)}\right] + \text{h.c.} \tag{7.14}$$

with $A_r^{(j)}$ and $B_r^{(j)}$ the Z_N charge and flux operators at site r, for the toric code oriented along plane j, respectively. The layers are coupled through the interactions

$$H_1' = -h \sum_{\langle r,r' \rangle} \left[Z_{rr'}^\dagger \widetilde{Z}_{rr'} + \text{h.c.}\right] - t \sum_{\langle r,r' \rangle} \left[X_{rr'} \widetilde{X}_{rr'} + \text{h.c.}\right] \tag{7.15}$$

Following our previous analysis, we consider the limit $h \gg J, t$, where we find that the ground-state exhibits 3D Z_N topological order. In this limit, we may identify a single Z_N degree of freedom on each link of the cubic lattice (with logical operators $\mathbf{X}, \mathbf{Z}$), and obtain the effective Hamiltonian $H_{\text{toric}}' - t \sum_{rr'} [\mathbf{X}_{rr'} + \text{h.c.}]$ where H_{toric}' is now the 3D Z_N toric code Hamiltonian [200]. Alternatively, when $t \gg J, h$ so that we have condensed the "Z_N composite flux loop", we obtain the effective Hamiltonian

$$H_{\text{eff}}' = H_{\text{X-cube}_N} - h \sum_{\langle r,r' \rangle} \left[\mathbf{Z}_{rr'} + \mathbf{Z}_{rr'}^\dagger\right] \tag{7.16}$$

where

$$H_{\text{X-cube}_N} = -K \sum_c [\mathcal{O}_c + \mathcal{O}_c^\dagger] - J \sum_{r,j} [A_r^{(j)} + (A_r^{(j)})^\dagger] \tag{7.17}$$

is the solvable Hamiltonian for the Z_N generalization of the X-cube model. The microscopic

form of the operators $\mathcal{O}_c$ and $A_r^{(j)}$ are explicitly given in Fig. 7-5.

Since the operators $\mathcal{O}_c$ and $A_r^{(j)}$ commute, the ground-state of (7.17) again satisfies $\mathcal{O}_c |\Psi\rangle = A_r^{(j)} |\Psi\rangle = |\Psi\rangle$, and gapped excited states may be created by acting with straight Wilson line or flat membrane operators, in a straightforward generalization of the operators in the Z_2 X-cube model. Now however, the dimension-1 quasiparticles and fracton excitations carry a Z_N electric and magnetic charge, respectively, which is inherited from the underlying 2D Z_N toric codes. As a result, a pair of fractons which are mobile in a plane have bosonic self-statistics, but non-trivial mutual statistics $e^{i\theta_{pq}}$ with a dimension-1 quasiparticle of charge $q \in \{1, \ldots, N-1\}$ in its plane of motion. Here, the statistical angle $\theta_{pq} = 2\pi pq/N$, where p is the magnetic charge carried by the fracton excitation.

7.1.4 Degeneracy of the Z_N X-Cube Model

We now discuss the topological degeneracy of the Z_N X-cube models on the three-torus. We begin by elaborating on the degeneracy of the X-cube phase introduced in Ref. [6], as understood from our isotropic layer construction.

The topological degeneracy of the X-cube fracton topological phase – which was previously obtained [7] by counting independent constraints on the operators $\mathcal{O}_r$, $A_r^{(j)}$ on the three-torus using an algebraic representation of the solvable Hamiltonian [46] – may also be understood by counting the number of topological sectors of the decoupled, two-dimensional toric codes that are made equivalent after condensation of the composite flux. For example, the vacuum sector of the completely decoupled theory is equivalent, after flux loop condensation, to the topological sector where a single Wilson line – which creates two-dimensional Z_2 flux excitations at its ends – wraps around all of the xy planes in the x-direction $W_x^{(xy)}$ and all of the yz planes in the z-direction $W_z^{(yz)}$. We label this topological sector of the decoupled toric codes as $W_x^{(xy)} W_z^{(yz)}$, which is now equivalent to the vacuum sector after composite flux condensation. By cyclically permuting the x, y and z indices and by taking products of the Wilson line operators, we obtain seven additional topological sectors of the decoupled theory that are equivalent to the vacuum sector in the flux condensed phase [we may explicitly enumerate these sectors, adopting the previous notation, as $W_y^{(yz)} W_x^{(xz)}$, $W_z^{(xz)} W_y^{(xy)}$, $W_x^{(xy)} W_z^{(yz)} W_y^{(yz)} W_x^{(xz)}$, $W_x^{(xy)} W_z^{(yz)} W_z^{(xz)} W_y^{(xy)}$, $W_y^{(yz)} W_x^{(xz)} W_z^{(xz)} W_y^{(xy)}$, and $W_x^{(xy)} W_z^{(yz)} W_y^{(yz)} W_x^{(xz)} W_z^{(xz)} W_y^{(xy)}$]. Since eight topological sectors of the decoupled theory are identified after condensation, we are led to conclude that on an $L_x \times L_y \times L_z$ three-torus, the X-cube fracton phase has topological degeneracy $D = 4^{L_x + L_y + L_z}/8$ or $\log_2 D = 2(L_x + L_y + L_z) - 3$ which reduces to the previously known degeneracy on the length-L three-torus when L is odd [7].

We may also compute the topological degeneracy of the Z_p generalization of the X-cube phase, which we have introduced in the main text, when p is prime. This fracton phase is constructed in the main text by coupling together copies of the Z_p toric code, whose charge and flux operators are shown in Fig. 7-6.

For the Z_p generalization of the X-cube phase, we find that the degeneracy on the length-L
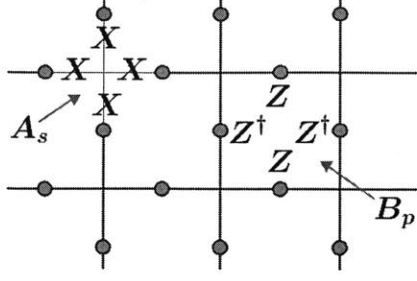
Figure 7-6: **2D Z_N Charge and Flux Operators**: Show are the star A_s and plaquette B_p operators that measure the Z_N charge and flux, respectively, in the 2D Z_N toric code.

three-torus is given by $\log_p D = 6L - 3$ when $L = p^n - 1$, through an extension of the arguments presented in Ref. [6]. First, the algebraic representation [46, 47] of the Z_N generalization of the X-cube model is described by a stabilizer map $S = S_x \oplus S_z$ where

$$S_x = \begin{pmatrix} -1 + \bar{x} & 1 - \bar{x} & 0 \\ 1 - \bar{y} & 0 & 1 - \bar{y} \\ 0 & -1 + \bar{z} & -1 + \bar{z} \end{pmatrix} \tag{7.18}$$

and

$$S_z = \begin{pmatrix} -(1 - z)(1 - y) \\ -(1 - x)(1 - z) \\ -(1 - y)(1 - x) \end{pmatrix}. \tag{7.19}$$

Here, $\bar{x} \equiv x^{-1}$, $\bar{y} \equiv y^{-1}$, $\bar{z} \equiv z^{-1}$, and the polynomials shown are elements of the Laurent polynomial ring $\mathbb{F}_p[x, \bar{x}, y, \bar{y}, z, \bar{z}]$ over the field $\mathbb{F}_p$ with prime p. Let R be the quotient ring $R \equiv \mathbb{F}_p[x, y, z]/\langle x^L - 1, y^L - 1, z^L - 1 \rangle$. The degeneracy of the Z_p X-cube model on the length-L three-torus is given by $\log_p D = k_x + k_z$ where the quantities k_x and k_z are given by

$$k_x = \dim_{\mathbb{F}_p} \left[\frac{R}{\langle (1 - z)(1 - y), (1 - x)(1 - z), (1 - y)(1 - x) \rangle} \right]$$

and

$$k_z = \dim_{\mathbb{F}_p} \left[\frac{R^2}{\left(\begin{matrix} -1 + x & 1 - y & 0 \\ 1 - x & 0 & -1 + z \end{matrix} \right)} \right]$$

In the second expression, we have taken advantage of the fact that only two of the columns of S_x are linearly independent. Both quantities k_x and k_z may be evaluated in the algebraic closure of $\mathbb{F}_p$, which we denote $\mathbb{F}$, when the length $L = p^n - 1$, so that $x^L - 1$ has L distinct roots. In this

169

case, we determine $k_x = 3L - 2$ by localizing at the maximal ideal $\langle x - t, y - 1, z - 1 \rangle$, where $t \neq 1$ is a root of $x^L - 1$. Similarly, k_z is determined from the fact that the second determinantal ideal of $\begin{pmatrix} -1 + x & 1 - y & 0 \\ 1 - x & 0 & -1 + z \end{pmatrix}$ is precisely $\langle (1 - z)(1 - y), (1 - x)(1 - z), (1 - y)(1 - x) \rangle$. As a result, localizing again at the maximal ideal $\langle x - t, y - 1, z - 1 \rangle$ yields $k_z = 3L - 1$. This yields the desired result for the topological degeneracy of the Z_p generalization of the X-cube model on a three-torus of length $L = p^n - 1$.

Chapter 8

Generalizations of Non-Abelian Anyons in Three Dimensions

A core concept in the quantum theory of indistinguishable particles is quantum statistics. While fundamental particles in nature only obey either Bose or Fermi statistics, the notion of particle statistics also applies to quasiparticles – emergent, point-like excitations in many-body systems with an energy gap – through the geometric phase accumulated in a braiding process, whereby two identical quasiparticles are adiabatically interchanged. The allowed statistics are constrained by the topology of quasiparticle trajectories in the braiding process. As a consequence of the non-trivial topology of braids in $(2 + 1)$-dimensional spacetime, certain quasiparticles in two dimensions – known as anyons [201] – are allowed to have statistics other than Bose or Fermi [202, 156]. Non-Abelian anyons [85, 44] are particularly interesting, since a state of well-separated non-Abelian anyons carries a degeneracy that cannot be lifted through local perturbations. Braiding a pair of these excitations can implement a unitary transformation on this space of states. Efforts to search for non-Abelian anyons are underway [203, 204].

Do particles with neither Bose nor Fermi statistics exist in three dimensions? A standard argument rules out this possibility based on the observation that exchanging a pair of particles twice in a $(3+1)$-dimensional spacetime is topologically equivalent to no exchange. This implies that two exchanges must leave the quantum state invariant, hence a single exchange can only generate a phase factor ± 1, corresponding to Bose or Fermi particle statistics, respectively.

Despite this no-go argument, the possibility of lifting anyons to three dimensions has long fascinated physicists. It is known that in three-dimensional lattice gauge theories with a discrete, non-Abelian gauge group, point-like charge excitations can carry a protected internal degeneracy with integer "quantum dimension" [205, 206]. Nonetheless, these excitations still have Bose or Fermi statistics, and their internal state remains unchanged under braiding. Other possibilities have also been explored. An intriguing study [207] suggested that Majorana zero modes on the surface of a superconducting topological insulator [14] display braiding properties analogous to non-Abelian anyons, despite living in a three-dimensional system. However, these Majorana zero

$$\sim G_{j,\ell} \equiv \Gamma^{(f)}_{j,\ell} \mathcal{O}_{j,\ell} \Gamma^{(f)}_{j,\ell+1}$$

$$\Gamma^{(f)}_{j,\ell} \equiv (-1)^{f^\dagger_{j,\ell} f_{j,\ell}}$$

$$\sim \prod_{(i,j)\in \partial p} \Gamma^{(c)}_{ij,\ell}$$

$$\Gamma^{(c)}_{ij,\ell} \equiv (-1)^{c^\dagger_{ij,\ell} c_{ij,\ell}}$$

$\bullet = f, f^\dagger$
$\circ = c, c^\dagger$
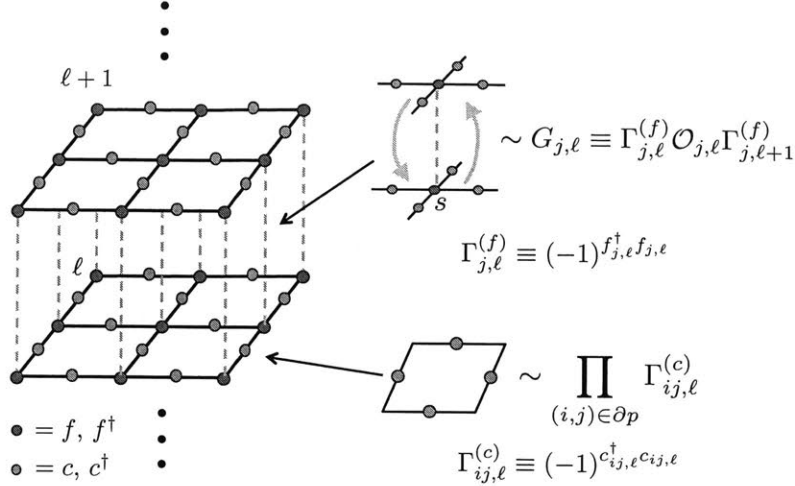
Figure 8-1: **The Model:** We consider layers of of complex fermions on the sites of a square lattice (f), coupled to fermions that lie on the links (c) which play the role of a static Z_2 gauge field. Within each layer, the hopping and pairing interaction of the fermions are mediated by the fermions on the links, which interact at each plaquette as shown. The gauge symmetry of the Hamiltonian (8.1) is implemented by the operator $G_{j,\ell} = \Gamma^{(f)}_{j,\ell-1} \mathcal{O}_{j,\ell} \Gamma^{(f)}_{j,\ell+1}$ which couples adjacent layers, with $\mathcal{O}_{j,\ell}$ as defined in the main text. The ground-state realizes an exotic phase with immobile, point-like excitations that carry a protected internal degeneracy.

modes cannot be spatially separated at finite energy cost [208]. Such objects, now commonly referred to "twist defects", are *not* deconfined quasiparticles.

In this chapter, we build on our understanding of exotic, three-dimensional quantum phases by demonstrating the existence of a new type of deconfined point-like excitation in three dimensions, which carries a protected degeneracy as non-Abelian anyons in two dimensions do, but cannot move freely without paying an energy cost. These fundamentally immobile particles – termed "fractons" [6] – have been theoretically discovered [46, 178, 177, 7] and have attracted increasing interest in such diverse fields as topological quantum matter, lattice gauge theory, quantum information, and many-body localization [7, 197, 179, 5, 209, 210, 151, 211, 198]. Being unable to move, fractons evade the standard argument for particle statistics relying on the topology of worldlines. This enables our generalization of the notion of non-Abelian particles to three dimensions. The non-Abelian fractons discussed in this chapter can provide an alternate platform for quantum computation, with possibly increased robustness against thermal errors.

We introduce two lattice models which support such "non-Abelian fracton" excitations. The first is an exactly solvable fermion model that describes a chiral phase where the fractons have *irrational* quantum dimension. This phase is constructed from two-dimensional layers of $p_x + ip_y$ superconductors interacting with Z_2 gauge field, and by further coupling these layers in a nontrivial way. The interlayer coupling turns fluxes into deconfined, immobile point-like excitations, i.e., fractons. As a result, when the parent superconducting state on each layer is topologically nontrivial, the fluxes acquire a $\sqrt{2}$ quantum dimension, yielding "non-Abelian"

fracton excitations in a three-dimensional phase. Certain pairs of these fractons behave as non-Abelian anyons with well-defined statistics. The second model we present is constructed from interacting layers of two-dimensional G-gauge theories for a finite group G [19], which are stacked along all three directions. This isotropic layer construction yields point-like, immobile excitations with integer quantum dimension. In both models, fractons can only be created, in multiples of four, at the corners of an operator with support on a membrane-like region. This defining property of fractons is fundamentally distinct from that of anyons, which are created in pairs, at the ends of string-like Wilson line operators.

8.1   A Solvable Model

We begin with a detailed description of our first model. Consider a vertical stack of two-dimensional square lattice planes, as shown in Fig. 8-1. Within each plane ℓ, there are two types of fermions living on the sites (denoted $f_{j,\ell}$) and bonds (denoted $c_{ij,\ell}$) of the lattice. Our solvable Hamiltonian is given by:

$$H = \sum_{\ell} H_\ell - K \sum_{\ell,p} B_{p,\ell} - \sum_{\ell,j} G_{j,\ell}. \tag{8.1}$$

where H_ℓ is defined for every layer (ℓ), $B_{p,\ell}$ for every plaquette (p), and $G_{j,\ell}$ at every site j on adjacent planes ℓ and $\ell+1$, as indicated in Fig. 8-1.

The first term in the Hamiltonian takes the form

$$H_\ell = \sum_{\langle i,j \rangle} \left[-t\, f_{i,\ell}^\dagger\, \Gamma_{ij,\ell}^{(c)}\, f_{j,\ell} + \Delta_{ij}\, f_{i,\ell}^\dagger\, \Gamma_{ij,\ell}^{(c)} f_{j,\ell}^\dagger + \text{h.c.} \right] - \mu \sum_i f_{i,\ell}^\dagger f_{i,\ell}. \tag{8.2}$$

where

$$\Gamma_{ij,\ell}^{(c)} \equiv (-1)^{c_{ij,\ell}^\dagger c_{ij,\ell}} = 1 - 2c_{ij,\ell}^\dagger c_{ij,\ell} \tag{8.3}$$

is the parity of the fermions along link (i,j) in layer ℓ. H_ℓ describes f fermions in a $(p_x + ip_y)$-wave paired state on each plane, with a nearest-neighbor hopping t and pairing Δ_{ij} on the two-dimensional square lattice, with $\Delta_{ij} = \Delta$ on $+x$ links and $i\Delta$ on $+y$ links. Importantly, these "matter fermions" f interact with "gauge fermions" c via Ising gauge coupling, with the parity of the c fermions on the links $\Gamma^{(c)} = \pm 1$ playing the role of a Z_2 gauge field.

In the second term of (8.1), the operator $B_{p,\ell}$ is given by the product of the fermion parities $\Gamma_{ij,\ell}^{(c)}$ along the links surrounding plaquette p in layer ℓ

$$B_{p,\ell} \equiv \prod_{\langle i,j \rangle \in \partial p} \Gamma_{ij,\ell}^{(c)} \tag{8.4}$$

The ± 1 eigenvalue of $B_{p,\ell}$ measures the Z_2 flux of the gauge field through this plaquette.

The last term in the Hamiltonian describes an interaction between fermions on adjacent layers. The operator $G_{j,\ell}$, which is shown schematically in Fig. 8-1, is defined on the sites of the square lattice as

$$G_{j,\ell} \equiv \Gamma^{(f)}_{j,\ell} \, \mathcal{O}_{j,\ell} \, \Gamma^{(f)}_{j,\ell+1} \tag{8.5}$$

where $\Gamma^{(f)}_{j,\ell} = (-1)^{f^\dagger_{j,\ell} f_{j,\ell}}$ is the fermion parity of the matter fermion on site s in layer ℓ and

$$\mathcal{O}_{j,\ell} = \prod_{i \in \mathrm{star}(j)} \left[\frac{1}{2}(c^\dagger_{ij,\ell} - c_{ij,\ell})(c^\dagger_{ij,\ell+1} + c_{ij,\ell+1}) \right]$$

is an eight-body interaction that couples the fermions on the links forming a "star" configuration around site s in layer ℓ and in layer $\ell + 1$. The operators $G_{i,\ell}$ mutually commute, and satisfy $G^2_{i,\ell} = 1$. Remarkably, $G_{i,\ell}$ also commute with the Hamiltonian (8.1) since (i) H_ℓ is invariant under the local Z_2 transformation $f_{i,\ell} \to -f_{i,\ell}$, $\Gamma^{(c)}_{ij,\ell} \to -\Gamma^{(c)}_{ij,\ell}$ and (ii) $B_{p,\ell}$ overlaps with $G_{i,\ell}$ on two links. For $t, \mu, \Delta, K \ll 1$, all low-lying eigenstates of H satisfy the "gauge constraint"

$$G_{i,\ell}|\Psi\rangle = |\Psi\rangle \tag{8.6}$$

at every site i and layer ℓ. In the following, we will restrict our attention to these gauge-invariant states.

It is instructive to first study the model (8.1) in the limit $t = \Delta = 0$. The ground state is then simply a direct product state of the gauge and matter fermions $|\Psi_{\mathrm{gs}}\rangle = |g_c\rangle \otimes |0_f\rangle$. Here $|0_f\rangle$ is the vacuum state of matter fermions with $\Gamma^{(f)} = 1$ at every lattice site (assuming $\mu > 0$), while $|g_c\rangle$ is the ground state of the reduced Hamiltonian for the gauge fermions

$$H_c = -K \sum_{\ell,p} B_{p,\ell} - \sum_{j,\ell} \mathcal{O}_{j,\ell}. \tag{8.7}$$

This commuting Hamiltonian was introduced in Ref. [6] as an exactly solvable model for a fracton topological phase, whose universal properties are robust under any local perturbations. When placed on the $L \times L \times L$ three-torus, H_c exhibits 2^{3L-3} degenerate ground states that are locally indistinguishable. An elementary π-flux excitation is obtained when the eigenvalue of an operator $B_{p,\ell}$ on a plaquette is flipped. Remarkably, these π-flux excitations can only be created in multiples of four by acting with a *membrane* operator on the ground state, which flips the eigenvalues of $B_{p,\ell}$'s at the corners of the membrane. Therefore, a single π-flux is a fracton— it cannot be moved without creating additional fractionalized excitations. A self-contained discussion of this model has been provided in Sec. 5.1 .

Apart from the π-flux, our model also hosts gapped fermionic quasiparticles originating from the matter fermions on every layer. The fermionic excitations carry gauge charge, however, and must bind additional excitations in order to be gauge invariant. Adding or removing a bare

matter fermion $f_{j,\ell}$ flips the parity of $\Gamma^{(f)}_{j,\ell}$ and locally violates the gauge constraint (8.6). Instead, a gauge-invariant quasiparticle is obtained by binding a matter fermion with an excitation of gauge fermions having $\mathcal{O}_{j,\ell} = -1$ and $\mathcal{O}_{j,\ell-1} = -1$. Such a gauge excitation can only move within the plane, and has π mutual statistics with the π-flux excitation, which is a fracton. As a result, the fermionic quasiparticle also has π mutual statistics with the π-flux, reminiscent of a conventional Z_2 gauge theory with charged matter fields. When $t, \Delta \neq 0$, gauge-invariant eigenstates of H take the general form $|\Psi\rangle = P\,|\eta\rangle \otimes |\varphi\rangle_\eta$ where $|\eta\rangle$ is a state of gauge fermions with a fixed fermion parity on every link, so that $\Gamma^{(c)}_{ij,\ell}\,|\eta\rangle = \eta_{ij,\ell}\,|\eta\rangle$ with $\eta_{ij,\ell} = \pm 1$. $|\varphi\rangle_\eta$ is an eigenstate of the matter fermions in gauge field configuration η. That is, $|\varphi\rangle_\eta$ is obtained by substituting the operators $\Gamma^{(c)}_{ij,\ell}$ with their eigenvalues $\eta_{ij,\ell}$ in the first term of H, and then solving the resulting quadratic Hamiltonian for the matter fermions. Finally, P is a projection operator, which projects the wavefunction of the matter and gauge fermions onto the gauge invariant subspace

$$P \equiv \prod_{j,\ell} \left(\frac{1 + G_{j,\ell}}{2} \right). \tag{8.8}$$

To verify that the above wavefunction is an eigenstate of H, we note that (i) $[P, H] = 0$ and that (ii) by construction, $|\eta\rangle \otimes |\varphi\rangle_\eta$ is an eigenstate of the first two terms in H, whose eigenvalue we denote $E(\eta, \varphi)$. It follows that

$$H\,|\Psi\rangle = HP\,|\eta\rangle \otimes |\varphi\rangle_\eta = PH\,|\eta\rangle \otimes |\varphi\rangle_\eta = P\Big(E(\eta, \varphi) - \sum_{j,\ell} G_{j,\ell} \Big)\,|\eta\rangle \otimes |\varphi\rangle_\eta$$

$$= \Big[E(\eta, \varphi) - N \Big]\,|\Psi\rangle, \tag{8.9}$$

where we have used the identity $PG_{j,\ell} = P$, and N is the number of f fermion sites. The energy spectrum of H is thus determined by that of the quadratic Hamiltonian for the matter fermions in a fixed gauge flux configuration.

When $K \gg t, \Delta$, the ground state belongs to the zero-flux gauge sector (e.g. with $\eta_{ij,\ell} = 1$ on all links), and the matter fermions realize a $p_x + ip_y$ superconductor on every layer. As a result of the gauge-matter coupling, π-flux excitations of the gauge field are now bound to vortices of the $p_x + ip_y$ superconductor. When $|\mu| > 4t$, the $p_x + ip_y$ superconducting state of the matter fermions is fully gapped and adiabatically connected to the $t = \Delta = 0$ limit. Therefore, π-flux excitations are topologically equivalent to the fractons of the Hamiltonian (8.7) of gauge fermions only. When $|\mu| < 4t$, however, the matter fermions in the zero-flux gauge sector realize a fully-gapped $p_x + ip_y$ topological superconductor on every layer. In this case, π-flux excitations become non-Abelian fractons with internal topological degeneracy, as we now show.

Recall that a two-dimensional $p_x + ip_y$ topological superconductor hosts localized Majorana zero modes in vortex cores [86, 16]. When this superconductor is coupled to a Z_2 gauge field, the π-flux-vortex composite object becomes a deconfined quasiparticle, which is a well-studied

example of a non-Abelian anyon—the Ising anyon [44]. N well-separated Ising anyons carry d^N degenerate internal states which cannot be split by local perturbations, with the quantum dimension $d = \sqrt{2}$ originating from the Majorana zero mode. Bringing two Ising anyons (σ) together, however, can split the degeneracy, resulting in either a fermionic excitation (ψ) or a trivial boson (1). This behavior is captured by the fusion rules

$$\sigma \times \sigma = 1 + \psi \tag{8.10}$$

as well as the rules $\sigma \times \psi = \sigma$, $\psi \times \psi = 1$ and $1 \times a = a$, with $a = 1, \psi, \sigma$. Braiding Ising anyons generates a non-trivial unitary transformation on their internal states.

In our three-dimensional model, when $|\mu| < 4t$, the π-flux bound to a vortex on a single layer hosts a Majorana zero mode, and hence acquires a protected internal degeneracy with quantum dimension $d = \sqrt{2}$. Unlike Ising anyons, however, these π-fluxes are fundamentally immobile point-like excitations; this property originates from the fractons in the model (8.7) for the gauge fermions before coupling to matter fields. We thus refer to these fractons, with a topologically protected internal degeneracy, as "non-Abelian fractons".

We now study the nature of composite excitations made from a pair of non-Abelian fractons in our model. First, we show that the internal degeneracy of pairs of non-Abelian fractons in *distinct* layers is protected, even when they are brought close together. Splitting the degeneracy requires quasiparticle tunneling between the two Majorana zero modes. This process is forbidden, however, since there is no gauge-invariant operator that can transfer quasiparticles between distinct layers. This can be seen by observing that the local gauge constraint $G_{j,\ell} = +1$ gives rise to conserved fermion parity on every pair of adjacent planes: $\prod_j G_{j,\ell} = U_\ell^{(f)} U_{\ell+1}^{(f)} = +1$, where $U_\ell^{(f)} \equiv \prod_j \Gamma_{j,\ell}^{(f)}$ is the fermion parity in layer ℓ. This parity conservation naturally forbids inter-layer quasiparticle tunneling in the gauge-invariant subspace, so that a pair of non-Abelian fractons in distinct layers ℓ and ℓ' – referred to schematically as $\sigma_\ell \times \sigma_{\ell'}$ – forms a topological excitation with quantum dimension $(d_\sigma)^2 = 2$. This excitation is a non-Abelian anyon that can only move within the xy plane. Braiding this non-Abelian anyon around a fracton enclosed in its plane of motion can implement a unitary transformations on this degenerate Hilbert space; a particular example is explicitly given in Appendix C.1.

8.2 Coupled Layer Construction

We now summarize an alternate prescription for obtaining a non-Abelian fracton topological phase where the fracton excitations carry integer quantum dimension, which is motivated by an isotropic, layer construction [5, 209] of a particular fracton phase introduced in Ref. [7]. The starting point for this construction is an array of two-dimensional lattice gauge theories for a finite gauge group G that are stacked in the xy, yz and xz directions, as shown in Fig. 8-2a. Initially, distinct layers are decoupled and each layer is in the deconfined phase of the G gauge theory, which hosts gapped charge and flux excitations that are labeled by irreducible
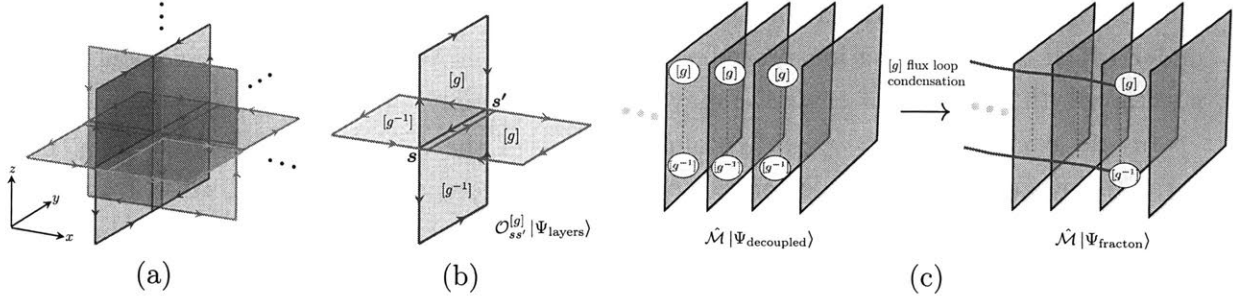
Figure 8-2: **Coupled 2D G gauge theories:** Intersecting layers of 2D gauge theories for finite the group G, stacked in the xy, yz and xz planes as shown in (a). "Condensing" the excitation in (b) – a composite of four $[g]$ fluxes – can produce a fracton topological phase, where the fracton excitation inherits certain properties from the non-Abelian $[g]$ flux as shown in (c) and described in the main text.

representations and conjugacy classes of G, respectively. Starting from this isotropic array, we now introduce an interaction on the bonds of the lattice; when acting on the ground-state of the decoupled layers, this coupling has the effect of creating a pair of fluxes (labeled $[g]$) in orthogonal layers as shown in Fig. 8-2b. We refer to this as a "$[g]$ composite flux loop", since this excitation forms a closed loop on the dual lattice. Increasing the strength of the inter-layer coupling eventually condenses this excitation, yielding a ground-state given by a superposition of loop-like excitations built from the 2D $[g]$ fluxes.

We observe that a fracton topological phase is obtained by considering the excitations that remain deconfined after this condensation procedure. When the layers are decoupled, we may act with an array of Wilson line operators in parallel layers to create a sequence of $[g]$ fluxes, as shown in Fig. 8-2c. This excitation carries an $O(L)$ energy cost, where L is the linear dimension of the array. After condensation of the composite $[g]$ flux loop, the bulk of this excitation is indistinguishable from a configuration of fluxes that appear in the ground-state. As a result, in the condensed phase, the bulk of this excitation costs no energy. The membrane-like operator formed from the array of Wilson lines may create excitations at its *corners*, however, as the corners appear to be points where the composite $[g]$ flux loops have broken open, as shown in Fig. 8-2c. Due to the geometry of this operator, these point-like excitations cannot be moved without nucleating other excitations in the system, and we conclude that a single $[g]$-flux has become an immobile fracton excitation. The charges and dyons of the two-dimensional G gauge theory will generically be confined due to their non-trivial statistics with the $[g]$ flux. However, the condensation procedure may bind these into emergent excitations with reduced mobility.

When the gauge group $G \cong Z_2$, this condensation procedure yields the so-called X-cube fracton topological phase [7, 5, 209]; Z_N generalizations of the X-cube phase may be constructed in a similar fashion [5]. However, G can also be a finite *non-Abelian* group. In this case, condensing a composite flux loop made of non-Abelian fluxes of the G gauge theory will produce a non-Abelian fracton topological phase where the immobile fracton excitations carry a protected internal degeneracy, so long as a single $[g]$-flux remains deconfined after this condensation pro-

cedure. Due to the non-trivial statistics and fusion rules of the $[g]$ fluxes, the general conditions under which this condensation procedure will yield a non-Abelian fracton topological phase is not known, though certain examples may be explicitly analyzed.

In the Appendix C.2, we study coupled layers of the S_3 gauge theory, where S_3 is the permutation group on three elements. Condensing the composite flux loop formed from the S_3 fluxes with quantum dimension 3 yields a fracton topological phase, where the non-Abelian flux becomes an immobile topological excitation. The condensation procedure also has the effect of binding certain two-dimensional charges into excitations with restricted mobility, while all mobile charge excitations are confined. For example, while an isolated charge excitation that corresponds to the alternating representation of S_3 is confined, *pairs* of these charges remain well-defined excitations that may only move along lines. It would be interesting if a similar layer construction using other "string-net" models [43] could also yield exotic, 3D phases with immobile fractionalized excitations.

Part III

Scrambling and the Dynamics of Quantum Information

In this section, we study entanglement growth and the dynamics of operator spreading in random unitary circuits, which provide minimal models for chaotic quantum dynamics. Exact calculations of averaged quantities, such as the out-of-time-ordered commutator, reveal connections to classical stochastic growth processes. These relations motivate new heuristics for the propagation of quantum information and entanglement that may apply in more generic quantum many-body systems with conservation laws. This section is based on Ref. [9, 10].

Chapter 9

Operator Spreading in Random Unitary Circuits

A key challenge for many-body physics is to identify universal properties of quantum dynamics and the approach to thermalization. Particularly important are universal results that hold for generic quantum systems. Examples of such universal properties include the existence of effective light cones for the propagation of quantum information [212] and the existence of universal scaling forms for the growth and saturation of the von Neumann entanglement entropy in 1+1D [50, 52, 62, 63, 213, 53, 77, 64, 9, 214, 67, 68, 69, 74].

By definition, generic systems lack the structures (for example large numbers of symmetries or conservation laws) that allow for exact results in typical solvable many-body systems. Surprisingly, insight into generic systems can come from studying dynamics with even *less* structure than a generic Hamiltonian system, such as the dynamics generated by a random quantum circuit. Random circuit dynamics provide a minimally structured model with which real Hamiltonian dynamics can be compared [215, 216, 217, 218, 219, 220, 221, 222, 223]. Despite its simplicity, this model is able to capture universal scaling forms for entanglement growth both in 1+1D and in higher dimensions [9]. Random circuits are also toy models for information scrambling in black holes and other strongly coupled systems [215, 216, 217, 218, 219, 220, 221, 222, 223, 224].

In this chapter, we provide both exact results and coarse-grained descriptions for the spreading of quantum operators under random circuit dynamics, as measured by the 'out-of-time-order correlator' (OTOC). The OTOC originally appeared in the study of quasi-classical approximations to superconductivity [225], and is closely related to the commutator norm that appears in Lieb-Robinson bounds [212], but it has been studied recently as a means of quantifying the scrambling of quantum information [226, 227, 228, 229]. It has been argued that early-time exponential growth of the OTOC is a characteristic feature of chaotic quantum systems, and such growth has been obtained within the AdS/CFT correspondence and in a range of physical systems [230, 231, 232, 233, 234, 235, 236, 237]. The OTOC has also been applied to characterize slow dynamics in the presence of disorder and in the many-body localized
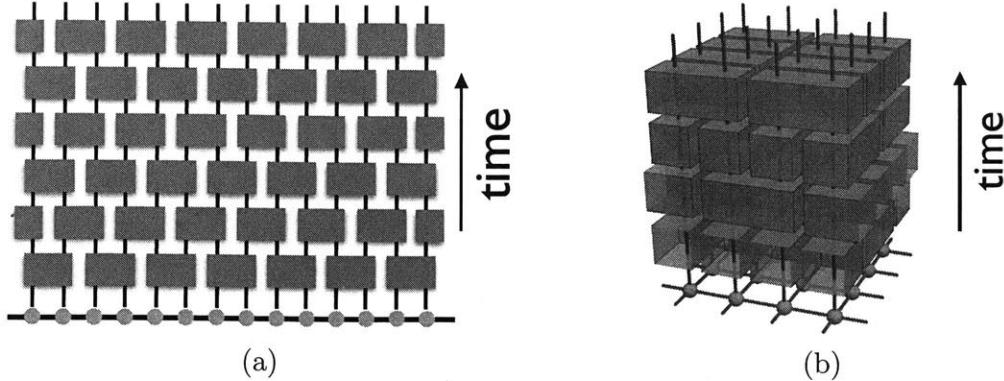
Figure 9-1: **Random unitary circuit** in (a) (1+1)D and (b) (2+1)D. Each "block" represents an independently Haar-random unitary, acting on the Hilbert space of two adjacent 'spins' of local Hilbert space dimension q. In (b), we show the geometry of the $(2+1)$D Haar-random circuit that we study in later sections.

phase [238, 239, 240, 78, 241, 242, 243, 244]. It has been calculated in 2D conformal field theories [245] and integrable chains [246], and studied numerically in nonintegrable 1D systems [247, 248, 249]. Following theoretical proposals [250, 251, 252], experiments addressing the OTOC have been conducted [253, 254, 255].

Random quantum circuits provide an ideal theoretical setting for the exact calculation of quantities such as the OTOC. While the behaviour of the OTOC in a random circuit is interesting in its own right, we conjecture that the long-distance properties of the OTOC that we derive will also be applicable to deterministic dynamics. Therefore we believe that these results will provide a useful starting point for understanding the generic spatial structure of spreading operators.

An operator $\mathcal{O}_0$ which is initially localized near the spatial origin (say, on a single site of a spin chain) will evolve under Heisenberg time evolution into a vastly more complicated operator $\mathcal{O}_0(t) = U^\dagger(t)\mathcal{O}_0 U(t)$ that acts nontrivially on many sites. The 'size' of $\mathcal{O}_0(t)$ is the size of the region in which $\mathcal{O}(t)$ fails to commute with a typical local operator Y_x at position x. This may be measured by

$$\mathcal{C}(x,t) \equiv \frac{1}{2}\operatorname{Tr}\rho[\mathcal{O}_0(t), Y_x]^\dagger[\mathcal{O}_0(t), Y_x] \tag{9.1}$$

where the expectation value has been taken in an appropriate Gibbs state. (For our purposes this will be taken to be the infinite temperature Gibbs state ρ_∞, which is the state to which random circuit dynamics equilibrate.) To make the connection with the out-of-time-order correlator (OTOC), we may expand out the commutators in (9.1). For simplicity let us assume for the moment that the operators $\mathcal{O}_0$ and Y_x are both Pauli-like operators squaring to the identity. We then have

$$\mathcal{C}(x,t) = 1 - \operatorname{Tr}\rho_\infty \mathcal{O}_0(t) Y_x \mathcal{O}_0(t) Y_x. \tag{9.2}$$

The second term, in which the operators are not time ordered, is the OTOC. Other measures of the structure of an operator could be defined (for example correlation functions involving higher powers of the commutator) but in this chapter we will restrict to the OTOC.

At a given time t, the range of x where the commutator $\mathcal{C}(x,t)$ is significantly larger than zero gives a measure of the size of the operator. This region typically grows ballistically [256], even when local conserved quantities exhibit diffusive transport [230, 237, 247, 248].[1] The immediate natural questions about $\mathcal{C}(x,t)$ include: What is the 'butterfly' velocity v_B associated with this ballistic growth? What is the spatial structure of $\mathcal{C}(x,t)$? Is there a 'hydrodynamic' equation for $\mathcal{C}(x,t)$ at large time and distance scales? Are there important differences between 1+1D and higher dimensions? We will answer all these questions for the case where the time evolution operator $U(t)$ is a circuit composed of Haar random unitaries, as in Fig. 9-1.

We demonstrate that, both in 1D and in higher dimensions, operator spreading and the growth of the OTOC can be mapped to classical stochastic growth models. We show via an exact calculation that operator spreading in 1+1D can be understood in terms of an equation involving diffusion and drift. The 'front' of the operator propagates at a finite velocity v_B. However the front also *broadens* diffusively, so that its width is proportional to $\sqrt{t}$ (Fig. 9-2). We conjecture that this physics also occurs in generic (nonintegrable) 1D systems undergoing deterministic Hamiltonian dynamics. For random circuit dynamics, we must also consider how the averaged correlator $\overline{\mathcal{C}}$ differs from the correlator $\mathcal{C}$ within a given realization of the random circuit. We argue that fluctuations between realizations are small: typical variations in the front position between different realizations are $O(t^{1/4})$, so negligible in comparison with the $\sqrt{t}$ broadening of the front.

Turning to higher dimensions, we show by an exact mapping that there is a remarkable relationship with a classical droplet growth problem in the Kardar–Parisi–Zhang universality class [82]. (To avoid confusion, we note that this is *not* related to the connection between entanglement growth and KPZ introduced in [9].) We use this relationship to quantify the broadening of the 'front' of a growing operator in a higher dimensional random circuit. In 2+1D the front broadens like $t^{1/3}$ [82], and in 3+1D like $t^{0.240}$ [257].[2] In the two-dimensional case, and in the absence of lattice anisotropies, recent breakthroughs in the theory of interface growth [258, 259, 260, 261, 262, 263, 264, 265, 266, 267, 268, 269, 270] also translate to an exact form for the OTOC, in terms of the celebrated Tracy-Widom distribution (Fig. 9-3). The broadening of the front of the OTOC is summarized in Fig. 9-2. Again, we conjecture that these universal scaling forms extend to nonintegrable models with time-independent Hamiltonians, although we note that a previous calculation in a different setting has instead found a front that does not broaden with time, and is governed by a traveling wave equation [230] (see also [236, 237]). (A traveling wave equation arises from our mappings if we make a certain mean

---

[1] Strongly disordered Hamiltonians in 1+1D provide counterexamples to this ballistic spreading.

[2] The phase diagram of the KPZ equation in higher dimensions [82] indicates that in 4+1D and above, two distinct universality classes may be possible for operator growth in a random circuit, one with a growing front width and one without.

d	α
1	1/2
2	1/3
3	0.24
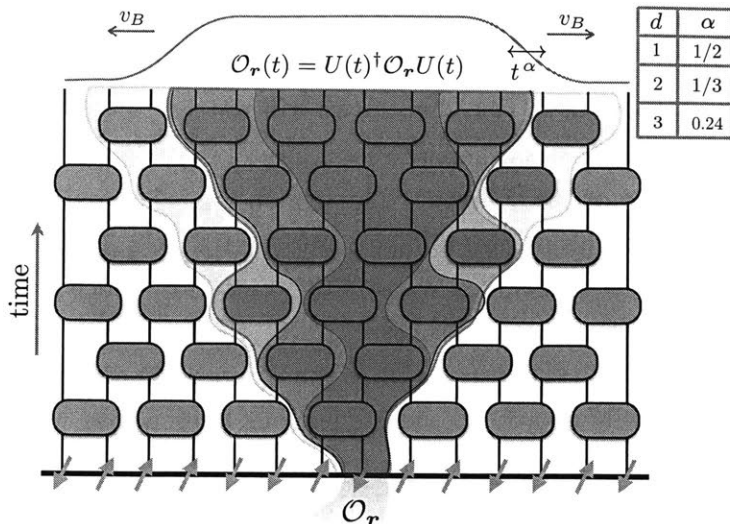
Figure 9-2: **"Operator Spreading" and the Schematic Behavior of the OTOC:** We find that the average OTOC $\overline{\mathcal{C}}(x,t)$ (where the average is over the local unitaries in the quantum circuit) has a front which broadens as t^α, with the indicated exponents in various spatial dimensions d.

field treatment, Appendix. E.9. But this mean field is not valid in physical dimensionalities.)

In higher dimensions the *shape* of the spreading operator[3] is also of interest. At first sight one might expect the shape of the operator to be asymptotically spherical at late times. Instead, we argue that in systems with an underlying lattice, which have only discrete spatial symmetries, the spreading operator will not become spherical. Its asymptotic shape is determined by a model-specific velocity function $v_B(\hat{n})$, the speed of the front depending on the local normal vector $\hat{n}$. We verify this for random circuits by simulation in 2+1D.

The results above are for random circuits composed of generic (Haar-random) unitary matrices. It is interesting to compare with random circuits composed of unitaries from the Clifford group, a discrete subgroup which leads to efficiently simulable dynamics [271, 272]. In this case the dynamics of the operator is much simpler [9], and randomness-induced fluctuations are much more severe. But remarkably the results for the *averaged* OTOC $\overline{\mathcal{C}}$ coincide with the results for generic unitaries. This is a consequence of the fact that the Clifford group is a unitary 2-design [273].

In one dimension we give a complementary exact calculation of the averaged OTOC, using a mapping to the partition function of a classical Ising model. These Ising degrees of freedom have a similar origin to those found in calculations in random tensor networks [274]. We show that special structure arising from the unitarity of the quantum circuit means that this partition function is exactly calculable for any value of the local Hilbert space dimension.

Another important question is how the speed v_B associated with operator spreading relates

---

[3]That is, the shape of the spatial region in which $\mathcal{C}$ has saturated. We can neglect here the broadening of the front, since at late times the length scale associated with this broadening is parametrically smaller than the size of the operator.
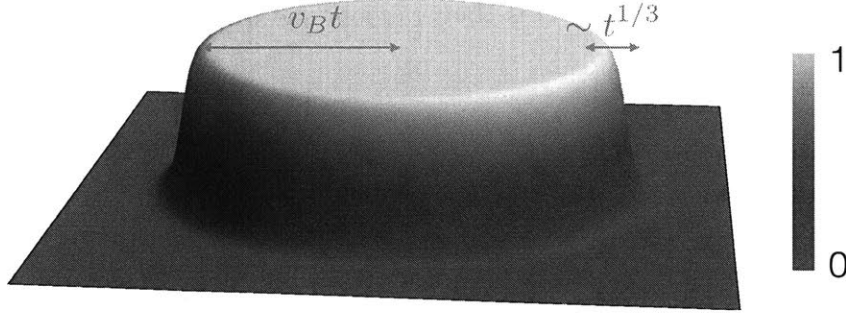
Figure 9-3: **Cartoon for the form proposed here for the OTOC in two spatial dimensions,** when lattice anisotropy can be neglected. The functional form is given by the Tracy Widom distribution F_2.

to the speed v_E which can be associated with entanglement growth following a quench in 1D [50, 51, 52, 62, 213, 53, 77, 64, 214, 9]. Refs. [9, 214] pointed out that in general v_E is smaller than v_B, unlike the situation in a 1D conformal field theory [52]. We extend this here, showing that arbitrarily small values of v_E/v_B can be achieved without fine-tuning.

We also use the Ising mapping described above to give an exact calculation of the average entanglement purity [275, 276, 277] (the exponential of the second Renyi entropy) for a random circuit, complementing the scaling picture, in terms of a coarse-grained minimal cut, of Ref. [9].

9.1 Operator dynamics in 1+1D

We begin by defining the random circuit dynamics which we consider in 1+1D, and describing the 'hydrodynamic' continuum picture we propose for the OTOC in 1+1D. In Sec. 9.3 we give an alternative exact calculation of the OTOC, confirming and extending the results below.

9.1.1 Hydrodynamic equation for averaged OTOC

We consider time evolution by a quantum circuit on an infinite 1D spin chain where each spin (qudit) has local Hilbert space dimension q. The structure of the quantum circuit is shown in Fig. 9-2a. Two-site unitaries are applied to 'even' bonds on even time steps and 'odd' bonds on odd time steps (a 'running bond' layout in the language of bricklaying). Each two-site unitary is drawn independently from the uniform distribution on the two-site unitary group $\mathbb{U}(q^2)$. Formally, our time evolution operator is $U(t) = U(t, t-1)U(t-1, t-2) \cdots U(1, 0)$, where a single layer of the circuit is given by

$$U(t', t'-1) = \begin{cases} \displaystyle\bigotimes_{x \in 2\mathbb{Z}} U_{x,x+1}(t', t'-1) & \text{if } t' \text{ is even,} \\ \displaystyle\bigotimes_{x \in 2\mathbb{Z}+1} U_{x,x+1}(t', t'-1) & \text{if } t' \text{ is odd.} \end{cases} \tag{9.3}$$

Each two-site unitary $U_{x,x+1}(t', t'-1)$ is Haar random and independent of all of the others.

Given an operator $\mathcal{O}$, we write $\mathcal{O}(t) = U(t)^\dagger \mathcal{O} U(t)$. We will evaluate the following out-of-time order correlator with respect to this time evolution:

$$\mathcal{C}(x,t) \equiv \frac{1}{2} \operatorname{Tr} \rho_\infty [X_0(t), Y_x]^\dagger [X_0(t), Y_x] = -\frac{1}{2} \operatorname{Tr} \rho_\infty [X_0(t), Y_x]^2. \tag{9.4}$$

Here, ρ_∞ is the infinite temperature Gibbs state, i.e., the mixture of all possible spin configurations with equal weights. X_0 is a Hermitian operator located at the origin of the spin chain, and Y_x is a Hermitian operator located at site x. We take both X and Y to be traceless, and normalized such that $\operatorname{Tr} X^2 = \operatorname{Tr} Y^2 = q$. For example if $q = 2$ (the spin–1/2 chain) we can take X and Y to be Pauli matrices at sites 0 and x, respectively.

Since the unitaries in the circuit are random, we must distinguish between averaged quantities (denoted by $\mathbb{E}_U$, or whenever unambiguous by an overline $\overline{[\cdots]}$) and quantities within a given realization of randomness. However, we will argue that fluctuations induced by the random circuit are small, meaning that the spatial profile of $\mathcal{C}(x,t)$ in a given realization of the circuit is, at large times, parametrically close to the average value $\overline{\mathcal{C}(x,t)}$. Fig. 9-2 is a schematic of the spatial profile we will show for $\overline{\mathcal{C}(x,t)}$ at fixed large time. The 'size' of the operator is determined by a butterfly speed which is

$$v_B(q) = \frac{q^2 - 1}{q^2 + 1}. \tag{9.5}$$

Within a region of size $\sim 2v_B(q)t$ the commutator $\mathcal{C}(x)$ has saturated to a value very close to unity. Note that for finite q the butterfly velocity is smaller than the 'naive' speed limit of unity, which is set by the geometry of the quantum circuit, while in the limit $q \to \infty$ they coincide. The 'front' of the operator, i.e. the region in which $\mathcal{C}$ varies between 0 and 1, broadens diffusively. The width of the front is proportional to

$$\sigma(q,t) = \frac{2q}{q^2 + 1} \sqrt{t}. \tag{9.6}$$

More precisely, letting Φ denote the error function (the cumulative density function of the Gaussian distribution, $\Phi(y) = \frac{1}{\sqrt{2\pi}} \int_{-\infty}^y e^{-x^2/2} dx$, which tends to zero for $y \ll 0$ and to 1 for $y \gg 0$), we have

$$\overline{\mathcal{C}(x,t)} \simeq \Phi\left(\frac{v_B t + x}{\sigma(t)}\right) \Phi\left(\frac{v_B t - x}{\sigma(t)}\right). \tag{9.7}$$

In Sec. 9.3 we will see that Eq. (9.7) is the partition function of an Ising-like statistical mechanics

problem, and will derive an exact formula on the lattice:

$$\overline{\mathcal{C}(x,t)} = (1-\xi)\, g\left(t-1, \frac{t-x-3}{2}, p\right)\, g\left(t-1, \frac{t+x-3}{2}, p\right)$$
$$+ \xi\, g\left(t-1, \frac{t-x-1}{2}, p\right)\, g\left(t-1, \frac{t+x-1}{2}, p\right), \tag{9.8}$$

where $p = 1/(q^2+1)$, and $\xi = q^4/(q^4-1)$, while

$$g(n,a,p) = \sum_{k=0}^{a} \binom{n}{k}(1-p)^{n-k} p^k.$$

Here we show how Eq. (9.7) can be related to a continuum hydrodynamic equation which is asymptotically accurate at large times. For x near the operator's right hand front, $\mathcal{C}$ is related to a diffusing conserved density ρ, i.e.

$$\overline{\mathcal{C}}(x,t) = \int_x \mathrm{d}x'\, \overline{\rho}(x',t), \tag{9.9}$$

with

$$\partial_t \overline{\rho}(x,t) = v_B(q)\partial_x \overline{\rho}(x,t) + D(q)\partial_x^2 \overline{\rho}(x,t). \tag{9.10}$$

We will explain the quantity ρ below.

We begin by focusing on the spin–1/2 chain ($q=2$). At time t we may write the operator in the basis of products of Pauli matrices [256, 64, 214, 221, 222],

$$X_0(t) = \sum_{\mathcal{S}} a_{\mathcal{S}}(t)\mathcal{S} \tag{9.11}$$

where $X_0(t=0)$ is a single site operator. Here the 'string' $\mathcal{S}$ can be any product of Pauli matrices on distinct sites. The number of strings in the sum generically grows exponentially with time (at the naive lightcone velocity, set by the geometry of the circuit). The $\mathcal{S}$ are normalized as

$$\mathrm{Tr}\,\rho_\infty \mathcal{S}\mathcal{S}' = \delta_{\mathcal{S}\mathcal{S}'}, \tag{9.12}$$

and X_0 is also normalized so $\mathrm{Tr}\,\rho_\infty X_0^2 = 1$, implying

$$\sum_{\mathcal{S}} a_{\mathcal{S}}(t)^2 = 1. \tag{9.13}$$

It is useful also to introduce $\rho(x,t)$, the 'fraction' of strings ending at x:

$$\rho(x,t) = \sum_{\substack{\text{strings } \mathcal{S} \\ \text{ending at } x}} a_{\mathcal{S}}(t)^2, \qquad\qquad \sum_x \rho(x,t) = 1. \tag{9.14}$$

187

We observe that the OTOC is determined by $a_{\mathcal{S}}(t)^2$ as follows. Let Y_x be the Pauli matrix σ^y at site x. (This choice does not sacrifice generality due to Haar randomness of the circuit.) Since distinct Pauli matrices anti-commute, we see

$$[X_0(t), Y_x]^2 = \left(\sum_{\mathcal{S}} a_{\mathcal{S}}(t)[\mathcal{S}, Y_x] \right)^2 = \left(\sum_{\mathcal{S}:\mathcal{S}_x = \sigma^y, \sigma^z} 2 a_{\mathcal{S}}(t) \mathcal{S} Y_x \right)^2. \tag{9.15}$$

Due to the orthonormality in Eq. (9.12), we have

$$\mathcal{C} = -\frac{1}{2} \operatorname{Tr} \rho_\infty [X_0(t), Y_x]^2 = \sum_{\mathcal{S}:\mathcal{S}_x = \sigma^y, \sigma^z} 2 a_{\mathcal{S}}(t)^2. \tag{9.16}$$

This tells us that if we determine the evolution of $\overline{a_{\mathcal{S}}(t)^2}$, then the averaged OTOC is also determined. The dynamics of $\overline{a_{\mathcal{S}}(t)^2}$ turns out to be remarkably simple, as shown in Refs. [221, 222]. It is best understood if we first consider a system of just two sites (rather than an infinite chain) over which a Haar random unitary is applied at time t. It is straightforward to calculate (see Appendix E.1) that for arbitrary q

$$\overline{a_{\mathcal{S}'}(t+1)^2} = \sum_{\mathcal{S}} W_{\mathcal{S}'\mathcal{S}} \, \overline{a_{\mathcal{S}}(t)^2} \tag{9.17}$$

where

$$W_{\mathcal{S}'\mathcal{S}} = \delta_{\mathcal{S}',I} \delta_{\mathcal{S},I} + \frac{1}{q^4 - 1}(1 - \delta_{\mathcal{S}',I})(1 - \delta_{\mathcal{S},I}). \tag{9.18}$$

Note two features. First, the result is linear in $\overline{a_{\mathcal{S}}(t)^2}$. Second, $\mathcal{S}'$ must be the identity if and only if $\mathcal{S}$ is, but otherwise $\overline{a_{\mathcal{S}'}(t+1)}$ is a constant for all $\mathcal{S}' \neq I$. In other words, the random unitary introduces a (fictitious) Markov process on the probabilistic ensemble $\{(\mathcal{S}, \overline{a_{\mathcal{S}}(t)^2})\}$ of strings [221, 222]. This Markov process describes a single string $\mathcal{S}$ which is stochastically updated over time. If $\mathcal{S}$ is nontrivial, each update maps it to any nontrivial string, with uniform probability. The generalization to multiple spins is immediate: for each pair of spins that interact in a given timestep, the stochastic update is applied to the corresponding two-site substring of $\mathcal{S}$. This Markov process will also be used in higher dimensional setting below, as it is not specific to the 1+1D setting. Note that the fictitious stochastic dynamics, which involves a single evolving string, is entirely different from the stochastic dynamics of the operator $X_0(t)$ itself (which is a superposition of exponentially many strings).

Returning to the average of the OTOC, we realize that it only matters whether or not the string component of $X_0(t)$ at the site x is the identity. In the ensemble $\{(\mathcal{S}, a_{\mathcal{S}}(t)^2)\}$, the fraction

$$\mu(x, t) = \sum_{\mathcal{S}:\mathcal{S}_x \neq I} a_{\mathcal{S}}(t)^2 \tag{9.19}$$

of strings that occupy the site x, may fail to commute with Y_x. There are $q^2 - 1$ possible nontrivial operators at the the site, which are all equally probable in the ensemble of string components of $X_0(t)$. In the present case of $q = 2$, this yields[4]

$$\overline{\mathcal{C}(x,t)} = \frac{q^2}{q^2 - 1}\, \overline{\mu(x,t)} \tag{9.20}$$

In turn, the average occupation number $\mu(x,t)$ can be related to the endpoint density ρ, assuming that x is far to the right of the left-hand front of the operator:

$$\overline{\mu(x,t)} = \mu_0 \sum_{x' \geq x} \overline{\rho(x',t)}, \qquad\qquad \mu_0 = \frac{q^2 - 1}{q^2} \tag{9.21}$$

The constant of proportionality μ_0 has been determined by assuming local equilibration of the structure of the strings.[5] Therefore

$$\overline{\mathcal{C}(x,t)} = \sum_{x' \geq x} \overline{\rho(x',t)}. \tag{9.22}$$

It is natural to conjecture that local equilibration of the strings, together with the exponentially large number of strings contributing to ρ, will make this identity valid asymptotically even without the average.

It remains to analyze the dynamics of $\overline{\rho}(x,t)$. The above Markov process implies a simple autonomous dynamics for $\overline{\rho}$:

$$\overline{\rho(t+1,x)} = p \left[\overline{\rho(x,t)} + \overline{\rho(t,x+1)} \right],$$
$$\overline{\rho(t+1,x+1)} = (1-p) \left[\overline{\rho(x,t)} + \overline{\rho(t,x+1)} \right], \tag{9.23}$$

where

$$p = \frac{q^2 - 1}{q^4 - 1} = \frac{1}{q^2 + 1} \tag{9.24}$$

is calculated by counting the non-identity two-site operators S that have the identity at $x + 1$, and the overline denotes averaging over unitaries applied up to a given time.

Recalling that unitaries are applied on even and odd bonds alternately, Eq. 9.23 gives a

---

[4] For general q, one has to start with an operator basis that obeys our normalization condition in Eq. (9.12). It is easy to construct such a basis. Define $X = \sum_{k \in \mathbb{Z}_q} |k+1\rangle \langle k|$ and $Z = \sum_{k \in \mathbb{Z}_q} e^{2\pi i k/q} |k\rangle \langle k|$. Then, the discrete group generated by these two matrices contains exactly q^2 elements up to unimportant phase factors. These are not hermitian, but no problem arises if one considers $|a_S|^2$. Over Haar random unitaries, one easily obtains $\overline{\mathcal{C}(x,t)} = \frac{q^2}{q^2 - 1} \overline{\mu(x,t)}$.

[5] To find μ_0, make the ansatz that each $\mu(x)$ is independent from $\mu(x')$ for $x \neq x'$. Under this ansatz, the probability that a pair of sites is partially or fully occupied is $1 - (1 - \mu_0)^2$, and such an occupied pair evolves to fill one of the pair with probability $1 - p$. Therefore, setting $\mu_0 = (1-p)(2\mu_0 - \mu_0^2) = \frac{q^2 - 1}{q^2}$ yields the stationary state.

complete description of the dynamics of $\overline{\rho(x,t)}$. This is a lattice diffusion equation for the conserved density $\bar{\rho}$. Formally, $\bar{\rho}$ behaves like the probability density for a random walker who starts at the origin, and who prefers to travel to the right since $p < \frac{1}{2}$. In the continuum (i.e. at long timescales) $\bar{\rho}$ satisfies a simple diffusion equation,

$$\partial_t \overline{\rho(x,t)} = v_B(q)\partial_x \overline{\rho(x,t)} + D(q)\partial_x^2 \overline{\rho(x,t)}, \tag{9.25}$$

whose drift and diffusion constants are determined in Appendix. E.2:

$$v_B(q) = \frac{q^2 - 1}{q^2 + 1}, \qquad\qquad D(q) = \frac{2q^2}{(q^2 + 1)^2}. \tag{9.26}$$

The peak in ρ corresponds to the front of the spreading operator $X_0(t)$. It travels at speed $v_B(q)$ and broadens as $\sigma(q,t)$ (Eq. 9.6). We emphasize that this fictitious random walker should not be thought of as 'the endpoint' of the operator $X_0(t)$, which is a superposition of many strings with different endpoints.

From (9.22), or in the continuum

$$\overline{\mathcal{C}(x,t)} = \int_x \mathrm{d}x' \overline{\rho(x',t)} \tag{9.27}$$

we see that $\overline{\mathcal{C}}$ obeys the same equation as $\overline{\rho(x,t)}$ but with different boundary conditions,

$$\partial_t \overline{\mathcal{C}(x,t)} = v_B(q)\partial_x \overline{\mathcal{C}(x,t)} + D(q)\partial_x^2 \overline{\mathcal{C}(x,t)}. \tag{9.28}$$

Taking into account the similar behaviour at the left hand front gives (9.7).

Above we had to make two (very natural) assumptions. One was that we can ignore the interaction between the left end and the right end, and the other was that the occupation density $\overline{\mu(x,t)}$ reaches its equilibrium value. In Section 9.3 we give an exact calculation of the averaged OTOC (including exact results for finite t and x, not necessarily large) without making any approximation.

9.1.2 Hydrodynamic description including fluctuations

Having determined the averaged OTOC, the key question is about the fluctuations between different realizations of the random circuits. From the point of view of exact results this is a much harder question (it is possible to obtain bounds in regions far from the front: we return to this in Sec. 9.3.3). However, we conjecture that the universal physics of fluctuations in $\rho(x,t)$ can be obtained by upgrading Eq. 9.25 to a *stochastic* diffusion equation for the random quantity $\rho(x,t)$. This description indicates that fluctuations are strongly suppressed at late times. Since the diffusive broadening is present in a single realization (i.e. is not an artefact of disorder averaging) it is natural to conjecture that it will also be present in generic non-random 1D many-body systems.

The postulated stochastic diffusion equation may contain noise in both the diffusion constant and the drift, but we restrict to noise in the latter since it is more relevant in the RG sense:

$$\partial_t \rho(x,t) = \partial_x \left(v_B + \eta(x,t) \right) \rho(x,t) + D \partial_x^2 \rho(x,t). \tag{9.29}$$

Here $\eta(x,t)$ is white noise, uncorrelated in space and time.

The statistical properties of this equation are easy to analyze. In the absence of the noisy drift term, $\rho(x,t)$ forms a 'wavepacket' whose width grows like $\sqrt{t}$ and whose center of mass is at $x_{\rm cm} = v_B t$. When the noisy drift is turned on, it induces statistical fluctuations in $x_{\rm cm}$ whose magnitude scales with time as

$$\Delta x_{\rm cm} \sim t^{1/4}. \tag{9.30}$$

A quick way to see this is to ask what the drift velocity has been in a given realization, *averaged* over the spacetime region visited by the wavepacket. The wavepacket visits a spacetime volume of order $\int^t dt' \sqrt{t'} \sim t^{3/2}$. Averaging the drift velocity $\eta(x,t)$ over this spacetime volume yields $v_{\rm av} \sim t^{-3/4}$. The typical random displacement of the wavepacket is thus of order $\Delta x_{\rm cm} \sim v_{\rm av} t \sim t^{1/4}$. A standard perturbative calculation in Appendix E.3 reproduces this exponent $1/4$, which also characterizes the spreading of directed waves in random media [278].

The quantity $\Delta x_{\rm cm}$ is parametrically smaller than $\sqrt{t}$, the width of the front of the averaged commutator. Therefore this heuristic argument indicates that the front profile of the averaged OTOC also applies to the OTOC within a given instance of the random circuit. This is somewhat surprising. To see why, let us contrast the above Haar random dynamics with Clifford dynamics for $q = 2$.

9.1.3 Comparison with Clifford Circuit Dynamics

The Clifford group is a discrete subgroup of the unitary group, defined by the property that any Pauli matrix is mapped to a product of Pauli matrices. When the quantum circuit consists of Clifford operators, an initial Pauli matrix remains a single string (rather than evolving into a superposition of exponentially many strings as for dynamics with generic unitaries) and at any given time the endpoint density $\rho(x,t)$ is localized on a single site.

However, uniformly random Clifford circuits have a crucial relationship with Haar random circuits. Under a uniformly random Clifford update on a pair of sites, a nontrivial operator is mapped with equal probability to any of the nontrivial operators, and thus the dynamics satisfies the master equation of the Markov process in Eq. (9.17) [9]. As a result, the *averaged* quantities such as the average end point density $\overline{\rho(x,t)}$, the average occupation number $\overline{\mu(x,t)}$, and, most importantly, the average OTOC $\overline{C(x,t)}$, obey exactly the same dynamics as the Haar random case. Formally, this is a consequence of the fact that random Clifford operators form a unitary 2-design [273]; see Appendix E.4 for the definition of design and a proof for random Clifford. One may say that Clifford dynamics realizes the *a priori*-fictitious Markov process in

a physical system.[6]

Despite the equivalence of averaged quantities, the quantities *within* a realization are entirely different. In the Clifford case the endpoint density ρ and the OTOC $\mathcal{C}$ are strongly fluctuating, while we have argued that for generic unitaries they are self-averaging (fluctuations are parametrically small).

9.2 Higher dimensions

We now address the structure of the out of time order correlator $\mathcal{C}(x,t)$ in spatial dimensions greater than one, by exploiting the relationship between the averaged OTOC and a fictitious classical Markov process (Sec. 9.1.1). We show that this process is a classical droplet growth problem whose universal physics can be understood in terms of the Kardar–Parisi–Zhang equation [82]. By taking appropriate averages, we then obtain exact universal exponents and scaling forms for the OTOC in a circuit composed of Haar random unitary matrices. We conjecture that these scaling forms also apply to more realistic Hamiltonian dynamics in non-integrable lattice models and field theories.

Somewhat surprisingly, we show that the 'shape' of the spreading operator at late times does not become spherical, unless the microscopic dynamics has symmetry under continuous spatial rotations. In a lattice model, the spreading operator remembers forever that the lattice has only discrete point group symmetries. Our argument for this is not specific to random circuit dynamics. The point is simply that 'the' butterfly velocity v_B, which sets the speed at which the operator's front moves, generically depends on the front's orientation, resulting in an anisotropic profile for the spreading operator at long times. Another surprising outcome, given previous work in the context of many-body perturbation theory including Ref. [230], is that for the dynamics considered here the averaged OTOC $\overline{\mathcal{C}}$ does not satisfy a local differential equation.

In 2+1D, when lattice anisotropy is absent (e.g. in an appropriate continuum model) or negligible, recent results in KPZ theory [258, 259, 260, 261, 262, 263, 264, 265, 266, 267, 268, 269, 270] yield the the full functional form of $\overline{\mathcal{C}(x,t)}$ as a function of position and time. For an initially localized operator, this is expressed in terms of the GUE Tracy Widom distribution [262, 265] (which describes the extremal eigenvalue statistics for the Gaussian Unitary Ensemble of Hermitian matrices [279, 280]).

9.2.1 Higher dimensions: Setup & Mapping to Classical Growth

We now describe the unitary dynamics for which we wish to study operator spreading and the OTOC. We choose a circuit where in each timestep Haar-random two-site unitaries are applied to bonds of a d-dimensional cubic lattice in a manner that generalizes the 1+1D protocol. We describe the 2+1D case for concreteness; the generalization to higher dimensions is immediate.

---

[6] All the statements here hold for any prime power q such as $q = 2, 3, 4, 5, 7, 8, 9, 11, 13, 16, \ldots$.
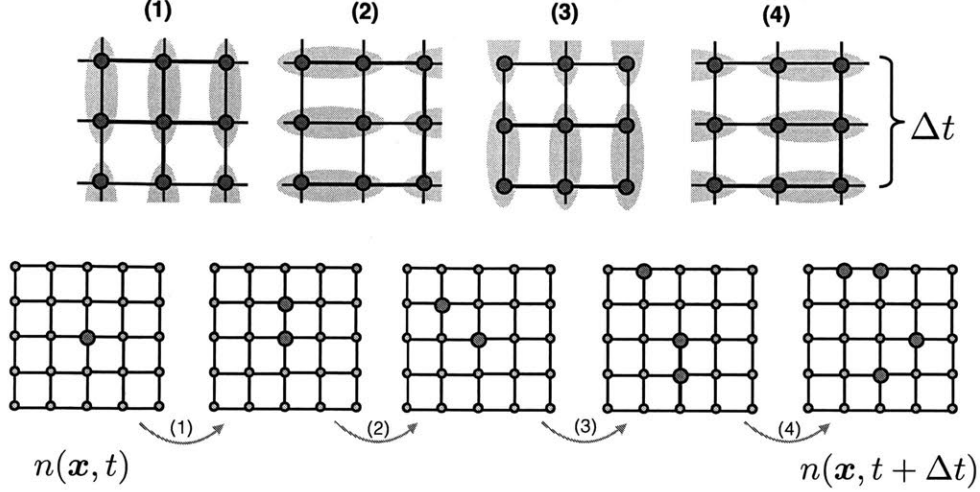
Figure 9-4: **Top: 2+1D Haar-Random Quantum Circuit:** We consider unitary dynamics in which two-site Haar-random unitaries are applied on the bonds of a two-dimensional square lattice, in the columnar dimer configurations shown in (1-4). **Bottom:** allowed updates in the corresponding stochastic process.

The periodicity of the circuit is 4 layers. Four successive layers cycle through the four columnar 'dimer coverings' of the square lattice as shown schematically in Fig. 9-4 and Fig. 9-1b, so that the site at the origin interacts sequentially with its neighbours at $\boldsymbol{x} = (0,1)$, $(-1,0)$, $(0,-1)$, $(1,0)$.

We relate the dynamics of $\overline{\mathcal{C}}$ to a fictitious classical stochastic process for a growing cluster, described by the evolution of 'occupation numbers'

$$n(\boldsymbol{x}) = 0 \text{ or } 1 \tag{9.31}$$

at each site. These arise from the higher-dimensional generalization of the one-dimensional stochastic process for an evolving string $\mathcal{S}$ described in Sec. 9.1, in which we define the string's occupation number $n(\boldsymbol{x})$ to be 1 if the string has support on site $\boldsymbol{x}$ and zero otherwise. The effective stochastic process for these occupation numbers is simple (Appendix E.1). Consider two adjacent sites $\boldsymbol{x}$ and $\boldsymbol{y}$ which undergo a joint update in a given timestep. If both sites are initially empty $(n(\boldsymbol{x}) = n(\boldsymbol{y}) = 0)$ they remain so after the update. If at least one of the sites is initially occupied $(n(\boldsymbol{x}) = 1$ or $n(\boldsymbol{y}) = 1$ or both) then the configuration after the update can be $n(\boldsymbol{x}) = 1$, $n(\boldsymbol{y}) = 0$ with probability p, or $n(\boldsymbol{x}) = 0$, $n(\boldsymbol{y}) = 1$ with the same probability, or $n(\boldsymbol{x}) = n(\boldsymbol{y}) = 1$ with probability $1 - 2p$, where as before

$$p = \frac{1}{q^2 + 1}. \tag{9.32}$$

If we consider the OTOC for a spreading operator which is initially localized at a single site, then the corresponding classical model is initialized with $n = 1$ at the origin and $n = 0$ everywhere

193
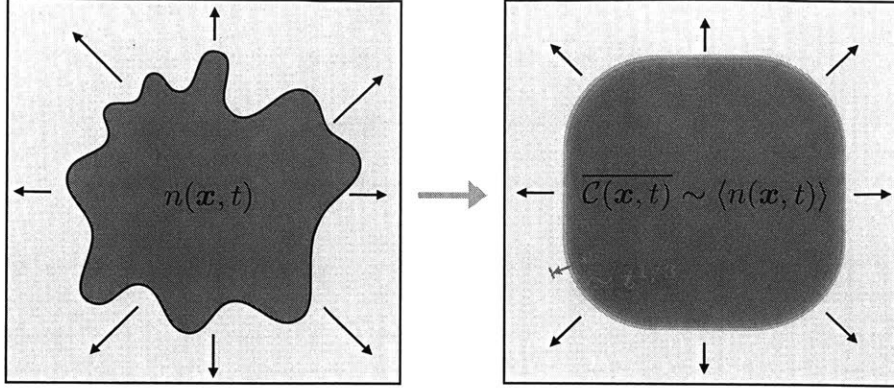
Figure 9-5: **Growth of a Classical Droplet and the OTOC:** We relate the behavior of the OTOC (averaged over the unitaries in the circuit) to a classical stochastic process for the growth of a droplet in two spatial dimensions. A given configuration of the classical droplet is specified by a binary occupation number $n(\boldsymbol{x}, t)$ as shown the left. Remarkably, the average droplet profile $\langle n(\boldsymbol{x}, t)\rangle$ precisely reproduces the averaged OTOC.

else. A possible evolution of $n(\boldsymbol{x})$ in a single timestep is shown in Fig. 9-4.

The Haar-avaraged OTOC is related to the mean occupation number for this Markov process at time t by the relation

$$\overline{\mathcal{C}(\boldsymbol{x}, t)} = \frac{q^2}{q^2 - 1} \langle n(x, t)\rangle_{\text{classical}} \tag{9.33}$$

as illustrated schematically in Fig. 9-5. The averages on the two sides of the above equation have different meanings. On the left, the bar denotes an average over realizations of a unitary circuit, and $\mathcal{C}$ is a correlator for this quantum dynamics. On the right, the angle brackets denote an average in a classical stochastic process. The real number $\mathcal{C}$ and the integer n are only related after averaging. (As we noted above, the fictitious Markov process can be physically realized by random Clifford dynamics, whenever q is a prime power.)

9.2.2 Classical model in 2+1D: Analytical & Numerical Results

The 'seed' at the origin grows to produce a cluster of linear size $\sim t$. In the interior of this cluster the state equilibrates rapidly to a state in which nearby sites are essentially uncorrelated, with average occupation $\langle n(x, t)\rangle_{\text{classical}} = (q^2 - 1)/q^2$. In a given realization there is an interface between the occupied and unoccupied regions which is sharp on length-scales of the order of the lattice spacing. The evolution of the droplet is very similar to well-studied growth models such as the Eden model [281], and reduces to the stochastic growth of this one-dimensional interface. The size of the occupied region grows linearly in time, with statistical fluctuations in the shape of the interface. (The average shape in our 2D model is not circular, but has only four-fold rotational symmetry; we discuss this in Sec. 9.2.5.)

194

Typically such interface growth processes are in the universality class of the Kardar-Parisi-Zhang (KPZ) equation [82]. Consider a section of the interface, with ξ a coordinate parallel to the interface and h its height in the perpendicular direction. The KPZ equation is

$$\partial_t h = c + \nu \partial_\xi^2 h + \frac{\lambda}{2}(\partial_\xi h)^2 + \zeta(x,t), \qquad (9.34)$$

where ζ is uncorrelated spatiotemporal noise. The constant c contributes to the average normal growth rate for the interface, while the ν term describes diffusive smoothing of sharp features. Finally, the non-linear λ term encodes the dependence of average growth rate on the slope. (In the present setting, lattice symmetry also allows a term $\propto \partial_\xi h$ if the ξ axis is at a generic angle to the lattice axes. This term may be removed by a coordinate boost.) The KPZ equation renormalizes to a nontrivial fixed point. One of its most basic properties is the fact that the fluctuations in the height at a given position ξ grow with time as t^β, with $\beta = 1/3$.

The KPZ description above is justified on RG grounds, assuming that the relevant length-scales for the fluctuations of the classical interface are much larger than the lattice spacing. (See Ref. [282] for a review of lattice growth models.) We will show numerically that KPZ scaling does indeed apply to the growing droplet, so long as the front is not locally parallel to the lattice axes, where — as a result of the discrete spacetime geometry we have chosen — an additional effect can come into play. (We expect this additional subtlety to be absent in models in continuous time.)

Let us write the shape of the droplet as a parameterized curve in polar coordinates, with $R(\theta)$ the radius at angle θ from the origin. (As mentioned above, the interface is sharp on an $O(1)$ lengthscale, and therefore $R(\theta)$ is well defined up to an $O(1)$ uncertainty; this is sufficient since the properties we discuss below are on parametrically larger lengthscales when t is large.) From KPZ scaling we would expect

$$\langle R(\theta, t) \rangle = r(\theta)\, t - A(\theta) t^\beta + \cdots \qquad (9.35)$$

$$\sqrt{\langle R(\theta,t)^2 \rangle - \langle R(\theta,t) \rangle^2} = C(\theta)\, t^\beta + \cdots \qquad (9.36)$$

with the exactly-known exponent $\beta = 1/3$. We will discuss the nonuniversal function $r(\theta)$ below and in Sec. 9.2.5, and we will discuss more detailed universal properties in the next section.

We have examined the growth of the droplet for spin-1/2 degrees of freedom ($q = 2$) on the square lattice, by tracking the average, evolving support of a cluster over $M = 2 \times 10^3$ realizations of the classical dynamics up to time $t = 1000$. We store only the density $\langle n(x,t) \rangle$, averaged over all M realizations, as a function of position and time, as this is the quantity with a direct interpretation in the quantum setting. We have also investigated smaller values of q: these do not have an interpretation in the quantum circuit, but in the classical model decreasing q simply corresponds to increasing the probability p in the update. Taking $q < 2$ is a convenient way to explore two regimes (discussed below) which differ in the properties of a lattice-aligned
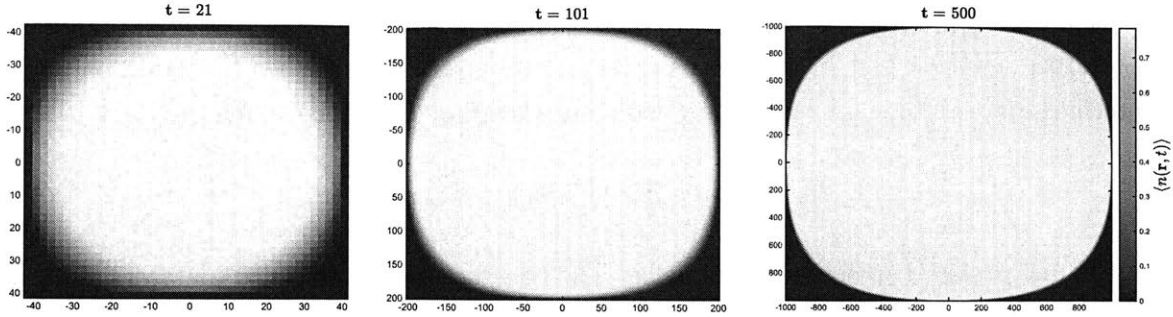
Figure 9-6: **Growth of a 2D Cluster ($q = 2$):** We determine the behavior of the averaged OTOC by simulating the stochastic growth of a two-dimensional cluster over $M = 2 \times 10^3$ realizations, with local updates applied at each timestep, as described in the text. The average occupation number for the cluster $\langle n(\boldsymbol{x}, t) \rangle$ is shown for the indicated times in the evolution as it approaches its asymptotic shape.

front; both regimes could also be accessed at fixed q, say $q = 2$, by varying other parameters in the random circuit such as the circuit geometry.

At each time slice, the form of $\langle n(\boldsymbol{x}, t) \rangle$ is fitted, along cuts through lattice symmetry axes, to extract the cluster size and the the width of the front (where $\langle n(\boldsymbol{x}, t) \rangle$ is appreciably different both from zero and from its $t \to \infty$ value). We observe linear growth of the size as expected. Note that the fluctuations in the second equation of (9.35) imply that the width of the front region is expected to scale like $t^{1/3}$.

Fig. 9-7 (top) shows the growing width of the front for cuts along the diagonal, $\theta = \pm\pi/4$. There, at the largest times we can access, the fitted exponent is $\beta = 0.3305 \pm 0.0269$, extracted from a fit to the blue data points in Fig. 9-7. As expected, this value is consistent with the KPZ value $\beta = 1/3$.

A slight surprise is that the behaviour along the axis, e.g. at $\theta = 0$ is rather different: see Fig. 9-7 (bottom), which does not show KPZ growth. Generically the only stable fixed point for the growth of a 1D interface is believed to be the KPZ fixed point. However anomalous growth is possible in this model, for q greater than a critical value $q_c \lesssim 2$, when the direction of the front's local normal vector is fine-tuned to coincide with one of the axes, as occurs at $\theta = 0$. In this regime, a front with normal parallel to a lattice axis moves at a speed exactly equal to the naive light-cone speed, $v_B = 2$, and does not roughen. This is a known phenomenon in various lattice growth models in discrete time which have synchronous parallel updates, and can be understood by a relationship with directed percolation [283, 284, 285, 286, 287]: see Appendix. E.5 for an explanation. While interesting, this phenomenon is an artefact of the specific discrete spacetime geometry we have chosen, which could be eliminated by modifying this geometry,[7] and we certainly do not expect it to be relevant to continuous time dynamics. (It would be interesting to look for this effect in appropriate deterministic Floquet dynamics,

---

[7]The effect disappears for smaller q. For example for $q = 1.4$ we see clear KPZ growth both at $\theta = 0$ (fitted exponent value $\beta = 0.3223 \pm 0.0199$) and at $\theta = \pi/4$ ($\beta = 0.3304 \pm 0.0149$).

196
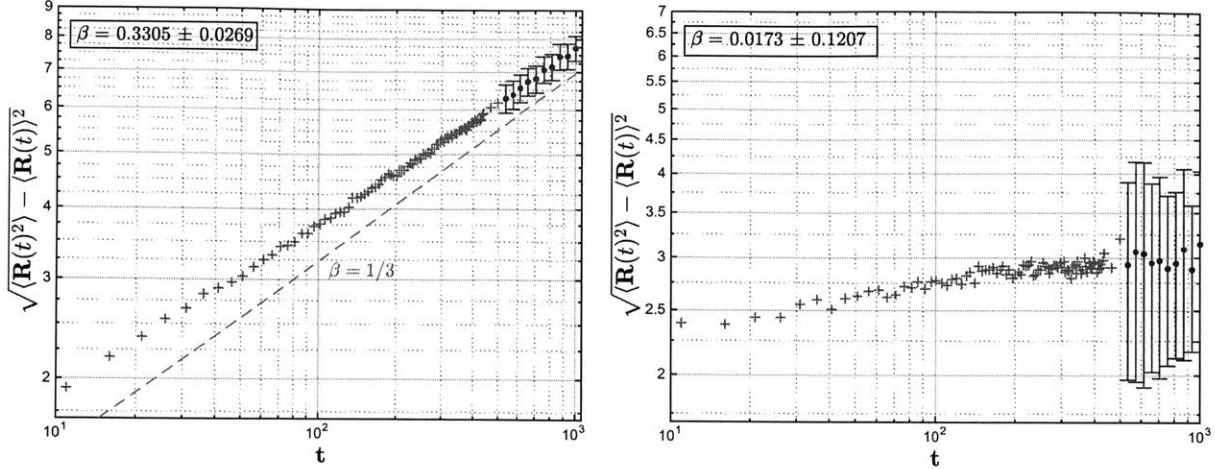
Figure 9-7: **Fluctuation Exponent** β: We fit the profile of the evolving droplet for $q = 2$ along the $\theta = \pm\pi/4$ directions (top) to extract the mean operator size and magnitude of the fluctuations about the mean. The fluctuations exhibit power-law growth with exponent $\beta = 0.3305 \pm 0.0269$, consistent with the KPZ value $\beta = 1/3$. When fitting the profile along $\theta = 0$ (bottom), we observe no appreciable growth of the fluctuations; we argue in Appendix E.5 that this occurs for sufficiently large q when the front's local normal vector is precisely aligned with a lattice axis (as a result of the specific circuit geometry).

however.) It has an effect on the shape of the droplet, leading to flat 'facets' on the front close to $\theta = 0$, $\pi/2$, π and $3\pi/2$ (Sec. 9.2.5).

We now discuss the OTOC scaling that results from the KPZ mapping, neglecting effects of lattice anisotropy (which we will return to in Sec. 9.2.5).

9.2.3 Scaling of the OTOC in 2+1D

We have already mentioned the basic consequence of KPZ growth, which is the $t^{1/3}$ broadening of the front. But, unusually for a nontrivial fixed point, not only the exact critical exponents but also certain exact scaling functions are known for the growth of an interface in 1D [258, 259, 260, 261, 262, 263, 264, 265, 266, 267, 268, 269, 270] (see [288, 289, 290, 291] for reviews). We can now apply this information to the OTOC to obtain scaling functions which we propose are generic.

To simplify things let us consider a case where lattice anisotropy is absent or very weak, so that the spreading operator is circular and the OTOC depends only on a radial coordinate and time. Weak anisotropy could certainly be engineered in an appropriate random circuit. More importantly, we conjecture that the scaling form below captures universal scaling in realistic rotationally invariant many-body systems and field theories.

For the growth of a droplet, the probability distribution of the interface radius is given by the GUE Tracy Widom distribution [262, 265] (which has been been observed experimentally in striking experiments on the growth of a turbulent domain in liquid crystals [292, 293]). Following

convention we write

$$R(\theta, t) = v_B t + c t^{1/3} \chi(\theta, t), \qquad (9.37)$$

where the non-universal constants v_B and c are of order one, and $\chi(\theta, t)$ is a random variable whose mean and variance are of order one at large times. Focussing on a fixed value of θ, the cumulative probability distribution of χ at a fixed time is t–independent at large times and given by the Tracy Widom distribution F_2:

$$\Pr(\chi < s) = F_2(s). \qquad (9.38)$$

Remarkably, this allows us to fix the full functional form of $\overline{C(x, t)}$ in two dimensions, in the case where lattice anisotropy is absent. In polar coordinates (r, θ), and in the continuum, Eq. 9.33 is

$$\overline{C(r, \theta, t)} = \langle \Theta\left[R(\theta, t) - r\right] \rangle_{\text{classical}}, \qquad (9.39)$$

where Θ is the Heavyside step function. The right hand side is precisely the probability that χ is greater than $(r - v_B t)/c t^{1/3}$. We suppress the θ dependence since we are assuming rotational symmetry:

$$\overline{C(r, t)} = 1 - F_2\left(\frac{r - v_B t}{c\, t^{1/3}}\right). \qquad (9.40)$$

The form of $\overline{C(r, t)}$ is shown in Fig. 9-8. The asymptotic behaviour near the trailing edge, close to saturation, i.e. for $[v_B t - r]/c t^{1/3} \gg 1$, is [294, 295]

$$\overline{C(r, t)} = 1 - b_1 \frac{c^{1/8}\, t^{1/24}}{|r - v_B t|^{1/8}} \exp\left[\frac{(r - v_B t)^3}{12 c^3 t}\right] + \cdots \qquad (9.41)$$

where $b_1 = 2^{1/24} e^{\zeta'(-1)}$ with $\zeta'(-1) \approx -0.165$, the derivative of the Riemann zeta function. Near the leading edge, $[r - v_B t]/c t^{1/3} \gg 1$,

$$\overline{C(r, t)} = \frac{c^{3/2}\, t^{1/2}}{16\pi (r - v_B t)^{3/2}} \exp\left[-\frac{4(r - v_B t)^{3/2}}{3 c^{3/2} t^{1/2}}\right] + \cdots. \qquad (9.42)$$

The former asymptotic expansion of F_2 was achieved only recently [294, 295].

One can also consider operator spreading with other initial conditions. For example we can initialize an operator in a half-plane so that $C(x, t)$ has a straight, rather than a circular, front. The scaling form for $C(x, t)$ will then be given by the Tracy Widom distribution of the Gaussian orthogonal ensemble, denoted F_1. The objects F_1 and F_2 are of fundamental importance in a broad range of mathematical and physical problems and it would be very interesting to see whether any of these connections shed light on operator growth.

It should be noted that the mapping to a classical growth process described above gives
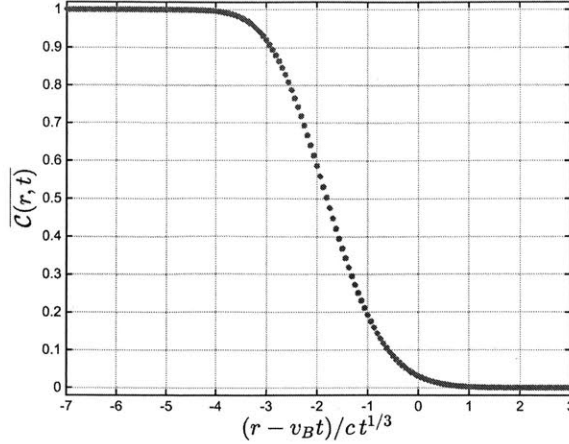
Figure 9-8: The OTOC in (2+1)D: Plot of the front of the averaged OTOC $\overline{\mathcal{C}(r,t)}$ in two spatial dimensions and in the absence of lattice anisotropy, as determined from the exact expression in terms of the Tracy-Widom distribution in the main text.

exact results for the averaged OTOC $\overline{\mathcal{C}}$ but does not immediately give access to the fluctuations in $\mathcal{C}$ between different realizations of the circuit. (These circuit-to-circuit fluctuations in the quantum expectation value should not be confused with the stochastic fluctuations of $n(x)$ in the auxiliary classical model.) A calculation of, say, $\overline{\mathcal{C}^2} - \overline{\mathcal{C}}^2$ would need to go beyond the mapping provided here for $\overline{\mathcal{C}}$. Nevertheless we conjecture that, by analogy with the 1D case described in Sec. 9.1.2, circuit-to-circuit fluctuations in $\mathcal{C}$ are parametrically small at late times whenever the front broadens with time.

9.2.4 Scaling of the OTOC in $3 + 1$D and above

The basic features of the 3+1D case are very similar to those in 2+1D. The KPZ equation extends to an interface of arbitrary dimensionality [82]. For the the 3+1D quantum problem, the dimensionality of the interface is two and the critical exponent β relevant to the width is $\beta \simeq 0.240$ (Ref. [257] and references therein). The analogue of F_2 which yields the universal form of $\overline{\mathcal{C}}$ is not known analytically, but has been determined numerically [291]. Numerical simulations for the 3+1D random circuit, along the lines of those above, would be feasible.

Dimensions equal to or higher than 4+1 are of course inaccessible experimentally, but they are nonetheless interesting because in these high dimensionalities the KPZ equation yields a phase transition as a function of the strength of nonlinearity [82]. Both a rough phase, in which fluctuations grow as t^β with $\beta > 0$, and a smooth phase, where fluctuations remain of order one as $t \to \infty$, exist. It would be interesting to know whether both phases are accessible in appropriate many-body systems.
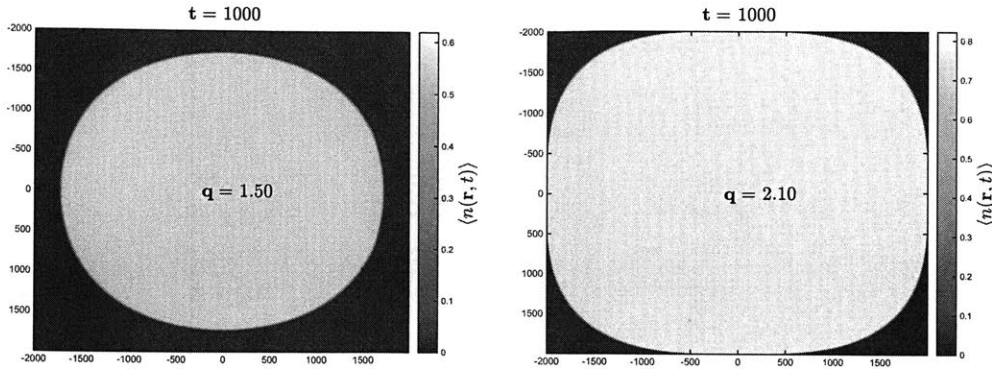
Figure 9-9: **"Faceting" of the Cluster:** Shown are the cluster shapes at fixed time $t = 10^3$, for the indicated values of q. When q is sufficiently large (third panel), the cluster develops "facets" along the $\theta = 0$, π directions, where the normal growth speed is the maximum possible given the circuit geometry. The region shown is the naive light cone.

9.2.5 Shape of the operator at late times

It is interesting to consider the shape of the spreading operator at late times — i.e. the shape of the growing spatial region in which the OTOC $\overline{C(x, t)}$ has already saturated to its late time value (to within an exponentially small correction). Rescaling distances by a factor of t^{-1} gives a 'droplet' of $O(1)$ size, which we expect to reach a fixed asymptotic shape.[8] What is this shape?

At first glance, one might expect that asymptotically the front is a circle in two spatial dimensions and a sphere in higher dimensions. For example, this would be expected if the OTOC satisfied a local nonlinear differential equation in which derivatives higher than 2 could be neglected, as discrete lattice symmetries would ensure that such an equation had symmetry under continuous spatial rotations. Instead, we argue that for many body systems on the lattice the shape of the operator is model-dependent and retains information about the discrete symmetries of the lattice, even at arbitrarily late times. For the random circuit model this follows immediately from the mapping to domain growth processes, for which anisotropy is a well-known feature [296, 297, 298, 299, 300]. Figure. 9-9 shows the shape of the droplet in the present model for various values of q.

For concreteness consider the 2D case (similar statements hold in higher dimensions). The asymptotic droplet shape is described by a radius $R(\theta) = h(\theta)t$ depending on the polar coordinate θ. Since the size of the operator is large at large times, the curvature of the front is parametrically small, except possibly at isolated θ values where $h(\theta)$ is not smooth. Away from such isolated points, the local *velocity* of the front, in the direction of its normal vector, can depend only on the orientation of this local normal vector. This dependence is captured by a velocity function $v_B(\phi)$, where $\phi = \phi(\theta)$ is the angle of the local normal vector to the x-axis. A

---

[8]In this scaling limit the width of the front is negligible.
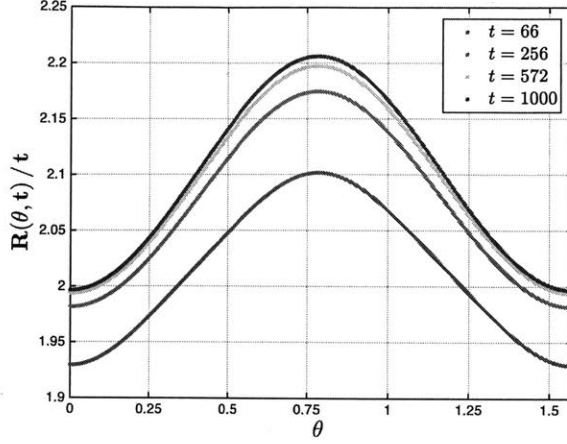
Figure 9-10: **Anisotropy in the Cluster Profile:** Numerically determined anisotropy in the average shape of the 2D cluster $R(\theta,t)/t$, at the indicated times. The anisotropy in the cluster shape grows in time, and appears to asymptote to a non-trivial steady-state shape.

priori $v_B(\phi)$ is constrained only by lattice symmetry; for example on the square lattice

$$v_B(\phi) = v_0 + v_1 \cos 4\phi + v_2 \cos 8\phi + \dots. \tag{9.43}$$

It is evident that the asymptotic shape cannot be a circle except when $v_B(\phi)$ is a constant function. Since the front of the operator advances by $v_B(\phi)dt$ in the normal direction $\hat{n}$, the distance between the front and the origin grows by $v_B(\hat{n})dt/\hat{n}\cdot\hat{r}$, which must be equal to $h(\hat{r})dt$. Expressing the normal vector in terms of h, one obtains

$$v_B(\phi(\theta)) = \frac{h(\theta)^2}{\sqrt{h(\theta)^2 + (\partial_\theta h(\theta))^2}} \tag{9.44}$$

where $\phi(\theta)$ is the angle of the normal at polar position θ on the interface. This equation is solved by a geometrical construction described in Ref. [299, 300]: $h(\theta) = \min_\phi \frac{v_B(\phi)}{\cos(\phi-\theta)}$. When the effect of lattice anisotropy is weak (as is likely to be the case in many realistic situations when the relevant degrees of freedom are long-wavelength modes), we expect $v_B(\phi)$ to be a smooth, weakly varying function, and we may also solve for the shape perturbatively in $w(\phi) = v'_B(\phi)/v_B(\phi)$, as described in Appendix E.6. Restoring the time dependence,

$$R(\theta) = v_B(\theta)\,t\,\exp\left(-\frac{1}{2}w(\theta)^2 + \frac{1}{6}\partial_\theta w(\theta)^3 + \dots\right). \tag{9.45}$$

However when $v_B(\phi)$ varies sufficiently strongly, the asymptotic shape $R(\theta)$ can include sharp corners or straight segments on the boundary: in this regime the perturbative solution above is no longer appropriate.

For many-body systems in continuous time we expect $v_B(\phi)$ to be analytic. In the present lattice model, $v_B(\phi)$ is analytic for $q < q_c$ ($q_c \lesssim 2$) while for $q > q_c$ this function is nonanalytic

near $\phi = 0$ as a result of the anomalous behaviour of a lattice-aligned front: $v_B(\phi) \simeq 2+$const. $|\phi|$ [287]. This leads to flat facets near $\theta = 0$ in the asymptotic shape [287]. This change in the surface morphology as q is varied is shown in Fig. 9-9.

For the random circuit model, it is straightforward to determine $v_B(\theta)$ in the extreme limit $q = \infty$ where growth becomes deterministic. The propagation of the front in this limit is similar to that of the 'next nearest neighbour' deterministic Eden model introduced in Ref. [301] and has the same nonanalytic angular dependence of the velocity[9] [301]:

$$v_B^{q=\infty}(\phi) = 2\left(|\cos\phi| + |\sin\phi|\right).$$ (9.46)

In this limit, the growing operator is simply a square.

Fig. 9-10 shows the angular dependence of the radius for the 2+1D random circuit dynamics at $q = 2$, for several values of the time, showing a clear anisotropy. Note also that $R(\theta = 0) \to 2t$ at late times: the front has a small facet near $\theta = 0$ which moves at the naive lightcone speed for propagation along an axis direction. In the light of our 1D results where, for finite q, v_B is always less than the speed associated with the naive lightcone, it is remarkable that in a higher dimensional circuit it is possible for the OTOC front to propagate at the maximal speed in some directions. However we emphasize that this effect relies on the specific discrete spacetime geometry.

Before returning to 1D, we restate the higher-dimensional results of Sec. 9.2.1 in a more formal language which parallels our discussion in 1D. We introduce a density on clusters, C, where C is a collection of sites:

$$\rho(C) = \sum_{\mathcal{S};\ \mathrm{supp}(\mathcal{S})=C} a_{\mathcal{S}}^2, \qquad\qquad \sum_C \rho(C) = 1.$$ (9.47)

Here supp$(\mathcal{S})$ is the support of $\mathcal{S}$. After coarse-graining, we can represent C by a closed surface of spherical topology, namely the boundary of the coarse-grained cluster. Therefore $\rho(C)$ is the natural analogue of the 'endpoint density' $\rho(x)$ in 1D. The surface growth picture implies that the effective dynamics of $\rho(C)$ are the dynamics of the probability distribution of a growing interface. Therefore, when this is KPZ, $\rho(C)$ satisfies the Fokker-Planck equation corresponding to the KPZ equation. We will discuss this further elsewhere.

9.3   Exact calculation of OTOC in 'spacetime' picture

We now give an analytical treatment of the OTOC from a 'spacetime' point of view. This leads to connections with domain walls in an effective Ising model. Similar Ising degrees of freedom have appeared in work on random tensor networks [274]. Here the effective Ising model looks complicated at first sight, but turns out to be much simpler than those encountered in random

---

[9]This is seen by following the evolution of a front through the four layers comprising the time step.
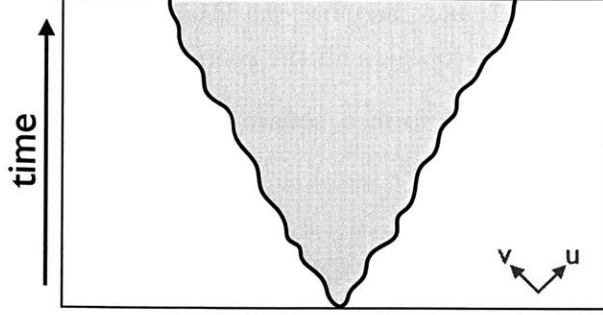
Figure 9-11: The calculation of the OTOC in the spacetime picture leads to a partition function for two nonintersecting directed random walks (domain walls in an effective Ising model). These walks have a bulk energy cost (Eq. 9.67), and a boundary potential (Eq. 9.68) that biases them to a positive and negative velocity respectively. Directions of null coordinates u, v used in the text are indicated.

(non-unitary) tensor networks, due to special structure arising from unitarity. We arrive at a problem of two nonintersecting directed walks, shown schematically in Fig. 9-11.

This spacetime picture may be much more generalizable than the dynamical point of view above. In Sec. 9.4 we will use it to calculate an entanglement–related quantity. In the future, we hope that the tools introduced in this section will be generalizable to higher moments of the OTOC which capture fluctuations ($\overline{C^2}$ etc.), or higher powers of the commutator, or to a direct calculation of the von Neumann entropy. We note that the OTOC is not the only tool for characterizing operator spreading: the operator entanglement entropy of a spreading operator is also of interest [302, 303]. Scaling forms for this quantity will be discussed in Ref. [304].

Our exact result for the OTOC for arbitrary x and t (not necessarily large) is given in Eq. 9.8. There are no approximations in this equation. Approximating g by the cumulative density function $\Phi(y) = \frac{1}{\sqrt{2\pi}} \int_{-\infty}^{y} e^{-x^2/2} dx$ of the Gaussian distribution, we reproduce Eqs. 9.5, 9.6, 9.7 above. This approximation is valid when t is large.

Although the spin chain is spatially infinite in both directions and so is our quantum circuit, the time evolved operator $U^\dagger(t) X_0 U(t)$ is supported only on the interval $[-t, t-1]$ of length $2t$. Therefore, it suffices to consider an observable Y inserted in this interval, and our correlator becomes the trace of a $q^{2t} \times q^{2t}$ matrix. The infinite temperature Gibbs state reduces to the identity matrix divided by the dimension q^{2t}. Expanding the commutator, we see

$$-\frac{1}{2} \operatorname{Tr} \rho_\infty ([U^\dagger(t) X_0 U(t), Y_x])^2 = q^{-2t} \left(\operatorname{Tr}[U^\dagger(t) X_0^2 U(t) Y_x^2] - \operatorname{Tr}[X_0(t) Y_x X_0(t) Y_x] \right)$$
$$= q^{-2t} \operatorname{Tr}[U^\dagger(t) X_0^2 U(t) Y_x^2] - F \qquad (9.48)$$

The Haar average of the first term is easy to evaluate. The observable X_0^2 is conjugated by a unitary $U_{-1,0}(1,0)$ and after taking the Haar average becomes proportional to the identity. The constant of proportionality is fixed by the trace-preserving condition. By the normalization

convention, $\operatorname{Tr} X_0^2 = q = \operatorname{Tr} Y_x^2$, and therefore the Haar average of the first term is equal to $q^{-2t} \operatorname{Tr} I = 1$. The second term F contains all the complexity.

Observe that the local unitaries form a square lattice that is rotated by $45°$. It is thus natural to introduce null coordinates as

$$u := (t + x + 1)/2, \qquad\qquad v := (t - x + 1)/2, \qquad (9.49)$$
$$t = u + v - 1, \qquad\qquad x = u - v. \qquad (9.50)$$

Due to the cylic property of the trace, the only unitaries in the circuit that could affect the correlator are those in the intersection (a rectangle) of the future light cone of X_0 and the past light cone of Y_x. From now on, let us use ℓ_u and ℓ_v to denote the linear sizes of this intersection along u- and v-direction, respectively. There are $\ell_u \ell_v$ local unitaries contained in the intersection of the lightcones.

9.3.1 Reduction to Ising spins

For each local unitary U the expression F contains two Us and two $U^\dagger$s. We will see that averaging over the local unitaries allows us to express F as a partition function for a set of classical Ising spins. To see why such Ising spins arise, consider the standard expression for the Haar average of a single unitary matrix in $\mathbb{U}(n)$:

$$\mathbb{E}_{U \in \mathbb{U}(n)} \, U_{a'a} U_{b'b}^* U_{c'c} U_{d'd}^* = \frac{1}{n^2 - 1} \Big[\delta_{a'b'} \delta_{c'd'} \times \delta_{ab} \delta_{cd} + \delta_{a'd'} \delta_{b'c'} \times \delta_{ad} \delta_{bc} \qquad (9.51)$$
$$- \frac{1}{n} (\delta_{a'b'} \delta_{c'd'} \times \delta_{ad} \delta_{bc} + \delta_{a'd'} \delta_{b'c'} \times \delta_{ab} \delta_{cd}) \Big].$$

(See Appendix E.7 for a self-contained derivation of this formula.) It is convenient to regard the above expression as a matrix whose rows are labelled by the multi-index (a', b', c', d') and whose columns are labelled by (a, b, c, d). Note that two types of contraction appear for the unprimed indices, namely $\delta_{ab} \delta_{cd}$ and $\delta_{ad} \delta_{bc}$, and similarly for the primed ones. Correspondingly, in bra–ket notation the above matrix can be written in terms of two vectors which we denote $|I_\uparrow\rangle$ and $|I_\downarrow\rangle$ (the reason for the notation will become clear below):

$$\overline{U \otimes U^* \otimes U \otimes U^*} = \frac{n^2}{n^2 - 1} \left((|I_\uparrow\rangle \langle I_\uparrow| + |I_\downarrow\rangle \langle I_\downarrow|) - \frac{1}{n} (|I_\uparrow\rangle \langle I_\downarrow| + |I_\downarrow\rangle \langle I_\uparrow|) \right). \qquad (9.52)$$

In the natural basis, these vectors are

$$\langle abcd \, | I_\uparrow \rangle = \frac{1}{n} \delta_{ab} \delta_{cd}, \qquad\qquad \langle abcd \, | I_\downarrow \rangle = \frac{1}{n} \delta_{ad} \delta_{cb}. \qquad (9.53)$$

204

With this definition, we may write (9.52) as

$$\overline{U \otimes U^* \otimes U \otimes U^*} = \frac{n^2}{n^2 - 1} \sum_{s,s'=\uparrow,\downarrow} w(s,s') \left| I_s \right\rangle \left\langle I_{s'} \right|, \tag{9.54}$$

with

$$w(s,s') = \begin{cases} 1 & \text{if } s = s' \\ -\dfrac{1}{n} & \text{if } s \neq s'. \end{cases} \tag{9.55}$$

We see that the unitary may be associated with a *pair* of classical Ising 'spins' s and s'.

For the application of interest to us the unitaries are two-site unitaries acting on the q^2-dimensional space associated with spins i and $i+1$. In this case it is easy to see that

$$\left| I_\uparrow \right\rangle = \left| \uparrow \right\rangle_i \left| \uparrow \right\rangle_{i+1}, \qquad\qquad \left| I_\downarrow \right\rangle = \left| \downarrow \right\rangle_i \left| \downarrow \right\rangle_{i+1}, \tag{9.56}$$

with

$$\left\langle \alpha\beta\gamma\delta \, | \uparrow \right\rangle = \frac{1}{q} \delta_{\alpha\beta}\delta_{\gamma\delta}, \qquad\qquad \left\langle \alpha\beta\gamma\delta \, | \downarrow \right\rangle = \frac{1}{q} \delta_{\alpha\delta}\delta_{\gamma\beta}, \tag{9.57}$$

and now $\alpha, \ldots, \delta$ run over the q basis vectors associated with a given spin. The vectors $\left| \uparrow \right\rangle$ and $\left| \downarrow \right\rangle$ have norm 1 and satisfy

$$\left\langle \uparrow \, | \, \downarrow \right\rangle = \frac{1}{q}. \tag{9.58}$$

When we consider F, the spins arising from each unitary in the circuit will form an interacting network. The interactions between spins from the same unitary will be given by $w(s,s')$, while the interactions between spins from different unitaries will arise from the inner products of kets $\left| \uparrow, \downarrow \right\rangle_i$ associated with a given spin. As a result of the second line of Eq. 9.55, the weight of an Ising configuration may be negative. However we will see that the weights simplify when we integrate out half of the spins. This leads to a simpler Ising partition function which can be treated exactly in terms of domain walls.

As a final piece of notation, we generalize the definition of $\left| I_\uparrow \right\rangle$ and $\left| I_\downarrow \right\rangle$. Given an operator $\mathcal{O}_{ab}$ on the n-dimensional space, we define n^4-dimensional vectors $\left| \mathcal{O}_\uparrow \right\rangle$ and $\left| \mathcal{O}_\downarrow \right\rangle$ via

$$\left\langle abcd \, | \mathcal{O}_\uparrow \right\rangle = \frac{\mathcal{O}_{ab}\mathcal{O}_{cd}}{\operatorname{Tr} \mathcal{O}\mathcal{O}^\dagger}, \qquad\qquad \left\langle abcd \, | \mathcal{O}_\downarrow \right\rangle = \frac{\mathcal{O}_{ad}\mathcal{O}_{cb}}{\operatorname{Tr} \mathcal{O}\mathcal{O}^\dagger}. \tag{9.59}$$

Choosing $\mathcal{O}$ to be the identity gives the vectors $\left| I_{\uparrow,\downarrow} \right\rangle$.

Before we evaluate F for arbitrary ℓ_u and ℓ_v, let us consider the simplest case where $\ell_u =$

$\ell_v = 1.$

$$\overline{F} = q^{-2}\mathbb{E}_U \operatorname{Tr} UXU^\dagger YUXU^\dagger Y = q^{-2}\mathbb{E}_U \sum_{i_1,\ldots,i_8=1}^{q^2} Y'_{i_8 i_1} Y'_{i_4 i_5} U_{i_1 i_2} U^*_{i_4 i_3} U_{i_5 i_6} U^*_{i_8 i_7} X'_{i_2 i_3} X'_{i_6 i_7}$$

$$= q^2 \left\langle (I \otimes Y)_\downarrow \middle| \overline{U \otimes U^* \otimes U \otimes U^*} \middle| (I \otimes X)_\uparrow \right\rangle. \tag{9.60}$$

In the third line, $X' = I \otimes X$ and $Y' = I \otimes Y$, and the fourth employs the formal correspondence between matrices and normalized vectors introduced above.

The Haar average of the tensor product of four unitaries is given by (9.52) with $n = q^2$. To complete the evaluation of $\overline{F}$ we observe that $\langle (I \otimes X)_\uparrow | (I_{q^2})_\uparrow \rangle = q^{-4}(\operatorname{Tr} X)^2 (\operatorname{Tr} I_q)^2 = 0$, $\langle (I \otimes X)_\uparrow | (I_{q^2})_\downarrow \rangle = q^{-4}(\operatorname{Tr} X^2)(\operatorname{Tr} I_q) = q^{-2}$, $\langle (I \otimes Y)_\downarrow | (I_{q^2})_\uparrow \rangle = q^{-4}(\operatorname{Tr} Y^2)(\operatorname{Tr} I_q) = q^{-2}$, and $\langle (I \otimes Y)_\downarrow | (I_{q^2})_\downarrow \rangle = q^{-4}(\operatorname{Tr} Y)^2 (\operatorname{Tr} I_q)^2 = 0$. This gives $\overline{F} = -1/(q^4 - 1)$.

When $\ell_u, \ell_v > 1$, we map the layout of local unitaries to a partition function for the spins s, s' in Eq. 9.54. To facilitate the mapping, we decompose the input bra $\langle I_{s'} |$ and output ket $| I_s \rangle$ into separate 'legs' corresponding to the two physical spins, as in Eq. (9.56),

$$\overline{U \otimes U^* \otimes U \otimes U^*} = \frac{q^4}{q^4 - 1} \sum_{s,s'=\uparrow,\downarrow} w(s, s') |s\rangle |s\rangle \langle s'| \langle s'|. \tag{9.61}$$

Similarly, the vectors encountered above for the case $\ell_u = \ell_v = 1$ can be decomposed as $|(IX)_\uparrow\rangle = |\uparrow\rangle |X_\uparrow\rangle$ and $|(IY)_\downarrow\rangle = |\downarrow\rangle |Y_\downarrow\rangle$, which satisfy

$$\langle \uparrow |Y_\downarrow\rangle = q^{-2} \operatorname{Tr} Y^2 = \frac{1}{q}, \qquad\qquad \langle \downarrow |Y_\downarrow\rangle = q^{-2}(\operatorname{Tr} Y)^2 = 0,$$

$$\langle \uparrow |X_\uparrow\rangle = q^{-2}(\operatorname{Tr} X)^2 = 0, \qquad\qquad \langle \downarrow |X_\uparrow\rangle = q^{-2} \operatorname{Tr} X^2 = \frac{1}{q}. \tag{9.62}$$

The expression Eq. (9.60) is now depicted as in Fig. 9-12a.

It is now clear that for general ℓ_u, ℓ_v we may regard the array of unitaries as a tensor network composed of tensors of the form (9.61). The boundaries of this tensor network — i.e. the external legs of the array of $\ell_u \times \ell_v$ unitaries — involve inner products with fixed vectors. Two of the boundary legs are dressed with $q |X_\uparrow\rangle$ and $q \langle Y_\downarrow|$; see Fig. 9-12a. Apart from these, the external legs on the top boundary are dressed by states $q \langle \downarrow|$, while those on the bottom boundary are dressed with $q |\uparrow\rangle$. In addition $\overline{F}$ includes an overall dimension factor q^{-2t} coming from the infinite temperature Gibbs state. For convenience, we absorb the overall dimension factor q^{-2t} into the vectors on the lower boundaries; these vectors are taken to be normalized, whereas the boundary bras in the top boundaries have norm q.

We may now interpret $\overline{F}$ as a partition function for the Ising spins $s_{u,v}$ and $s'_{u,v}$ which according to Eq. (9.61) are associated with the unitary at position (u, v). These spins take the values $\uparrow$, $\downarrow$. The weight associated with the 'bond' between $s_{u,v}$ and $s'_{u,v}$ comes from the single-unitary Haar average and is $\frac{q^4}{q^4-1}$ if $s_{u,v} = s'_{u,v}$, and $\frac{-q^2}{q^4-1}$ if $s_{u,v} \neq s'_{u,v}$. The leg of

206
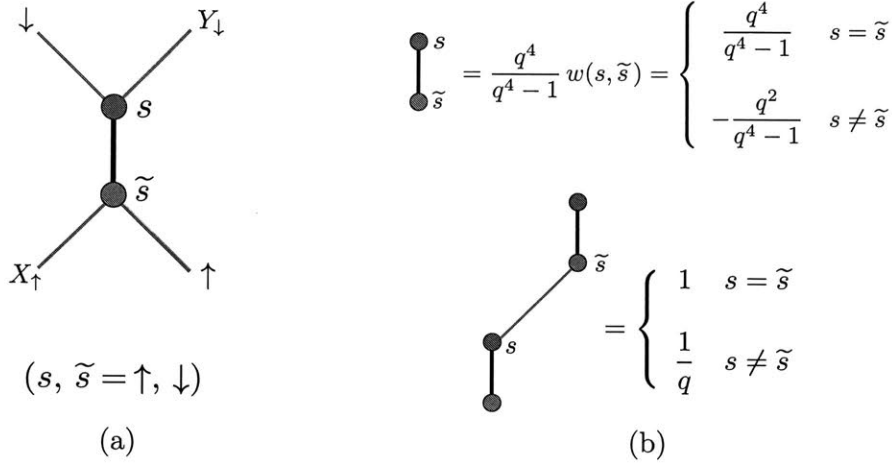
Figure 9-12: In (a), we show the elementary tensor for computation of $\overline{F}$. The boundary conditions in the top-left figure are for $\ell_u = \ell_v = 1$. Shown in (b), are the weights due to the interaction between adjacent Ising variables arising from the same unitary (top) and from unitaries at adjacent time steps (bottom). After integrating out the 'bra' Ising variable s', we obtain the weights shown in Fig. 9-13.

the tensor network connecting the unitary at (u, v) to that on (for example) its lower right at $(u, v - 1)$ yields an interaction between $s'_{u,v}$ and $s_{u,v-1}$ which comes simply from the inner product $\langle s'_{u,v-1} | s_{u,v} \rangle$. This gives weight 1 if $s'_{u,v} = s_{u,v-1}$, and weight $\frac{1}{q}$ if $s'_{u,v} \neq s_{u,v-1}$. See Fig. 9-12b.

We have thus mapped the Haar average of the out-of-time correlator to a partition function for Ising degrees of freedom on a honeycomb lattice (with the q–dependence residing in the interactions on the bonds). At first sight, this may appear to be a formidable problem. Note in particular that some configurations have negative weight. However, a simplification is possible, as a result of the unitarity of the underlying dynamics. A hint that a simplification is possible comes from the fact that the expression for F, Eq. (9.48), becomes trivial if one of the operators X_0 and Y_x is the identity operator. In the Ising language this corresponds only to a slight change of boundary conditions. The simplification is effected by integrating out the 'bra' variable $s'_{u,v}$ from each unitary. This generates a three-spin interaction among the 'ket' variables $s_{u,v}$, $s_{u-1,v}$, and $s_{u,v-1}$. The calculation is straightforward and yields the table of weights in Fig. 9-13. For example, if $s_{u,v} = s_{u,v-1} = s_{u-1,v}$, then the weight is $\frac{q^4}{q^4-1} \cdot 1 \cdot 1 + \frac{-q^2}{q^4-1} \cdot \frac{1}{q} \cdot \frac{1}{q} = 1$.

We are left with an effective Ising model for the s spins only. One s spin is associated with each unitary in the quantum circuit. The fact that the weight in Fig. 9-13 is zero for two of the configurations means that only a very restricted subset of Ising configurations are allowed. We will show that these can be summed exactly by viewing the configurations in a dual description, in terms of domain walls.

Let us specify the new boundary conditions. The rules of Fig. 9-13 apply along the bottom boundary (with the lower spins of Fig. 9-13 being fixed up spins) due to our normalization
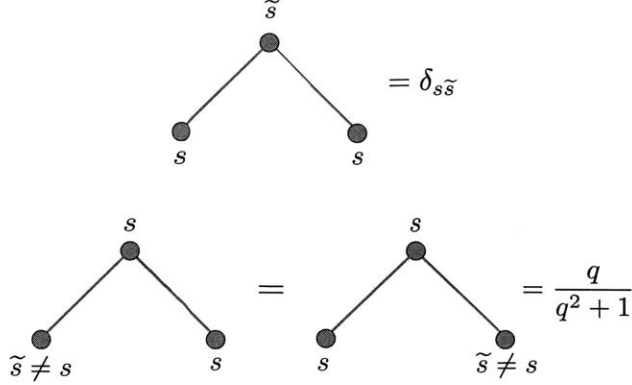
Figure 9-13: Weights for the 3-body interaction which arises after integrating out half of the Ising variables (the bra variables).

convention for the boundary kets, except for the site where the observable ket $|X_\uparrow\rangle$ is dangling.

$$= \frac{-1}{q^4 - 1}, \qquad = \frac{q^2}{q^4 - 1} \qquad (9.63)$$

The top boundary bras, which have norm q, follow the rule that

$$= 1, \qquad = q, \qquad = 1, \qquad = 0 \qquad (9.64)$$

9.3.2 Partition function for two directed paths

Now the problem is reduced to a partition function of Ising variables with the three-body interaction and the boundary interaction. We first simplify the partition function by relating it to one with modified boundary conditions as follows. We denote the weight of a given configuration by $W_{X,Y}(s)$, where the subscripts indicate the dependence on the boundary conditions induced by the operators X and Y. Because of the last rule in Eq. (9.64), the spin at the site where Y_x is attached — null coordinate (ℓ_u, ℓ_v) — has to be $s_{\ell_u,\ell_v} = \uparrow$. As a result we can replace $Y_\downarrow$ with $\downarrow_{\text{fixed}}$, which according to Eq. (9.64) gives the same weight when $s_{\ell_u,\ell_v} = \uparrow$. Let us denote the weight of a configuration s under this modified top boundary condition by $W_X(s)$, dropping the subscript Y. We may then write the desired quantity $\overline{F} = \sum_s W_{X,Y}(s)$ as

$$\overline{F} = \sum_{\substack{s:\\ s_{\ell_u,\ell_v}=\uparrow}} W_X(s) = \sum_s W_X(s) - \sum_{\substack{s:\\ s_{\ell_u,\ell_v}=\downarrow}} W_X(s). \qquad (9.65)$$

208
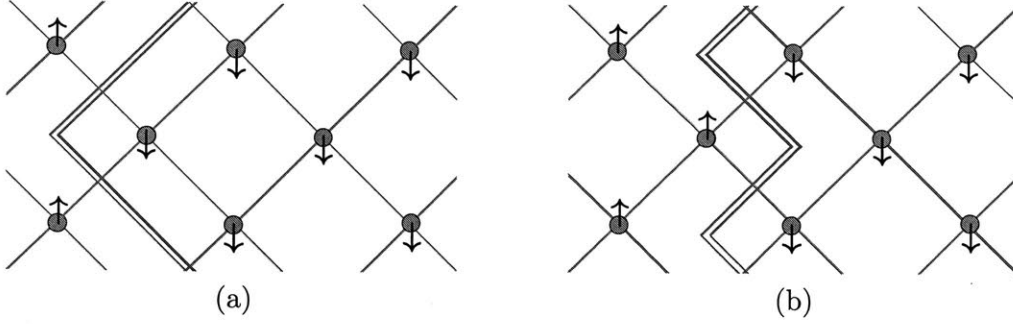
Figure 9-14: A section of one of the domain walls in the bulk (double line). The two configurations shown have equal weight.

We claim that the first term is equal to 1, and thus

$$-\frac{1}{2}\operatorname{Tr}\rho_\infty\overline{[U(t)X_0U(t)^\dagger, Y_x]^2} = 1 - \overline{F} = \sum_{\substack{s\,:\\s_{\ell_u,\ell_v}=\downarrow}} W_X(s). \tag{9.66}$$

The claim can be shown in two ways. First, the out-of-time correlator $1 - \overline{F}$ must vanish if the operator Y is replaced by the identity. The boundary vector $|Y_\downarrow\rangle$ then becomes $|\downarrow\rangle$, and the partition function for $\overline{F}$ becomes precisely $\sum_s W_X(s)$. Therefore $1 - \sum_s W_X(s) = 0$. The other way to show the claim is by directly integrating out the Ising variables inductively, starting from the top line with respect to the all–$\downarrow$ boundary condition along the top boundary. This is a nontrivial consistency check on our reduction.

Now we focus on $W_X(s)$ with the variable at null-coordinate (ℓ_u, ℓ_v) fixed to be $\downarrow$. If the bottom variable where X is attached is $\uparrow$, then the second rule in Fig. 9-13 together with the boundary condition along the bottom boundary dictates that all the bulk variables be $\uparrow$. This cannot be fulfilled for the spin at (ℓ_u, ℓ_v), implying that the weight is zero.

Hence, we have fixed two Ising variables at the bottom and top boundaries to be $\downarrow$ where the observables X_0 and Y_x are attached. Let us think of domain walls instead of spins. The key point is the first rule in Fig. 9-13, which leads to the domain walls being directed, drastically simplifying the partition function. If we follow a domain wall from the top to the bottom, it should always go down-left or down-right. This implies that there are two non-intersecting domain walls extending from the bottom to the top boundary. The starting vertices of the right and left domain walls have null coordinates $(1,0)$ and $(0,1)$, respectively.

The domain wall has a weight

$$\left(\frac{q}{q^2+1}\right)^{t-1} \tag{9.67}$$

from the 3-spin interactions in Fig. 9-13, excluding that involving the spin at null coordinate $(1,1)$. The domain wall can fluctuate freely in the bulk without changing this weight, see Fig. 9-14.

However, the end position of the domain wall at the top boundary *does* affect the weight, and we will need to count the number of domain walls for each ending position. For the right domain wall, the end position can be at a vertex $(t-v, v)$ in null coordinates for some $v = 0, 1, \ldots, \ell_v - 1$. Likewise, the end position of the left domain wall can be $(u, t - u)$ for some $u = 0, 1, \ldots, \ell_u - 1$. The weight from the top boundary interaction is then

$$q^{2t-2u-2v} \tag{9.68}$$

by Eq. (9.64). It remains to count the number of domain walls given their end positions. The right domain wall connects $(1, 0)$ to $(t-v, v)$ while the left domain wall connects $(0, 1)$ to $(u, t-u)$, with the constraint that they must not intersect. To handle the constraint, we use a reflection trick. Regard the domain walls as random walkers. The right random walker randomly chooses between up-left and up-right edges, to proceed from $A = (1, 0)$ to $B = (t - v, v)$. Similarly, the left random walker proceeds from $C = (0, 1)$ to $D = (u, t - u)$. Any pair of paths $A \to B$ and $C \to D$ that have a common point can be viewed as a pair of paths $A \to D$ and $C \to B$. Conversely, any pair of paths $A \to D$ and $C \to B$, which must meet at at a point, can be viewed as a pair of paths $A \to B$ and $C \to D$ with a common point. Therefore, the number of pairs of paths from $A \to B$ and $C \to D$ without intersection is the number of all unrestricted pairs from $A \to B$ and $C \to D$, minus the number of all unrestricted pairs from $A \to D$ and $C \to B$. The number of our domain wall configurations is therefore

$$\binom{t-1}{v}\binom{t-1}{u} - \binom{t-1}{v-1}\binom{t-1}{u-1} \tag{9.69}$$

where the second factor vanishes when $u = 0$ or $v = 0$.

Finally we combine the results above:

$$\sum_{\substack{s\,:\\ s_{\ell_u,\ell_v}=\downarrow}} W_X(s) = \underbrace{\frac{q^2}{q^4-1}}_{\text{Eq. (9.63)}} \underbrace{\left(\frac{q}{q^2+1}\right)^{2t-2}}_{\text{Eq. (9.67)}} \sum_{u=0}^{\ell_u-1}\sum_{v=0}^{\ell_v-1} \underbrace{q^{2t-2u-2v}}_{\text{Eq. (9.68)}} \underbrace{\left[\binom{t-1}{v}\binom{t-1}{u} - \binom{t-1}{v-1}\binom{t-1}{u-1}\right]}_{\text{Eq. (9.69)}}.$$

This correctly reproduces the answer $q^4/(q^4 - 1)$ when $\ell_u = \ell_v = 1$. This can be conveniently rewritten as

$$\overline{\mathcal{C}(t,x)} = \frac{(1-p)^2}{1-2p}\, g(t-1, \ell_v - 1)\, g(t-1, \ell_u - 1)$$

$$- \frac{p^2}{1-2p}\, g(t-1, \ell_v - 2)\, g(t-1, \ell_u - 2) \tag{9.70}$$

where

$$t = \ell_u + \ell_v - 1, \qquad x = \ell_u - \ell_v, \qquad p := \frac{1}{q^2+1}, \tag{9.71}$$

and

$$g(n, a) := \sum_{k=0}^{a} \binom{n}{k} (1-p)^{n-k} p^k.$$ (9.72)

Further simplification is possible since $g(t-1, a) \simeq g(t-1, a-1)$ for large t.

$$\overline{\mathcal{C}(t,x)} \simeq g(t-1, \ell_v - 1, p) g(t-1, \ell_u - 1, p) \simeq \Phi\left(\frac{v_B t + x}{\sigma}\right) \Phi\left(\frac{v_B t - x}{\sigma}\right)$$ (9.73)

where

$$v_B = \frac{q^2 - 1}{q^2 + 1}, \quad \sigma = \frac{2q\sqrt{t}}{q^2 + 1}, \quad \Phi(y) = \frac{1}{\sqrt{2\pi}} \int_{-\infty}^{y} e^{-x^2/2} \mathrm{d}x.$$ (9.74)

9.3.3 Bounds on Fluctuations

Here we estimate the fluctuation of $\mathcal{C}(t,x)$ due to the *randomness of the unitaries*. One might wish to calculate this fluctuation directly, using a similar technique that we employ for the average of $\mathcal{C}(t,x)$, but we found the exact computation unwieldy as it involves high powers of unitaries. (See [276].) Nevertheless, we can argue that the fluctuations are negligible in two regimes.

Since the random variable $\mathcal{C}(t,x)$ takes values between 0 and 2, the variance is upper bounded by $2\bar{\mathcal{C}}$. Therefore, the standard deviation is upper bounded by

$$\sqrt{\overline{\mathcal{C}(t,x)^2} - \overline{\mathcal{C}(t,x)}^2} \leq \sqrt{2\overline{\mathcal{C}(t,x)}} \simeq O(1) \exp\left(-\frac{1}{4}\left(\frac{|x| - v_B t}{\sigma}\right)^2\right).$$ (9.75)

This bound is valid for any t, x, but only meaningful when $|x| \gg v_B t$. This basically says that there is almost no "leakage" of operators beyond the lightcone defined by v_B. (In passing, we note that one can also use Markov inequality $\Pr[X \geq a] \leq a^{-1}\mathbb{E}X$ which holds for any positive random variable X and a positive number a to have a probability tail bound.)

In the opposite regime where $|x| \ll v_B t$, we have shown that the average $\overline{\mathcal{C}(t,x)}$ is almost 1; the discrepancy is upper bounded by $O(1)\exp(-(v_B t - |x|)^2/2\sigma^2)$. Thus, in this regime the fluctuation is basically given by

$$\mathbb{E}_U F^2(U) = N^{-2} \mathbb{E}_U (\mathrm{Tr}\, UXU^\dagger Y UXU^\dagger Y)^2 \geq 0$$ (9.76)

where F is defined in Eq. (9.48) and N is the dimension of the Hilbert space of spins where $UXU^\dagger Y$ is supported on. Here U includes all the local unitaries in the evolution quantum circuit.

To estimate the fluctuation, we consider a slightly different system where $2ct$ spins form a ring, where c is some absolute constant that depends on q only. If $c > 1$, this does not modify the dynamics at all, since the evolved operator $UX_0U^\dagger$ is supported on $2t$ spins. For $c < 1$, while
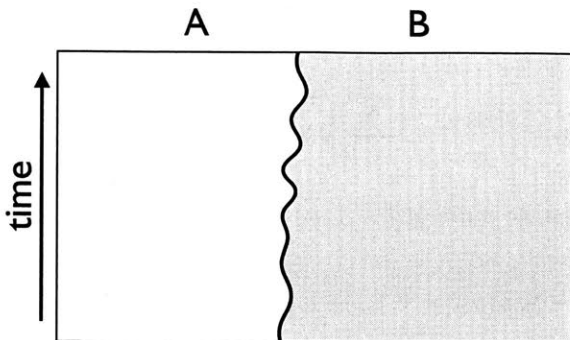
Figure 9-15: The average entanglement purity $\overline{\mathcal{P}}$ maps to the partition function for a directed random walk. At the top boundary the walk terminates at the position of the entanglement cut between subsystems A and B. At the bottom boundary the endpoint is free.

we do not insist that this allows us to compute the fluctuation rigorously, we anticipate that qualitative conclusions from this modified setting carry over to the original open chain system.

In Appendix E.8, we show that if $c = M_q^{-1} = \tilde{O}(q^{-2})$, then for all $|x| < ct$

$$\mathbb{E}_U F^2(U) \leq 11 q^{-4ct}. \tag{9.77}$$

That is, deep in the lightcone, there is a region in spacetime bounded by a nonzero speed where the fluctuation of $\mathcal{C}(t, x)$ is suppressed exponentially in t. It is likely that this is only a bound, rather than a tight estimate of fluctuation. Eq. (9.77) is proved using previous results on approximate unitary designs [223], and estimates for $\mathbb{E}_U F^2(U)$ when U is truly Haar random [305].

9.4   Entanglement growth

Entanglement can by quantified in various ways, but perhaps the simplest measure is the entanglement purity $\mathcal{P} = \mathrm{Tr}\left(\mathrm{Tr}_{A^c} |\psi\rangle \langle\psi|\right)^2 \leq 1$, where A is some region. A pure state $|\psi\rangle$ on $A \cup A^c$ is entangled if and only if the purity is not equal to 1. The logarithm of the entanglement purity is the Renyi-2 entropy

$$S_2(A) = -\log \mathcal{P}. \tag{9.78}$$

In this section, we calculate exactly the average purity of 'half' of the infinite chain, for arbitrary t, under the evolution protocol in Section 9.1, with an initial product state. Previously, a bound on the saturation time for $q = 2$ was obtained [222]. Also, the evolution of average entanglement purity has been calculated using other techniques under a protocol where random two-site unitaries are applied to random bonds [275] and other protocols [276].

Here we show that the averaged purity $\overline{\mathcal{P}}$ can be mapped to the partition function for a directed walk, shown schematically in Fig. 9-15. Our calculation technique below will be very

212

similar to the OTOC calculation in the previous section; the difference is only in the boundary conditions.

9.4.1 Random walk picture

Let A be the left half of our chain, and B be the right half. The initial pure density matrix is $\rho(t=0) = \cdots \otimes P_{-1} \otimes P_0 \otimes P_1 \otimes \cdots$, where P_i is the projector $|i\rangle \langle i|$ onto the initial state at site i. If U is the full time-evolution unitary consisting of local unitaries, the entanglement purity $\mathcal{P}$ across the cut between A and B is

$$\overline{\mathcal{P}(t)} = \sum_{a,a'=1}^{q^{|A|}} \sum_{b,b'=1}^{q^{|B|}} \overline{\langle ab| \, U\rho(0)U^\dagger \, |a'b\rangle \langle a'b'| \, U\rho(0)U^\dagger \, |ab'\rangle}$$

$$= q^{|A|+|B|} \times \langle \uparrow^{\otimes|A|}\downarrow^{\otimes|B|}| \; \overline{U \otimes U^* \otimes U \otimes U^*} \; |\cdots (P_0)_\uparrow (P_1)_\uparrow \cdots\rangle \qquad (9.79)$$

The notation $|\uparrow\rangle, |\downarrow\rangle$ is the same as in Sec. 9.3.1. For a one-dimensional projector P on q-dimensional space, the q^4-dimensional vector $|P_\uparrow\rangle$ satisfies

$$\langle \uparrow |P_\uparrow\rangle = \frac{1}{q} = \langle \downarrow |P_\uparrow\rangle . \qquad (9.80)$$

The expression for the purity can be thought of as a partition function for classical Ising spins as in Sec. 9.3.1. There are two Ising spins associated with each local unitary; see Eq. (9.54). Due to Eq. (9.80), for any configuration of the Ising spins, the weight factor from the bottom boundary is $q^{-|A|-|B|}$, which cancels the factor $q^{|A|+|B|}$ in front of Eq. (9.79). Hence, the average purity is simply the sum of weights from the domain wall in the bulk (e.g. see Fig. 9-14).

In Sec. 9.3.1, we first integrated out the 'bra' Ising variables s', but here we find it simpler to integrate out the 'ket' Ising variables s. The transition rules of Fig. 9-13 are now upside down, but otherwise the same. Then, we have a single domain wall starting from the top boundary to reach the bottom. Any domain wall has length exactly t, giving rise to weight $\left(\frac{q}{q^2+1}\right)^t$. The domain wall can choose between left-down or right-down moves as it proceeds from the top, and therefore there are 2^t domain walls. We conclude that

$$\overline{\mathcal{P}(t)} = \left(\frac{2q}{q^2+1}\right)^t . \qquad (9.81)$$

Note that the factor $2q/(q^2+1)$ is directly related to the average "entangling power" of Ref. [306]. We may define the 'purity speed'

$$\overline{\mathcal{P}(t)} \equiv q^{-v_P t}, \qquad\qquad v_P = \log_q \frac{q^2+1}{2q} . \qquad (9.82)$$

This quantity gives a bound on the growth rate of the second Renyi entropy:

$$\overline{S_2(\rho(t)_A)} = \overline{-\log_q \mathcal{P}(t)} \geq -\log_q \overline{\mathcal{P}(t)} = v_P t \tag{9.83}$$

The inequality is because the function $f(x) = -\log x$ is convex. Note that this expression bounds the growth rate of S_2 but does not fix it. The distribution of S_2 fluctuates in a window of small size compared to its mean [9],[10] but since S_2 appears in the exponential in $\overline{q^{-S_2}}$, this does not rule out the possibility that this quantity is affected by rare anomalously small values of S_2, making it very different from $q^{-\overline{S_2}}$.

The von Neumann entropy S_{vN} is always greater than or equal to S_2, so the growth rate v_E of S_{vN} is also bounded by v_P:

$$v_E \geq v_P = \log_q \frac{q^2 + 1}{2q} = 1 - \frac{\log 2}{\log q} + O\left(\frac{1}{q^2 \log q}\right) \tag{9.84}$$

where the expansion is for large q.

In Ref. [9] we argued that the universal fluctuations of the entanglement in random circuit dynamics may be understood in terms of a coarse-grained minimal cut, of random shape, through the random circuit. This picture may be contrasted with the domain wall calculation of the averaged purity, which reduces to a statistical mechanics problem without quenched randomness. This is reminiscent of the difference between a quenched and an annealed average in the statistical mechanics of disordered systems [307]. A direct exact calculation of $\overline{S_2}$ (not to mention $\overline{S_{vN}}$, or of the fluctuations in the entropy) for finite[11] q would be much more difficult than the calculation above, as a replica-like limit [307] would be required to handle the logarithm. However structure arising from unitarity might make this calculation tractable. This is an interesting task for the future.

The scaling limit of the representation obtained in this section, where we take length and time scales to be large and of the same order, yields a 'deterministic' domain wall configuration. This is simply a vertical line for the infinite geometry considered here.[12] We expect that extending the calculation to higher dimensions will give, in the scaling limit, a formula for $-\log \overline{\mathcal{P}}$ as the 'energy' of a minimal surface (representing the Ising domain wall) which has a deterministic coarse-grained geometry, obtained from an effective elastic energy minimization problem. This is precisely the scaling picture proposed in Ref. [9] for the growth of entanglement in higher-dimensional systems.

---

[10] Ref. [9] argued that the width of the distribution scales as $t^{1/3}$. The mean value is of order t.

[11] In the limit $q \to \infty$ it is easy to show that $v_E = v_P$ in the present model.

[12] This is because the $\sqrt{t}$ fluctuations in the transverse position of the domain wall are negligible compared to t; compare [9] where the minimal cut configuration is also deterministic in the scaling limit.
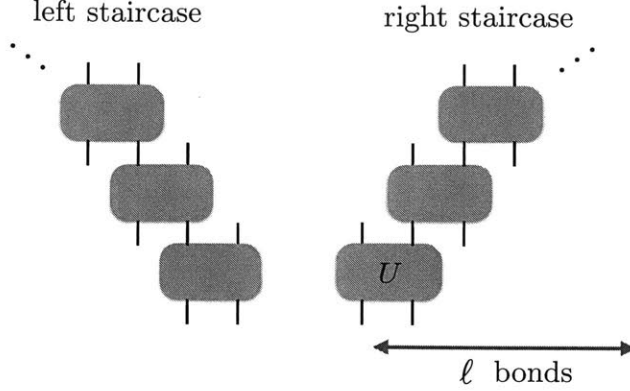
Figure 9-16: **Random Circuit built from "Staircase" Unitaries:** We use "left" and "right" staircases — built from random two-site unitary operators as shown, and extending over ℓ bonds — as the building blocks for a random quantum circuit in which the ratio of the entanglement and butterfly velocities v_E/v_B may be made arbitrarily small.

9.4.2 Non-Universality of the Ratio v_E/v_B

In Ref. [9], see also Ref. [214], we showed that the speed v_E associated with entanglement growth is in general smaller than the operator growth speed v_B, and gave explicit models displaying a ratio $v_E/v_B < 1$. In these models[13] this ratio happened to be $1/2$. Values close to $1/2$ were also found numerically in Ref. [214] and Ref. [249]. These results might lead one to wonder whether this value is in some sense generic. Here we show that it is not, by constructing random circuit dynamics, involving interactions of large but finite range, which give *arbitrarily small* values of v_E/v_B without any fine tuning. The construction uses random unitaries made up of 'staircases' of length $O(q^2)$ which are made up of smaller random unitaries (Fig. 9-16). When q is large, we obtain a ratio v_E/v_B which is at most of order $1/q^2$. (In a deterministic spin chain with quenched spatial disorder it is even possible to have $v_E/v_B = 0$ [239], but here we insist on *statistical* translational invariance: i.e. we insist that the probability distribution for the circuit is invariant under translations.)

Consider quantum circuit dynamics in which 'staircase unitaries' are applied at random locations and at random times in a Poissonian fashion. A staircase is a collection of 2–site unitaries arranged as in Fig. 9-16. Left and right-oriented staircases are applied with equal probability. The staircase acts on ℓ bonds and we take ℓ large but finite, satisfying $\ell/q^2 \gg 1$. Let r be the rate at which staircases are dropped at a given location.

A single staircase can increase the entanglement across a given bond by at most 2 units, implying $v_E \leq 2r\ell$. On the other hand a single staircase can move the endpoint of an operator a long way when $\ell \gtrsim q^2 \gg 1$. The random walk picture of Sec. 9.1.1 shows that in the limit of large ℓ/q^2, a staircase advances the front of the OTOC by an average distance $\sim q^2/2$. This involves an average over the two staircase orientations, only one of which is effective in

---

[13] This was determined analytically for a certain large q model, distinct from that here, and numerically for various circuits composed of Clifford gates.

advancing the front a long distance. The large value is because, when q is large, the small value of $p = 1/(q^2 + 1)$ (Eq. 9.24) means the random walker can 'run' a long way up a rightward-oriented staircase before falling off. The previous implies $v_B \simeq q^2 r \ell / 2$ at leading order in ℓ. This yields a ratio $v_E/v_B \lesssim 4/q^2$ in this regime, which can be made arbitrarily small by taking q (and hence ℓ) to be large.

9.5 Outlook

We have argued that universal scaling forms for the out-of-time-order correlator can be obtained using mappings to paradigmatic problems in classical statistical mechanics. In one dimension we gave an extremely simple hydrodynamic picture in terms of diffusion. In higher dimensions we gave a mapping to classical surface growth and the KPZ equation:[14] the OTOC is given by the averaged density for a growth process in the KPZ universality class.

These mappings were derived exactly for random unitary circuits, which are natural 'least structured' models for chaotic quantum dynamics in situations where conserved quantities are not playing an important role. We have conjectured that the universal scaling forms found here also apply to OTOCs at asymptotically late times in generic, nonintegrable many body systems and quantum field theories. It will be interesting to test this conjecture in other situations where calculations are possible.

This picture differs from that obtained in a number of previous calculations using many-body perturbation theory [230, 232, 237, 236], and it will be interesting to understand the reasons for these differences. Ref. [230] found an operator front that did not broaden in time, whereas here we find a broadening front in all dimensions below $4 + 1$. Additionally, in Ref. [230] the OTOC was found to obey a local, nonlinear traveling wave equation, which is unlike what we found for random circuits. In 1D we obtained a *linear* hydrodynamic equation, while in higher dimensions $\overline{C}(x, t)$ in a random circuit is not governed by a local differential equation at all, contrary to standard lore about OTOCs.

Interestingly, a *mean field* approximation to the classical growth process would yield a local differential (or rather difference) equation for the OTOC, of traveling wave form. This is discussed in Appendix. E.9. However, the mean field approximation is not valid in physical dimensionalities.

Assuming that the results here do indeed apply to realistic systems with Hamiltonians that are fixed in time, it will be interesting to consider extensions of the present coarse-grained pictures which take conserved quantities into account.

We have also given exact results for entanglement growth in 1+1D which support the scaling ideas put forward in [9], as discussed in Sec. 9.4. In this picture (in any D) entanglement growth

---

[14] Ref. [9] obtained a connection between entanglement growth in 1+1D random unitary circuits and the KPZ equation. To avoid confusion we emphasize that the connection with KPZ discussed here is physically entirely distinct from that one, and is not even in the same number of spatial dimensions.

is determined by a minimal surface in spacetime, whose geometry becomes well-defined[15] in an appropriate scaling limit and is determined essentially by an elastic minimization problem. Furthermore, it was argued in that paper and in Ref. [214] that generically $v_E < v_B$, where v_E is the speed characterizing the growth of entanglement. Here we have shown that it is possible to have arbitrarily small v_E/v_B in a random quantum circuit.

The effective Ising partition functions for calculating the OTOC and the purity turned out to have interesting structure, making them drastically simpler than they appeared at first sight, and much simpler than the analogous partition function for a non-unitary tensor network [274]. It would be very interesting to explore whether similar simplifications occur when the averaging involves higher powers of the unitary circuit. If so this would permit calculations of, say, modified versions of the OTOC involving higher powers of the commutator (here we have considered only the square). Similar techniques would also allow a calculation of fluctuations in the OTOC due to randomness in the circuit. We have conjectured that these fluctuations are small whenever the front broadens with time, but we have not attempted a direct calculation, except via a heuristic argument in 1D.[16] Even more interesting would be a direct calculation of the von Neumman entropy, which would have to use a replica limit to handle the logarithm.

OTOCs involving higher powers of the commutator are important for comparison with the Lieb-Robinson bound. The OTOC considered here can be thought of as the squared Frobenius norm of the commutator divided by the Hilbert space dimension, whereas the Lieb-Robinson bound is on the operator norm of the commutator. The two norms are related as the operator norm is always upper bounded by the Frobenius norm, but our results do not put any nontrivial bound on the operator norm, due to the large dimension factor. The exact relation of the two quantities is yet to be determined.

In addition to exploring implications for realistic many-body systems, interesting questions remain that are specific to the random circuit context. (Note that, at the most basic level, our results show that operator growth saturates the naive causal lightcone of the quantum circuit as $q \to \infty$, but not for finite q.) The randomness in the circuit necessarily implies statistical fluctuations in all observables including $\mathcal{C}(x, t)$. We have argued that these statistical fluctuations are (perhaps counterintuitively) a subleading effect at late times. We have shown this in regimes far from the front of the OTOC by giving inequalities, and we have given a heuristic argument for it in the region near the front. This argument was based on a phenomenological extension of the hydrodynamic equation for $\overline{\mathcal{C}(x, t)}$ in the 1D case to allow for statistical fluctuations in $\mathcal{C}(x, t)$ (Eq. 9.29). It would be desirable to give a microscopic derivation of Eq. 9.29. (For the entanglement entropy, statistical fluctuations were investigated in Ref. [9].) It also remains to characterize the classical growth problem in Section 9.2 more fully, for example by obtaining the nonuniversal constants via an approximate analytic treatment.

The KPZ equation is connected to a remarkable array of topics in classical statistical me-

---

[15]But model dependent above 1+1D

[16]Circuit-to-circuit fluctuations in the OTOC should not be confused with KPZ fluctuations in the auxiliary classical model.

chanics [308], including the directed polymer in a random medium [309] and one-dimensional hydrodynamics [310], and has beautiful experimental applications [292, 293]. Through the Tracy-Widom distribution [279], it is also connected to random matrix theory and an array of combinatorial problems (for example the longest increasing subsequence problem and the statistics of random permutations [311, 312]). It will be interesting to explore which members of this array can shed light on operator growth.

Chapter 10

Dynamics of Entanglement Growth

In this chapter, we focus on heuristics for the dynamics of entanglement growth in generic, non-integrable systems, both in 1D and in higher dimensions. We arrive at these pictures by studying 'minimally structured' models for quantum dynamics: dynamics that are spatially local, and unitary, but random both in time and space ('noisy'). Concretely, we will focus on quantum circuit dynamics with randomly chosen quantum gates. Entanglement growth in these systems exhibits a remarkable universal structure in its own right, related to paradigmatic problems in *classical* statistical mechanics. We emphasize that the mapping presented here is distinct from the relation between operator spreading and classical stochastic processes demonstrated in the previous chapter, as the entanglement entropy is a non-local quantity, and its dynamics cannot be extracted from the behavior of any single operator under Heisenberg evolution.

Random circuits provide a theoretical laboratory which allows us to derive scaling pictures for entanglement growth and the so-called 'entanglement tsunami' [213] which, we conjecture, generalize to quenches in many-body systems *without* noise. For example we propose a simple 'minimal membrane' picture which can be used to derive scaling forms for the growth of the entanglement. We also argue that generically there is a well-defined 'entanglement speed' v_E, but this is generically smaller than the 'butterfly speed' v_B governing operator growth, and we give a physical explanation for this phenomenon.

We will show that noisy entanglement growth allows a long-wavelength description with an emergent universal structure. Physically, the class of noisy dynamics includes closed, many-body systems whose Hamiltonian $H(t)$ contains fluctuating noise terms, and also quantum circuits in which qubits are acted on by randomly chosen unitary gates. In this setting, we pin down both the leading order deterministic behaviour of the entanglement and the subleading fluctuations associated with noise. We argue that fluctuations and spatial correlations in the entanglement entropy are characterized by universal scaling exponents, expected to be independent of the details of the microscopic model.

For noisy systems in one spatial dimension (1D), we argue that the critical exponents for entanglement growth are those of the Kardar—Parisi—Zhang (KPZ) equation, originally introduced to describe the stochastic growth of a surface with time t [313]. In the simplest setting,

219

we find that the 'height' of this surface at a point x in space is simply the von Neumann entanglement entropy $S(x, t)$ for a bipartition which splits the system in two at x. The average entanglement grows linearly in time, while fluctuations are characterized by non-trivial exponents. We support this identification with analytical arguments and numerical results for discrete time quantum evolution (unitary circuits).

A remarkable feature of the KPZ universality class is that it also embraces two classical problems that at first sight are very different to surface growth [313, 314]. These connections lead us to powerful heuristic pictures for entanglement growth, both in 1D and higher dimensions. The KPZ universality class embraces the statistical mechanics of a directed polymer in a disordered potential landscape [309], and 1D hydrodynamics with noise (the noisy Burgers equation [310]). These problems, together with surface growth, are sometimes known as the 'KPZ triumvirate' [315]. They are summarized in Fig. 10-1. We will show that entanglement growth can usefully be related to all three of the classical problems in in Fig. 10-1.

In the quantum setting, the directed polymer is related to the 'minimal cut', a curve in space-time which bisects the unitary circuit representing the time evolution. This picture is more general than the surface growth picture, as it allows one to consider the entropy for any bipartition of the system. It also allows us to generalize from 1D to higher dimensions. The picture is reminiscent of the Ryu-Takayanagi prescription for calculating the entanglement entropy of conformal field theories in the AdS-CFT correspondence, which makes use of a minimal surface in the bulk space [316], and analogous results for certain tensor network states [317, 318, 274]. Here however the cut lives in spacetime rather than in space, and in a noisy system its shape is random rather than deterministic. (For a different use of the idea of a minimal cut in spacetime, see Ref. [77].) In $d + 1$ spacetime dimensions the minimal cut becomes a d-dimensional membrane pinned by disorder. This picture allows us to obtain approximate critical exponents for noisy entanglement growth in any number of dimensions.

This picture also leads us to a conjecture for entanglement growth in systems *without* noise, both in 1D and higher dimensions, as we discuss below. According to this conjecture, the calculation of the entanglement in higher dimensions reduces to a *deterministic* elastic problem for the 'minimal membrane' in spacetime. In 1D, it results in particularly simple universal scaling functions, which agree with scaling forms in holographic 1+1D CFTs [213, 76, 77], and which we suggest are universal for generic, nonintegrable, translationally invariant 1D systems.

The third member of the triumvirate in Fig. 10-1 is a noisy hydrodynamic equation describing the diffusion of interacting (classical) particles in 1D. We show that this can be related to the spreading of quantum operators under the unitary evolution, giving a detailed treatment of the special case of stabilizer circuits. Note that while the minimal cut picture generalizes to higher dimensions, the KPZ and hydrodynamic pictures are special to 1D.

We propose that noisy dynamics are a useful toy model for quantum quenches in generic (nonintegrable, non-conformally–invariant) systems, even without noise. The logic of our approach is to pin down the universal behaviour of noisy systems (Secs. 10.1—10.5), to establish simple
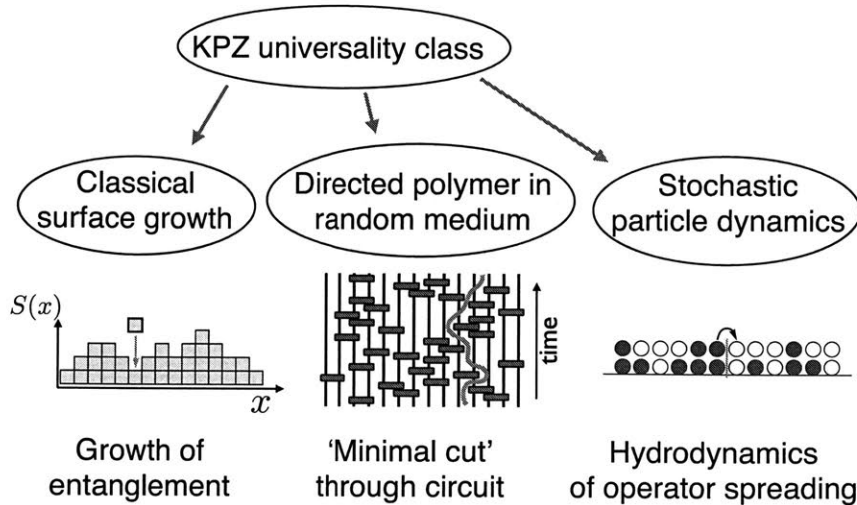
Figure 10-1: The KPZ 'triumvirate' is made up of three very different problems in classical statistical mechanics which all map to the KPZ universality class. As we will discuss, each of them can be usefully related to entanglement in 1+1D.

heuristics capturing this behaviour (Secs. 10.2, 10.3), and then to extend these heuristic pictures to dynamics without noise (Secs. 10.4, 10.6).

The detailed physics of the entanglement fluctuations (including KPZ exponents) certainly relies on noise. However the coarser features of the dynamics are in fact deterministic. These include the leading order time dependence of the entanglement entropy and mutual information when the length and time scales are large. We conjecture that this leading order behaviour, as captured by the directed polymer and hydrodynamic pictures, carries over to Hamiltonian dynamics without noise. On the basis of this we address (Sec. 10.4) features of entanglement growth that have previously been unclear. We argue that in generic 1D systems the entanglement growth rate can be interpreted as a well-defined *speed* v_E, but that this speed is generically *smaller* than another characteristic speed, which is the speed v_B at which quantum operators spread out under the dynamics (the 'butterfly' speed). Sec. 10.4 also addresses universal scaling forms for the entanglement entropy in 1D. In Sec. 10.6 we discuss the geometry-dependence of the dynamical entanglement in higher-dimensional systems: we argue that there is again a scaling picture in terms of a minimal surface, but that more nonuniversal parameters enter into the time dependence than in 1+1D.

10.1   Surface growth in 1D

We begin by studying entanglement growth under random unitary dynamics in one dimension. After summarizing the KPZ universal behavior, we derive this behaviour analytically in a solvable model, using a mapping to a classical surface growth problem. In the following sections we provide alternative derivations of this universal behaviour by relating the 'minimal cut' bound

on the entanglement to the classical problem of a directed polymer in a random environment, and by relating the spreading of quantum operators to a 1D hydrodyamics problem.

Consider a chain of quantum spins with local Hilbert space dimension q (for example spin-1/2s with $q = 2$). We take open boundary conditions, and label the *bonds* of the lattice by $x = 1, \ldots L$. We consider only unitary dynamics, so the full density matrix $\rho = |\Psi\rangle \langle \Psi|$ represents a pure state. For now we consider the entanglement across a single cut at position x; we will generalize to other geometries later in the paper. The reduced density matrix ρ_x is defined by splitting the chain into two halves at x and tracing out the left-hand side (Fig. 10-2). The nth Renyi entropy for a cut at x is defined as

$$S_n(x) = \frac{1}{1-n} \log \left(\mathrm{Tr}\, \rho_x^n \right). \tag{10.1}$$

Logarithms are taken base q. In the limit $n \to 1$ the Renyi entropy becomes the von Neumann entropy,

$$S_{\mathrm{vN}}(x) = - \mathrm{Tr}\, \rho_x \log \rho_x. \tag{10.2}$$

A basic constraint on the von Neumann entropy is that neighboring bonds can differ by at most one[1]:

$$\left| S_{\mathrm{vN}}(x+1) - S_{\mathrm{vN}}(x) \right| \leq 1. \tag{10.3}$$

In this section we focus on the growth of the bipartite entropies $S(x,t)$ with time, starting from a state with low entanglement. (Here $S(x,t)$, without a subscript, can denote any of the Renyi entropies with $n > 0$.) For simplicity we take the initial state to be a product state, but we expect the same long-time behaviour for any initial state with area-law entanglement.[2] We will argue that for noisy unitary dynamics, the universal properties of $S(x,t)$ are those of the Kardar–Parisi–Zhang equation:

$$\frac{\partial S}{\partial t} = \nu\, \partial_x^2 S - \frac{\lambda}{2}(\partial_x S)^2 + \eta(x,t) + c. \tag{10.4}$$

This equation was introduced to describe the stochastic growth of a 1D surface or interface with height profile $S(x)$ [313]. It captures an important universality class which has found a wealth of applications in classical nonequilibrium physics, and its scaling properties have been verified in high-precision experiments [293, 292]. The constant c in Eq. 10.4 contributes to the positive average growth rate, while $\eta(x,t)$ is noise which is uncorrelated in space and time. The ν term describes diffusive smoothing of sharp features. The nonlinear term, with coefficient λ, describes how the average growth rate depends on the slope; the negative sign is natural here, as discussed in Sec. 10.1.1 (and implies that B in Eq. 10.6 below is positive).

KPZ scaling is characterized by an exponent β governing the size of fluctuations in the

---

[1] This follows from subadditivity of the von Neumann entropy.

[2] The setup with area-law entanglement in the initial state is analogous to a quantum quench which starts in the ground state of a non-critical Hamiltonian. We briefly consider initial states with non-area-law entanglement in Sec. 10.7.
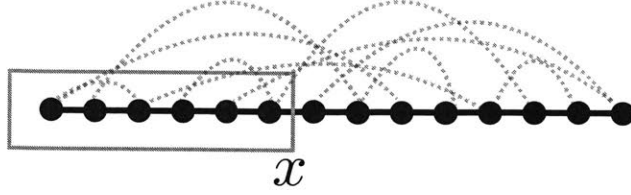
Figure 10-2: Spin chain with open boundary conditions. $S(x)$ denotes the entanglement entropy (von Neumann or Renyi depending on context) between the part of the chain to the left of bond x, indicated by the box, and the part to the right.

interface height, an exponent α governing spatial correlations, and a dynamical exponent z determining the rate of growth of the correlation length ($z = \alpha/\beta$ by a scaling relation). These are known exactly [313]:

$$\beta = 1/3, \qquad\qquad \alpha = 1/2, \qquad\qquad z = 3/2. \qquad (10.5)$$

In our context the height of the surface is the bipartite entanglement $S(x,t)$. This is a random quantity which depends on the realization of the noise in the quantum dynamics. The mean height/entanglement grows linearly in time, with a universal sub-leading correction:

$$h(x,t) \equiv \langle S(x,t) \rangle = v_E t + Bt^\beta. \qquad (10.6)$$

Angle brackets denote an average over noise. The linearity of the leading t dependence is expected from rigorous bounds for various 1+1D random circuits [220, 319, 320]. Linear growth is also generic for quenches in translationally invariant 1D systems [52, 62]. The fluctuations grow as

$$w(x,t) \equiv \langle \langle S(x,t)^2 \rangle \rangle^{1/2} = Ct^\beta. \qquad (10.7)$$

We will refer to w as the 'width' of the surface. The ratio C/B is universal (the constants v_E and B are not). The KPZ fluctuations are non-Gaussian: remarkably, their universal probability distribution has been determined analytically [260, 261, 262, 263, 264, 265, 266, 267, 268, 269, 270].

The correlation length governing spatial correlations in the fluctuations grows with time as

$$\xi(t) \sim t^{1/z}, \qquad (10.8)$$

and the equal time correlation function has the scaling form

$$G(r) \equiv \left\langle [S(x,t) - S(x+r,t)]^2 \right\rangle^{1/2} = r^\alpha g\left(r/\xi(t)\right). \qquad (10.9)$$

On length scales $1 \ll r \ll \xi(t)$, the surface profile $S(x)$ resembles the trace of a 1D random walk: this is consistent with the exponent $\alpha = 1/2$. On scales $r \gg \xi(t)$ the fluctuations in $S(x,t)$ and $S(x+r,t)$ are essentially uncorrelated.

223

At short times the entanglement growth is affected by initial conditions, while on very long timescales, of the order of the system size, the entanglement saturates. The formulae (10.6)—(10.9) apply *prior* to this saturation. In a finite system the asymptotic $\langle S(x) \rangle$ profile is that of a pyramid, with a maximum at height $x = L/2$, whose height is $L/2$, minus an $O(1)$ correction [321, 322]. This profile is reached at a time

$$t_{\text{saturation}} \simeq \frac{L}{2v_E}, \tag{10.10}$$

with bonds closer to the boundary saturating sooner (Secs. 10.2, 10.4). Saturation is also captured in the surface growth description, once we note that there are Dirichlet boundary conditions on the entropy: $S(0,t) = S(L+1,t) = 0$.

Note that the scaling described in Eqs. 10.6, 10.8 implies the existence of two distinct diverging lengthscales during entanglement growth. The fact that $\langle S(x,t) \rangle$ is of order t implies that spins are entangled over distances of order t. In fact we will show in Sec. 10.4 that $v_E t$ is a sharply defined lengthscale. But prior to saturation, the relevant lengthscale for spatial variations in $S(x,t)$ is parametrically smaller than $v_E t$, namely $\xi(t) \sim t^{2/3}$.

Before deriving KPZ for entanglement, let us briefly consider the status of this equation. At first sight we might try to justify this description of $S(x,t)$ simply on grounds of symmetry and coarse graining. *If* we were describing classical surface growth, we would appeal to translational symmetry in the growth direction ($S \rightarrow S + $ const.) in order to restrict the allowed terms, and would note that the right-hand-side includes the lowest–order terms in ∂_x and $\partial_x S$. But for entanglement we cannot rely on this simple reasoning. First, the transformation $S \rightarrow S + $ const. is not a symmetry (or even a well-defined transformation) of the quantum system. More importantly, it is not clear *a priori* that we can write a stochastic differential equation for $S(x,t)$ alone, since the full quantum state contains vastly more information than $S(x,t)$. Despite these differences from simple surface growth, we will show that the above equation does capture the universal aspects of the entanglement dynamics.

In the next section we exhibit a solvable quantum model which maps to a classical surface growth problem that is manifestly in the KPZ universality class. Then in the two following sections we give heuristic arguments for more general systems by making connections with the other members of the KPZ triumvirate. Together with the results for the solvable model, these arguments suggest that KPZ exponents should be generic for entanglement growth in any quantum system whose dynamics involves time-dependent randomness. In Sec. 10.5 we perform numerical checks on KPZ universality for quantum dynamics in discrete time.

10.1.1   Solvable 1D model

We now focus on a specific quantum circuit model for the dynamics of a spin chain with strong noise. We take random unitaries to act on pairs of adjacent spins (i.e. on bonds) at random locations and at random times, as illustrated in Fig. 10-3. For simplicity we discretize time and
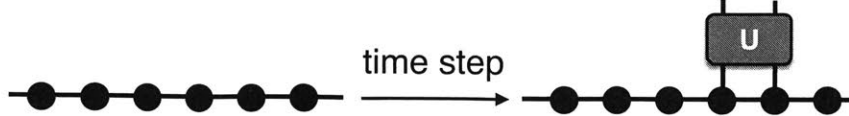
Figure 10-3: Dynamical update in the solvable model: application of a random unitary U to a randomly chosen pair of adjacent spins.

apply one unitary per time step. (Dynamics in continuous time, with unitaries applied to the links at a fixed rate in a Poissonian fashion, are equivalent.) We choose the initial state to be a product state, with $S_n(x) = 0$ for all n and x. We choose the unitaries from the uniform (Haar) probability distribution on the unitary group for a pair of spins, $U(q^2)$. This model is solvable in the limit of large local Hilbert space dimension q.

Dynamics of Hartley entropy

A useful starting point is to consider the $n \to 0$ limit of the Renyi entropy, S_0. This is known as the Hartley entropy, and quantifies (the logarithm of) the number of nonzero eigenvalues of the reduced density matrix. Equivalently, the Hartley entropy determines the minimal necessary value of the local *bond dimension* in an exact matrix product representation [72, 323] of the state:

$$S_0(x) = \log\left(bond\ dimension\ at\ x\right). \tag{10.11}$$

Like the von Neumann entropy, the Hartley entropy of neighboring bonds can differ by at most one:

$$\left|S_0(x+1) - S_0(x)\right| \leq 1. \tag{10.12}$$

Recall that logarithms are base q. For the present we keep q finite.

For the random dynamics described above (Sec. 10.1.1), the Hartley entropy obeys an extremely simple dynamical rule. In a given time step, a unitary is applied at a random bond, say at x. Applying this unitary may change the Hartley entropy across the bond x; the entropy remains unchanged for all other bonds. The rule for the change in $S_0(x)$ is that, with probability one, it increases to the *maximal* value allowed by the general constraint (10.12):

$$S_0(x, t+1) = \min\{S_0(x-1, t), S_0(x+1, t)\} + 1. \tag{10.13}$$

This 'maximal growth' of S_0 occurs with probability one when all unitaries are chosen randomly. Fine-tuned unitaries (e.g. the identity) may give a smaller value, but these choices are measure zero with respect to the Haar distribution.

We present a rigorous proof of Eq. 10.13 in Appendix D.1. The appendix also gives a heuristic parameter-counting argument which suggests the same result, but as explained there

225

the more rigorous argument is necessary as the heuristic argument can be misleading. We note that Ref. [324] observed that the growth in bond dimension, when a unitary is applied to a matrix product state, is upper-bounded by the right hand side of Eq. 10.13 and used this to obtain an upper bound on bond dimension growth during a quantum computation.

For the random dynamics we are considering, the dynamical rule in Eq. 10.13 leads to a simple but nontrivial stochastic process. Before discussing its properties, we use Eq. 10.13 as a starting point to show that in the limit of large Hilbert space dimension the von Neumann entropy (and in fact all the higher Renyi entropies) obeys the *same* dynamical rule. This requires an explicit calculation in the limit $q \to \infty$. The von Neumann entropy is of more interest than S_0, since the latter behaves pathologically in many circumstances.[3]

Properties of the Solvable Model

The present quantum circuit dynamics lead to a solvable model in the limit of large local Hilbert space dimension, $q \to \infty$. In this limit *all* the Renyi entropies obey the dynamical rule in Eq. 10.13.

To show this we consider the reduced density matrix for a cut at x, where x is the bond to which we are applying the unitary in a given time step. We may write $\rho_x(t+1)$ in terms of $\rho_{x-1}(t)$ and the applied unitary matrix. Averaging $\mathrm{Tr}\,\rho_x^2$ *over the choice of this unitary*, we then obtain:

$$\left\langle \mathrm{Tr}\,\rho_x(t+1)^2 \right\rangle_{\mathrm{Haar}} = \frac{q}{q^2+1} \left(\mathrm{Tr}\,\rho_{x-1}(t)^2 + \mathrm{Tr}\,\rho_{x+1}(t)^2 \right).$$

See Appendix D.2 for details. In terms of the second Renyi entropy S_2 this is:

$$\left\langle q^{-S_2(x,t+1)} \right\rangle_{\mathrm{Haar}} = \frac{q^{-S_2(x-1,t)-1} + q^{-S_2(x+1,t)-1}}{1+1/q^2}. \tag{10.14}$$

The general constraint $S_2 \leq S_0$ allows us to write

$$S_2(x,t) = S_0(x,t) - \Delta(x,t) \tag{10.15}$$

with $\Delta \geq 0$. We now use Eqs. 10.13, 10.14 to show that Δ is infinitesimal at large q. Rewriting Eq. 10.14 in terms of Δ, and substituting Eq. 10.13, immediately shows

$$\left\langle q^{\Delta(x,t+1)} \right\rangle_{\mathrm{Haar}} < q^{\Delta(x-1,t)} + q^{\Delta(x+1,t)}. \tag{10.16}$$

For a simple bound[4], define $\Delta_{\mathrm{max}}(t)$ to be the maximal value of $\Delta(x,t)$ in the entire system.

---

[3]This is because it simply counts up all the (nonzero) eigenvalues in the spectrum of ρ_x, regardless of how small they are. For example, Hamiltonian dynamics in continuous time — as opposed to unitary circuits like the above — will generally give an infinite growth rate for S_0, in contrast to the finite growth rate for S_{vN} and the higher Renyi entropies.

[4]For a large system, this bound on $\left\langle q^{\Delta_{\mathrm{max}}} \right\rangle$ will be far from the tightest possible since we have not exploited the large size of the system.
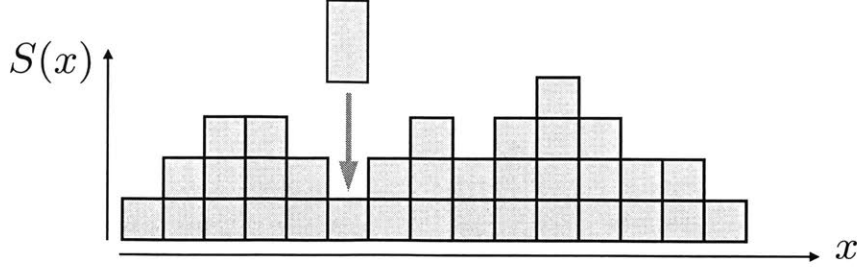
Figure 10-4: Surface growth model for entanglement $S(x,t)$ across a cut at x, in the large q limit. Applying a unitary to bond x can increase the height of the surface locally (Eq. 10.19), corresponding to dropping a 'block' of height $\Delta S = 1$ or $\Delta S = 2$.

The equation above implies

$$\left\langle q^{\Delta_{\max}(t+1)}\right\rangle_{\text{Haar}} < 2q^{\Delta_{\max}(t)} \tag{10.17}$$

We may iterate this by averaging over successively earlier unitaries:

$$\left\langle e^{(\ln q)\Delta_{\max}(t)}\right\rangle_{\text{Haar}} < 2^t. \tag{10.18}$$

This shows that as $q \to \infty$ at fixed time t, the probability distribution for Δ concentrates on $\Delta = 0$, so that S_2 and S_0 become equal.

This implies that the entanglement spectrum is flat, so in fact all the Renyi entropies obey Eq. 10.13 for the application of a unitary across bond x.

The dynamical rule we have arrived at for the bipartite von Neumann and Renyi entropies at large q,

$$S(x, t+1) = \min\{S(x-1, t), S(x+1, t)\} + 1 \tag{10.19}$$

defines a stochastic surface growth model in which $S(x,t)$ is always an integer-valued height profile (Fig. 10-4). The remaining randomness is in the choice of which bond is updated in a given time step. At each time step, a bond x is chosen at random, and the 'height' $S(x)$ is increased to the maximal value allowed by the neighbors. Fig. 10-5 gives examples of local configurations before and after the central bond is updated.

This model is almost identical to standard models for surface growth [325, 326]. It is in the KPZ universality class (it is straightforward to simulate the model and confirm the expected KPZ exponents) and some non-universal properties can also be determined exactly (see below). Note that the boundary conditions $S = 0$ on the right and the left, and the restriction $|S(x+1) - S(x)| \le 1$, imply that the entanglement eventually saturates in the expected pyramid profile.

When we move to the continuum (KPZ) description of the interface (10.4) the nonlinear λ term appears with a negative sign, meaning that entanglement growth is slower when the coarse-grained surface has a nonzero slope. This is natural given the microscopic dynamics: if the slope is maximal in some region, local dynamics cannot increase the entropy there.
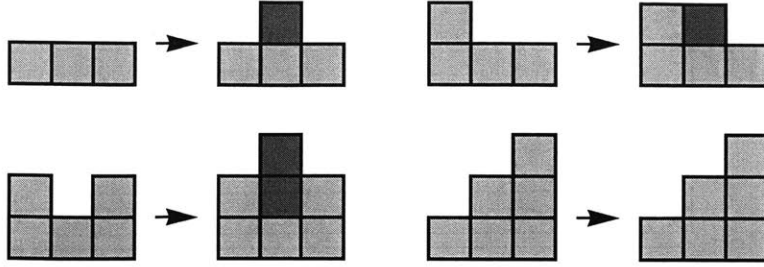
Figure 10-5: Entanglement growth in the large q model: Effect of applying a random unitary to the central bond, for four choices of the initial local entropy configuration of three adjacent bonds.

In the present model the difference in height between two adjacent bonds is either $\Delta S = \pm 1$ or $\Delta S = 0$. At early stages of the evolution both possibilities occur. However one may argue that the 'flat points', where $\Delta S = 0$, become rarer and rarer at late times.[5] At late times the model therefore becomes equivalent to the well-known 'single step' surface growth model [325], in which $\Delta S = \pm 1$ only. An appealing feature of this model is that, for a certain choice of boundary conditions,[6] the late-time probability distribution of the growing interface can be determined exactly [325]. This shows that on scales smaller than the correlation length (and prior to saturation) the interface looks like a 1D random walk with uncorrelated $\Delta S = \pm 1$ steps. This confirms the expected KPZ exponent $\alpha = 1/2$. It also allows the mean growth rate of the surface to be calculated [325]: the mean height increase in a given timestep can be calculated by averaging over the four possible initial configurations for a bond and its two neighbours. After rescaling time so that one unit of time corresponds to an average of one unitary per bond, this gives an entanglement growth rate (10.6) of

$$v_E = 1/2. \tag{10.20}$$

As we will discuss below (Secs. 10.3, 10.4) one can also associate a speed v_B with the growth of quantum operators under the random dynamics; in the present large q model this speed is[7]

$$v_B = 1. \tag{10.21}$$

It is interesting to note that here $v_E < v_B$, contrary to 1D CFTs (where $v_E = v_B$ [50]) and contrary to previous conjectures about generic systems [64]. In Sec. 10.3 we will give an appealing

---

[5]Flat points can disappear by 'pair annihilation' (Fig. 10-5, top left), and can diffuse left or right (Fig. 10-5, top right), but cannot be created. As a result their density decreases with time.

[6]The solvable case corresponds to choosing periodic BCs in the classical problem. (These BCs are useful for understanding the classical model, but they do not have an interpretation in terms of entanglement.) In this setting the mean height grows indefinitely, but the probability distribution for the height fluctuations reaches a well-defined steady state.

[7]The result $v_B = 1$ arises because in the large q limit the growth of a typical operator is limited only by the structure of the circuit. In Ref. [327] we give explicit derivations of v_B in random circuits for arbitrary q.

228
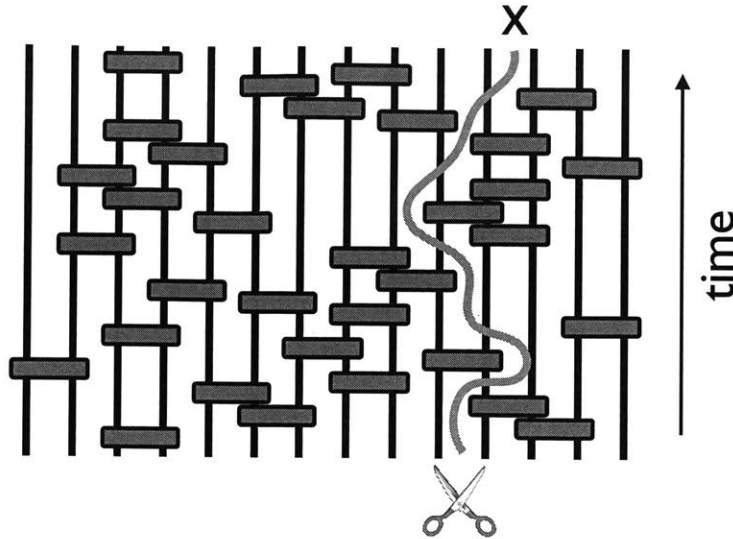
Figure 10-6: Any cut through the unitary circuit which separates the legs to the left and right of x (on the top boundary) gives an upper bound on $S(x,t)$. The best such bound is given by the minimal cut (note that the cut shown in the figure is not the minimal one). Finding the minimal cut in a random network is akin to finding the lowest energy state of a polymer in a random potential landscape.

intuitive picture for why v_E can be smaller than v_B for the case of Clifford circuits.

The mapping to surface growth gives us a clean derivation of universal entanglement dynamics in a solvable model. However this surface growth picture is restricted to the entropy for a single cut (as opposed to the entropy of a region with multiple endpoints) and to one dimension. It will be useful to find a more general language which extends the above results. To do this we now make a connection with the second member of the KPZ triumvirate (Fig. 10-2), the statistical mechanics of a polymer in a random environment.

10.2 Directed polymers and a "Minimal Cut" Prescription

In this section we relate the dynamics of $S(x,t)$ to the geometry of a 'minimal cut' through the quantum circuit which prepares the state (Fig. 10-6). This provides an alternative perspective on the exact result (10.19) for the solvable model, and also a useful heuristic picture for noisy quantum dynamics in general. This line of thinking reproduces KPZ behaviour in 1D. Importantly, it also allows us to generalize to higher dimensions and to more complex geometries.

Our starting point is the minimal cut bound for tensor networks. This very general bound has been related to the Ryu-Takayanagi formula for entanglement in holographic conformal field theories [316, 317, 318, 274, 328], and has also been applied to unitary networks as a heuristic picture for entanglement growth [77].

Consider again a random quantum circuit in 1+1D, and a curve like that in Fig. 10-6 which bisects the circuit and divides the physical degrees of freedom into two at position x. *Any* such

curve gives an upper bound on the entanglement: all the Renyi entropies satisfy $S(x) \leq S_{\text{cut}}$, where S_{cut} is the number of 'legs' that the curve passes through. (This relies only on linear algebra: the rank of the reduced density matrix ρ_x is at most[8] $q^{S_{\text{cut}}}$.)

The *best* bound of this type is given by the minimal cut, which passes through the smallest number of legs. We denote the corresponding estimate for the entropy $S_{\text{min-cut}}(x)$. If the geometry of the circuit is random, $S_{\text{min-cut}}(x)$ and the corresponding curve are also random. Finding $S_{\text{min-cut}}(x)$ amounts to an optimization problem in a classical disordered system.

In the solvable large q model, $S_{\text{min-cut}}(x)$ in fact gives the von Neumann entropy exactly. This follows straightforwardly from the results of the previous section (see below). In a typical microscopic model, on the other hand, $S_{\text{min-cut}}$ is only a bound on the true entropy. Nevertheless we conjecture that the following picture based on the minimal cut is generally valid as a *coarse-grained* picture: i.e. that it correctly captures the universal properties of the entanglement dynamics in noisy systems. This conjecture is equivalent to the applicability of the KPZ description to generic noisy systems; further evidence for the latter is in Secs. 10.3, 10.5.

The problem of finding the minimal curve is a version of a well studied problem in classical statistical mechanics, known as the directed polymer in a random environment or DPRE [309, 329]. Here the 'polymer' is the curve which bisects the circuit, and its energy $E(x)$ is equal to $S_{\text{cut}}(x)$, the number of legs it bisects. The spatial coordinate of the polymer's upper endpoint is fixed at x, while the lower endpoint is free. Finding $S_{\text{min-cut}}(x)$ is equivalent to finding the minimal value of the polymer's energy. This corresponds to the polymer problem at zero temperature; however the universal behaviour of the DPRE is the same at zero and at nonzero temperature.[9]

DPRE models with short-range-correlated disorder are in the same universality class as the KPZ equation [313]. Let $E(x,t)$ be the minimal energy of the polymer in a sample of height t. We may increase t by adding an additional layer to the top of the sample. $E(x, t + \delta t)$ can then be expressed recursively in terms of $E(y, t)$ for the various possible values of y. In the continuum limit, this leads to an equation for $E(x, t)$ which is precisely the KPZ equation (see Refs. [313, 330] for more details of the mapping between DPRE and KPZ). The KPZ exponents given in Sec. 10.1 may therefore be applied to the energy of the polymer. The exponent $z = 3/2$ also determines the lengthscale for transverse fluctuations of the polymer on large length and time scales:

$$\Delta x \sim (\Delta t)^{2/3}. \tag{10.22}$$

Since in our case the minimal E is simply $S_{\text{min-cut}}$, we find that the latter executes KPZ

---

[8]The cut divides the tensor network into two parts connected by S_{cut} bonds. One part contains the physical legs for subsystem A and the other part contains those for the complement. Regarding the two parts of the circuit as composite tensors L and R gives a representation of the state as $|\psi(t)\rangle = \sum_{i=1}^{q^{S_{\text{cut}}}} \sum_{a,b} L_a^i R_b^i |a\rangle_A |b\rangle_{\bar{A}}$, where $|a\rangle_A$ and $|b\rangle_{\bar{A}}$ are basis states in A and $\bar{A}$ respectively. This implies that the Schmidt rank for a bipartition into A and $\bar{A}$ is at most $q^{S_{\text{cut}}}$, so that S_0, which is the logarithm of the Schmidt rank, is at most S_{cut}. In turn, $S_n \leq S_0$ for any $n \geq 0$.

[9]For any finite temperature, the DPRE flows under renormalization to a zero temperature fixed point at which temperature is an irrelevant perturbation.

growth. In the light of the previous section, this is not surprising. In fact in our solvable model, $S_{\text{min-cut}}$ is exactly equal to the true entanglement entropy (in the large q limit). This follows from the fact that the recursive construction of $E(x, t)$ described above (on the lattice, rather than in the continuum) precisely matches the large q dynamics of Eq. 10.19. Examples of non-unitary tensor networks in which the minimal cut bound becomes exact are also known [318], including a large-bond-dimension limit similar to that discussed here [274].

The utility of the DPRE picture is that it is far more generalizable than the surface growth picture, which is restricted to the entropy across a single cut in 1D. As noted above, the value of $S_{\text{min-cut}}$ in a given microscopic model is typically not equal to any of the physical entropies S_n with $n > 0$. Nevertheless we conjecture that the DPRE and KPZ pictures are valid universal descriptions for all noisy models, so long as they are not fine tuned or nonlocal. This includes noisy Hamiltonian dynamics in continuous time (we discuss this case further in the Outlook section). If we restrict to the leading order deterministic behaviour we can also make conjectures about Hamiltonian systems without noise.

10.2.1 Scaling form for entanglement saturation

At leading order in time, the growth of the 'height' $S(x, t)$ is deterministic: fluctuations are a subleading effect when t is large. Similarly, Eq. 10.22 shows that the coarse-grained minimal cut is essentially vertical (prior to saturation of the entropy): the lengthscale for its transverse fluctuations is negligible in comparison with t. These pictures therefore have well-defined and simple deterministic limits. They lead directly to deterministic scaling forms for the leading order behaviour of the entanglement, which we will discuss in more detail in Sec. 10.4. Here we consider the simplest case, the saturation of the entanglement entropy $S(x, t)$ across a single cut (or for a single interval). We reproduce a simple scaling function known from other contexts [62, 213, 77].

The definition of the entanglement growth rate implies that the 'energy' E of such a vertical cut is $v_E t$ to leading order. The entanglement in a finite system grows at this rate until time $t_{\text{saturation}} = x/v_E$, when it reaches its saturation value $S = x$. (Here we are neglecting subleading terms, and assuming $x < L - x$.) After this time a vertical cut is no longer favourable: instead the minimal cut exits the circuit via the left-hand side. Its shape is no longer unique, but it can be taken to be horizontal, and it has 'energy' $E = x$. This picture corresponds to a simple scaling form (again, neglecting subleading terms)

$$S(x, t) = v_E t\, f(x/v_E t), \tag{10.23}$$

with

$$f(u) = \begin{cases} u & \text{for} \quad u < 1 \\ 1 & \text{for} \quad u \geq 1 \end{cases} \tag{10.24}$$

For a finite interval of length l in an infinite system there is a crossover between a configuration

with two vertical cuts, and one with a single horizontal cut, giving instead $S(t) = 2v_E t \, f(l/2v_E t)$.

These scaling forms are our first confirmation that v_E is really a *speed*, as well as a growth rate for the entanglement. We will give an independent derivation of this fact for Clifford circuits in the following section, and will test the above scaling form numerically in Sec. 10.5.2. We will discuss the interpretation of v_E further in Sec. 10.4.

Note that fluctuations have dropped out of Eq. 10.23 as a result of considering only the leading order behaviour of $S(x, t)$. These scaling forms agree with the results for holographic CFTs [213] and with a heuristic application of the minimal cut formula to a regular tensor network [77]. Here we see them emerging from a simple and well-defined coarse-grained picture, suggesting that they are *universal* for all generic 1D systems, including for example translationally invariant but nonintegrable spin chains.[10] It is also worth noting that Eq. 10.24 is capable of distinguishing generic systems from (nonrelativistic) integrable systems. In the latter case the quasiparticle picture applies and yields different profiles for $S(t)$ [52, 60]. For relativistic systems in which the quasiparticle picture holds (rational CFTs), all quasiparticles travel at the same speed, and as a result (10.24) does apply [50, 52] (however the entanglement of more complex regions will differ between the quasiparticle picture on the one hand, and the results from holographic systems and the minimal cut picture on the other [52, 53, 76]).

In Secs. 10.4, 10.6 we propose that the above picture in terms of a *coarse-grained* minimal cut is the simplest way to understand the basic features of the 'entanglement tsunami' for generic many-body systems (with or without noise) both in 1D and higher dimensions.

10.3 Entanglement Dynamics from Operator Hydrodynamics

An alternative way to think about the quantum dynamics is in terms of the evolution of local operators $\mathcal{O}_i$. For example, a Pauli operator initially acting on a single spin (e.g. $\mathcal{O}_i \equiv Y_i$; we denote the Pauli matrices by X, Y, Z) will evolve with time into an operator $\mathcal{O}_i(t)$ which acts on many spins. Operators typically grow ballistically [331], in the sense that the number of spins in the support of $\mathcal{O}_i(t)$ grows linearly with t. In this section we relate the growth of the bipartite entanglement to the spreading of operators. We focus on the special case of unitary evolution with Clifford circuits (defined below), but we expect the basic outcomes to hold for more general unitary dynamics. We find that the entanglement growth rate is not given by the rate at which a single operator grows, but is instead determined by collective dynamics involving many operators. Remarkably, in 1D these collective dynamics have a long wavelength hydrodynamic description.

This hydrodynamic description turns out to be the noisy Burgers equation, which is related to the KPZ equation by a simple change of variable and is the final member of the KPZ triumvirate shown in Fig. 10-1. In the present case the hydrodynamic mode is the density of certain fictitious

---

[10]Ref. [239] includes numerical tests of scaling forms derived from the directed polymer picture in deterministic systems, including extensions to inhomogeneous systems (a chain with a weak link).
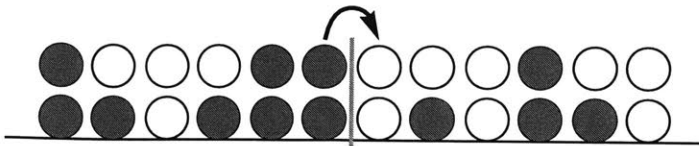
Figure 10-7: Spreading of stabilizer operators defining the quantum state (Sec. 10.3). Each blue particle marks the right *endpoint* of some stabilizer (the rightmost spin on which it acts). Blue particles hop predominantly to the right. Whenever a particle enters the right-hand region (A) the entanglement S_A increases by one bit. The particle density is described by the noisy Burgers equation, which maps to KPZ. A 'hole' (empty circle) marks the left-hand endpoint of some stabilizer.

'particles', shown in blue in Fig. 10-7. The quantum state is defined by a set of operators (Sec. 10.3.1) which spread out over time, and the particles are markers which show how far these operators have spread. We will derive their coarse-grained dynamics in Sec. 10.3.2 after introducing the necessary operator language.

In generic many-body systems (with local interactions) this process of operator growth is characterized by a speed known as the butterfly speed, v_B. This speed defines an effective lightcone within which the commutator between the spreading operator $\mathcal{O}(t)$ and a typical local operator is appreciable. The quantity v_B is a characteristic speed for the spreading of quantum information in a given model, and can be extracted from appropriate correlation functions. In deterministic systems (time-independent evolution) v_B can depend on temperature, and typically does not saturate the well-known Lieb Robinson bound [332, 235]. Generic noisy systems equilibrate to infinite temperature, so in the present models there is no notion of temperature dependence — v_B is a constant defined entirely by the dynamics.

The scaling forms discussed in the previous section show that in 1D there is a well-defined speed v_E associated with entanglement spreading. The following picture gives a physical interpretation of this speed, in terms of a certain set of growing operators. However it also shows that in general the speed v_E is smaller than the speed v_B. This is perhaps surprising: in 1D CFTs the two speeds are equal, and it has been conjectured that they are equal in general [64]. (Note that we have already encountered a solvable model with $v_E = v_B/2$ in Sec. 10.1.1.)

10.3.1 Stabilizer operators

It will be convenient to use the language of 'stabilizer' operators to describe the entanglement dynamics. We may define the initial state $|\Psi_0\rangle$ by specifying L stabilizers under which it is invariant (in this section we take the number of sites to be L). These operators, denoted $\mathcal{O}_i$ ($i = 1, \ldots, L$) satisfy

$$\mathcal{O}_i |\Psi_0\rangle = |\Psi_0\rangle \,. \tag{10.25}$$

For example, if the spins are initially polarized in the y direction we may take $\mathcal{O}_i = Y_i$. At a later time, the above equation still holds, with each stabilizer $\mathcal{O}_i$ replaced with the time-evolved stabilizer $\mathcal{O}_i(t) = U(t)\mathcal{O}_i U^\dagger(t)$, where $U(t)$ is the unitary operator that evolves the initial state to the state at time t.[11]

In the following, we focus on evolution of the initial state with unitary gates in the *Clifford group* [271]. Such gates have recently been used in toy models for many-body localization [70]. The defining feature of Clifford unitaries is that they have a simple action on Pauli operators: single-spin Pauli operators are mapped to *products* of Pauli operators.

Any product of Pauli matrices can be written as a product of X and Z matrices, so to follow the dynamics of a given stabilizer $\mathcal{O}_i(t)$, we need only keep track of which X_i and Z_i operators appear in this product. Furthermore, the overall sign of the stabilizer $\mathcal{O}_i(t)$ does not affect the entanglement properties of a system undergoing Clifford evolution, so we do not keep track of it. By writing $\mathcal{O}_i(t)$ as

$$\mathcal{O}_i(t) \propto X_1^{v_{1x}} Z_1^{v_{1z}} \dots X_L^{v_{Lx}} Z_L^{v_{Lz}}, \tag{10.26}$$

we may specify any stabilizer by a binary vector $\vec{v}$ with $2L$ components:

$$\vec{v} = (v_{1x}, v_{2x}, \dots, v_{Lx}, v_{Lz}). \tag{10.27}$$

For example, the first component of the vector $v_1 = 1$ if X_1 appears in the product, and $v_1 = 0$ otherwise. The binary vector corresponding to a stabilizer $\mathcal{O}_i = Y_i$ is

$$\vec{v} \equiv (0, \dots, 0, 1, 1, 0, \dots, 0), \tag{10.28}$$

where the locations of the nonzero elements correspond to X_i and Z_i.

We consider the dynamics in two stages. First we consider the evolution of a single operator. Then we will generalize this to understand the dynamics of the state.

How does a single stabilizer $\mathcal{O}_i(t)$ evolve? Applying a one or two-site Clifford unitary to $\mathcal{O}_i(t)$ corresponds to applying simple local updates to the string $\vec{v}$. Although the precise details of these updates will not be crucial, we now give some explicit examples of gates which we will encounter again in the numerical simulations.

As single-site examples, consider the Hadamard and Phase gates. The Hadamard is a rotation on the Bloch sphere[12] which exchanges the X and Z axes,

$$R_H = \frac{1}{\sqrt{2}}(X + Z) \tag{10.29}$$

so applying a Hadamard to site i updates the string by $v_{ix} \longleftrightarrow v_{iz}$. The Phase gate is a rotation

---

[11]Note that $\mathcal{O}_i(t)$ is not the standard Heisenberg picture operator, which would have U and $U^\dagger$ in the other order.

[12]The rotation is by π around the $(1, 0, 1)$ axis.

around the Z axis which maps X_i to $Y_i = iX_iZ_i$

$$R_P = \sqrt{Z}\,. \tag{10.30}$$

This means that an additional Z_i is generated whenever X_i is present in the string, or equivalently $v_{iz} \to v_{iz} + v_{ix}$ (mod 2). For a two-site example, consider the left and right controlled-NOT (CNOT) gates acting on the leftmost spins in the chain. In the Z basis, the action of these operators is to flip the 'target' spin iff the 'control' spin is down:

$$\mathrm{CNOT}^{(\mathrm{L})} = \frac{1}{2}\left[(1 + Z_1) + (1 - Z_1)X_2\right], \tag{10.31}$$
$$\mathrm{CNOT}^{(\mathrm{R})} = \frac{1}{2}\left[(1 + Z_2) + (1 - Z_2)X_1\right].$$

Conjugating the Pauli matrices by $\mathrm{CNOT}^{(\mathrm{L})}$ yields:

$$X_1 \to X_1X_2, \qquad Z_1 \to Z_1, \qquad X_2 \to X_2, \qquad Z_2 \to Z_1Z_2.$$

We see that the operator X_2 is added to the string if X_1 is present (and similarly for Z_1 and Z_2). Applying $\mathrm{CNOT}^{(\mathrm{L})}$ therefore updates $\vec{v}$ by

$$v_{2x} \to v_{2x} + v_{1x} \text{ (mod 2)}, \qquad\qquad v_{1z} \to v_{1z} + v_{2z} \text{ (mod 2)}.$$

$\mathrm{CNOT}^{(\mathrm{R})}$ acts similarly with the roles of the spins reversed.

It is simple to argue that random application of such operations causes the region of space in which $\vec{v}$ is nonzero to grow ballistically. This corresponds to the operator spreading itself over a region of average size $2v_Bt$, where v_B is the operator spreading (Butterfly) velocity for this system [235]. (For the present system, this velocity is also the analogue of the Lieb Robinson velocity.) The value of v_B depends on the precise choice of dynamics, but it is the same for all initial operators so long as the dynamics (the probability distribution on gates) is not fine-tuned. Further, one may argue that the interior of the region where the string $\vec{v}$ is nonzero is 'structureless'. Within the interior, $\vec{v}$ rapidly 'equilibrates' to become a completely random binary string.[13]

Now consider the dynamics of a quantum state. Once the sign information in Eq. 10.26 is dropped, the relevant information in the state $|\Psi(t)\rangle$ is contained in binary vectors $\vec{v}^1, \ldots, \vec{v}^L$

---

[13]Consider the late time dynamics of an operator, or equivalently its string $\vec{v}$, in an L-site system. Random application of Clifford gates gives random dynamics to $\vec{v}$. It is easy to see that the *flat* probability distribution on $\vec{v}$ is invariant under the dynamics, regardless of the probabilities with which the gates are applied. By standard properties of Markov processes, this is the unique asymptotic distribution to which the system tends, so long as the choice of Clifford gates is not fine-tuned to make the process non-ergodic. (If the gate set includes each gate and its inverse with the same probability, detailed balance is also obeyed, but this is not necessary.) We expect $\vec{v}$ to equilbrate locally to this structureless state on an $O(1)$ timescale, and similarly for the internal structure of operators smaller than L.

corresponding to the L stabilizers. We may package this information in a $2L \times L$ matrix:

$$\Psi(t) = \left(\vec{v}^{1\top}, \dots, \vec{v}^{L\top} \right). \tag{10.32}$$

Each *column* corresponds to a stabilizer, and each *row* to a spin operator X_i or Z_i. The dynamical updates correspond to row operations (with arithmetic modulo two) on this matrix. For example, a Hadamard gate exchanges the rows corresponding to X_i and Z_i.

A crucial point is that there is a large *gauge freedom* in this definition of the state. This gauge freedom arises because we can redefine stabilizers by multiplying them together. For example if a state is stabilized by $\{X_1, Z_2\}$, then it is also stabilized by $\{X_1 Z_2, Z_2\}$, and vice versa. This freedom to redefine the stabilizers corresponds to the freedom to make column operations on Ψ, or equivalently the freedom to add the vectors $\vec{v}^i$ modulo two. Note that by making such a 'gauge transformation' we may be able to reduce the size of one of the stabilizers, giving a more 'compact' representation of the state.

The final fact we need is an expression for the entropy $S_A(t)$ of a region A in terms of the stabilizers. Heuristically, this is given by the number of stabilizers that have spread into region A from outside. More precisely, define I_A as the number of stabilizers that are *independent* when restricted to region A.[14] (Independence of the stabilizers corresponds to linear independence of the vectors $\vec{v}^i$, with arithmetic modulo two, once they are truncated to region A.) The entropy is equal to [333, 334]

$$S_A(t) = I_A - |A|, \tag{10.33}$$

where $|A|$ is the number of sites in A. See Appendix D.3 for a simple derivation of Eq. 10.33. For Clifford dynamics all Renyi entropies are equal, so we omit the Renyi index on S. The maximal value of I_A is $2|A|$, so S_A is bounded by $|A|$ as expected.

This formula has a simple interpretation. In the initial product state we may take one stabilizer to be localized at each site, so $I_A = |A|$ and the entanglement is zero. As time goes on, stabilizers that were initially localized outside of A grow and enter A. Each time a new independent operator appears in A, the entanglement $S_A(t)$ increases by one bit. The linear independence requirement in the definition of I_A is crucial, as it leads to effective interactions between the stabilizers which we discuss in the following subsection.

From now on we take A to consist of the spins to the *right* of the bond x, and revert to the notation $S_A = S_x$ used in the rest of the text for the entanglement across a cut at x.

Figure 10-8: Left: the initial product state represented in terms of the fictitious particles. Right: a state with maximal $S(x)$.

10.3.2 Coarse-Grained Operator Dynamics

Each stabilizer $\mathcal{O}_i(t)$ (labelled $i = 1, \ldots L$) has a left and a right endpoint l_i and r_i, marking the extremal spins included in the stabilizer. We view l_i and r_i as the positions of two fictitious particles of type l and r, represented in white and blue respectively in Figs. 10-7, 10-8. There are L of each type of particle in total.

In the initial product state, $\mathcal{O}_i(0)$ is a single Pauli operator on site i, say Y_i. This means that each site has one l particle and one r particle (since $l_i = r_i = i$) as shown in Fig. 10-8 (left). As time increases the r particles will typically move to the right and the l particles to the left.

The nature of this motion depends on how we define the stabilizers. At first sight the obvious choice is to define $\mathcal{O}_i(t)$ as the unitary time evolution of the initial stabilizer, $\mathcal{O}_i(t) = U(t)Y_iU^\dagger(t)$. But in fact it is useful to exploit the gauge freedom in the choice of stabilizers to impose a different 'canonical' form. One result of this is that the stabilizers effectively grow more slowly than the Butterfly velocity v_B (discussed in the previous subsection) for the spreading of an operator considered in isolation.

Let $\rho_l(i)$ and $\rho_r(i)$ be the number of particles of each type at site i. The constraint that we impose is:

$$\rho_l(i) + \rho_r(i) = 2. \tag{10.34}$$

To see that we can impose this constraint, consider the situation $\rho_l(i) = 3$, so that there are three stabilizers that start at i. The initial element of each string can be either X, Y, or Z. If $\rho_l(i) = 3$, it is impossible for all three initial elements to be independent. We can then redefine one of the stabilizers, by multiplying it by one or both of the others, in such a way that its length decreases by one.[15] Making reductions of this kind wherever possible guarantees that $\rho_l(i) \leq 2$, and also that if $\rho_l = 2$, the initial elements of the two stabilizers are distinct. (And similarly for ρ_r.) With this convention it also follows that $\rho_l(i) + \rho_r(i) \leq 2$: otherwise the operators involved could not commute, which they must.[16] (The initial stabilizers commute, and this is preserved by the unitary dynamics and the redefinitions of the stabilizers.) Since there are a total of $2L$

---

[14]We truncate all stabilizers to region A by throwing away all the spin operators acting outside A. In this process some of the stabilizers become trivial, and some become redundant: i.e., equal to products of the others. I_A is the number of stabilizers that are independent when truncated to A. Equivalently, I_A is the rank of the matrix Ψ after the rows corresponding to the complement of A have been deleted; this is how we calculate the entropy numerically for Sec. 10.5.1.

[15]By choosing the longer stabilizer we avoid adding length at the right-hand side.

[16]Consider the case where $\rho_r(i) = 1$: for example let the corresponding stabilizer read $\mathcal{O} = \ldots X_i$. Any stabilizer contributing to $\rho_l(i)$ must be of the form $X_i \ldots$ in order to commute with $\mathcal{O}$. By the rule imposed in the text this means that $\rho_l(i) \leq 1$.

particles which all have to live somewhere, we have Eq. 10.34.

With this convention, the dynamics of the bipartite entropy $S(x)$ is simply related to the hopping dynamics of the particles. By Eq. 10.34 it suffices to consider only the r particles: an l particle is just an r 'hole'. We will write the density ρ_r of r particles as ρ. See Fig. 10-7 for a typical configuration in a subregion of the system.

The utility of the canonical form (10.34) is that the independence requirement becomes trivial. One can easily check that all the operators which have spread into A (the region to the right of x) are independent.[17] Therefore to find $S(x)$ we need only count the number of r particles to the right of the cut and subtract the number of sites:

$$S(x) = \sum_{i>x} (\rho_i - 1).$$
(10.35)

To reiterate, the entanglement increases by one every time an r particle drifts rightward across bond x (and decreases by one if it drifts across in the other direction).

Now consider the dynamics of the particles. Microscopically, a dynamical time step involves (1) application of a unitary gate, and (2) potentially a 'clipping' of stabilizers to enforce the canonical form. Effectively, the particles perform *biased* diffusion, with the restriction that more than two particles cannot share a site,

$$\rho \leq 2.$$
(10.36)

This constraint leads to 'traffic jam' phenomena familiar from the so-called asymmetric exclusion process [308], and to the same continuum description. Our essential approximation is to neglect the detailed *internal* structure of the stabilizers, and to treat the dynamics of the endpoints as effectively Markovian. We expect this to be valid at long length and time scales for the reason mentioned in the previous subsection: the internal structure of the operators is essentially featureless, and characterized by finite time scales.

We now move to a continuum description. The coarse-grained density obeys a continuity equation

$$\partial_t \rho = -\partial_x J$$
(10.37)

with J the particle current. Further, there is a symmetry under spatial reflections, which exchange left and right endpoints ($\rho_l \leftrightarrow \rho_r$). Writing

$$\rho = 1 + \Delta\rho,$$
(10.38)

---

[17]Consider the stabilizers which act in region A, i.e. the stabilizers with $r_i > x$. We may argue by contradiction that they remain independent after truncation to subsystem A. If not, this means there is some product of the truncated stabilizers which equals one. Let the rightmost spin appearing in any of these stabilizers be j. But by our convention for 'clipping' the stabilizers, it is impossible for the Pauli matrices acting on spin j to cancel out when they are multiplied together. Therefore the operators must in fact be independent.

where $\Delta\rho$ is the deviation from the mean density, the reflection symmetry is

$$x \to -x, \qquad\qquad \Delta\rho \to -\Delta\rho. \qquad\qquad (10.39)$$

To obtain a long wavelength description, we write the current as a power series in $\Delta\rho$ and ∂_x. Keeping the lowest order terms that respect the symmetry,

$$J = c - \nu\partial_x\Delta\rho - \frac{\lambda}{2}(\Delta\rho)^2 + \eta. \qquad\qquad (10.40)$$

These terms have a transparent physical meaning. The drift constant $c > 0$ reflects the fact that the average motion is to the right (i.e. operators grow over time). The ν term is simple diffusion. The noise η reflects the randomness in the dynamics. Most importantly, the nonlinear λ term is the effect of the constraint (10.34). It reflects the fact that the current is maximal when the density is close to one. The current evidently vanishes when $\rho = 0$, since there are no particles, but also when $\rho = 2$ (the particles cannot move if the density is everywhere maximal). Therefore we expect $\lambda > 0$.

From the above formulas, the density obeys

$$\partial_t\rho = \nu\partial_x^2\rho + \frac{\lambda}{2}\partial_x(\rho - 1)^2 - \partial_x\eta, \qquad\qquad (10.41)$$

known as the noisy Burgers equation [308]. The entanglement $S = \int_x(\rho - 1)$ obeys $\partial_t S = J$, leading to the KPZ equation:

$$\partial_t S = c + \nu\partial_x^2 S - \frac{\lambda}{2}(\partial_x S)^2 + \eta. \qquad\qquad (10.42)$$

The sign of λ is in agreement with that obtained from the surface growth picture in Sec. 10.1 and from the directed polymer picture in Sec. 10.2. While we have focussed here on dynamics of a restricted type (Clifford), this derivation of KPZ for entanglement provides independent support for the arguments in the previous sections.

In the language of the particles, the initial state corresponds to uniform density $\rho = 1$. Saturation of the entanglement corresponds (neglecting fluctuations) to all of the r particles accumulating on the right hand side and all of the l particles on the left (Fig. 10-8), i.e to a step function density.

As an aside, it is interesting to consider fluctuations in $S(x)$ at late times, i.e. long after the saturation of $\langle S(x)\rangle$. Let us revert to our previous notation, where the system has $L + 1$ sites and bonds are labelled $x = 1,\ldots,L$. Without loss of generality we take $x \le L/2$. When fluctuations are neglected, the region to the left of x is empty of r particles, and the entropy is maximal, $S_{\max}(x) = x$. Fluctuations will reduce the average. But in order for $S(x)$ to fluctuate downward, a blue r particle must diffuse leftward from the right half of the system in order to enter the region to the left of x, as in Fig. 10-9. This is a fluctuation by a distance $\sim (L/2 - x)$.
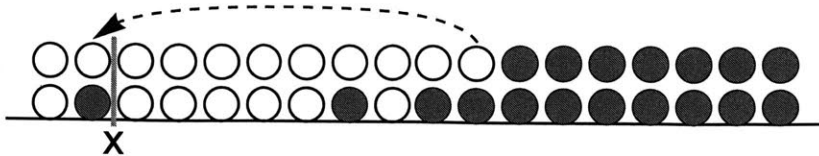
Figure 10-9: Fluctuations at late times, after saturation of $\langle S(x) \rangle$, in the Clifford case. When $x \ll L/2$ it requires a rare fluctuation (fighting against the net drift) to remove a particle from region A, leading to an exponentially small $S_{\max}(x) - \langle S(x) \rangle$.

Such fluctuations are exponentially rare events, because they fight against the net rightward drift for the r particles. Thus when $L/2 - x$ is large we expect

$$S_{\max} - \langle S(x) \rangle \sim e^{-\alpha(L/2 - x)}. \tag{10.43}$$

Our coarse-grained picture does not determine the numerical constants.

The detailed nature of these exponentially small corrections will differ between Clifford circuits and more general unitary circuits.[18] Nevertheless the functional form above agrees with the late time result for generic gate sets, which is simply the mean entanglement in a fully randomized pure state [321, 322]:

$$S_{\max} - \langle S(x) \rangle \simeq \frac{2^{|A| - |\bar{A}|}}{2 \ln 2} = \frac{4^{-(L/2 - x)}}{4 \ln 2}. \tag{10.44}$$

$|A| = x$ and $|\bar{A}| = L - x + 1$ are the numbers of sites in A and its complement. For (generic) Clifford dynamics, the probability distribution of the entanglement at asymptotically late times will be that of a random stabilizer state. This has been calculated in Ref. [335].

10.4   The Entanglement Tsunami: Speeds and Scaling Forms

It is not *a priori* obvious that the rate v_E governing entanglement growth can be viewed as a *speed* in generic systems (see Ref. [235] for a recent discussion), although this is known to be the case in holographic CFTs [213]. Our results in the directed polymer picture and in the operator spreading picture suggest that v_E is indeed a well-defined speed in generic systems. (We saw in the previous section that there is a simple visual interpretation of this speed in the stabilizer formalism.) However, this speed is in general smaller than the speed v_B which governs the spreading of an operator considered in isolation: 'thermalization is slower than operator spreading'.

In the stabilizer context the difference between v_E and v_B arises because in enforcing Eq. 10.34 we 'clip' the stabilizers, reducing their rate of growth. We believe the phenomenon

---

[18]For example in the Clifford case S_n is independent of n, while in general the corrections will depend on n [322].

of v_E being smaller than v_B to be general and relevant also to non-noisy dynamics. This picture is contrary to that of e.g. Ref. [64] where the operator spreading velocity is assumed to determine the entanglement growth rate. In the presence of noise, one may also argue that a picture of independently spreading operators underestimates the exponent governing the growth of fluctuations.[19]

The language of a 'tsunami' is often used in discussing entanglement spreading, so it is nice to see that — at least in 1D — entanglement spreading can be related to a hydrodynamic problem. (The motivation for the tsunami terminology is the idea that for a region A, the entanglement S_A is dominated by a subregion close to the boundary which grows ballistically, like the advancing front of a tsunami.) In higher dimensions the boundary of an operator has a more complicated geometry, so the hydrodynamic correspondence described above does not generalize.

In order to understand the 'entanglement tsunami' better, we now return briefly to the directed–polymer–in–a–random–medium picture developed for noisy systems in Sec. 10.2.

When all length and time scales are large, fluctuations in the entanglement are subleading. Neglecting them is equivalent to saying that the 'coarse-grained' minimal cut (prior to saturation) is a straight vertical line. This *deterministic* picture generalizes to the entanglement or mutual information of arbitrary regions, and also to higher dimensions (Sec. 10.6). We conjecture that these pictures are valid for the long-time behaviour of entanglement quite generally. The setup relevant to us in the non-noisy case is a quench, in which the initial state is a ground state of one Hamiltonian, and a different Hamiltonian is used for the evolution.

In the 1D case, the deterministic scaling form for the entanglement (of an arbitrary region) which results from the leading-order directed polymer picture is rather simple, and is not new — it agrees with holographic results [213, 76], and as noted in Ref. [77], can also be obtained from a more microscopic minimal cut picture in which the geometry of the minimal cut is highly non-unique. We propose that coarse-graining fixes the geometry of the minimal cut. The derivation of these scaling forms from a simple coarse-grained picture suggests that they are universal in non-integrable, translationally invariant systems. (These scaling forms are generally not the same as those obtained from the quasiparticle picture for rational CFTs [52, 53].) Our derivation also opens the door to generalizations to higher dimensions (Sec. 10.6.2) and to 1D systems with quenched disorder [239].

We now consider some examples of the scaling of the mutual information. This will help clarify the operational meaning of the speed v_E.

To calculate the entanglement S_A of a region A, we must take a cut, or multiple cuts,

---

[19]Considering the unitary evolution of a single operator in isolation, its right endpoint executes a biased random walk, traveling an average distance $v_B t$ with fluctuations $O(t^{1/2})$. If we were to neglect the independence requirement in Eq. 10.33 then the entanglement would be estimated (incorrectly) as the number of independently spreading operators which have reached A. The mean of this quantity is $v_B t$ and the fluctuations are of order $t^{1/4}$. This is related to the difference between the KPZ universality class of surface growth, which is generic, and the Edwards-Wilkinson universality class which applies when the strength of interactions is fine-tuned to zero [313].
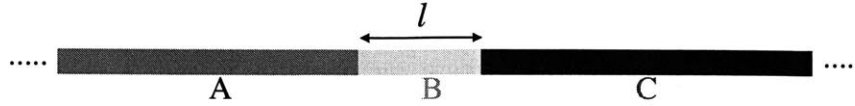
Figure 10-10: Infinite chain with regions A, B, C marked. B is of length l while A, C are semi-infinite. The mutual information between A and C is nonzero so long as $l < 2v_E t$: correlations exist over distances up to $2v_E t$, not $v_E t$.
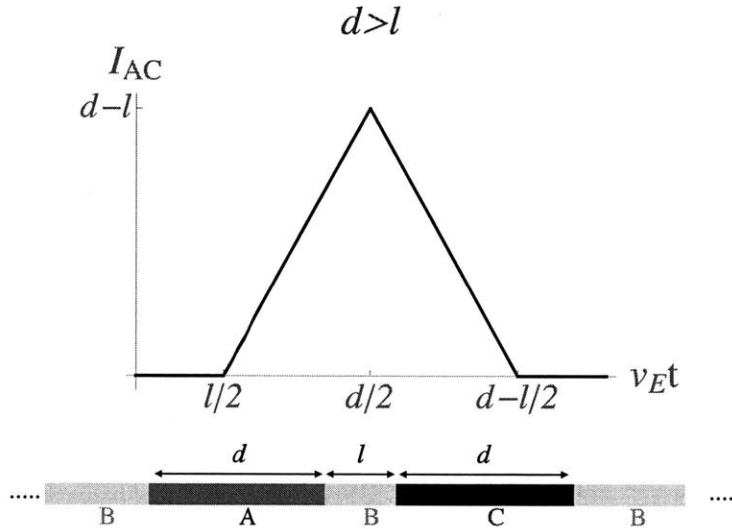
Figure 10-11: Bottom: Infinite chain with finite regions A and C each of length d, separated by distance l. Top: The mutual information between A and C in the case $d > l$. In the opposite regime the mutual information vanishes.

with endpoints on the boundary points of A at the top of the spacetime slice. These cuts can either be vertical, in which case they cost an 'energy' $v_E t$ (to use the language of Sec. 10.2), or they can connect two endpoints, in which case we take them to be horizontal and to have an energy equal to their length. The entanglement $S_A(t)$ is given by minimizing the energy of the cut configuration. It is a continuous piecewise linear function, with slope discontinuities when the geometry of the minimal cut configuration changes. To generalize the conjecture to systems without noise, we must allow for the fact that the asymptotic value of the entanglement depends on the energy density of the initial state. We therefore replace the entanglement S in the formulas with S/s_{eq}, where s_{eq} is the equilibrium entropy density corresponding to the initial energy density [51, 213]. This ensures that the entanglement entropy of an l-sized region matches the equilibrium thermal entropy when $v_E t \gg l/2$, as required for thermalization. Heuristically, s_{eq} defines the density of 'active' degrees of freedom at a given temperature [235].

To clarify the meaning of v_E, consider the mutual information between two semi-infinite regions that are separated by a distance l (Fig. 10-10). With the labelling of the regions as in
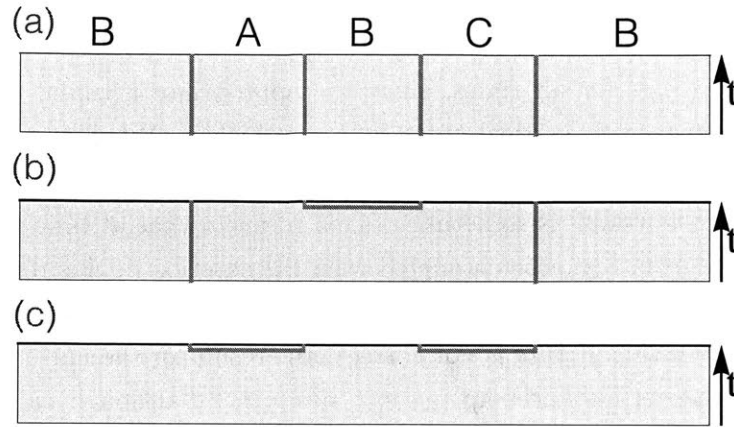
Figure 10-12: Sequence of minimal cut configurations (red lines) determining the entropy of region B in Fig. 10-11. (a) gives way to (b) when $2v_E t = l$ and (b) gives way to (c) when $2v_E t + l = 2d$.
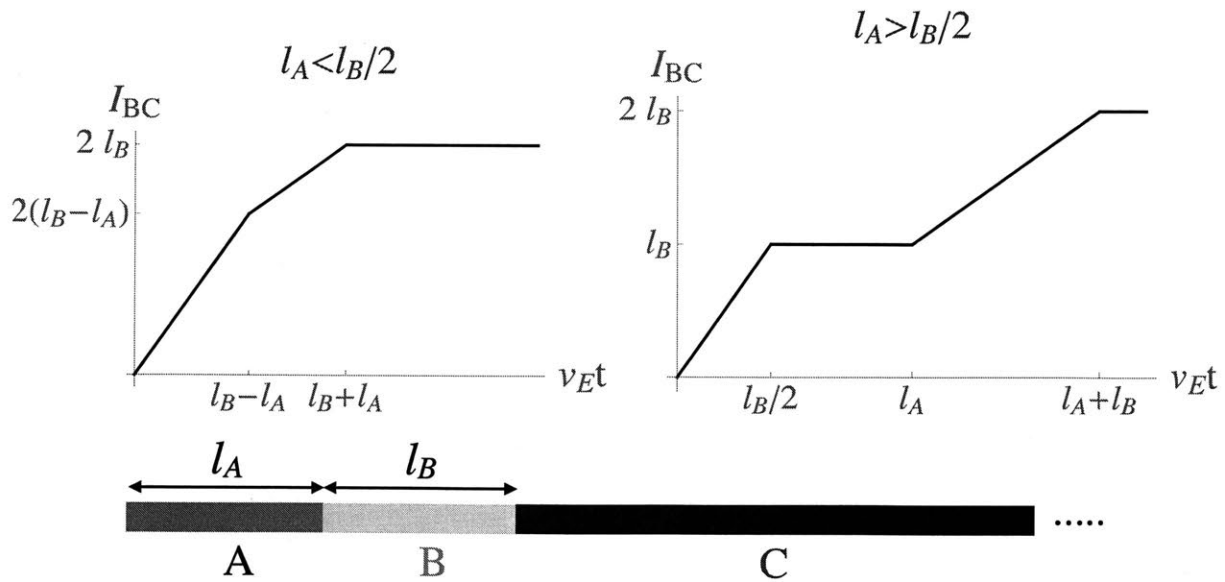
Figure 10-13: Bottom: Semi-infinite chain with regions A, B (length l_A, l_B respectively) and C adjacent to the boundary. Top: The mutual information between B and C for this geometry, for the two regimes indicated.

the figure, this is given by

$$I_{AC} = S_A + S_C - S_{A \cup C} = S_A + S_C - S_B. \tag{10.45}$$

We have $S_A = S_C = v_E t$ for all times, since the appropriate minimal cuts are vertical. If $l > 2v_E t$, S_B is given by two vertical cuts, so I_{AC} vanishes. When $l < 2v_E t$, S_B is instead dominated by a horizontal cut, so that $I_{AC} = 2v_E t - l$.

The 'entanglement tsunami' is sometimes taken to mean that at time t, a 'boundary layer' of width $v_E t$ inside a given region is entangled with the exterior. If this region were maximally entangled with the exterior, this would reproduce the correct value of the entanglement across a cut ($S = v_E t$). However this picture is not correct: the result for the mutual information shows that correlations exist over distances up to $2v_E t$, not $v_E t$. So although v_E is a speed, it should not be thought of as the speed at which the boundary of the entangled region moves.

Although the rule for calculating the entanglement is almost trivial, the consequences are not always intuitively obvious. First consider the case where the regions A and C above are finite rather than infinite (and embedded in an infinite chain); see Fig. 10-11. When the length d of the regions A and C exceeds their separation l, the time-dependence of the mutual information is as shown in Fig. 10-11. [The sequence of minimal cut configurations required for calculating S_B in this case is (a), (b), (c) shown in Fig. 10-12.] By contrast, when the separation l exceeds the length d, the mutual information is always zero (or more precisely, exponentially small[20]). [The sequence of cuts for S_B in this case is simply (a), (c)].

Finally, consider the effect of a boundary. Take a semi-infinite chain with regions A, B, C adjacent to the boundary as in Fig. 10-13 (C is semi-infinite). Consider the mutual information between B and C, $I_{BC} = S_B + S_C - S_A$. We must distinguish the case $l_A < l_B/2$ from the case $l_A > l_B/2$.[21] The resulting expressions for I_{BC} are plotted in Fig. 10-13.

10.5 Numerical evidence for KPZ growth

We now give numerical evidence that noisy entanglement growth in 1D is in the KPZ universality class. We study the time evolution of spin-$\frac{1}{2}$ chains with open boundary conditions, taking the initial state to be a product state with all spins pointing in the same direction (either the positive y or z direction) and keeping track of the entanglement entropy across each bond during the evolution. The discrete time evolution is a circuit of one- and two-site unitaries. Fig. 10-14 shows the structure of a single time step: two layers of 2-site unitaries are applied, one layer on odd and one on even bonds, together with single-site unitaries. Each unitary is chosen

---

[20]For a simpler example of exponentially small values of the mutual information, consider $\langle I_{AC} \rangle$ at infinite times in a finite system. If the system contains L qubits and $A \cup C$ contains N qubits, the mutual information is exponentially small whenever $N < L/2$, and given by Eq. 10.44 as $\langle I_{AC} \rangle \sim (2 \ln 2)^{-1} 2^{-(L-2N)}$.

[21]In the former case the first 'event' is that the minimal cut at the boundary of A goes from being vertical to being horizontal; in the latter the first event is that the two vertical cuts at the boundary of B are replaced by a horizontal one.
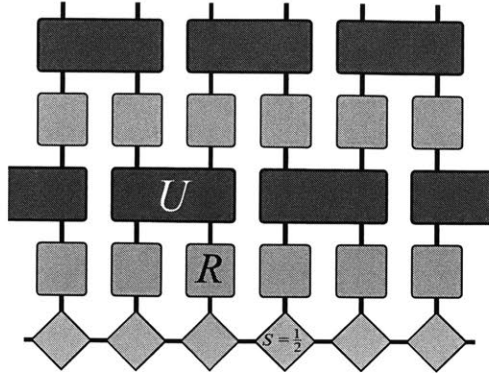
Figure 10-14: Schematic structure of a layer in the quantum circuits used for simulations.

independently and randomly (from a certain set specified below). We will use the symbol R to denote a generic single-site unitary, and U to denote a 2-site unitary.

We consider three kinds of dynamics, distinguished by the choice of unitaries. To begin with we study '*Clifford evolution*' in which the unitaries are restricted to the set of so-called Clifford gates (Sec. 10.3). Clifford evolution can be simulated efficiently (in polynomial time) using the stabilizer representation discussed in Sec. 10.3. This allows us to access very long times and to pin down KPZ exponents accurately. Next we study more general dynamics for which polynomial-time classical simulation is impossible, giving evidence that KPZ behaviour holds more generally. The two types of non-Clifford dynamics studied here are referred to as the '*phase evolution*' and the '*universal evolution*': details are given below. For these dynamics we use a matrix product representation of the state implemented via ITensor [336].

The fingerprints of KPZ behaviour that we search for are the two independent critical exponents β and α (Sec. 10.1). We extract β both from the fluctuations in the von Neumann entropy and from the corrections to the mean value (Eqs. 10.6, 10.7), and we extract α from the spatial correlations in the entanglement at distances shorter than the correlation length $\xi(t)$ (Eq. 10.9). For Clifford circuits we will also touch on the entanglement probability distribution.

10.5.1 Clifford evolution

Clifford circuits, or 'stabilizer circuits', are a special class of quantum circuits which play an important role in quantum information theory. As shown by Gottesman and Knill, they can be simulated efficiently, even when the entanglement entropy grows rapidly, by representing the quantum state in terms of stabilizers [175]: see Sec. 10.3.

The time evolution operator for a Clifford circuit belongs to the Clifford *group*, a subgroup of the unitary group on the full Hilbert space. This group may be generated by a small set of local Clifford gates: the two-site controlled NOT gates (Eq. 10.31) and the single-site Hadamard and Phase gates R_H and R_P (Eqs. 10.29,10.30). For circuits built from these gates, time-evolving the state on L spins up to a time t takes a computational time of order Lt and measuring the
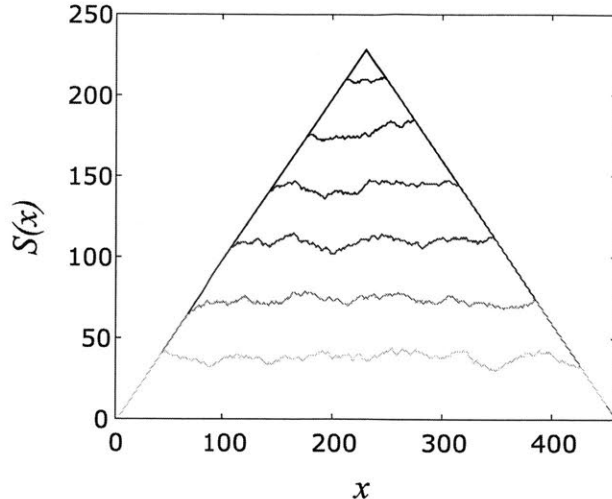
Figure 10-15: The von Neumann entropy $S(x,t)$ for a system of length $L = 459$, as a function of x, for several successive times ($t = 340, 690, 1024, 1365, 1707, 2048$ and 4096), in the Clifford evolution. The figure shows how the state evolves from a product state to a near-maximally entangled one. Prior to saturation the entanglement displays KPZ-like stochastic growth. $S(x,t)$ is in units of $\log 2$.

entanglement across a given bond in the final state takes a time of order L^3 at most. This is in sharp contrast to the exponential scaling which is inevitable for more general circuits.

In all our simulations, each *two*-site unitary U in the circuit is chosen with equal probability from three possibilities: the two types of CNOT gate (Eq. 10.31) and the identity matrix:

$$U \in \left\{ 1, \text{CNOT}^{(L)}, \text{CNOT}^{(R)} \right\}. \tag{10.46}$$

In this section we discuss the simplest Clifford dynamics, which includes *only* these gates, and no 1-site unitaries ($R = \mathbb{1}$). When the initial state is polarized in the y–direction, this set of gates is sufficient to give nontrivial entanglement evolution, with universal properties that turn out to be the same as those for more generic gate sets. We have also studied the 'full' Clifford dynamics in which all the Clifford generators are used, choosing the single site unitaries randomly from the three options

$$R \in \{1, R_H, R_P\} \tag{10.47}$$

Results for this case are similar and are given in Appendix. D.5.

To begin with, Fig. 10-15 shows the evolution of the bipartite von Neumann entropy $S(x)$ (in units of $\log 2$) for a single realization of the noise (i.e. a particular random circuit) in a system of $L = 459$ sites. The curves show successively later times. Note that the entropy saturates more rapidly closer to the boundary, because the maximum entanglement across a bond is proportional to its distance from the boundary. At very late times $S(x,t)$ saturates to a pyramid-like profile representing close-to-maximal entanglement. Our interest is in the stochastic growth *prior* to saturation, which we will show is KPZ–like. All observables in the
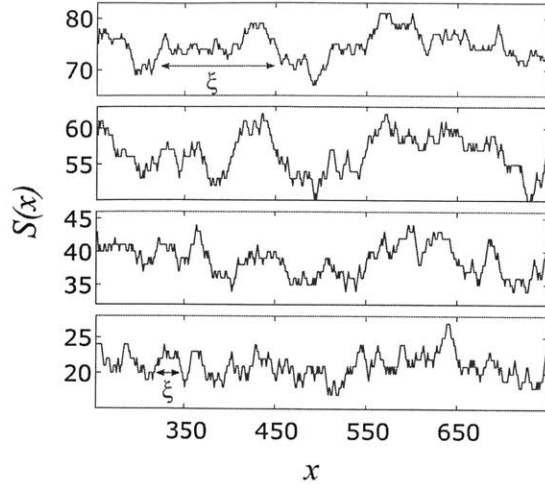
Figure 10-16: The von Neumann entropy $S(x,t)$ in units of $\log 2$, far from the boundaries, in a system of length $L = 1025$ at various times (from bottom to top $t = 170, 340, 512$ and 682) evolved with the Clifford evolution scheme. ξ schematically shows the typical correlation length Eq. [10.8] which grows in time like $t^{1/z}$.

Table 10.1: Summary of all fitting parameters to Eq. 10.49 used in this section. The Errors set the estimated 2σ uncertainty.

Evolution	v_E	β_h	B	β_w
Clifford	0.1006 ± 0.0001	0.33 ± 0.01	0.66 ± 0.04	0.32 ± 0.02
Phase	0.133 ± 0.03	–	0.54 ± 0.04	–
Universal	0.202 ± 0.001	–	0.09 ± 0.005	–

Evolution	C	η	D
Clifford	0.28 ± 0.05	0.08 ± 0.1	0.16 ± 0.04
Phase	0.223 ± 0.004	–	0.168 ± 0.03
Universal	0.14 ± 0.003	–	0.36 ± 0.01

following are measured far from the boundary, in order to avoid finite-size effects associated with saturation.

Fig. [10-16] shows successive snapshots for a subregion of a larger system of $L = 1025$ bonds (times $t = 170, 340, 512, 682$, from bottom to top). The maximal slope that can appear is 1, in accord with Eq. 10.3. Note the gradual roughening of the surface and the growing correlation length.

Fig. 10-17 shows the 'height' and 'width' of the growing surface,

$$h(t) = \langle S_{\mathrm{vN}}(x,t) \rangle, \qquad\qquad w(t) = \sqrt{\langle\langle S_{\mathrm{vN}}^2(x,t)\rangle\rangle} \qquad (10.48)$$

for very long times. These quantities have been averaged over at least 10^5 realisations. In each realisation only the entanglement across the center bond is used (therefore all data points are
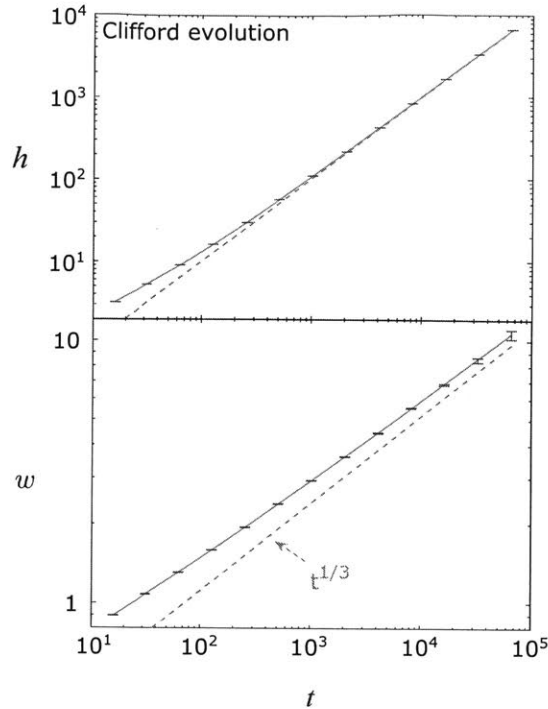
Figure 10-17: Top: Growth of the mean entanglement with time for the Clifford evolution with only CNOT gates (in units of $\log 2$). The solid red curve is a fit using Eq. [10.49]. The exponent β is found to be $\beta = 0.33 \pm 0.01$, in agreement with the KPZ prediction $\beta = 1/3$. Dashed line shows asymptotic linear behaviour. Bottom: Growth in the fluctuations in the entanglement with time. The dashed line shows the expected asymptotic behaviour, $w(t) \sim t^\beta$ with $\beta = 1/3$. The fit includes a subleading correction: Eq. [10.49], with $\beta = 0.32 \pm 0.02$. Error bars denote the 1σ uncertainty.

uncorrelated) and the system size is $L = at$, where a is chosen to avoid finite size effects (see Sec 10.5.2). We obtain estimates β_h and β_w of the exponent β by fitting the data to the expected forms (cf. Eqs. 10.6, 10.7):

$$h(t) = v_E\,t + B\,t^{\beta_h}, \qquad\qquad w(t) = C\,t^{\beta_w} + D\,t^\eta. \qquad (10.49)$$

Here η (with $\eta < \beta_w$) captures subleading corrections. We find:

$$\beta_h = 0.33 \pm 0.01, \qquad\qquad \beta_w = 0.32 \pm 0.02. \qquad (10.50)$$

Both estimates of β are in excellent agreement with the KPZ value $\beta = 1/3$. The solid lines in Fig. 10-17 show the fits (the fit parameters are in Table 10.1). The dashed lines show the slopes corresponding to the expected asymptotic power laws, $h(t) \sim t$ and $w(t) \sim t^{1/3}$.

The analysis in Sec. 10.3 implies that v_E is a well-defined velocity, and $v_E t$ is a sharply-defined *lengthscale* characterizing the range of entanglement in the state. We may confirm this by measuring this lengthscale directly, see the subsection below.

248
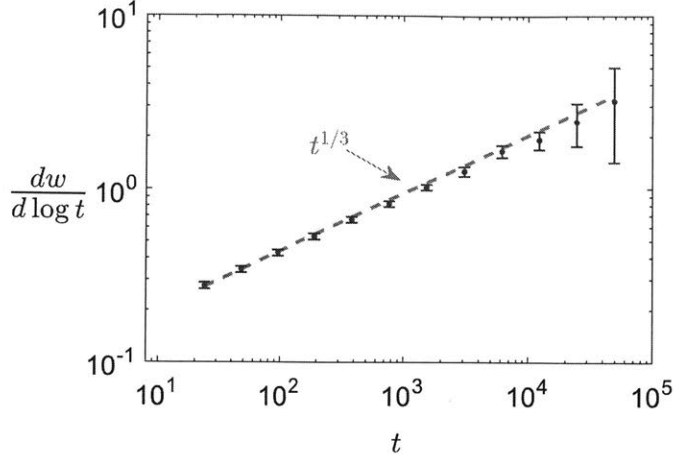
Figure 10-18: The logarithmic derivative of the width, $dw/d\log t$, vs. time for the Clifford evolution. The universal behavior with exponent $t^{1/3}$ is observed at shorter time scales compared with Fig. 10-17.

Note the small value of the subleading exponent η obtained from the fit. This implies that finite time corrections are reduced if we plot the numerical derivative $dw/d\log t$ rather than w itself (both quantities scale as $t^{1/3}$ at long times). This is done in Fig. 10-18. The data fits well to the $t^{1/3}$ law even at short times. This will be useful for the more general dynamics where long times are not available.

To complete the check of the two independent KPZ exponents, Fig. 10-19 shows the spatial correlator $G(r)$ defined in Eq. 10.9, as a function of separation r, for three successive times. For small r the correlation grows like a r^α with $\alpha \simeq 1/2$, in agreement with the KPZ prediction for this exponent. For distances $r \gg \xi(t)$, the correlator saturates to a value proportional to $w(t)$. The figure gives an idea of the size of the correlation length $\xi(t)$ for these times.

Finally, recent advances in KPZ theory have yielded an analytical expression for the full probability distribution of the KPZ height field [260, 261, 262, 263, 264, 265, 266, 267, 268, 269, 270]. In Appendix D.7 we show that this analytical result compares well with Clifford numerics, providing further support for KPZ universality in this system.

10.5.2 Numerics on Speeds and Scaling Forms

We argued in Sec. 10.4 that in addition to determining the entanglement growth rate, v_E can also be viewed as a speed. This is the speed of the fictitious particles in Sec. 10.3. Operationally, the simplest manifestation of this speed is in the saturation behaviour of the entanglement. The analytical arguments imply that to leading order (at large t and l) the entanglement across a cut at position l ($l \leq L/2$) has the simple scaling form given above in Eq. 10.24,

$$S_A = v_E t\, f(l/v_E t), \quad f(u) = \begin{cases} u & \text{for} \quad u < 1 \\ 1 & \text{for} \quad u \geq 1 \end{cases} \tag{10.51}$$

249
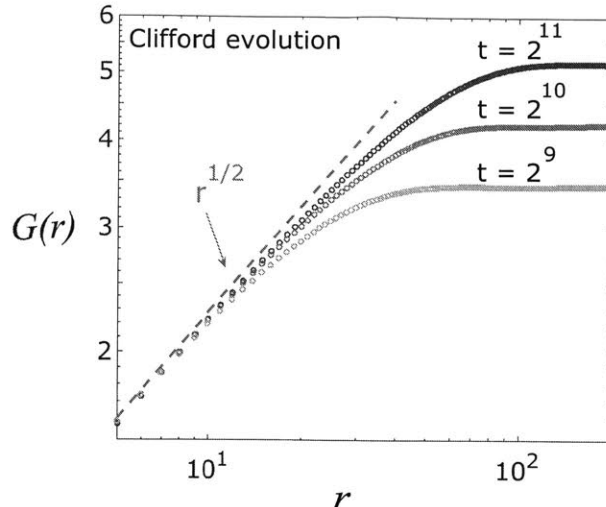
Figure 10-19: Correlation function $G(r) = \langle [S(r) - S(0)]^2 \rangle^{1/2}$ at time $t = 512, 1024$ and 2048 for the Clifford evolution, showing excellent agreement with the KPZ prediction $G(r) \sim r^\chi$ with $\chi = 1/2$ in the regime $r \ll \xi(t)$.

This gives simply $S_A = v_E t$ for $t < l/v_E$, and $S_A = l$ for $t > l/v_E$. This means that there is no influence of the boundary at times $t < l/v_E$. (See also the numerical results in Refs. [220, 319], indicating sharp saturation in circuits where interactions between any pair of spins are allowed.)

In Fig. 10-20 we test this result numerically for the Clifford evolution. We set $l = L/2$ and plot

$$\frac{S(L/2, t)}{v_E t} \quad \text{vs.} \quad \frac{L/2}{v_E t} \tag{10.52}$$

as a function of L, for several values of the time ($t = 2^9, 2^{10}, 2^{11}$ and 2^{12}). Here $v_E = 0.1$ is taken from the fits to Fig. 10-17. According to (10.51), this plot should converge for large t to a plot of $f(u)$ against u. The results are in excellent agreement with the scaling form, confirming, for the case of Clifford circuits, that v_E is a meaningful velocity.

It is also interesting to compare the entanglement velocity, v_E, with the butterfly velocity, v_B. We obtain v_B from the average spatial extent W of a growing Pauli string (see Sec. 10.3.1) under the unitary Clifford dynamics at time t, as $v_B = W/2t$. Remarkably, we find that $v_E = v_B/2$ within numerical precision for both the CNOT-only Clifford dynamics and the 'full' Clifford dynamics defined above. This is shown in Fig. 10-21, where we plot W starting vs. time for the two protocols. The initial Pauli strings we consider in this simulation are single-site Y operators.[22] We compare W with four times the average entanglement entropy, $4S(t)$. The two curves lie on top of each other, consistent with $v_E/v_B = 1/2$.

We also found the same ratio for v_E/v_B in the exactly solvable large-q model (Sec. 10.1.1). However it is possible to construct non-fine-tuned random circuits, involving Haar-random unitaries at finite q, in which the ratio is less than $1/2$ [327], so this value is not universal. A

---

[22]The CNOT dynamics is not ergodic on the space of Pauli strings (unlike the full Clifford dynamics). Nevertheless, any operator grows in size at the same rate v_B.
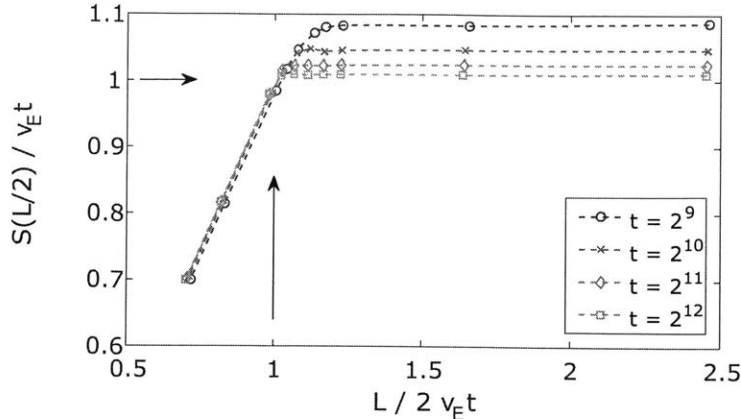
Figure 10-20: The entropy across the centre of the chain (in units of log 2) divided by $v_E t$ vs. $L/2v_E t$ for various fixed values of t. This plot converges nicely to the scaling form in (10.51).

natural question is whether it is generic for random Clifford circuits.

10.5.3 Universal and Phase evolution

The 'Phase' and 'Universal' dynamics take us outside the Clifford realm, and cannot be simulated efficiently on a classical computer (in polynomial time). We will give evidence that the correspondence with KPZ continues to hold in this more generic situation. However, our results will not be as conclusive as in the Clifford evolution as we will not have access to such long times.

The simulations are performed on spin-1/2 chains of length $L = 500$ bonds (501 spins) using the ITensor package [336]. The two types of dynamics are defined as follows. (The 2-site unitaries are always chosen from the set in Eq. 10.46; the initial state is taken polarized in the y-direction.)

Phase evolution: Each single-site unitary is chosen randomly and uniformly from the set of eightfold rotations about the z axis in spin space: $R = \exp(\pi i n \sigma^z / 8)$ with $n \in 1, \ldots, 8$.

Universal evolution: This set of gates, unlike the others, is 'universal' in the quantum information sense (any unitary acting on the full Hilbert space of the spin chain can be approximated, arbitrarily closely, by a product of gates from this set). The single-site gates include the eightfold rotations mentioned above, together with the Hadamard gate R_H (10.29). R_H is applied with probability 1/2 and the rotations with probability 1/16 each.

Fig. [10-22] shows the height and width $h(t)$ and $w(t)$ for the two protocols (averaged over 380 realisations for the Phase evolution and 200 realisations for the Universal evolution, and over bonds x with $20 < x < 480$). The figure shows fits to the forms in Eq. 10.49 with β_h and β_w *fixed* to the KPZ value and η fixed to zero (fit parameters are in Tab. 10.1). The fits with Eq. 10.49 are consistent with the data. It is not possible to extract precise estimates for β from the slope of the log-log plot of $w(t)$, although for the Phase evolution the slope at late times is in reasonable agreement with the expected KPZ value, shown by the dashed grey trendline.

251
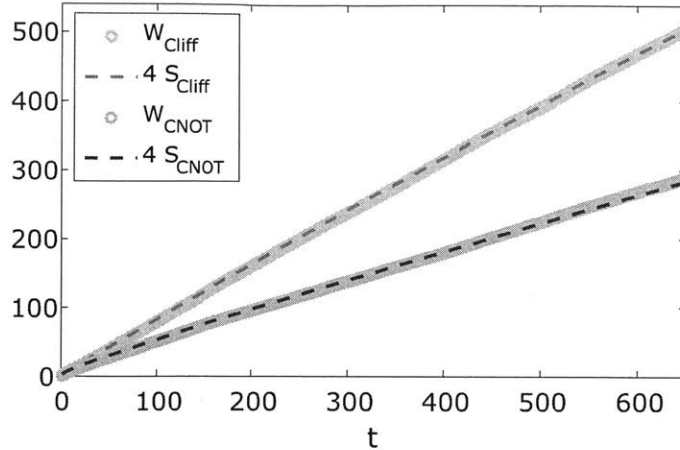
Figure 10-21: The average size W of a growing Pauli string as a function of time for two protocols, CNOT evolution (subscript 'CNOT') and the full Clifford evolution (subscript 'Cliff'). The correspondence with the dashed lines, showing the average entanglement entropy multiplied by four, is consistent with $v_E = v_B/2$. (Taken from a system of size $L = 1024$.)

For an alternative attack on β we plot the numerical derivative $dw(t)/d\ln t$. We found in the Clifford case that the slope of this quantity (when plotted against time on a log-log plot) had smaller finite size corrections than the slope for $w(t)$ itself. The corresponding plot is shown in Fig. 10-23, for times up to $t = 25$ (averaging over more than 5000 realisations). The dashed grey lines are the $t^{1/3}$ trendlines. Results for both types of dynamics are in good agreement with the expected slope $\beta = 1/3$.

Next we examine the spatial correlator (10.9) in Fig. 10-24. For both types of dynamics, the behaviour for $r \ll \xi(t)$ agrees well with the KPZ exponent value $\alpha = 1/2$ at the largest available time.

The very long times accessible in the Clifford simulation allowed us to establish KPZ exponents with high accuracy there. For the more generic dynamical rules we cannot reach the same level of precision, but nevertheless the KPZ exponent values are compatible with the data.

10.6 Higher dimensions

We have discussed several ways of thinking about entanglement growth in 1D. One of these, the directed polymer picture, generalizes naturally to higher dimensions: the polymer is simply replaced by a d–dimensional membrane embedded in $(d + 1)$–dimensional spacetime. As in 1D, we think of this membrane as as a coarse-grained version of a minimal cut bisecting a unitary circuit. The membrane is subject to pinning by 'disorder' in space–time arising from the dynamical noise. See Fig. 10-25 for the two-dimensional case.

We can explore two kinds of question using this picture. First, we can examine universal properties that are specific to the noisy scenario: as in 1D, fluctuations are governed by universal exponents. Second, we can calculate leading order properties of $S(t)$ that do not involve
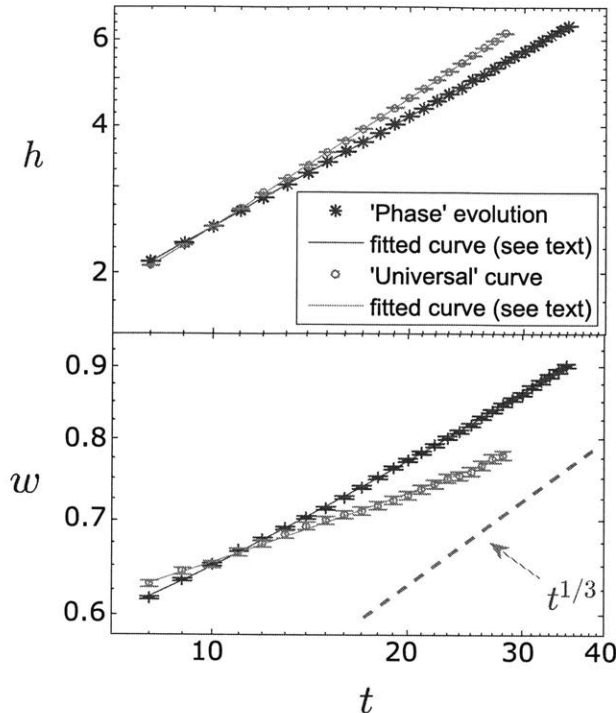
Figure 10-22: Top: Growth of the mean entanglement as a function of time for the universal and phase gate set fitted to Eq. 10.49 with β set to 1/3. The dashed line shows the expected asymptotic behaviour for comparison. Error bars indicate one standard deviation (1σ) uncertainty.

fluctuations and which are therefore likely to be valid even in the absence of noise, i.e. for dynamics with a time–independent Hamiltonian. In higher dimensions the behaviour of $S(t)$ has nontrivial dependence on the geometry of the region for which we calculate the entanglement. We suggest the 'minimal membrane in spacetime' as a simple and general heuristic for such calculations. Below we discuss the case of a spherical region (Sec. 10.6.2) and contrast our results with an alternative simple conjecture. For other toy models for entanglement spreading, see Refs. [64, 77].

Denoting the region for which we wish to calculate the entropy by A, and its boundary by ∂A, the membrane lives in a spacetime slice of temporal thickness t, and terminates at ∂A on the upper boundary of this time slice: see Fig. 10-25. For simple shapes and for times shorter than the saturation time, the membrane also has a boundary on the lower slice, as shown in Figs. 10-25, 10-26. In this section we will focus on entanglement growth prior to saturation.

10.6.1 Universal fluctuations of $S(t)$ in noisy systems

Consider the entanglement $S(t)$ for a region A whose boundary ∂A has length or area $|\partial A|$. In the $d = 2$ case, shown in Fig. 10-25, $|\partial A|$ is the length of the spatial boundary. Neglecting fluctuations, the 'world volume' of the minimal membrane scales as $|\partial A| \times t$. This gives the leading scaling of the membrane's energy and hence of the entanglement. As in 1D, subleading

253
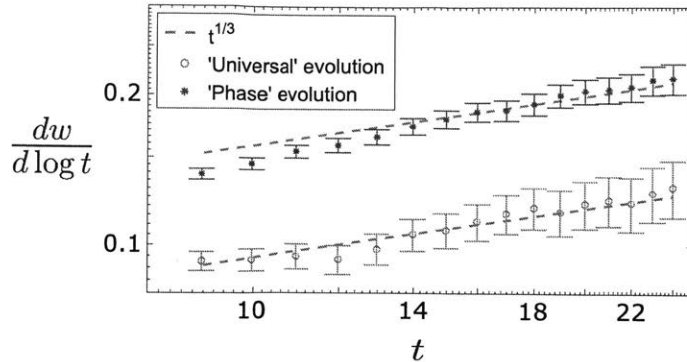
Figure 10-23: The logarithmic derivative of the width $dw/d \log t$ vs. time for the Phase and Universal evolution protocols. For comparison we plot the universal behavior with exponent $t^{1/3}$ in grey (dashed). (The derivative is calculated using three data points. Errors are estimated from maximal and minimal slopes obtained within one standard deviation from the averaged data points.)

terms encode universal data. We now consider these terms.

The pinning of a membrane or domain wall by disorder is well studied [309, 337, 338, 339, 340] (a brief summary is in Appendix D.6). Translating standard results into the language of the entanglement in a d–dimensional noisy quantum system, we find that in both $d = 1$ and $d = 2$ there is a unique dynamical phase with nontrivial critical exponents. The same is true for continuum systems[23] in $d = 3$. However if a lattice is present, two stable phases (and thus a dynamical phase transition) are possible in $d = 3$; one with nontrivial exponents and one with trivial ones. In the trivial phase the membrane is 'smooth' and is pinned by the lattice. In the nontrivial phases the membrane is instead pinned by disorder in a 'rough' configuration. We will discuss the nontrivial phases (which are the only ones possible in $d < 3$ and for continuum systems in $d = 3$).

Generally fluctuations have a weaker effect in higher dimensions than in 1D. For simplicity, take a quantum system which is infinite in one direction and of size L in the other $d-1$ directions, and consider the entanglement for a cut perpendicular to the infinite direction. Since A and its complement are both infinite, $S(t)$ will grow indefinitely for this geometry. However there are two regimes, $t \lesssim L$ and $t \gg L$ (here we drop a dimensionful prefactor). For times $t \lesssim L$ (see Appendix D.6 for details):

$$\langle S(t) \rangle = L^{d-1} \left(v_E t + B t^{\theta+1-d} + \ldots \right) \tag{10.53}$$

$$\langle\langle S(t)^2 \rangle\rangle^{1/2} \propto L^{(d-1)/2} t^{\theta - (d-1)/2}, \tag{10.54}$$

where the exponent θ is defined below. This reproduces the 1D result with $\theta = \beta$. Note that when $d > 1$, fluctuations are suppressed with respect to the mean by a factor of $|\partial A|^{1/2}$: distant regions of the boundary give rise to essentially independent fluctuations which add up

---

[23]More precisely, for systems with continuous (statistical) spatial translational symmetry.
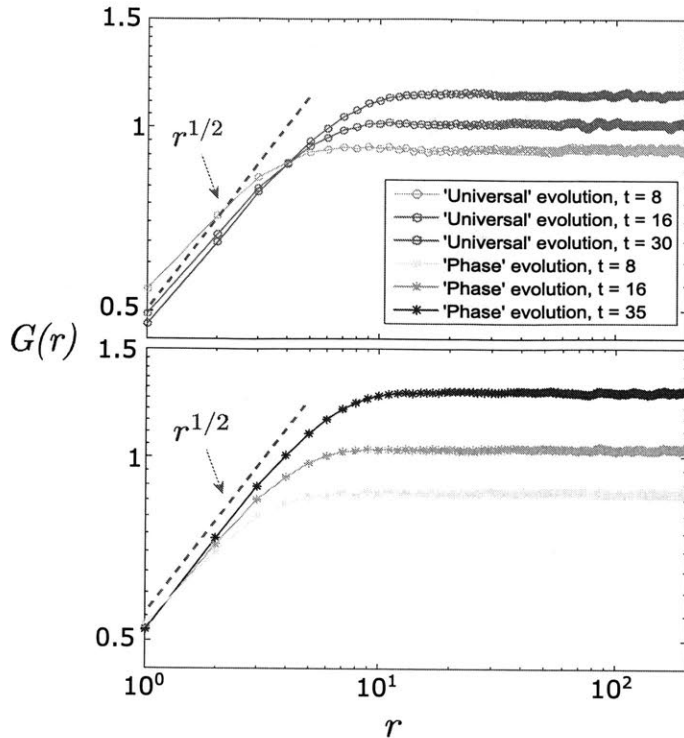
Figure 10-24: Correlation function $G(r) = \langle [S(r) - S(0)]^2 \rangle^{1/2}$ at three values of the time for the Phase (top) and Universal (bottom) gate sets, showing good agreement with the KPZ exponent value $\alpha = 1/2$.

incoherently. In the opposite regime $t \gg L$, the temporal dimension of the membrane is much larger than its spatial dimensions, so there is a crossover to the 1D directed polymer problem. However, the exponent of the higher dimensional problem appears in the universal L dependence of the growth rate:

$$S(t) = (vL^{d-1} + wL^{\theta-1})t + \ldots \tag{10.55}$$

(The higher corrections will include the $t^{1/3}$ term associated with the 1D universality class.) Numerically, the exponent is $\theta = 0.84(3)$ in $d = 2$, and $\theta = 1.45(4)$ in $d = 3$ [340]. The subleading exponent in Eq. 10.53 is negative for $d > 1$, so this correction may be hard to observe numerically.

10.6.2 Minimal membrane picture for dynamics without noise

In higher dimensions we can ask how $S(t)$ depends on the geometry of region A when this geometry is nontrivial. Interestingly, the membrane picture makes predictions about this which do not involve the noise-induced fluctuations, and which are likely also to be valid for Hamiltonian dynamics without noise (with the replacement $S \to S/s_{\text{eq}}$ discussed in Sec. 10.4).

As an instructive special case, take A to be a disc-shaped region of radius R in $d = 2$. (A ball in higher dimensions is precisely analogous.) We assume continuous rotational symmetry, at

255
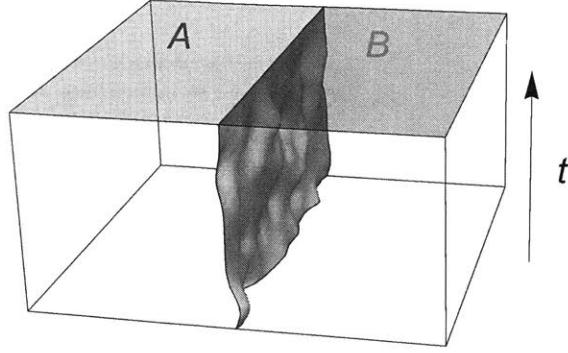
Figure 10-25: Minimal membrane picture for the entanglement of two regions in $d = 2$.

least on average. At short times, the leading scaling of the entanglement is $S(t) \simeq 2\pi v_E R t$, since the worldsheet area of the membrane is approximately $2\pi R \times t$. However there are corrections to this arising from the curvature of ∂A.

We consider the limit of large t and large R with a fixed ratio t/R. In this regime the effects of fluctuations may be neglected, and instead the energetics of the membrane are determined by deterministic elastic effects. We write the energy of the membrane as

$$E = \int \mathrm{d}^2 S \, \mathcal{E}, \tag{10.56}$$

where $\mathrm{d}^2 S$ is the membrane's area element and $\mathcal{E}$ is its 'energy' density. $S(t)$ is got by minimising E with appropriate boundary conditions.

Next we Taylor expand $\mathcal{E}$ in terms of local properties of the membrane. For a flat 'vertical' membrane (i.e. with normal perpendicular to the t axis) $\mathcal{E} = v_E$. In general however $\mathcal{E}$ will depend on the angle φ by which the surface locally deviates from verticality, as well as, for example, the local curvatures κ_s and κ_t in the spatial and temporal directions. Using rotational symmetry to parametrise the membrane by the radius $r(t')$,

$$\mathrm{d}^2 S \, \mathcal{E} = v_E r \mathrm{d}\theta \mathrm{d}t \left(1 + a\dot{r}^2 + b\kappa_t^2 + c\kappa_s^2 + c\dot{r}^4 + \ldots \right). \tag{10.57}$$

However this simplifies in the limit of interest. We *first* send $t, R \to \infty$ with t/R fixed. In this limit $\dot{r}(t')$ remains finite but the curvature terms become negligible (see for example the explicit solution below) so we can write $\mathcal{E} = \mathcal{E}(\dot{r})$. Now we make the second approximation that t/R is small, meaning that we can keep only the $O(\dot{r}^2)$ correction.

The boundary condition at the top of the spacetime slice is $r(t) = R$. We will consider times prior to saturation, so the membrane also has a free boundary on $t = 0$. In the relevant limit its 'energy' is

$$E = 2\pi v_E \int_0^t \mathrm{d}t' \, r(t') \left(1 + a\dot{r}(t')^2 + \ldots \right). \tag{10.58}$$
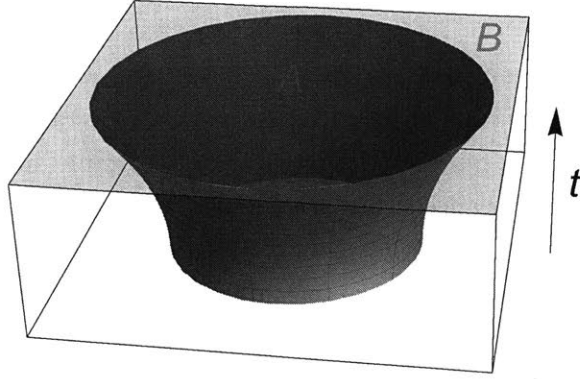
Figure 10-26: Minimal membrane for a disc-shaped region in $d = 2$.

Minimal energy requires the boundary condition $\dot{r}(0) = 0$. When t/R is small we may expand in $1/R$. This gives $r(t') \simeq R - (t^2 - t'^2)/(4aR)$, as illustrated in Fig. 10-26. The corresponding entropy is

$$S(t) = 2\pi v_E R t \left(1 - \frac{t^2}{12aR^2} + \dots \right). \tag{10.59}$$

This calculation generalises trivially to higher dimensions, where the correction is of the same order. Corrections due to fluctuations come in with negative powers of t, and are negligible in the limit we are discussing.

Note that the first correction in the brackets in Eq. 10.59 is of order $(t/R)^2$, and not of order t/R. This result differs from what one might naively have expected if one guessed that at time t an annulus of width $\tilde{v} \times t$ inside the disc is entangled with the outside, where $\tilde{v}$ is a tsunami velocity. This picture gives an entropy proportional to the area of the annulus,

$$S(t) \stackrel{?}{\sim} \pi R^2 - \pi(R - \tilde{v}t)^2 = 2\pi R \tilde{v} t \left(1 - \frac{\tilde{v}t}{R} \right), \tag{10.60}$$

leading to a negative correction of order t/R. The difference between Eqs. 10.59, 10.60 also indicates that a picture in terms of independently spreading operators is misleading, in agreement with what we found in 1D.

It is interesting to note that in the regime where t/R is of order one, the full $\dot{r}$ dependence of $\mathcal{E}(\dot{r})$ plays a role. This suggests that an infinite number of nonuniversal parameters enter the expression for $S(t)$ in this regime, and that there is no general, universal scaling form for the entanglement of a sphere in $d > 1$. However we do expect saturation to remain discontinuous, as in 1D (Eq. 10.24), occurring via a transition between an optimal membrane configuration which reaches the bottom of the spacetime slice and one (with $E = \pi R^2$) which does not.

10.7 Outlook

Quantum quenches generate complex, highly entangled states whose dynamics cannot usually be tracked explicitly. For this reason, analytical approaches to quenches have typically relied on additional structure in the quantum dynamics: for example integrability, or absence of interactions, or conformal invariance. This paper has instead studied dynamics that are as *unstructured* as possible. We propose that noisy dynamics are a useful toy model for quantum quenches in generic (non-integrable, non-conformally–invariant) systems.

Many of our results are of course specific to noisy dynamics: in particular the emergence of KPZ behaviour at long wavelengths in 1D, and the detailed pictures for entanglement growth afforded by the 'KPZ triumvirate'. But we have suggested that some of our heuristic pictures apply to non-noisy entanglement growth as well (with the replacement $S \to S/s_{eq}$ mentioned above). We proposed a general directed polymer picture/minimal membrane picture for the scaling of the entanglement and mutual information (Secs. 10.4, 10.6.2) and we used the operator spreading picture to clarify the meaning of the 'entanglement velocity' and its distinction from the operator spreading velocity (Sec. 10.4). 'Thermalization is slower than operator spreading' in generic 1D systems (i.e. in general v_E is smaller than v_B): by contrast this is not true in 1+1D CFTs [51], or in certain toy models [64]. It would be interesting to make more detailed comparisons with holographic models [213].

Many interesting questions remain. First — within the realm of noisy systems — an analytical treatment for the regime with *weak* noise would be desirable, i.e. for dynamics of the form

$$H(t) = H_0 + \lambda H_1(t), \tag{10.61}$$

where H_0 is a time-independent many-body Hamiltonian, $H_1(t)$ represents noise, and λ is small. Our conjecture is that KPZ exponents apply for any nonzero value of λ (unless $H(t)$ is fine-tuned) — i.e. that there is no universal distinction between continuous time dynamics and quantum circuits. (Note that there is no distinction between these two cases at the level of conservation laws: once noise is added, energy is not conserved even in the continuous time case.) However our derivations and numerics correspond, roughly speaking, to the large λ regime. Perhaps the opposite regime could be addressed using a more explicit RG treatment, although it is not obvious how to set this up.

Such an RG treatment might also shed light on the nature of the entanglement *spectrum*, or equivalently the dependence of $S_n(t)$ on the index n. While we believe that all the Renyi entropies execute KPZ growth in the presence of noise, we have not pinned down the n–dependence of the various constants. The solvable models suggest that the leading order behaviour may be independent of n at large times. What is the appropriate scaling form for the spectrum? Limited timescales prevented us from addressing this numerically (except for Clifford circuits, where all the S_n are trivially equal).[24]

---

[24] The entanglement spectrum is one window on the structure of the quantum states generated by the random

As a more speculative question in the domain of noisy dynamics, we may ask whether there exist time-independent Hamiltonians which show KPZ entanglement fluctuations, despite the absence of explicit noise, in some dynamical regimes. We emphasize that this seems unlikely on asymptotically long timescales for a generic system (since *local* reduced density matrices and observables will eventually thermalize) but it may hold on intermediate timescales in certain systems in which some degrees of freedom act effectively as chaotic classical variables and provide effective noise.

In the text we have only discussed initial states with area law entanglement. A natural extension is to initial states with, for example, sub-maximal volume law entanglement. The natural expectation, say in 1D, is that the directed polymer picture extends to this case if we glue the unitary circuit to a tensor network representation of the initial state. Then the entropy $S(x,t)$ would include a fluctuating part with KPZ exponents together with a contribution from the initial state. Another natural direction to explore is the role of conserved quantities. Turning to higher dimensions, it would also be useful to test the higher-dimensional membrane pictures of Sec. 10.6, perhaps exploiting Clifford circuits to reduce the numerical difficulty of higher-dimensional dynamics.

dynamics. We can also ask in what ways these states differ from ground states of random Hamiltonians, when the amount of entanglement is similar.

Appendix A

Quantum Information Processing with Majorana Zero Modes

A.1 Calculation of the Persistent Current

To estimate the magnitude of the persistent current in a Majorana interferometer with a metallic arm or another Majorana island, we compute the persistent current in a free electron ring with one and two weak links.

A.1.1 Single Weak Link

Consider a free electron ring of length L with a single weak link. The bosonized form of the action $S = S_0 + S_{\text{weak}}$ where S_0 is [341, 342]

$$S_0 = \frac{1}{2v_F} \int_0^L dx \int_0^\beta d\tau \left[(\partial_\tau \phi)^2 + v_F^2 (\partial_x \phi)^2 \right] \tag{A.1}$$

with v_F is the Fermi velocity of the metal. The "weak link" is modeled by a weak hopping between the ends of the ring [343, 344] $S_{\text{weak}} = -\int d\tau \left[\tilde{t}\,\psi^\dagger(L,\tau)\psi(0,\tau) + \text{h.c.} \right]$, with ψ and $\psi^\dagger$ the electron creation/annihilation operators respectively. After bosonizing, the most relevant term in the action for the weak hopping is given by

$$S_{\text{weak}} = -\tilde{t} \int_0^\beta d\tau \, \cos\left[\sqrt{\pi}\left(\phi(L,\tau) - \phi(0,\tau) \right) + \Theta \right]$$

with

$$\Theta \equiv \frac{2\pi\Phi}{\Phi_0} \tag{A.2}$$

the flux through the ring, in units of the flux quantum $\Phi_0 = h/e$.

We observe that the fields $\phi(x,\tau)$ for $x \neq 0$, L may be integrated out to obtain an effective

action that only involves the phase difference $\vartheta(\tau) \equiv \frac{1}{2}[\phi(L,\tau) - \phi(0,\tau)]$ [343, 344]. Expanding the phase difference as

$$\vartheta(\tau) = \frac{1}{\beta} \sum_{i\omega_n} e^{i\omega_n \tau} \vartheta(\omega_n) \tag{A.3}$$

with Matsubara frequencies $\omega_n \equiv 2\pi n/\beta$, and integrating out the bulk fields results in the effective action for a finite-size system

$$S_{\text{eff}} = \frac{1}{\beta} \sum_{i\omega_n} |\omega_n| \coth\left[\frac{|\omega_n|L}{2v_F}\right] |\vartheta(\omega_n)|^2 - \tilde{t} \int_0^\beta d\tau \, \cos\left[2\sqrt{\pi}\, \vartheta(\tau) + \Theta\right] \tag{A.4}$$

We may determine the persistent current $I = \beta^{-1}(\partial \ln Z/\partial \Phi)$ perturbatively in the coupling $\tilde{t}$, where $Z = \int D\phi\, e^{-S_{\text{eff}}}$ is the path integral. The leading contribution to the persistent current comes at $O(\tilde{t})$; observe that

$$I = \frac{1}{\beta} \frac{\partial \ln Z}{\partial \Phi} = \frac{e\tilde{t}}{\beta} \int_0^\beta d\tau \, \left\langle \sin\left[2\sqrt{\pi}\, \vartheta(\tau) + \Theta\right] \right\rangle_0 + \cdots$$
$$= e\tilde{t} \sin\left(2\pi \frac{\Phi}{\Phi_0}\right) e^{-2\pi \langle \vartheta(\tau)^2 \rangle} + \cdots \tag{A.5}$$

where $\langle \cdots \rangle_0$ denotes the expectation value with respect to the Gaussian part of the action. From the two-point correlation function

$$\langle \vartheta(\tau)\vartheta(0) \rangle_0 = \frac{1}{\beta} \sum_{i\omega_n} \frac{e^{i\omega_n \tau}}{|\omega_n| \coth\left[\frac{|\omega_n|L}{2v_F}\right]} \tag{A.6}$$

we determine that the persistent current at *zero temperature* is given, to leading order in the weak hopping, and after restoring factors of $\hbar$, by

$$I = -e\tilde{t} \left(\frac{\pi \hbar v_F}{\epsilon_F L}\right) e^{-\gamma} \sin\left(2\pi \frac{\Phi}{\Phi_0}\right) + O(t^2) \tag{A.7}$$

where γ is the Euler-Mascheroni constant. Here, $\hbar\tilde{t}$ – the hopping strength across the Majorana island – is given by $\hbar\tilde{t} = t^2(1/E_+ + 1/E_-)$ with $E_\pm$ the energy difference between adjacent charge states on the Majorana island as defined in the main text, and t, the tunneling amplitude into a single Majorana zero mode. We may re-express the persistent current in terms of $E_\pm$ as well as the tunnel-coupling Γ and the level-spacing in the metallic wire δ. The persistent current is then given by $I = I_0 \sin(2\pi\Phi/\Phi_0)$ with

$$I_0 = \frac{2e\Gamma\delta}{\hbar} \left(\frac{1}{E_+} + \frac{1}{E_-}\right) e^{-\gamma} \tag{A.8}$$

Taking the tunnel-coupling Γ to be approximately one-tenth of the superconducting gap Δ,

which determines the level-broadening of the Majorana edge-states we find that $I_0 \approx 10$ nA.

A.1.2 Double Weak Link

A similar answer is obtained in the case of a metallic wire with two weak links, which we model as two independent wires, each of length $L/2$, whose ends are weakly coupled. In this case, the bosonized action is given by $S = S_0 + S_{\text{weak}}$ with

$$S_0 = \frac{1}{2v_F} \int_0^{L/2} dx \int_0^\beta d\tau \sum_{\ell=1,2} \left[(\partial_\tau \phi_\ell)^2 + v_F^2 (\partial_x \phi_\ell)^2 \right] \tag{A.9}$$

and

$$\begin{aligned} S_{\text{weak}} = &- \tilde{t}_1 \int_0^\beta d\tau \, \cos \left[\sqrt{\pi} \left(\phi_2(0,\tau) - \phi_1(L/2,\tau) \right) + \Theta \right] \\ &- \tilde{t}_2 \int_0^\beta d\tau \, \cos \left[\sqrt{\pi} \left(\phi_1(0,\tau) - \phi_2(L/2,\tau) \right) \right] \end{aligned} \tag{A.10}$$

with Θ again given by the flux through the ring $\Theta = 2\pi\Phi/\Phi_0$.

We now integrate out the bulk fields after expanding the phase differences $\vartheta_1(\tau) \equiv [\phi_2(0,\tau) - \phi_1(L/2,\tau)]/2$ and $\vartheta_2(\tau) \equiv [\phi_1(0,\tau) - \phi_2(L/2,\tau)]/2$ in terms of Matsubara frequencies $\vartheta_\ell(\tau) = \beta^{-1} \sum_{i\omega_n} e^{i\omega_n \tau} \vartheta_\ell(\omega_n)$ to obtain the effective action $S = S_0^{(\text{eff})} + S_{\text{weak}}^{(\text{eff})}$ where

$$S_0^{(\text{eff})} = \frac{1}{\beta} \sum_{i\omega_n} |\omega_n| \coth \left(\frac{|\omega_n|L}{2v_F} \right) \left\{ |\vartheta_1(\omega_n)|^2 + |\vartheta_2(\omega_n)|^2 + \text{sech} \left(\frac{|\omega_n|L}{2v_F} \right) [\vartheta_1^*(\omega_n)\vartheta_2(\omega_n) + \text{c.c.}] \right\}$$

$$S_{\text{weak}}^{(\text{eff})} = -\tilde{t}_1 \int_0^\beta d\tau \, \cos \left[2\sqrt{\pi} \, \vartheta_1(\tau) + \Theta \right] - \tilde{t}_2 \int_0^\beta d\tau \, \cos \left[2\sqrt{\pi} \, \vartheta_2(\tau) \right] \tag{A.11}$$

We again compute the persistent current perturbatively in the hoppings $\tilde{t}_{1,2}$. We begin by observing that in terms of the variable

$$\varphi(\omega_n) = \vartheta_1(\omega_n) + \text{sech} \left(\frac{|\omega_n|L}{2v_F} \right) \vartheta_2(\omega_n) \tag{A.12}$$

the Gaussian part of the action is now diagonal

$$S_0^{(\text{eff})} = \frac{1}{\beta} \sum_{\omega_n} |\omega_n| \left[\coth \left(\frac{|\omega_n|L}{2v_F} \right) |\varphi(\omega_n)|^2 + \tanh \left(\frac{|\omega_n|L}{2v_F} \right) |\vartheta_2(\omega_n)|^2 \right]. \tag{A.13}$$

The two-point correlation function

$$\langle \vartheta_2(\tau)^2 \rangle_0 = \frac{1}{\beta} \sum_{\omega_n} |\omega_n|^{-1} \coth \left(\frac{|\omega_n|L}{2v_F} \right) \tag{A.14}$$

263

diverges at low frequencies, so that

$$\left\langle \cos\left[2\sqrt{\pi}\,\vartheta_2(\tau)\right]\right\rangle_0 = 0. \tag{A.15}$$

As a result, the leading contribution to the persistent current comes at $O(\widetilde{t_1}\widetilde{t_2})$, as expected.

To leading order in the weak hopping, the persistent current now takes the form

$$I = \frac{e\widetilde{t_1}\widetilde{t_2}}{\beta}\int_0^\beta d\tau d\tau' \left\langle \sin\left[2\sqrt{\pi}\,\vartheta_1(\tau) + \Theta\right]\cos\left[2\sqrt{\pi}\,\vartheta_2(\tau')\right]\right\rangle_0$$

We may explicitly evaluate the above the expression, after using the correlation function (A.14) and the fact that

$$\left\langle \vartheta_1(\tau)\vartheta_2(0)\right\rangle_0 = -\frac{1}{\beta}\sum_{\omega_n} \frac{e^{i\omega_n\tau}}{|\omega_n|\sinh\left(\frac{|\omega_n|L}{2v_F}\right)}. \tag{A.16}$$

We find that at low temperatures T, the persistent current takes the form $I = I_0 \sin(2\pi\Phi/\Phi_0)$ where I_0, after re-writing in terms of the level-spacing δ, the charging-energy cost for the islands $E_\pm$, and the tunnel-coupling for each Majorana island Γ_i is given by

$$I_0 = \frac{8\pi e}{\hbar}\frac{\Gamma_1\Gamma_2}{k_B T}\delta^2\left(\frac{1}{E_+} + \frac{1}{E_-}\right)^2 e^{-2\gamma}. \tag{A.17}$$

Appendix B

Phase Diagram of the Coupled Z_N Topological Phases

We now turn to a discussion of the rich phase diagram of the coupled Z_N toric codes, as described by the Hamiltonian (7.13). Our results are summarized in the diagrams shown in Fig. B-1a and b when $N < 5$ and $N \geq 5$, respectively. Both figures include the four distinct phases discussed previously, i.e.

I. $J \gg h, t$: Decoupled 2D Z_N Topological Phase

II. $h \gg J, t$: 3D Z_N Topological Phase

III. $t \gg J, h$: Z_N X-Cube Fracton Phase

IV. $h, t \gg J$: Trivial, Confined Phase

The remaining details in the phase diagram arise from an interesting duality between the Hamiltonian (7.13) when $h = 0$, and the 3D Z_N toric code in the presence of a field; increasing the strength of this field eventually leads to condensation of the Z_N flux loops and results in a trivial, confined phase. From this duality, and from knowledge of the phase structure of Z_N lattice gauge theory, we deduce that when $N < 5$, the Z_N X-cube model has a direct, first-order transition to a phase where the layers are effectively decoupled. When $N \geq 5$, however, there is an intermediate phase which is dual to a Coulomb phase that is known to appear in the phase diagram of (3+1)-d Z_N lattice gauge theory [345, 346], along the line $h = 0$. We argue, however, that this phase is gapped and topologically trivial when $h > 0$. Interestingly, one of the transitions out of the gapless phase is believed to be continuous in numerical studies [18, 347], which presents the intriguing possibility that there exists a continuum field theory description for the Z_N X-cube phase.

Several features of the phase diagrams in Fig. B-1, including the manner in which these phases meet at the center of the phase diagram, as well as the generic behavior of the transitions between the Z_N X-cube and trivial confined phases, are unknown. We conclude by presenting a

<div style="text-align:center">(a) $N < 5$ (b) $N \geq 5$</div>
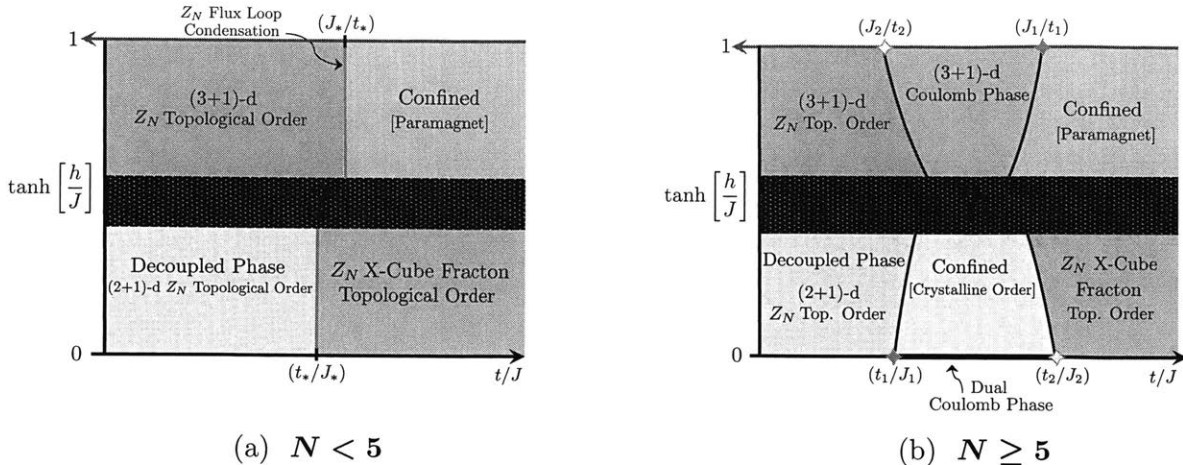
Figure B-1: **Schematic Phase Diagram of the Coupled System**: The duality derived in Sec. II relates the points $(x, y) = (t/J, 0)$ with $(J/t, 1)$ that lie along the black and blue arrows, respectively, in the schematic phase diagrams above. From knowledge of the phase diagram of (3+1)-d Z_N lattice gauge theory, we argue that when $N < 5$, there is a direct, first-order transition between the X-cube phase and the decoupled phase. Alternatively, when $N \geq 5$, there must be an intermediate phase along the line $h = 0$ which is dual to a Coulomb phase that appears in the phase diagram of the (3+1)-d Z_N lattice gauge system. We argue that this phase is unstable [17] and becomes a gapped, topologically trivial phase when $h > 0$. From Monte Carlo studies of the transition along the blue arrow, between the deconfined phase of Z_N gauge theory and the Coulomb phase [18], we believe that the dual transition along the $h = 0$ line, into the fracton topological phase in (b), is continuous.

solvable projector model in which the transition is believed to be first-order, and by speculating on directions for future work.

B.0.1 Confinement Transition from the Z_N Topological Phase

We begin from the top left corner of the phase diagram ($h \gg J, t$), where our system is in a 3D Z_N topological phase. Increasing the strength of the coupling t eventually leads to a condensation of Z_N flux loops, and the associated phase transition is captured by the finite-temperature behavior of the 4D classical Z_N lattice gauge theory with a "Wilsonian" imaginary time action $S_W[\theta] = \beta \widetilde{K} \sum_p \cos[(\Delta \times \theta)_p]$, where θ is a Z_N variable defined on the links of the 4D cubic lattice, while $(\Delta \times \theta)_p$ is the lattice curl around plaquette p, and the sum is over all plaquettes on the 4D lattice.

When $N < 5$, classical Monte Carlo studies [18, 347] have observed a direct, first-order phase transition between a disordered phase where the magnetic flux loops have condensed at high temperatures, to one where they remain energetically costly, with the expectation value of classical Wilson loop operators decaying as the exponential of the area of an enclosed region ("area-law") and as their total length ("perimeter-law"), respectively, in the two phases. In our problem, these two phases correspond to a trivial loop condensate and a phase with Z_N topological order, respectively, as indicated in the top portion of the phase diagram in Fig. B-1a.

When N is large ($N \geq 5$), *three* phases are observed in Monte Carlo studies of the classical 4D Z_N lattice gauge theory [18, 347, 348]. This rich phase structure may be understood in a variety of ways. To begin, we recall that a similar phenomenon occurs in 2D classical, Z_k-symmetric spin models when k is sufficiently large. In addition to a low-temperature symmetry-breaking phase and a disordered phase at high temperatures, there is an intermediate phase with algebraic correlations that resembles the low-temperature behavior of the XY model. The existence of this XY-like phase with an emergent global $U(1)$ symmetry may be motivated by recalling that in the classical 2D XY model, Z_k anisotropy is a marginally irrelevant perturbation when $k \geq 4$ [349]. A more rigorous argument for the existence of this phase, even when the anisotropy is infinitely strong, is provided in Ref. [345].

A similar argument may be used for the presence of an intermediate phase with emergent $U(1)$ gauge symmetry in the phase diagram of 4D Z_N lattice gauge theory in the large-N limit [348, 345, 346]. Ref. [346] studied a Villain form of the 4D Z_N gauge theory, which exhibits a discrete analog of the electric-magnetic self-duality of compact $U(1)$ gauge theory [350], and whose action may be re-written as that of Maxwell electrodynamics in the presence of both electric and magnetic charges. While the action exhibits only a Z_N gauge symmetry, it was argued that both the electric and magnetic excitations are strongly suppressed near the self-dual point in the large-N limit, so that the effective action is that of pure Maxwell electromagnetism. As a result, when $N \geq 5$, there is a "Coulomb phase" that is encountered in the top region of the phase diagram in Fig. B-1b, with the Z_N variable θ effectively behaving as the emergent $U(1)$ gauge field.

These three phases may be distinguished by the behavior of the gauge-invariant Wilson loop operator W_C, which creates a closed tube of electric flux, along with its (electric-magnetic) dual $\Gamma_{\widetilde{C}}$, which is a membrane-like operator that creates a closed magnetic flux loop along loop $\widetilde{C}$ on the dual lattice. In the deconfined phase of the Z_N gauge theory, a large Wilson loop W_C exhibits perimeter-law behavior while $\Gamma_{\widetilde{C}}$ has area-law behavior, while the opposite behavior occurs in the confined phase. In the intermediate phase, however, both charge and loop excitations are suppressed [346] and neither excitation has condensed. As a result, the Wilson loop operator W_C must exhibit perimeter-law behavior [346]. Since this phase is self-dual under the electric-magnetic duality transformation, the *same* behavior holds for $\Gamma_{\widetilde{C}}$. As argued in Ref. [351], due to the non-trivial statistics of Z_N charges and flux loops, perimeter-law behavior for both operators can only occur in the presence of a gapless gauge field, which is consistent with the emergence of a Coulomb phase.

It remains unclear whether the transition between the Coulomb and confined phases is continuous [352, 353] or weakly first-order [354, 355]. However, the transition between the deconfined phase of the Z_N gauge theory and the Coulomb phase appears continuous in Monte Carlo studies [18, 347, 348]. Finally, as N increases, the region of stability for the Z_N topological phase shrinks, while the second transition from the Coulomb phase to the confined phase remains robust [18]. This is consistent with the expectation that the limit "$N \to +\infty$", should somehow

reproduce the phase diagram of the pure (3+1)-d compact $U(1)$ gauge theory.

B.0.2 Transition(s) from the decoupled phase to the Z_N X-cube phase

We now study the bottom half of the phase diagrams shown in Fig. B-1a & b. We first demonstrate that the transition from the decoupled layers of 2D toric codes to the X-cube fracton phase is *dual* to the confinement transition for the (3+1)-d Z_N gauge theory, which is driven by the condensation of flux loops. This result is intuitively apparent from our "loop-gas" representation of the X-cube phase, which suggests that the transition from the decoupled layers must be driven by the condensation of a loop excitation. Physically, our duality transformation maps the closed composite flux loops in the ground-state of the X-cube phase into the closed electric flux loops in the ground-state of the Z_N topological phase. We emphasize that this duality relates the bulk spectrum of two seemingly distinct physical systems, and provides relations between certain local operators on both sides.

We begin by explicitly implementing our lattice duality transformation on the Hamiltonian for the coupled Z_2 toric codes (8.1) when $h = 0$, before discussing its consequences. In practice, our transformation is identical to the (2+1)-d Wegner duality that maps the transverse-field Ising model to the (2+1)-d Z_2 gauge theory [189], in *each layer* of our coupled system; as a result, the generalization of this duality for the Z_N case is apparent from our following discussion. Recall that the Hamiltonian (8.1) for the coupled toric codes when $h = 0$ is given by

$$H = -J \sum_{r,j} \left[A_r^{(j)} + B_r^{(j)} \right] - t \sum_{\langle r,r' \rangle} \sigma_{rr'}^x \mu_{rr'}^x \tag{B.1}$$

We recognize that the 2D Z_2 charge operator $A_r^{(j)}$ and the operator $\mathcal{O}_r = B_r^{(xy)} B_r^{(yz)} B_r^{(xz)}$ $B_{r+\hat{x}}^{(yz)} B_{r+\hat{y}}^{(xz)} B_{r+\hat{z}}^{(xy)}$, which is the product of six flux operators around an elementary cube, as in Eq. (7.11), commute with the Hamiltonian (B.1) and with each other $[\mathcal{O}_r, A_{r'}^{(j)}] = [A_r^{(j)}, H] = [\mathcal{O}_r, H] = 0$. Therefore, we work in a restricted Hilbert space where

$$A_r^{(j)} |\Psi\rangle = |\Psi\rangle \quad \text{and} \quad \mathcal{O}_r |\Psi\rangle = |\Psi\rangle \tag{B.2}$$

without loss of generality.

We now introduce a dual description of the transition from the decoupled theory $(t \ll J)$ to the X-cube phase $(J \gg t)$ that solves the first of these constraints, by introducing spins (η) on the links of the dual cubic lattice. These spins are to be interpreted as measuring the flux through a plaquette in the decoupled toric code layers. We implement the dual representation by performing the replacements

$$B_r^{(j)} \longrightarrow \eta_{r,j}^x \tag{B.3}$$

$$\sigma_{rs}^x \mu_{rs}^x \longrightarrow \mathcal{B}_{rs} \equiv \prod_{r',j \in \text{plaq}_{rs}} \eta_{r',j}^z \tag{B.4}$$
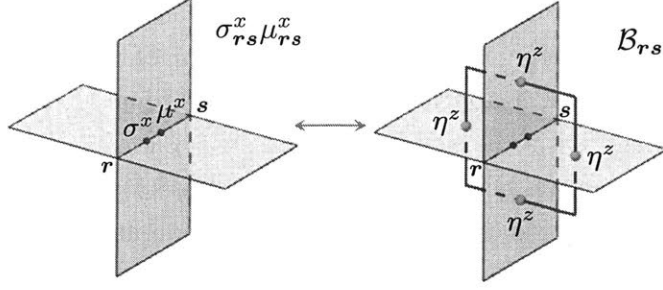
Figure B-2: **Bond-Plaquette Duality**: We provide a dual representation of the Hamiltonian (8.1) by introducing spins (η) on the links of the dual cubic lattice, which measure the flux through an elementary plaquette in the decoupled layers. This dual representation allows us to demonstrate that the transition from the decoupled layers to the Z_N X-cube phase is dual to a confinement transition in Z_N gauge theory.

where $\mathcal{B}_{rs}$ is a four-spin operator on a plaquette of the dual lattice pierced by the link $\langle r, s \rangle$ as shown in Fig. B-2.

The duality transformation preserves the algebra of local operators in (B.1), and naturally solves the constraint $A_r^{(j)} |\Psi\rangle = |\Psi\rangle$. Furthermore, the dual description of the operator $\mathcal{O}_r$ is given by

$$\mathcal{O}_r \longrightarrow \mathcal{A}_r = \prod_{s,j \in \text{star}_r} \eta_{s,j}^x \tag{B.5}$$

where $\mathcal{A}_r$ is precisely the six-spin Z_2 charge operator which acts along a "star" configuration of the η spins at each site of the dual cubic lattice. We therefore find that the dual Hamiltonian is precisely

$$H_{\text{dual}} = -J \sum_{r,j} \eta_{r,j}^x - t \sum_{\langle r, r' \rangle} \mathcal{B}_{rr'} \tag{B.6}$$

supplemented by the Z_2 Gauss's law constraint on the dual cubic lattice

$$\mathcal{A}_r |\Psi\rangle = |\Psi\rangle \tag{B.7}$$

which describes the confinement transition for a 3D Z_2 topological phase driven by the condensation of flux loops. As advertised, the lattice duality relates the Z_2 X-cube phase to the deconfined phase of (3+1)-d Z_2 gauge theory, while the decoupled toric code layers are dual to the trivial, confined phase.

Our duality transformation establishes that the bulk transition from the decoupled toric codes to the X-cube fracton phase is dual to flux loop condensation in the 3D Z_2 gauge theory, which is known to be a direct, first-order transition. The natural Z_N generalization of this duality transformation leads us to conclude that along the $h = 0$ line of the phase diagram (i) when $N < 5$, there is a direct, first-order transition between the decoupled layers and the X-cube

phase and (ii) when $N \geq 5$, there is an intermediate gapless phase for the layered system, which is dual to the Coulomb phase that emerges in the phase diagram of the (3+1)-d Z_N gauge theory. From our duality transformation, it appears that this gapless "dual Coulomb" phase along the $h = 0$ line of the phase diagram is characterized by an emergent $U(1)$ gauge symmetry, which should be generated by the natural generalization of the Gauss's law condition $\mathcal{O}_r = +1$ for the X-cube fracton phase. The $U(1)$ generalization of this condition may be read off from Fig. 7-5; if we consider an integer-valued "electric field" tensor E_{ij} with vanishing diagonal components $E_{ii} = 0$, and a conjugate gauge field A_{ij}, then this Gauss's law takes the simple form

$$\Delta_i \Delta_j E_{ij} = 0 \tag{B.8}$$

with Δ_i, the lattice derivative along direction i, and summation performed over repeated indices.

The "higher-rank" compact $U(1)$ gauge theory [198, 356] defined by this Gauss's law condition is equivalent to a generalized dimer model studied in Ref. [17], which was shown to be in a gapped phase with crystalline order due to the proliferation of topological defects in the gauge field configurations (i.e. "monopole" events). Due to this result, we believe that the dual Coulomb phase is unstable, and gives way to a gapped, topologically trivial phase with conventional long-range order when $h > 0$. The $h = 0$ line then corresponds to the fine-tuned limit where monopole events in the gauge field are suppressed. This conclusion is consistent with the fact that the perturbation $\sigma^z_{rr'} \mu^z_{rr'}$ corresponds to a highly non-local operator in terms of the dual η spins, and with our expectation for the behavior of the phase diagram in the $N \to +\infty$ limit. The nature of the transitions between this trivial phase, the X-cube phase and the decoupled layers are unknown when $h > 0$. When $h = 0$, however, our duality mapping suggests that the phase transition from the X-cube phase to the dual Coulomb phase is dual to the transition between the deconfined phase of (3+1)-d Z_N gauge theory and the ordinary Coulomb phase, which may be continuous [348, 18], though we are unaware of the continuum field theory that governs the properties of this transition.

We conclude this section by identifying the following order parameters

$$W_\Sigma \equiv \prod_{\langle r,s \rangle \in \Sigma} X_{rs} \widetilde{X}_{rs} \qquad \Gamma_\Sigma \equiv \prod_{(p,j) \in \Sigma} B_p^{(j)} \tag{B.9}$$

that distinguish the X-cube phase, the decoupled phase and the dual Coulomb phase along the line $h = 0$. Here, Σ is a two-dimensional region with area A_Σ and perimeter P_Σ. The product appearing in the definition of W_Σ is taken along the bonds perpendicular to the region Σ, and this operator may be thought of as inserting a composite flux loop along the boundary of Σ. Furthermore, Γ_Σ is the product of the plaquette operators that measure the 2D Z_N flux through the region Σ. Our notation is meant to emphasize that these operators are dual to the Wilson loop and membrane operators that distinguish the various phases of the Z_N gauge theory. From our discussion in Sec. IIA, we determine that the operators W_Σ, Γ_Σ exhibit the

following behavior along the $h = 0$ line, when the region Σ is sufficiently large:

- Decoupled Phase: $\langle W_\Sigma \rangle \sim e^{-\sigma A_\Sigma}$, $\langle \Gamma_\Sigma \rangle \sim e^{-cP_\Sigma}$

- Dual Coulomb Phase: $\langle W_\Sigma \rangle$, $\langle \Gamma_\Sigma \rangle \sim e^{-cP_\Sigma}$

- X-cube Phase: $\langle W_\Sigma \rangle \sim e^{-cP_\Sigma}$, $\langle \Gamma_\Sigma \rangle \sim e^{-\sigma A_\Sigma}$

B.0.3 Confinement of the X-cube fracton phase

The generic behavior of the confinement transition for the Z_N X-cube fracton topological phase – by condensing the dimension-1 quasiparticle excitations – are not known. This transition occurs in the far right region of the phase diagrams in Fig. B-1. Instead of studying this transition directly, however, we propose a solvable Hamiltonian that interpolates between the Z_2 X-cube fracton topological order and a confined phase in this section and determine that the transition is first-order within this model. It is unknown whether this captures the generic behavior of this transition, outside of the solvable model.

We construct a solvable projector model by placing spins (τ) on the links of a three-dimensional cubic lattice. Now, however, we consider the Hamiltonian

$$\mathcal{H} = -J\sum_{r,j} A_r^{(j)} + J\sum_{r,j}\left[\prod_{s\in\text{plane}_j(r)} e^{-h\tau_{rs}^z/J}\right] \tag{B.10}$$

supplemented by the constraint $\mathcal{O}_r |\Psi\rangle = |\Psi\rangle$, where $A_r^{(j)} = \prod_{s\in\text{plane}_j(r)} \tau_{rs}^x$ is the four-spin operator in the X-cube model that is oriented in the jth plane, and measures the presence of a dimension-1 quasiparticle excitation at site r. As before, the operator $\mathcal{O}_r$ is the 12-spin τ^z operator as defined in Eq. (7.11) that measures the fracton "charge" at a cube $\mathcal{O}_r = \prod_{s,r'\in\text{cube}(r)} \tau_{r's}^z$. We observe that the Hamiltonian $\mathcal{H}$ exhibits both the Z_2 X-cube fracton phase ($h \ll J$) as well as a trivial confined phase ($h \gg J$). Furthermore, when $h \ll J$, the Hamiltonian $\mathcal{H}$ reduces to the effective Hamiltonian considered previously for the confinement transition of the X-cube phase

$$\mathcal{H}_{\text{eff}} = -J\sum_{r,j} A_r^{(j)} - 2h\sum_{\langle r,r'\rangle} \tau_{rr'}^z + O(h^2/J) \tag{B.11}$$

The full Hamiltonian $\mathcal{H}$ (B.10) is a sum of projection operators

$$\Pi_{r,j} \equiv -A_r^{(j)} + \prod_{s\in\text{plane}_j(r)} e^{-h\tau_{rs}^x/J} \tag{B.12}$$

271

and therefore has a positive semi-definite spectrum. As a result, a ground-state of the Hamiltonian is found by explicitly constructing a zero-energy wavefunction. Projector Hamiltonians similar to (B.10) have been extensively studied by considering generalizations of the Rokhsar-Kivelson (RK) point in the two-dimensional quantum dimer model [357, 358, 359, 360, 361, 362], where the ground-state may be written as an equal-amplitude superposition of dimer configurations. For these generalized RK models, the Hamiltonian is related to the Markovian transition matrix for a classical system which satisfies detailed balance [359]. Spatial correlation functions of certain "diagonal" operators in the ground-state of the quantum model are identical to classical correlation functions in equilibrium.

Let $|\psi_{\text{fracton}}\rangle$ be a ground-state of the Hamiltonian $\mathcal{H}$ when $h = 0$, i.e. one of the ground-states of the solvable X-cube fracton Hamiltonian. We may write $|\psi_{\text{fracton}}\rangle$ explicitly as

$$|\psi_{\text{fracton}}\rangle = \prod_{r,j} \left(\frac{1 + A_r^{(j)}}{2} \right) |\tau_{ss'}^z = +1\rangle \tag{B.13}$$

where $|\tau_{ss'}^z = +1\rangle$ is the state with all spins polarized in the z-direction. The ground-state of $\mathcal{H}$ is then given by

$$|\Psi_{\text{gs}}\rangle \sim \prod_{\langle r, s\rangle} e^{h\tau_{rs}^z/2J} |\psi_{\text{fracton}}\rangle \tag{B.14}$$

It is straightforward to check that $|\Psi_{\text{gs}}\rangle$ is indeed a zero-energy eigenstate of the Hamiltonian, as it is annihilated by all of the projectors $\Pi_{r,j}$. It is convenient to re-cast the ground-state wavefunction in an alternate form. Observe that configuration of spins appearing in the state $|\psi_{\text{fracton}}\rangle$ may equivalently be specified by the action of the $A_r^{(j)}$ operators on the reference state $|\tau_{ss'}^z = +1\rangle$. As a result, the ground-state wavefunction $|\Psi_{\text{gs}}\rangle$ may be re-written in terms of dual Ising variables μ, σ at the sites of a three-dimensional cubic lattice, which label the presence or absence of a particular operator $A_r^{(j)}$ acting on the reference configuration. In this dual representation, the ground-state takes the form

$$|\Psi_{\text{gs}}\rangle = \frac{1}{\sqrt{\mathscr{Z}}} \sum_{\{\sigma\}} \sum_{\{\mu\}} e^{-\beta H/2} |\{\sigma\}, \{\mu\}\rangle \tag{B.15}$$

where the classical Hamiltonian βH is given by

$$\beta H = \frac{h}{J} \sum_r [\sigma_r \sigma_{r+\hat{x}} + \mu_r \mu_{r+\hat{y}} + \sigma_r \mu_r \sigma_{r+\hat{z}} \mu_{r+\hat{z}}] \tag{B.16}$$

and $\mathscr{Z}$ is the partition function $\mathscr{Z} = \sum_{\{\sigma\}} \sum_{\{\mu\}} e^{-\beta H}$ for this classical model.

Preliminary Monte Carlo studies of the classical Hamiltonian βH reveal a first-order phase transition when $h/J \approx 1.13$ [363, 364], which implies the presence of a first-order phase transition in our model. For example, the expectation value of the magnetization $M = \sum_{\langle r,r'\rangle} \tau_{rr'}^z$ is

precisely the energy of the classical system $E = \langle \Psi \,|\, M \,|\, \Psi \rangle$, which exhibits a discontinuity at the putative phase transition point [363, 364]. Classical correlation functions that are not invariant under the Z_2 transformation $\sigma \to -\sigma$, $\mu \to -\mu$ along any plane of the cubic lattice must vanish, as this is a symmetry of the classical Hamiltonian (B.16). To our knowledge, however, the behavior of higher-point correlation functions near the classical phase transition have not yet been studied. An intriguing possibility is that the *dynamical* behavior of this classical system is "glassy" in a certain range of couplings h/J [363, 364], which would imply in the quantum-mechanical problem that the Hamiltonian $\mathcal{H}$ has a gapless spectrum, and that certain correlation functions exhibit power-law decay in time [359, 360], while remaining spatially short-ranged. We leave an exploration of this exotic possibility to future work.

.

Appendix C

Non-Abelian Fracton Excitations in Three Dimensions

C.1   Non-Abelian Fractons and Braiding

In this section, we demonstrate that appropriately moving and braiding the non-Abelian anyon formed from a pair of fractons $(\sigma_\ell \times \sigma_{\ell'})$ in our model, implements a unitary transformation on the space of degenerate, locally indistinguishable states. The nature of the unitary transformation may be determined, up to an overall Abelian phase, by observing that a membrane-like operator that moves a pair of fractons in distinct layers must conserve the parity of the matter fermions $U_\ell^{(f)}$ within each layer, as required by gauge invariance, and so that no other excitations are created in the system. Therefore, a vertical membrane operator that exchanges pairs of well-separated fractons, as in Fig. C-1b, must affect the following transformation on the fermionic zero mode operators shown $\gamma_1 \to \gamma_2$, $\gamma_2 \to -\gamma_1$, $\gamma_3 \to \gamma_4$, $\gamma_4 \to -\gamma_3$, up to an overall choice of sign in each layer.

The resulting unitary transformation may be written by pairing the fractons as shown in Fig. C-1a, to form a basis for the protected, $2^{4-2} = 4$-dimensional Hilbert space shown. Using basis states $|1, 1\rangle$, $|1, \psi\rangle$, $|\psi, 1\rangle$, $|\psi, \psi\rangle$ which describe the fusion channels of a pair of fractons in layer ℓ_1 and in ℓ_2, respectively, and using the F- and R- matrices for Ising anyons [44], we observe that the fracton exchange shown in Fig. C-1b affects the diagonal transformation $B_1 = e^{i\theta_\Gamma} \operatorname{diag}\left(e^{-i\pi/4}, e^{i\pi/4}, e^{i\pi/4}, -e^{-i\pi/4}\right)$, while the exchange process in Fig. C-1c is off-diagonal

$$B_2 = e^{i\theta_\Gamma} B \otimes B. \tag{C.1}$$

where $B \equiv ie^{i\pi/4}(1 - i\tau^x)/2$ and τ^x is the spin-1/2 Pauli-X operator. Here, the overall Abelian Berry phase $e^{i\theta_\Gamma}$ can depend on the number of fractons that lie in the planes *between* ℓ_1 and ℓ_2, and that have been enclosed by the membrane operator used to exchange the fractons. Such a phase arises since pairs of fractons in the Majorana checkerboard model have π mutual statistics

275
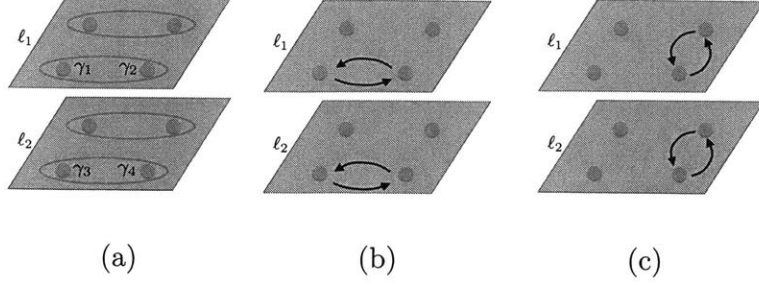
Figure C-1: **Braiding Transformations:** By applying membrane-like operators, we may exchange pairs of fractons in nearby layers to affect unitary transformations on the degenerate states in the Hilbert space.

with fractons contained within their plane of motion.

C.2   Coupled G Gauge Theories and Non-Abelian Fractons

Consider the quantum double model, as originally introduced in Ref. [19], which describes the zero-correlation length limit of the deconfined phase of a 2D gauge theory with finite gauge group G. Within each layer, degrees of freedom are placed on the oriented links of a square lattice, and labeled by the elements of the finite group G. The Hamiltonian takes the form

$$H_\ell = -\sum_s A_s - \sum_p B_p^{[1]} \tag{C.2}$$

where the "flux" operator at a plaquette p projects onto a state where the oriented product of the degrees of freedom along links surrounding p are equal to the identity. We define $B_p^{[g]}$ as

$$B_p^{[g]} \equiv \sum_{z_1 z_2 z_3 z_4 \in [g]} |z_1, z_2, z_3, z_4\rangle \langle z_1, z_2, z_3, z_4| \tag{C.3}$$

where $[g]$ is the conjugacy class associated with the group element $g \in G$. The "star" operator A_s multiplies the oriented links surrounding site s by elements of G as follows:

$$A_s \equiv \frac{1}{|G|} \sum_{g \in G} A_s^{(g)} \tag{C.4}$$

where

$$A_s^{(g)} \equiv \sum_{\{z_i\} \in G} |gz_1, z_4 g^{-1}, gz_5, z_6 g^{-1}\rangle \langle z_1, z_4, z_5, z_6| + \text{h.c.}$$

with $z_1, \ldots, z_6$ as shown in Fig. C-2a. The two operators A_s, $B_p^{[g]}$ commute and are both projection operators. As a result, the ground-state of a single layer satisfies $A_s |\Psi\rangle = B_p^{[1]} |\Psi\rangle = |\Psi\rangle$.

The quantum double model, which describes the zero correlation-length limit of all lattice gauge theories with a finite gauge group in (2+1)-dimensions, admits gapped charge and flux excitations, which live on the sites and plaquettes of the lattice, respectively, and are obtained by acting on the ground-state with a "ribbon"-like operator [19]. Pure charge excitations are labeled by irreducible representations of G, while pure fluxes are labeled by conjugacy classes $\mathcal{C}$ of the group. More generally, a charge-flux composite (dyon) is labeled by $\mathcal{C}$, as well as an irreducible representation of the *centralizer* of $\mathcal{C}$, denoted $C_{\mathcal{C}}$. As an example, $G = S_3$ – the permutation group on three elements – may be parametrized as

$$S_3 = \{1, x, y, y^2, xy, yx\} \tag{C.5}$$

where the elements x and y satisfy

$$x^2 = 1 \qquad y^3 = 1 \qquad yx = xy^2 \tag{C.6}$$

The three conjugacy classes of S_3 – $\{1\}$, $\{y, y^2\}$, and $\{x, xy, yx\}$, which we label as $[1]$, $[x]$ and $[y]$ respectively – have centralizers S_3, $\mathbb{Z}_2$ and $\mathbb{Z}_3$, respectively. The irreducible representations of S_3 include the trivial representation, the sign representation ("sgn"), as well as the standard two-dimensional representation. A full list of the eight excitations in the S_3 lattice gauge theory are given below

Excitation	Flux	Charge	d
A	·	·	1
B	·	sgn	1
C	·	2	2
D	$[x]$	·	3
E	$[x]$	-1	3
F	$[y]$	·	2
G	$[y]$	ω	2
H	$[y]$	$\overline{\omega}$	2

$$\tag{C.7}$$

Here ω and $\overline{\omega}$ label the two non-trivial representations of $\mathbb{Z}_3$ while -1 denotes the non-trivial representation of $\mathbb{Z}_2$. The last column is the quantum dimension of each excitation, which is given by

$$d_{\mathcal{C},\mathrm{Rep}(C_{\mathcal{C}})} \equiv |\mathcal{C}| \cdot \dim \mathrm{Rep}(C_{\mathcal{C}}). \tag{C.8}$$

The coloring of the excitations is to denote the neutral vacuum (black), pure charge (red), flux (blue) or a dyon (green) excitation. For our purposes, we will be concerned with the non-Abelian flux **D**, whose relevant fusion rules for our purposes we write suggestively as $\mathbf{D} \times \mathbf{A} = \mathbf{D}$; $\mathbf{D} \times \mathbf{F} = \mathbf{D} \times (1 + B)$; $\mathbf{D} \times \mathbf{D} = (1 + C) + \mathbf{F} \times (1 + C)$.
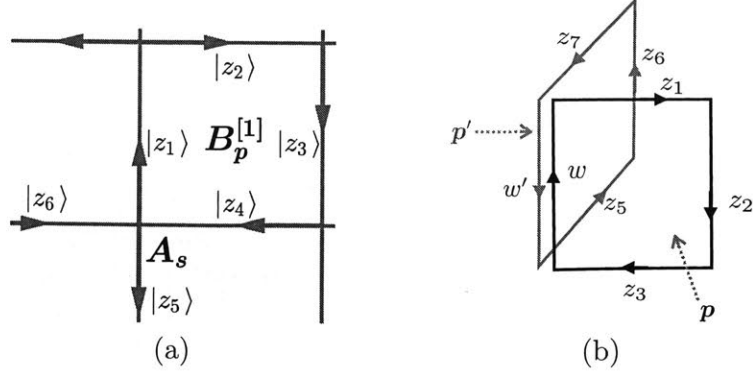
Figure C-2: **Quantum Double Layers:** In (a), we show single layer of the quantum double model [19] on the square lattice. The action of the star (A_s) and plaquette (B_p) operators on each link is described in the text. The setup for computing the commutator of $\mathcal{O}_{ss'}^{[g]}$ and O_c is shown in (b).

We now consider intersecting layers of the quantum double model for a group G, where each layer ℓ is described by the Hamiltonian

$$H_\ell = -\sum_s A_{s,\ell} - \sum_p B_{p,\ell}^{[1]} \tag{C.9}$$

The layers are placed in an intersecting configuration, as shown in Fig. 8-2a of the main text, to form a cubic lattice with two G-degrees of freedom per link. Furthermore, the layers are arranged so that a pair of overlapping links from orthogonal layers have opposite orientation, as shown in Fig. 8-2a. The state on link $\langle s, s' \rangle$ is now labeled $|z_{ss'}, w_{ss'}\rangle$. On a given link, we may explicitly write the operator that creates two pure flux excitations in each of the adjacent, orthogonal layers meeting at link $\langle s, s' \rangle$ as $W_{ss'}^{[g]} \otimes \widetilde{W}_{ss'}^{[g]}$ where

$$W_{ss'}^{[g]} \equiv \frac{1}{|G|} \sum_{z_{ss'} \in G} \sum_{h \in [g]} |z_{ss'} h\rangle \langle z_{ss'}| \tag{C.10}$$

acts on $z_{ss'}$, while $\widetilde{W}_{ss'}^{[g]}$ acts identically on other degree of freedom ($w_{ss'}$) on the same link. We claim that the following Hamiltonian for the coupled quantum double layers

$$H = \sum_\ell H_\ell - \Delta \sum_{\langle s, s' \rangle} \mathcal{O}_{ss'}^{[g]} \tag{C.11}$$

where

$$\mathcal{O}_{ss'}^{[g]} = W_{ss'}^{[g]} \otimes \widetilde{W}_{ss'}^{[g]} + \text{h.c.} \tag{C.12}$$

can give rise to a fracton topological phase in the limit that $\Delta \gg 1$, for an appropriate choice of flux $[g]$. The action of $\mathcal{O}_{ss'}^{[g]}$ on the decoupled layers of quantum double models is shown

278

schematically in Fig. 8-2b of the main text. We refer to this process for generating a fracton topological phase, where the immobile excitations carry a non-trivial quantum dimension, as composite $[g]$ flux loop condensation.

We now study the emergence of a fracton phase from an intersecting array of quantum double layers for the group $G = S_3$ – the permutation group on three elements – after condensing the composite flux loop formed from the non-Abelian flux **D** associated with the conjugacy class $[x]$. When $\Delta \gg 1$, the state on each link must satisfy

$$\mathcal{O}_{ss'}^{[x]} |\widetilde{h_{ss'}}\rangle = \frac{1}{2} |\widetilde{h_{ss'}}\rangle \tag{C.13}$$

and we may derive a low-energy effective theory that acts exclusively within this subspace. To derive this effective Hamiltonian, we begin by noting that $[A_{s,\ell}, \mathcal{O}_{ss'}^{[x]}] = 0$, which may be verified by explicit calculation. Additionally, observe that the flux operators $B_{p,\ell}^{[g]}$ do not generally commute with $\mathcal{O}_{ss'}^{[x]}$, since the latter has the effect of creating **D** flux excitations. Specific products of the charge and flux operators may commute with $\mathcal{O}_{ss'}^{[x]}$, however, as certain local conservation laws may remain even after condensing the non-Abelian **D** flux loop. When $\Delta \gg 1$, we find that the effective Hamiltonian takes the form

$$H_{\text{eff}} = -\sum_{s,\ell} A_{s,\ell} - K \sum_c O_c - \cdots \tag{C.14}$$

where $K \sim \Delta^{-6}$ is determined in perturbation theory, and the operator O_c is defined as

$$O_c \equiv \prod_{p,\ell \in \partial c} \left(2B_{p,\ell}^{[x]} - 1 \right) \tag{C.15}$$

with the product taken over the six plaquettes surrounding cube c. The ellipsis in (C.14) denotes other operators that commute with $\mathcal{O}_{ss'}^{[x]}$ at all sites that arise from higher-order perturbation theory.

The second term appearing in the effective Hamiltonian reflects the fact that after condensing the composite **D** flux loop, any configuration of fluxes appearing in the ground-state must be such that there are an even number of these fluxes at every cube on the lattice. The zero-flux condition in a single quantum double layer has been replaced by an emergent constraint on the parity of the **D** fluxes at each cube. We now verify that this is indeed an emergent conservation law (i.e. $[O_c, \mathcal{O}_{ss'}^{[x]}] = 0$) by explicitly by evaluating the commutator between the operators $(2B_{p,\ell}^{[x]} - 1)(2B_{p',\ell'}^{[x]} - 1)$ and $\mathcal{O}_{ss'}^{[x]}$ – as defined on the orthogonal plaquettes p and p' that overlap on the link $\langle s, s' \rangle$ as shown in Fig. C-2b – when acting on an arbitrary state $|\psi\rangle \equiv |z_1, z_2, z_3, z_4, z_5, z_6, w, w'\rangle$. Observe that

$$\left[\mathcal{O}_{ss'}^{[x]}, (1 - 2B_{p,\ell}^{[x]})(1 - 2B_{p',\ell'}^{[x]}) \right] |\psi\rangle = \frac{1}{|S_3|} \sum_{h,h' \in [x]} f(\{z_i\}, w, w', h, h') |\{z_i\}, wh, w'h'\rangle$$

279

where

$$f(\{z_i\}, w, w', h, h') = (1 - 2\,\delta_{z_6 z_7 w' z_5 \in [x]})(1 - 2\,\delta_{w z_1 z_2 z_3 \in [x]})$$
$$- (1 - 2\,\delta_{z_6 z_7 w' h' z_5 \in [x]})(1 - 2\,\delta_{w h z_1 z_2 z_3 \in [x]})$$

Here the Kronecker delta $\delta_{g \in [x]} = 1$ iff $g \in [x]$ and is 0 otherwise. We observe that $a \cdot b \in [x]$ iff only one of the elements a or b is a member of $[x]$. Therefore, for any g, $k \in S_3$ and $h \in [x]$, we find that $(1 - 2\delta_{ghk \in [x]}) = -(1 - 2\delta_{gk \in [x]})$. This immediately implies that $f(\{z_i\}, w, w', h, h') = 0$ and confirms the claim that $[O_c, \mathcal{O}_{ss'}^{[x]}] = 0$.

To summarize, we have shown that even after condensing the composite **D** flux loop, the parity of the fluxes at every cube on the lattice remains well-defined. While this parity is fixed to be $O_c = +1$ in the ground-state, acting with line- and membrane-like operators can create patterns of gapped excitations ($O_c = -1$) which are fundamentally immobile. Observe that when $\Delta \gg 1$, acting on the ground-state with a Wilson line [19] will create four such excitations, by anti-commuting with four of the cube operators O_c; each pair of excitations will be located at the two ends of the Wilson line. As explained in the main text, an array of these Wilson lines will create four such excitations that are well-separated and which are fundamentally immobile due the geometry of the membrane-like operator, i.e. a single excitation cannot be moved without creating other such excitations in the system. As in the Majorana checkerboard model, the product of the O_c operators along any plane is equal to the identity, after imposing periodic boundary conditions. This non-local constraint implies that the cube excitations may only be created in clusters of four at the corners of an operator with support on a flat, membrane-like region. As advertised, the non-Abelian **D** flux remains deconfined after coupling the S_3 quantum double layers, and has become an immobile fracton excitation in the condensed phase.

Other excitations also remain deconfined in the condensed phase. We do not present an exhaustive list of these excitations here, but instead argue that when $\Delta \gg 1$ a bound pair of the **B** charges in orthogonal layers, which is only free to move along a line without proliferating additional excitations (i.e. a "dimension-1 quasiparticle" in the language of Ref. [7]), remains a deconfined excitation with reduced mobility, while all of the pure charge excitations are confined. Recall that within a single layer of the 2D G gauge theory, the operator that creates a pure charge excitation, associated with the irreducible representation R of the group G is given by

$$\mathcal{W}_{ss'}^{(R)} = \sum_{z_{ss'} \in G} \chi_R(z_{ss'}) \, |z_{ss'}\rangle \, \langle z_{ss'}| \qquad \text{(C.16)}$$

where $\chi_R(g) = \text{Tr}_R(g)$ is a character of the representation R. The operator that creates the non-Abelian **D** flux does not commute with (C.16). Observe that $[W_{ss'}^{[x]}, \mathcal{W}_{ss'}^{(R)}] \neq 0$, so that an isolated charge cannot be created within the low-energy subspace defined by (C.13) when $\Delta \gg 1$. Notably, however, the operator that creates two **B** charges in orthogonal layers at a given link commutes with the composite **D** flux loop condensation, i.e. $[\mathcal{W}_{ss'}^{(\text{sgn})} \otimes \widetilde{\mathcal{W}}_{ss'}^{(\text{sgn})}, \mathcal{O}_{ss'}^{[x]}] = 0$, as may

be verified by explicit calculation, using the fact that the characters for the sign representation of S_3 are simply $\chi_{\text{sgn}}(1) = \chi_{\text{sgn}}(y) = 1$, $\chi_{\text{sgn}}(x) = -1$. Here, the operators $\mathcal{W}_{ss'}^{(\text{sgn})}$ and $\widetilde{\mathcal{W}}_{ss'}^{(\text{sgn})}$ act on the two degrees of freedom z and w at link $\langle s, s' \rangle$, respectively:

$$\mathcal{W}_{ss'}^{(R)} \otimes \widetilde{\mathcal{W}}_{ss'}^{(R)} \equiv \sum_{z, w \in G} \chi_R(z_{ss'}) \chi_R(w_{ss'}) \, |z_{ss'}, w_{ss'}\rangle \, \langle z_{ss'}, w_{ss'}|$$

Therefore, we conclude that while all of the isolated pure charge excitations are confined, a bound pair of $\mathbb{B}$ charges in orthogonal layers is a deconfined excitation, which may be moved along a line by sequentially applying the operator $\mathcal{W}_{ss'}^{(\text{sgn})} \otimes \widetilde{\mathcal{W}}_{ss'}^{(\text{sgn})}$. Since this excitation is formed from a composite of excitations in adjacent layers, it is only free to move along the line along which the layers intersect, and is therefore a dimension-1 quasiparticle in the language of Ref. [6].

Appendix D

Entanglement Dynamics in a Random Unitary Circuit

D.1 Growth of Hartley entropy S_0 in 1D

Consider a one-dimensional quantum spin chain of local Hilbert space dimension q, prepared initially in a product state, and apply a sequence of random unitaries that couple two neighboring spins. The location of the local unitary at a given time step is arbitrary. In the following we fix the location of the unitary, but take it to be Haar random.

We prove that in this situation the Hartley entropy S_0 generically (i.e. with probability 1) obeys

$$S_0(x, t + 1) = \min(S_0(x - 1, t), S_0(x + 1, t)) + 1, \tag{D.1}$$

if a unitary is applied at the bond x. The logarithm is of base q.

This formula can be interpreted in matrix-product-state (MPS) language. If d_x is the minimal value of the local bond dimension required for an exact MPS representation of the state, then $S_0(x) = \log d_x$. A heuristic parameter counting argument for the local bond dimension, given in Sec. D.1.3 below, suggests Eq. D.1.

However a more rigorous proof is necessary as such heuristic arguments can fail. In particular, one might naively conjecture a stronger statement: namely that for *any* state at time t, if the unitary at bond x is Haar random, then Eq. (D.1) is true with probability 1. This conjecture is false; a counterexample will be given below in Sec. D.1.2. We now give a proof of Eq. D.1.

D.1.1 Proof of Eq. (D.1)

Our genericity proof consists of two parts. First, we will show that given locations of unitaries, there exist certain unitaries such that at each time step, Eq. (D.1) is true. Second, we will show

the negation of Eq. (D.1)

$$S_0(x, t+1) < \min(S_0(x-1,t), S_0(x+1,t)) + 1 \qquad \text{(D.2)}$$

happens if and only if a system of polynomial equations in the entries of the unitaries is satisfied. (The inequality ">" never holds as we noted in the main text.) By the first part of the proof, the zero locus of these polynomial equations does not cover the entire set of unitaries. Therefore it is only a submanifold of strictly smaller dimension, which implies it has measure zero.

For the first part, it is sufficient to consider only three types of local unitaries: the identity I, the swap gate W, and a unitary E with the property that it turns a pair of unentangled polarized spins, $|11\rangle$, into $q^{-1/2} \sum_{i=1}^{q} |ii\rangle$, a maximally entangled state. Without loss of generality we may take the initial product state to be the polarized state $|\ldots 1111 \ldots\rangle$.

We are going to show that using these three types of unitaries at the given locations, one can construct a state whose entanglement entropy is given by Eq. (D.1). Since Eq. (D.1) defines the entropy inductively, we only have to show it inductively too.

At $t = 0$, all the spins are unentangled, so we can simply choose E for every designated location. Clearly, Eq. (D.1) is satisfied. At later times, if we do not apply E except on an unentangled pair of spins, then a spin can be either unentangled or maximally entangled with a single other spin. Therefore, at time $t > 0$ the spin s_L that is immediately left to the bond x can be

(i) unentangled,

(ii) entangled with a spin to the left of s_L,

(iii) entangled with the spin s_R that is immediately to the right of the bond y, or

(iv) entangled with a spin to the right of s_R.

These are exclusive possibilities, and similarly s_R has four options. Enumerating all 16 cases, which in fact reduces to 7 different cases excluding invalid ones and those related by reflection, one easily checks that there is always a choice among I, W, E that makes Eq. (D.1) true. Let us treat three exemplary cases here. If s_L and s_R are entangled at time t, then $S(x-1,t) = S(x+1,t)$ and $S(x,t) = S(x-1,t) + 1$, so one chooses the identity I. If s_L is entangled with a spin on the left of s_L and s_R is entangled with a spin on the right of s_R, then $S(x-1,t) = S(x+1,t) = 1 + S(x,t)$. One chooses the swap W to obtain $S(x,t+1) = S(x,t) + 2$. If s_L and s_R are both unentangled, then one applies the entangling unitary E to obtain $S(x,t+1) - 1 = S(x,t) = S(x-1,t) = S(x+1,t)$.

For the second part, recall that for any bipartite state

$$|\psi\rangle = \sum_{i,j} M_{i,j} |i\rangle |j\rangle, \qquad \text{(D.3)}$$

284

the number of nonzero Schmidt coefficients is equal to the number of nonzero singular values of the matrix M, which is nothing but the rank of M. For any positive integer r, the rank of M is *smaller* than r if and only if every $r \times r$ submatrix has determinant zero, i.e., all $r \times r$ *minors* vanish. Thus, a bipartite state $|\psi\rangle$ having Hartley entropy (log of rank of M) strictly smaller than $\log r$ is expressed by a system of polynomial equations on the coefficients of $|\psi\rangle$. If $|\psi\rangle$ is given by $U_t \ldots U_2 U_1 |0\rangle$ where $|0\rangle$ is a fixed product state, then the coefficients are some polynomials of the entries of the unitaries U_i, and hence the equations that expresses vanishing determinants are polynomial equations in the entries of the unitaries.

Our claim Eq. (D.1) completely determines the Hartley entropy based on the location of unitaries, and therefore the spatial configuration of the unitaries tells us which minors we should check. Namely, the size r of the minors we turn into the polynomial equations is given by (the exponential of) the right-hand side of Eq. (D.2). In other words, given a spatial configuration of unitaries, the polynomial equations that express Eq. (D.2) are determined. The polynomial equations are over tL variables, and the actual number of equations is much larger yet finite. We do not need explicit expressions for these polynomials, only the fact of their existence. These polynomials might a priori read $0 = 0$, i.e., they could be trivially satisfied. In that case, the solution to the polynomial equation would be the entire set of unitaries, and Eq. (D.1) could never be satisfied. However, we just showed in the first part that this cannot happen because there exists a choice of unitaries for which Eq. (D.1) is satisfied. This implies that the polynomial equations are nontrivial and define a measure zero subset of the entire set of unitaries. This completes the genericity proof.

D.1.2 Counterexample to the stronger conjecture

We have shown that (D.1) holds when all unitaries are chosen generically and the initial state is a product state. Naively one might make the stronger conjecture: that the update rule (D.1) holds whenever a generic unitary U is applied to an arbitrary — possibly fine-tuned — state $|\Psi\rangle$. We construct an explicit $|\Psi\rangle$ which is a counterexample to this stronger conjecture.

Consider four degrees of freedom $ABCD$. The spins B and C have dimension 2 each, and A and D have dimension 3 each. (To conform with our consideration of spin chains, the subsystems A and D should be regarded as subspaces of two or more spin-$\frac{1}{2}$'s.) The most general form of a quantum state on $ABCD$ is

$$\sum_{a,d=0}^{2} \sum_{b,c=0}^{1} T_{abcd} |a\rangle |b\rangle |c\rangle |d\rangle . \tag{D.4}$$

We consider $T_{abcd} = T'_{abd}\delta_{c,0}$, i.e., C is in $|0\rangle$, where

$$T'_{a0d} = \begin{pmatrix} 0 & 1 & 0 \\ 1 & 0 & 0 \\ 0 & 0 & 0 \end{pmatrix}_{ad} , \qquad\qquad T'_{a1d} = \begin{pmatrix} 0 & 0 & 1 \\ 0 & 0 & 0 \\ 1 & 0 & 0 \end{pmatrix}_{ad} . \tag{D.5}$$

(This does not give a normalized state, but we are only concerned about ranks.)

The Hartley entropy for the cut A/BCD is simple to compute. As remarked in the previous subsection, it is the rank of the coefficient matrix. Interpreting this matrix as a linear map, the rank is the dimension of the image of the map from BCD to A. The image is precisely the linear span of *columns* of T'_{a0d} and T'_{a1d}. They have three linearly independent columns, implying the Hartley entropy for A/BCD is $\log_2 3$. Similarly, the rank of the coefficient matrix for ABC/D is the dimension of the linear span of the *rows* of T'_{a0d} and T'_{a1d}, which reads 3. That is, the Hartley entropy for ABC/D is $\log_2 3$.

If Eq. (D.1) were to be true for generic choice of Haar random unitary on BC, then we should be able to find a unitary on BC such that

$$S_0(AB/CD) = \log_2 3 + 1 = \log_2 6. \tag{D.6}$$

We show this cannot hold. Applying the unitary U on BC the state, we obtain

$$\sum_{b,c} U_{b'c',bc} T_{abcd} = \underbrace{U_{b'c',00}}_{U_0} T'_{a0d} + \underbrace{U_{b'c',10}}_{U_1} T'_{a1d}. \tag{D.7}$$

where U_0 and U_1 are 2×2 matrices. The coefficient matrix for the cut AB/CD is then

$$V = U_0 \otimes T'_0 + U_1 \otimes T'_1 \tag{D.8}$$

whose rank should be 6 if $S_0(AB/CD) = \log 6$. Computing all the minors of the 6×6 matrix V for *arbitrary* matrices U_0 and U_1, we find that all (5×5)-minors vanish, implying that V has rank at most 4. Therefore, for this nongeneric initial state,

$$S_0(x, t+1) \neq \min(S_0(x-1, t), S_0(x+1, t)) + 1. \tag{D.9}$$

D.1.3   Parameter-counting argument

Consider a 1D state $|\Psi\rangle$ in a matrix product representation. Labelling the states of the qubits (spins) by $\sigma, \sigma' \dots$ running from 1 to q,

$$|\Psi\rangle = \sum_{\{\sigma\}} \sum_{\{a\}} \left(\dots A^{\sigma}_{a_{x-1},a_x} A'^{\sigma'}_{a_x,a_{x+1}} \dots \right) |\dots \sigma\sigma' \dots\rangle . \tag{D.10}$$

Since the state is not translationally invariant, we allow the bond dimension d_x to vary from bond to bond ($a_x = 1, \ldots, d_x$). In an efficient representation, d_x is equal to the rank of the reduced density matrix for a cut at x:

$$d_x = q^{S_0(x)}. \tag{D.11}$$

We ask how $S_0(x)$ changes when we apply a unitary U to the two spins, σ and σ', either side of bond x. This effects the change (repeated indices are summed)

$$A^\sigma_{a_{x-1},a_x} A'^{\sigma'}_{a_x,a_{x+1}} \longrightarrow U_{\sigma\sigma',\tau\tau'} A^\tau_{a_{x-1},a_x} A'^{\tau'}_{a_x,a_{x+1}}. \tag{D.12}$$

To update the matrix product representation we must find new matrices $\widetilde{A}$ and $\widetilde{A}'$ which satisfy

$$\widetilde{A}^\sigma_{a_{x-1},a_x} \widetilde{A}'^{\sigma'}_{a_x,a_{x+1}} = U_{\sigma\sigma',\tau\tau'} A^\tau_{a_{x-1},a_x} A'^{\tau'}_{a_x,a_{x+1}}. \tag{D.13}$$

In order to solve this equation for $\widetilde{A}$ and $\widetilde{A}'$, it will generally be necessary to increase the bond dimension at x to a new value d'_x. Naively, the necessary value of d'_x will generically be determined by equating the number of independent equations in (D.13) with the number of degrees of freedom in $\widetilde{A}$ and $\widetilde{A}'$. (However, the previous subsection shows that this expectation can fail for certain choices of A and A'.)

The number of equations is $q^2 d_{x-1} d_{x+1}$, since this is the number of possible values for the external indices in (D.13). The numbers of degrees of freedom in $\widetilde{A}$ and $\widetilde{A}'$ are $q d_{x-1} d'_x$ and $q d_{x+1} d'_x$ respectively. However, d'^2_x of these are redundant, because the state is unchanged by the transformation $\widetilde{A}^\sigma \to \widetilde{A}^\sigma M$, $\widetilde{A}'^{\sigma'} \to M^{-1} \widetilde{A}'^{\sigma'}$, with M an arbitrary $d'_x \times d'_x$ matrix. Equating the number of equations with the number of independent degrees of freedom gives

$$(d'_x - q d_{x-1})(d'_x - q d_{x+1}) = 0. \tag{D.14}$$

Choosing the smallest solution,

$$d'_x = q \times \min\{d_{x-1}, d_{x+1}\}. \tag{D.15}$$

This agrees with Eq. D.1 since $S_0(x) = \log d_x$.

D.2 Haar average for $\operatorname{Tr} \rho_x^2$

Let $\rho_x(t)$ be the reduced density matrix for a cut at x, obtained by tracing out the spins to the left of the cut. Each index on this matrix labels a configuration of the spins to the right of the cut. Let us temporarily label these spins $1, 2, \ldots$, and let the spin immediately to the left of the

287

cut be denoted 0. The indices on the reduced density matrices are then:

$$\rho_{x-1}(t)^{\sigma_0,\sigma_1,\sigma_2,\ldots}_{\mu_0,\mu_1,\mu_2,\ldots} \qquad\qquad \rho_x(t)^{\sigma_1,\sigma_2,\ldots}_{\mu_1,\mu_2,\ldots} \qquad\qquad \rho_{x+1}(t)^{\sigma_2,\ldots}_{\mu_2,\ldots} \qquad (\text{D.16})$$

In the following we assume that repeated indices are summed. After applying a unitary on bond x,

$$\rho_x(t+1)^{\sigma_1,\sigma_2,\ldots}_{\mu_1,\mu_2,\ldots} = U_{\tau\sigma_1,\sigma_0'\sigma_1'} U^*_{\tau\mu_1,\mu_0'\mu_1'} \rho_{x-1}(t)^{\sigma_0',\sigma_1',\sigma_2,\ldots}_{\mu_0',\mu_1',\mu_2,\ldots}$$

Let us average $\operatorname{Tr}\rho_x(t+1)^2$ over the choice of unitary, for a fixed initial state:

$$\left\langle \operatorname{Tr}\rho_x(t+1)^2 \right\rangle = \rho_{x-1}(t)^{\sigma_0',\sigma_1',\sigma_2,\ldots}_{\mu_0',\mu_1',\mu_2,\ldots} \rho_{x-1}(t)^{\mu_0'',\mu_1'',\mu_2,\ldots}_{\sigma_0'',\sigma_1'',\sigma_2,\ldots} \times \left\langle U_{\tau\sigma_1,\sigma_0'\sigma_1'} U^*_{\tau\mu_1,\mu_0'\mu_1'} U_{\nu\mu_1,\mu_0''\mu_1''} U^*_{\nu\sigma_1,\sigma_0''\sigma_1''} \right\rangle$$

The Haar average for four elements of a U(d) matrix (here $d=q^2$, and each index on U represents a pair of spin indices) is

$$\left\langle U_{a,b} U_{a',b'}\; U^*_{c,d} U^*_{c',d'} \right\rangle_{\text{Haar}} = \frac{1}{d^2-1}\left(\left\{ \delta_{a,c}\delta_{a',c'}\delta_{b,d}\delta_{b',d'} + \delta_{a,c'}\delta_{a',c}\delta_{b,d'}\delta_{b',d} \right\} \right. \qquad (\text{D.17})$$
$$\left. - \frac{1}{d}\left\{ \delta_{a,c}\delta_{a',c'}\delta_{b,d'}\delta_{b',d} + \delta_{a,c'}\delta_{a',c}\delta_{b,d}\delta_{b',d'} \right\} \right).$$

The index contractions give the result in the text,

$$\left\langle \operatorname{Tr}\rho_x(t+1)^2 \right\rangle_{\text{Haar}} = q(q^2+1)^{-1}\left(\operatorname{Tr}\rho_{x-1}^2 + \operatorname{Tr}\rho_{x+1}^2 \right). \qquad (\text{D.18})$$

D.3   Entanglement entropy of stabilizer states

A stabilizer state is a state of an n-qubit system defined by a complete set $\{g_1,\ldots,g_n\}$ of commuting tensor products of Pauli matrices through equations

$$g_i\,|\psi\rangle = +\,|\psi\rangle. \qquad (\text{D.19})$$

The group generated by $\{g_1,\ldots,g_n\}$ is naturally called a stabilizer group, and denoted by $\mathcal{G}$ [175, 365]. A trivial example is the all-spin-up state, defined as

$$Z_i\,|\psi\rangle = +\,|\psi\rangle \qquad (\text{D.20})$$

for all $i=1,\ldots,n$. The condition that $|\psi\rangle$ is nonzero and unique is equivalent to the condition that the operator

$$\frac{1}{|\mathcal{G}|}\sum_{g\in\mathcal{G}} g \qquad (\text{D.21})$$

288

is a projector of rank one [366, 367]. Since $|\psi\rangle$ is in the image of this projector, we see

$$|\psi\rangle\langle\psi| = \frac{1}{|\mathcal{G}|} \sum_{g\in\mathcal{G}} g. \tag{D.22}$$

Since this is a normalized pure density matrix, its trace is equal to 1. But a Pauli matrix has the property that it is traceless. Therefore, only the identity element on the right has nonzero trace:

$$1 = \frac{1}{|\mathcal{G}|} \dim(\mathbb{C}^2)^{\otimes n} = \frac{1}{|\mathcal{G}|} 2^n \tag{D.23}$$

From this expression, it is straightforward to obtain expressions for reduced density matrices. Suppose the n-qubit system is partitioned into two complementary regions A and B. Tracing out B, we have

$$\rho_A = \frac{1}{2^n} \sum_{g\in\mathcal{G}} \mathrm{Tr}_B(g). \tag{D.24}$$

$\mathrm{Tr}_B(g)$ is nonzero if and only if the tensor component corresponding to B is identity, in which case

$$\mathrm{Tr}_B(g) = 2^{|B|} g|_A \tag{D.25}$$

where $g|_A$ denotes the tensor components of g corresponding to A. The set of all $g|_A$ such that $\mathrm{Tr}_B(g) \neq 0$ can be regarded as a subgroup of $\mathcal{G}$, which we denote by $\mathcal{G}_A$. The formula for ρ_A now reads

$$\rho_A = \frac{2^{|B|}}{2^n} \sum_{g\in\mathcal{G}_A} g = \frac{|\mathcal{G}_A|}{2^{|A|}} \frac{1}{|\mathcal{G}_A|} \sum_{g\in\mathcal{G}_A} g. \tag{D.26}$$

It is immediate that ρ_A is proportional to a projector since it is a sum over a group. It follows that the rank of ρ_A is equal to $2^{|A|}/|\mathcal{G}_A|$. In particular, the (Rényi or von Neumann) entropy of ρ_A with base-2 logarithm is

$$S(\rho_A) = |A| - \log_2 |\mathcal{G}_A|. \tag{D.27}$$

The subgroup $\mathcal{G}_A$ has period 2, and therefore $\log_2 |\mathcal{G}_A|$ is an integer, which is equal to the number of independent stabilizers supported only on A. This expression for the entanglement entropy has also appeared in [333, 334].

Now, regard the stabilizer group $\mathcal{G}$ as a binary vector space V by ignoring the overall phase (sign) factors. Let Π_A be the truncation map retaining the components corresponding to the region A, and similarly Π_B be the truncation map for $B = \bar{A}$. It is routine to check that V decomposes as $V_A \oplus V_B \oplus V'$ for some subspace $V' \subseteq V$ where V_A and V_B are the spans of
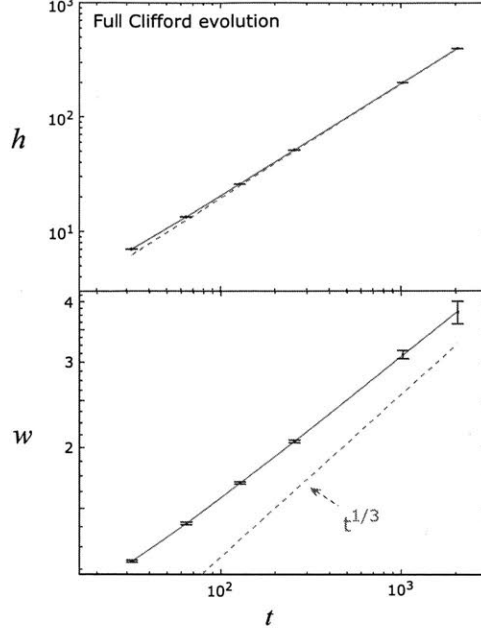
Figure D-1: Top: Growth of the mean entanglement in units of $\log 2$ as a function of time for the random Clifford evolution (only CNOT gates). The red solid curve is a fit using the form Eq. [10.49]. Dashed line shows asymptotic linear behaviour. Bottom: Growth in the fluctuations in the entanglement with time. The exponent β is found to be $\beta_{\mathrm{w}} = 0.3 \pm 0.04$, in agreement with the KPZ prediction $\beta = 1/3$. The dashed line shows the expected asymptotic behaviour, $\mathrm{w}(t) \sim t^{\beta}$ with $\beta = 1/3$.

stabilizers supported only on A and B, respectively. Both the truncation maps are injective on V'. It follows that $S_A = |B| - \dim_{\mathbb{F}_2} V_B = \dim_{\mathbb{F}_2}(\Pi_A V) - |A|$. This completes the proof of Eq. 10.33.

D.4 Free fermions are Non-Generic

The growth of entanglement in systems of *free* particles is highly non-generic. In the presence of noise the entanglement of a system of free particles on the lattice grows only as $S \sim \sqrt{t}$, in contrast to the behaviour $S \sim t$ of generic systems. The case of spatially homogeneous noise has been discussed recently [368]. The basic point is the same when the noise varies in space: the fact that the single-particle wavefunctions spread diffusively in the presence of noise implies that the entanglement cannot be larger than $O(\sqrt{t})$ [368].

As a concrete example, consider a short-range hopping Hamiltonian for free fermions,

$$H(t) = \sum_{ij} H_{ij}(t) c_i^\dagger c_j, \tag{D.28}$$

with noisy matrix elements $H_{ij}(t)$. For simplicity, take the initial state to consist of particles

localized at sites $i \in S$ for some set S; for example we could take S to consist of all the even-numbered sites:

$$|\Psi(0)\rangle = \prod_{i \in S} c_i^\dagger |0\rangle . \tag{D.29}$$

Under the evolution, each creation operator evolves into a superposition of creation operators,

$$c_i^\dagger \longrightarrow \sum_j \psi^{(i)}(j,t) c_j^\dagger , \tag{D.30}$$

where $\psi^{(i)}(j,t)$ is the solution of the time-dependent Schrodinger equation for a particle initially localized at i. In the absence of noise, $\psi^{(j)}$ spreads ballistically, but in the presence of noise it spreads only diffusively. The fact that each creation operator is spread out over only $O(\sqrt{t})$ sites after a time t immediately implies that the mean entanglement is at most of order $\sqrt{t}$. (See also Ref. [368].) Note however that this argument does not tell us how large the fluctuations are.[1]

We have confirmed numerically that $\langle S \rangle \propto \sqrt{t}$ for a noisy 1D hopping model, using the formalism of Ref. [370] to construct the reduced density matrix. This is much slower than the linear-in-time growth of generic interacting models. The $\sqrt{t}$ scaling should apply for free fermions in any number of dimensions. In 1D it also applies to certain noisy spin models via the Jordan Wigner transformation: for example the transverse field XY model,

$$H(t) = \sum_i \left(J_i(t) \left[\sigma_i^x \sigma_{i+1}^x + \sigma_i^y \sigma_{i+1}^y \right] + h_i(t) \sigma_i^z \right) . \tag{D.31}$$

However any generic perturbation to the spin chain spoils the free fermion correspondence. We then expect the generic KPZ behavior to reassert itself.

D.5 Numerics for full Clifford evolution

In Sec. 10.5.1 we have presented numerical results for random unitary evolution using only the CNOT gates Eq. 10.31. Here we present similar analysis using the full set of generators for the Clifford group, showing that the additional gates do not modify the universal behavior. The additional single-site gates are the Hadamard and phase gates defined in Eq. 10.29 and Eq. 10.30 respectively. (The Hadamard gate corresponds to swapping the X and Z vectors while the phase gate corresponds to adding the X vector to the Z vector.)

The von Neumann entropy in units of $\log 2$ and the corresponding width averaged over $\sim 2 \times 10^5$ realisations (except for the last data point where $\sim 2 \times 10^4$ realisations were used for the average) are plotted in Fig. [D-1]. The fit to the KPZ universal form Eq. 10.49 gives $\beta_h = 0.2 \pm 0.15$ and $\beta_w = 0.3 \pm 0.04$. We also obtain $v_E = 0.194 \pm 0.001$, $B = 0.4 \pm 0.2$, $C = 0.4 \pm 0.1$, $D = 0.4 \pm 0.6$ and $\eta = -0.4 \pm 0.8$. These results are consistent with the KPZ

---

[1]Random unitary evolution of a single wavepacket is discussed in Ref. [369]. However we must consider the full many-body wavefunction, since the formalism of Ref. [370] for the free fermion density matrix shows that the initially occupied orbitals do not simply contribute additively to the entanglement.

universality and with the data presented in Fig. 10-17.

D.6   Details of statistics of membranes

The exponents governing the membrane problem are traditionally denoted θ and ζ, and are related by $2\zeta - \theta = 2 - d$ [309]. Consider a patch of the membrane with linear dimensions scaling as ℓ. This includes both its temporal dimension and its internal spatial dimensions: after a rescaling of time, the membrane is statistically isotropic on large scales. The mean 'energy' of this patch of membrane scales as $\ell^d + \text{const} \times \ell^\theta$, with fluctuations of order ℓ^θ. The lengthscale for wandering of the membrane in the transverse direction is of order ℓ^ζ. The numerical results quoted in the main text are in good agreement with an epsilon expansion about $d = 4$ which gives $\zeta \simeq 0.208(4 - d)$ [339] (see also [371]). The scaling forms for the entanglement discussed in the text are easily found by regarding the membrane as made up of patches of appropriate linear size: size t for Eqs. 10.53, 10.54, and size L for Eq. 10.55.

Note that the geometry of the membrane, including the transverse lengthscale (which is $\Delta x \sim t^\zeta$ for the regime $t \lesssim L$) determines the dimensions of the spacetime region around ∂A for which the final entanglement is sensitive to small changes in $H(t)$, i.e. in the history of the noise.
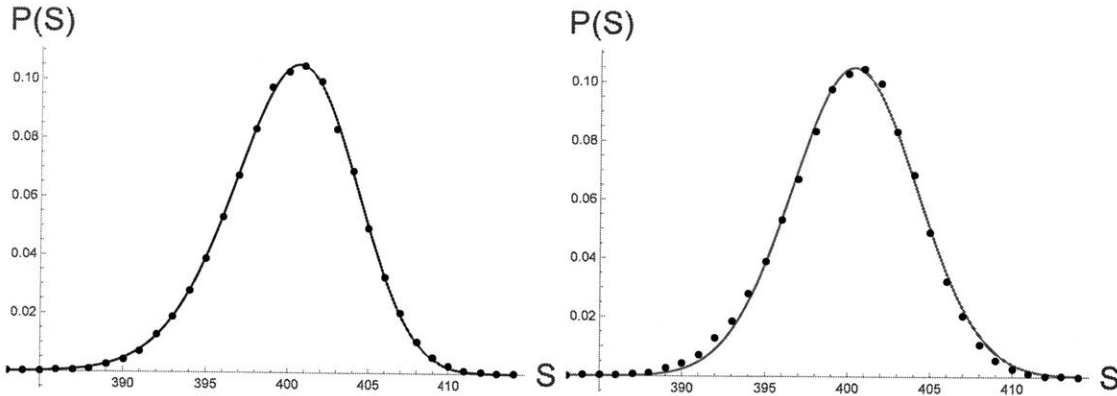
Figure D-2: Observed probability distribution for the entanglement entropy across the central bond of chain of length $L = 2048$ at time $t = 2048$ under the full Clifford dynamics, fitted to two probability distributions. Top: best fit to the Tracy-Widom (TW) distribution with $\beta = 1$. A fit to TW with $\beta = 2$ is not shown, but is indistinguishable at the scale of the figure. Bottom: best fit to the Gaussian. Clearly, the Tracy-Widom distribution fits the data better than Gaussian, as the latter shows systematic deviation. The $1 - R^2$ values for the fits are 2.1×10^{-4} for $\text{TW}_{\beta=1}$, 2.0×10^{-4} for $\text{TW}_{\beta=2}$, and 1.6×10^{-3} for Gaussian.

D.7 Entanglement probability distribution

As mentioned in the main text, a remarkable recent advance in KPZ theory has been the derivation of the full universal probability distribution for the height of the surface at fixed position and fixed large time [260, 261, 262, 263, 264, 265, 266, 267, 268, 269, 270]; see [289, 290, 291] for reviews. In our case this height corresponds to the entanglement S across a cut in a system undergoing noisy unitary dynamics. One may separate out the nonuniversal growth rate v_E, and the nonuniversal constant D governing the scale of fluctuations, by writing

$$S = v_E t + D t^\beta \chi. \tag{D.32}$$

The rescaled random variable χ is then expected to have a *universal* probability distribution $P(\chi)$ at late times. This probability distribution depends on the initial condition for the surface. For a surface which is initially flat, $P(\chi)$ is the Tracy-Widom distribution with $\beta = 1$. This is the case relevant to our setup where $S(x, t = 0) = 0$. (In the directed polymer interpretation this corresponds to a setup where the x–coordinate of the upper endpoint of the polymer is fixed but that of the lower endpoint is free; again this is the setup relevant to our minimal cut picture.) Other initial conditions for a growing surface can give different universal forms for $P(\chi)$ — for example the so-called 'narrow wedge' initial condition gives the Tracy-Widom distribution with $\beta = 2$. (The latter distribution is likely to be relevant to noisy growth of entanglement between two subsystems that are initially unentangled with each other, but separately highly entangled.[2])

In Fig. D-2 we fit numerical data for the probability distribution of S to the expected Tracy Widom form and, for comparison, to a Gaussian distribution. The data is for the 'full' Clifford dynamics (defined in Sec. 10.5.1) at time $t = 2048$. Each fit involves two parameters, corresponding to the mean and the variance. The Tracy Widom distribution used is the theoretically expected one with $\beta = 1$, but in fact the present data does not allow us to discriminate between $\mathrm{TW}_{\beta=1}$ and $\mathrm{TW}_{\beta=2}$. The Tracy Widom distribution is a much better fit to the data than the Gaussian, as quantified in the Figure caption. This is further confirmation of KPZ universality in the Clifford case. A more detailed investigation of the probability distribution is beyond the scope of this paper, in view of finite-time effects at the accessible timescales.

---

[2]The generalization of the directed polymer picture to entangled initial states (Sec. 10.7) indicates that the lower endpoint of the polymer is then no longer free, and instead favours $x = 0$.

Appendix E

Operator Spreading in Random Unitary Circuits

E.1 Evolving Distribution on Operator Strings

In this Appendix we give a more detailed explanation of the relationship between the dynamics of the coefficients $a_{\mathcal{S}}$ and a Markov process [221, 222] and of the derivation of the diffusion picture. We consider Haar-random, local unitary dynamics. In an N-site system with a q-dimensional Hilbert space at each site, a Hermitian operator that has evolved under the unitary circuit $\mathcal{O}(t) = U(t)^{\dagger}\,\mathcal{O}\,U(t)$ may expanded in a basis of $\mathrm{SU}(q^N)$ generators $\{\mathcal{S}\}$ as

$$\mathcal{O}(t) = \sum_{\mathcal{S}} a_{\mathcal{S}}(t)\mathcal{S} \tag{E.1}$$

Our normalization convention is $\mathrm{Tr}(\mathcal{S}\mathcal{S}') = q^N \delta_{\mathcal{S}\mathcal{S}'}$, so that $a_{\mathcal{S}}(t) = q^{-N}\mathrm{Tr}(\mathcal{O}(t)\mathcal{S})$. The squared coefficient $a_{\mathcal{S}}(t)^2$ evolves as

$$a_{\mathcal{S}}(t)^2 = q^{-2N} \sum_{\mathcal{S}',\mathcal{S}''} a_{\mathcal{S}'}(t-1) a_{\mathcal{S}''}(t-1) \mathrm{Tr}[\mathcal{U}\,\mathcal{S}'\mathcal{U}^{\dagger}\mathcal{S}]\,\mathrm{Tr}[\mathcal{U}\,\mathcal{S}''\mathcal{U}^{\dagger}\mathcal{S}]$$

$$= q^{-2N} \sum_{\mathcal{S}',\mathcal{S}''} a_{\mathcal{S}'}(t-1) a_{\mathcal{S}''}(t-1) \prod_{r} \mathrm{tr}[U_r\,S_r'U_r^{\dagger}S_r]\,\mathrm{tr}[U_r\,S_r''U_r^{\dagger}S_r]$$

where $\mathcal{U}$ is a layer of m-site unitaries that were applied at time $t-1$. In the second line, we have written $\mathcal{U} = \prod_r U_r$ where r is the coordinate of disjoint, m-site clusters on which the unitary $U_r \in \mathrm{U}(q^m)$ acts, and we have also decomposed $\mathcal{S} = \prod_r S_r$ as a product of basis elements acting on these m-site clusters. These operators are normalized according to $\mathrm{tr}[S_r S_r'] = q^m \delta_{S_r, S_r'}$ and $\mathrm{tr}[S_r] = q^m \delta_{S_r,1}$. The Haar average of the above expression is given by

$$\overline{\mathrm{tr}[U_r\,S_r'U_r^{\dagger}S_r]\,\mathrm{tr}[U_r\,S_r''U_r^{\dagger}S_r]} = \frac{\delta_{S_r',S_r''}}{1-q^{-2m}} \left\{ q^{2m}\delta_{S_r,1}\delta_{S_r',1} + 1 - \delta_{S_r',1} - \delta_{S_r,1} \right\} \tag{E.2}$$

295

And so, the Haar-averaged $a_\mathcal{S}(t)^2$ evolves *linearly*

$$\overline{a_\mathcal{S}(t)^2} = \frac{1}{q^{2N}} \sum_{\mathcal{S}',\mathcal{S}''} a_{\mathcal{S}'}(t-1) a_{\mathcal{S}''}(t-1) \prod_r \frac{\delta_{S'_r,S''_r} \left(q^{2m}\delta_{S_r,1}\delta_{S'_r,1} + 1 - \delta_{S'_r,1} - \delta_{S_r,1}\right)}{1-q^{-2m}}$$

$$= \sum_{\mathcal{S}'} W_{\mathcal{S}\mathcal{S}'} \, a_{\mathcal{S}'}(t-1)^2 \qquad\qquad (\text{E}.3)$$

with the real, symmetric matrix

$$W_{\mathcal{S}\mathcal{S}'} = \prod_r \left[\delta_{S_r,1}\delta_{S'_r,1} + \frac{(1-\delta_{S_r,1})(1-\delta_{S'_r,1})}{q^{2m}-1} \right] \qquad\qquad (\text{E}.4)$$

Averaging again over the unitaries applied in the previous timesteps gives an equation for $P_\mathcal{S}(t) \equiv \overline{a_\mathcal{S}^2(t)}$

$$P_\mathcal{S}(t) = \sum_{\mathcal{S}'} W_{\mathcal{S}\mathcal{S}'} P_{\mathcal{S}'}(t-1) \qquad\qquad (\text{E}.5)$$

which is formally a master equation for a fictitious Markov process [221, 222]; at a given time there is a single string $\mathcal{S}$ which is updated stochastically in each time step, via local updates involving a cluster of m sites. From the form of $W_{\mathcal{S}\mathcal{S}'}$ we see that the local update on m sites is performed by replacing a non-trivial generator on the cluster *randomly* by any one of the $q^{2m} - 1$ non-trivial generators. We emphasize that this fictitious Markov process is not the true unitary dynamics of the operator $\mathcal{O}(t)$.

This fictitious classical stochastic process dramatically simplifies through the following ob-servations. We focus here on one spatial dimension with updates on bonds. First, observe that the matrix elements $W_{\mathcal{S}\mathcal{S}'}$ only depend on the support of the generators $\mathcal{S}$ and $\mathcal{S}'$, so that (E.5) gives rise to a simpler Markov process for the binary occupation number $n(x)$, which is 1 if the corresponding generator has support at site x and 0 otherwise (if $\mathcal{S}$ acts as the identity at x). The probability distribution of the occupation numbers is given by

$$P[\{n\}; t] = \sum_{\mathcal{S}} {}' \, \overline{a_\mathcal{S}(t)^2} \qquad\qquad (\text{E}.6)$$

where the prime indicates that the sum is only over strings $\mathcal{S}$ that are compatible with the configuration $n(x)$. Further, the endpoint of the string observes an *autonomous* Markovian dynamics. Since $m = 2$, updates involving the endpoint either include the site to the right of it which is empty or that to the left which may be empty or full. The dynamical rule above implies that the probabilities for the position of the endpoint after the update are independent of whether the leftward site was initially occupied or empty. Formally the probability distribution

for the position of the endpoint in this fictitious dynamics is

$$p_{\text{end}}(x;t) = \sum_{\substack{n \text{ with} \\ \text{endpt at } x}} P[\{n\};t] = \sum_{\mathcal{S} \text{ ends at } x} \overline{a_{\mathcal{S}}(t)^2} \qquad (E.7)$$

which is precisely $\overline{\rho(x,t)}$, as defined in Sec 2. Therefore, for an endpoint at x or $x+1$, a single update applied to the sites x and $x+1$ leaves the endpoint at x with probability $p = (q^2 - 1)/(q^4 - 1) = 1/q^2 + 1$ and at $x+1$ with probability $1 - p$. This establishes the claim in Sec. 2 for the evolution of $\overline{\rho(x,t)}$ in a single timestep.

E.2   Velocity and diffusion constant for lattice diffusion equation

Our layout of the evolution operator is such that the local unitaries alternate between even and odd bonds. In other words, a bond at time step t is either at the left or right of the bond at $t-1$. Thus, it suffices to count the left and right moves to specify the position of the right end-bond of $X_0(t)$. As described in the main text the probability of a left move is p. Let $u \geq 0$ be the number of right moves, and $v \geq 0$ be the number of left moves. We have $u + v = t$, and $u - v$ (or $u - v \pm 1$) is the spatial coordinate of the right endpoint. Therefore, the probability distribution of the position of the right end bond is

$$f(u,v) = \binom{u+v}{u}(1-p)^u p^v. \qquad (E.8)$$

This is correctly normalized since $\sum_{u+v=t} f(u,v) = (1-p+p)^t = 1$. Then, the probability that a site x is left to the right end of $X_0(t)$ is

$$\sum_{u+v=t,\, u-v \geq x} f(u,v) = \sum_{v=0}^{(t-x)/2} \binom{t}{v}(1-p)^{t-v} p^v \simeq \Phi\left(\frac{v_B t - x}{\sigma}\right) \qquad (E.9)$$

where Φ is the cumulative density function of the normal distribution, and

$$v_B = \frac{q^2 - 1}{q^2 + 1}, \quad \sigma = \frac{2q\sqrt{t}}{q^2 + 1}. \qquad (E.10)$$

E.3   Noisy diffusion equation

Starting with Eq. 9.29, WLOG rescale space so $D = 1$ and set $v = 0$ by going to the moving frame. Let ρ_0 be the solution without noise, $\rho_0 = (4\pi t)^{-1/2} e^{-x^2/4t}$. In terms of the Green's

297

function

$$\rho(x,t) - \rho_0(x,t) = \int_{x',t'} G(x - x', t - t')\partial_{x'}\eta(x',t')\rho(x',t')$$

$$= \int_{x',t'} G'(x - x', t - t')\eta(x',t')\rho(x',t'). \qquad (E.11)$$

The centre of mass position of the wavepacket within a given realisation is $x_{\mathrm{cm}} = \int_x x\rho(x,t)$, so, if $\overline{x_{cm}}$ is the centre of mass position averaged over realisations,

$$x_{\mathrm{cm}} - \overline{x_{cm}} = \int_{x,x',t'} xG'(x - x', t - t')\eta(x',t')\rho(x',t') = -\int_{x,x',t'} G(x - x', t - t')\eta(x',t')\rho(x',t'),$$

$$(x_{\mathrm{cm}} - \overline{x_{cm}})^2 = \int_{\substack{x,\tilde{x},x',\\ \tilde{x}',t',\tilde{t}'}} G(x - x', t - t')G(\tilde{x} - \tilde{x}', t - \tilde{t}')\eta(x',t')\eta(\tilde{x}',\tilde{t}')\rho(x',t')\rho(\tilde{x}',\tilde{t}').$$

Averaging over the noise with $\langle \eta(x,t)\eta(x',t')\rangle = \lambda\delta(x - x')\delta(t - t')$,

$$\overline{[x_{\mathrm{cm}} - \overline{x_{cm}}]^2} = \lambda\int_{\substack{x,\tilde{x},\\ x',t'}} G(x - x', t - t')G(\tilde{x} - x', t - t')\rho(x',t')^2. \qquad (E.12)$$

For the leading order scaling, we replace ρ with ρ_0 on the right hand side. Then dimensional analysis applied to the integral gives

$$\sqrt{\overline{(x_{\mathrm{cm}} - \overline{x_{cm}})^2}} \propto \lambda^{1/2}t^{1/4} + \ldots \qquad (E.13)$$

This is a statistical variation in x_{cm} of order $t^{1/4}$, in agreement with the heuristic argument and with Ref. [278]. This variation is small compared to the width of ρ, indicating that $\rho - \rho_0 \ll \rho$ at late times. The typical size of $\partial_x\rho$ near the peak is $O(1/t)$, so $x_{\mathrm{cm}} - \overline{x_{\mathrm{cm}}} \sim t^{1/4}$ corresponds to $\rho - \rho_0 \sim t^{-3/4}$, as compared with $\rho \sim t^{-1/2}$. The approximation above is therefore self-consistent.

E.4 Random Clifford operators

Here we review that the left- and right- invariant probability distribution over the Clifford group on n q-dimensional qudits is a unitary 2-design when q is a prime number. In other words, for a qudit of prime power dimension q^n, the unitary group $U(q^n)$ has a finite subgroup that is a unitary 2-design, and there is a linear operator basis that remains closed under conjugations by this subgroup. This is a well-known result [273], but we include it here for readers' convenience.

To define the Clifford group, we first need the Pauli group. Define $X = \sum_{j=0}^{q-1} |j + 1 \mod q\rangle \langle j|$ and $Z = \sum_{j=0}^{q-1} e^{2\pi ij/q} |j\rangle \langle j|$. Then, the Pauli group is the subgroup of $U(q^n)$ generated by

matrices $X_1, Z_1, \ldots, X_n, Z_n$ where

$$X_j = I_q^{\otimes(j-1)} \otimes X \otimes I_q^{\otimes(n-j)},$$
$$Z_j = I_q^{\otimes(j-1)} \otimes Z \otimes I_q^{\otimes(n-j)}. \tag{E.14}$$

The Clifford group is defined to be the normalizer of the Pauli group in $U(q^n)$. The Pauli group quotiented out by its center $\langle \omega = e^{2\pi i/q} \rangle$ is abelian since $XZX^\dagger = \omega^{-1}Z$, and is isomorphic to the additive group $\mathbb{Z}_q^{2n}$. We define P_v for $v \in \mathbb{Z}_q^{2n}$ to be an element of the Pauli group (Pauli operator) as

$$P_v = X_1^{v_1} X_2^{v_2} \cdots X_n^{v_n} Z_1^{v_{n+1}} Z_2^{v_{n+2}} \cdots Z_n^{v_{2n}} \tag{E.15}$$

The center of the Pauli group is also contained in the center of $U(q^n)$, and therefore the conjugation action by the Clifford group on the Pauli group induces an action on $\mathbb{Z}_q^{2n}$. It turns out that this group $\mathcal{S}$ of action consists precisely of those that preserves the symplectic form

$$\lambda_n = \begin{pmatrix} 0 & -I_n \\ I_n & 0 \end{pmatrix} \tag{E.16}$$

over $\mathbb{Z}_q$.

A probability distribution ν of unitary matrices to form a 2-design means that

$$\mathbb{E}_{U \sim \nu} U \otimes U^* \otimes U \otimes U^* = \mathbb{E}_{U \sim \mu} U \otimes U^* \otimes U \otimes U^* \tag{E.17}$$

where μ is the Haar probability distribution over $U(q^n)$, and U^* is the complex conjugate of U. Tautologically, the Haar distribution is a 2-design. This is equilvalent to having that

$$\mathbb{E}_{U \sim \nu} UOU^\dagger \otimes UO'U^\dagger = \mathbb{E}_{U \sim \mu} UOU^\dagger \otimes UO'U^\dagger \tag{E.18}$$

for any $q^n \times q^n$ matrices O and O'. Since Pauli operators (the elements of the Pauli group defined above) generates over the complex numbers the full operator algebra, it is enough to have Eq. (E.18) with O and O' being Pauli operators.

Let ν be the left-invariant (hence right-invariant) probability distribution over the Clifford group. This is the uniform distribution over the finite Clifford group. Consider a $\mathbb{C}$-linear map Π_ν on the set of operators defined by

$$\Pi_\nu : O \otimes O' \mapsto \mathbb{E}_{U \sim \nu} UOU^\dagger \otimes UO'U^\dagger. \tag{E.19}$$

Since ν is a left-invariant distribution over a group of unitaries, Π_ν is a projector (which is hermitian under the Hilbert-Schmidt inner product). Since the Clifford group includes the

299

Pauli group, we have for arbitrary $a, b \in \mathbb{Z}_q^{2n}$

$$\Pi_\nu(P_a \otimes P_b^\dagger) = \sum_{x,y \in \mathbb{Z}_q^{2n}} \eta_{x,y}^{a,b} \, P_x \otimes P_y^\dagger$$

$$(\eta_{x,y} \in \mathbb{C}, \text{Pauli basis expansion})$$

$$= P_c^{\otimes 2} \Pi_\nu \left(P_a \otimes P_b^\dagger \right) (P_c^{\otimes 2})^{-1}$$

$$(\text{for any } c \in \mathbb{Z}_q^{2n} \text{ by the left-invariance of } \nu)$$

$$= \sum_{x,y \in \mathbb{Z}_q^{2n}} \eta_{x,y}^{a,b} \, \omega^{c^T \lambda_n (x-y)} \, P_x \otimes P_y^\dagger$$

$$(\text{commutation relation among Pauli operators})$$

$$= \sum_{x \in \mathbb{Z}_q^{2n}} \eta_{x,-x}^{a,b} \, P_x \otimes P_x^\dagger$$

$$(\det \lambda_n = 1, \text{ and } c \text{ was arbitrary}).$$

The use of inverse $P_b^\dagger$ here instead of P_b is for notational convenience later.

Now, observe that for any nonzero $x, y \in \mathbb{Z}_q^{2n}$ there exists a symplectic transformation $S \in \mathcal{S}$ such that $y = Sx$. For this step, it is essential that q is prime. By the right-invariance of ν by S, we see $\Pi_\nu(P_x \otimes P_x^\dagger) = \Pi_\nu(P_y \otimes P_y^\dagger)$. This implies that

$$\Pi_\nu(P_a \otimes P_b) = \eta_{0,0}^{a,b} I + \eta^{a,b} \sum_{x \in \mathbb{Z}_q^{2n} \setminus \{0\}} P_x \otimes P_x^\dagger. \tag{E.20}$$

We claim that this is a linear combination of the identity operator and the swap operator $\mathcal{F} = \sum_{u,v=0}^{q-1} |u\rangle \langle v| \otimes |v\rangle \langle u|$. This is easily verified once we expand $\mathcal{F}$ in the Pauli operator basis; using $\text{Tr}(\mathcal{F} O \otimes O') = \text{Tr}(OO')$ for any $q^n \times q^n$ matrices O and O', we see that $\mathcal{F} \propto \sum_{x \in \mathbb{Z}_q^{2n}} P_x \otimes P_x^\dagger$.

The identity operator and the swap operator commute with $U \otimes U$ where $U \in U(q^n)$. This implies that $\Pi_\nu(P_a \otimes P_b^\dagger)$ commutes with $U \otimes U$, and hence is equal to $\Pi_{\mu_{\text{Haar}}} \circ \Pi_\nu(P_a \otimes P_b^\dagger)$. By the right-invariance of the Haar distribution μ_{Haar}, we conclude that Eq. (E.18) is proved.

When q is not prime, any probability distribution over the Clifford group fails to be a unitary 2-design. Let $n = 1$. Since the image of Π_μ is a linear combination of the identity and the swap, we must have (see App. E.7 below)

$$\Pi_\mu(O \otimes O') = \sum_{s=\pm 1} \frac{\text{Tr}(O)\,\text{Tr}(O') + s\,\text{Tr}(OO')}{q(q+s)} \frac{I + s\mathcal{F}}{2}. \tag{E.21}$$

When $q = 6$, there are non-identity Pauli operators P and Q such that $P^2 = I$ and $Q^3 = I$. By Eq. (E.21), we have $\Pi_\mu(P \otimes P^\dagger) = \Pi_\mu(Q \otimes Q^\dagger) \neq 0$. However, $\Pi_\nu(P \otimes P^\dagger)$ is a linear combination of Pauli operators, each of which squares to identity, whereas $\Pi_\nu(Q \otimes Q^\dagger)$ is a linear combination of those that cube to identity, so they cannot be equal.

E.5 Anomalous behaviour of the front for $\phi = 0$

Above we noted that for sufficiently large p, $p > p_c$, the lattice growth process which we consider has anomalous behaviour when the front is oriented parallel to a lattice plane. This is a known phenomenon in various lattice growth models in discrete time which have *synchronous parallel updates* and is well understood in terms of directed percolation [283, 284, 285, 286, 287].

In the regime $p > p_c$ the lattice-aligned ($\phi = 0$) front has a speed $v_B(\phi = 0) = 2$ which is precisely the maximum possible speed allowed by causality. In this regime the front is pinned to the 'light front' and is not rough (i.e. the width is of order one). (Exactly at p_c, the aligned front is logarithmically rough [286].) For our lattice model it appears that $p_c \lesssim 2$.

This phenomenon is easily understood via a correspondence with directed percolation [285]. First consider a straight, lattice-aligned front in the trivial deterministic limit $p = 0$ ($q = \infty$). Apart from possibly on the first time step, this flat front advances by two lattice spacings every period: the front keeps pace with the 'light cone' which is the line $x = 2t$. Let $\tilde{n}(y, t) = 0, 1$ denote the occupation numbers of the column of sites at the lightcone: $\tilde{n}(y, t)$ is the occupation number of the site at position $(2t, y)$ at time t. When $p = 0$ we have $\tilde{n}(y, t) = 1$. We are interested in the density $\langle \tilde{n} \rangle$ (averaged over y) at late times when p is nonzero. If this density remains finite, that means the front has an $O(1)$ width, and is attached to the light cone. If it instead tends to zero, the front detaches from the light cone, and we expect to recover standard KPZ roughening. Note that, in order to determine $\tilde{n}$ at time $t + 1$, it is sufficient to know only $\tilde{n}$ at time t. The dynamics of the occupation numbers $\tilde{n}(y, t)$ are as follows. Under a horizontal dimer update (which advances the lightfront) each occupied y has a chance $(1 - p)$ of becoming unoccupied. Under a vertical update pairs of adjacent y undergo the pairwise update described in the main text. This allows occupied sites to 'reproduce'. This is therefore a birth-death process of the directed percolation type [307]. When p is large the death rate is small and the reproduction rate is large, and the process is in an 'active' phase with $\langle \tilde{n} \rangle > 0$, while when p is small the population of occupied sites dies out.

E.6 Shape of a spreading droplet for weakly varying $v(\phi)$

Consider an asymptotic front shape described by the parameterized curve $(\theta, r_t(\theta))$ in polar coordinates, which grows simply by rescaling: $r_t(\theta) = t \times r(\theta)$. Let $\phi(\theta)$ be the angle of the front's normal (to the x axis) at polar position θ. The radial growth rate is $\dot{r}_t(\theta) = v_B(\phi(\theta))/\cos[\phi(\theta) - \theta]$. Since the curve grows by rescaling we have $\partial_\theta[\dot{r}_t(\theta)/r_t(\theta)] = 0$. Note that

$$\partial_\theta \ln r(\theta) = -\tan[\phi(\theta) - \theta]. \tag{E.22}$$

Combining these gives [299]

$$(\tan[\phi(\theta) - \theta] + w(\phi(\theta))) \, \phi'(\theta) = 0. \tag{E.23}$$

Therefore at a location where $r(\theta)$ is smooth we either have $\phi'(\theta) = 0$, i.e. a straight segment, or

$$\tan[\phi(\theta) - \theta] = -w(\phi(\theta)). \tag{E.24}$$

If the solution is everywhere smooth then the above equation must be satisfied everywhere. (Such solutions exist for sufficiently weakly varying v_B.) It is straightforward to solve this equation in powers of w:

$$-\tan[\phi(\theta) - \theta] = w(\theta) - \frac{1}{2}\partial_\theta w(\theta)^2 + \frac{1}{6}\partial_\theta^2 w(\theta)^3 + \dots \tag{E.25}$$

We find that the RHS involves only total derivatives of periodic functions. (Just from looking at Eq. E.24 this is at first sight surprising since it emerges from various cancellations.) Therefore, integrating the right hand side according to (E.22) gives a periodic $r(\theta)$.

For a formal explanation for why the expansion of $\tan(\phi - \theta)$ contains only total derivatives of periodic functions, consider a flow in the space of functions $v_B(\phi)$ which interpolates between the function of interest and the trivial function $v_B(\phi)$=const. Let $v_1(\phi)$ and $v_2(\phi)$ be two functions that are infinitesimally close on this flow and let $\phi_1(\theta)$ and $\phi_2(\theta)$ be the corresponding solutions. Assuming that $\phi_1(\theta)$ is periodic and corresponds to a periodic $r(\theta)$ we show that this property is inherited by $\phi_2(\theta)$ to order $\phi_2 - \phi_1$. Using (E.22), (E.24) we obtain

$$\tan[\phi_1(\theta) - \theta] - \tan[\phi_2(\theta) - \theta] = \partial_\theta\left[\ln v_2(\phi_1(\theta)) - \ln v_1(\phi_1(\theta))\right] \tag{E.26}$$

As required, the RHS is indeed the total derivative of a periodic function (note that ϕ_2 does not appear on the RHS). Integrating along the flow then establishes the property for general $v_B(\phi)$ at the formal level — i.e. assuming that the solution evolves smoothly during the flow.

E.7 Haar average formula

Here we review a standard formula for the average of matrix elements of unitary matrix with respect to the Haar probability measure μ on $U(N)$. (See e.g. [276].) Let us abbreviate $\int_{U(N)} \mathrm{d}\mu(U)$ as $\mathbb{E}_U$. We are going to prove that

$$\mathbb{E}_U\, U\,|a\rangle\,\langle b|\,U^\dagger \otimes U\,|c\rangle\,\langle d|\,U^\dagger = \sum_{s=\pm} \frac{I + sF}{2N(N + s1)}(\delta_{ab}\delta_{cd} + s\delta_{cb}\delta_{ad}) \tag{E.27}$$

where F is the swap operator on $(\mathbb{C}^N)^{\otimes 2}$. Evaluating a particular matrix element, we have

$$\mathbb{E}_U\, U_{a'a}U_{b'b}^*U_{c'c}U_{d'd}^* = \frac{1}{N^2 - 1}\Big[\delta_{a'b'}\delta_{c'd'}\delta_{ab}\delta_{cd} + \delta_{a'd'}\delta_{b'c'}\delta_{ad}\delta_{bc}$$
$$- \frac{1}{N}(\delta_{ab}\delta_{cd}\delta_{a'd'}\delta_{b'c'} + \delta_{a'b'}\delta_{c'd'}\delta_{ad}\delta_{bc})\Big]. \tag{E.28}$$

Proof of Eq. (E.27). The average is a matrix on $\mathcal{H} = (\mathbb{C}^N)^{\otimes 2}$ that commutes with every $U^{\otimes 2}$. Hence, the average is block-diagonal in the basis where the representation of $U(d)$ is block-diagonal. The irreps appearing in $\mathcal{H}$ are the symmetric subspace and the anti-symmetric subspace. In each irrep, the average must be proportional to the identity $I_\pm$ by the Schur's lemma, and we need to evaluate the trace in order to determine the constant of proportionality. The projection onto the (anti-)symmetric subspace is $(I \pm F)/2$ where F is the swap operator: $F |ac\rangle = |ca\rangle$. So the trace is

$$\frac{1}{2} \operatorname{Tr} \left[U |a\rangle \langle b| U^\dagger \otimes U |c\rangle \langle d| U^\dagger \pm U |c\rangle \langle b| U^\dagger \otimes U |a\rangle \langle d| U^\dagger \right] = \frac{1}{2} [\delta_{ab}\delta_{cd} \pm \delta_{cb}\delta_{ad}] \quad \text{(E.29)}$$

This must be equal to $C_\pm \operatorname{Tr}(I_\pm) = C_\pm N(N\pm1)/2$ Therefore, the average is equal to $\sum_{s=\pm} C_s(I + sF)/2$. $\qquad\square$

E.8 Proof of Eq. (9.77)

Let N be the Hilbert space dimension of n q-dimensional qudits; $N = q^n$. For any $N \times N$ unitary U, denote by $U^{\otimes t,t}$ the tensor product $(U \otimes U^*)^{\otimes t}$, where U^* is the complex conjugate of U. Let μ be the Haar probability distribution on $U(N)$, and define for any probability distribution ν on $U(N)$, a real number

$$g(\nu, t) = \left\| \underbrace{\mathbb{E}_{U\sim\nu} U^{\otimes t,t}}_{\Pi_\nu} - \underbrace{\mathbb{E}_{U\sim\mu} U^{\otimes t,t}}_{\Pi_\mu} \right\|_\infty. \quad \text{(E.30)}$$

Here, $\|\cdot\|_\infty$ denotes the maximum singular value. Due to left and right invariance of μ, it follows that $\Pi_\mu^2 = \Pi_\mu = \Pi_\nu \Pi_\mu = \Pi_\mu \Pi_\nu$. ($\Pi_\nu$ is not in general a projector.) Therefore,

$$g(\nu^{*m}, t) = \|\Pi_\nu^m - \Pi_\mu\|_\infty = \|(\Pi_\nu - \Pi_\mu)^m\|_\infty = g(\nu, t)^m, \quad \text{(E.31)}$$

where ν^{*m} is the m-fold convolution of ν, i.e., ν^{*m} is the distribution of the product $U_1 U_2 \cdots U_m$ when every U_i obeys distribution ν.

Now, let ν be the distribution on $U(N)$ obtained by applying one layer of even bond local Haar random unitaries $(U(q^2))$ and then one layer of odd bond local Haar random unitaries. Brandao-Harrow-Horodecki's result [223] implies that

$$g(\nu, t) \le \exp(-1/M_{t,q}), \quad \text{(E.32)}$$

$$M_{t,q} = 4250\lceil \log_q(4t) \rceil^2 q^2 t^5 t^{3.1/\log q}. \quad \text{(E.33)}$$

Their theorem does not directly cover this, but they have lemmas that are good enough for our purpose; eq. (48) of Ref. [223] is what we actually need.

Consider $f(U) = N^{-2}(\operatorname{Tr} UXU^\dagger YUXU^\dagger Y)^2 \ge 0$ where all the matrices U, X, Y are $N \times N$.

$f(U)$ can be thought of as $\langle \tilde{X} | U^{\otimes 4,4} | \tilde{Y} \rangle$ for some vectors $|\tilde{X}\rangle$ and $|\tilde{Y}\rangle$. Assume $\text{Tr}(X) = \text{Tr}(Y) = 0$, but $\text{Tr}(X^2) = \text{Tr}(Y^2) = N$. Then, the Euclidean norms of $|\tilde{X}\rangle$ and $|\tilde{Y}\rangle$ are both N^2. Normalizing so that $|X\rangle := |\tilde{X}\rangle /N^2$ and $|Y\rangle := |\tilde{Y}\rangle /N^2$, we can write $f(U) = N^2 \langle X | U^{\otimes 4,4} | Y \rangle$.

By Eqs. (E.31) and (E.32), we have

$$|\mathbb{E}_{U \sim \nu^{*m}} f(U) - \mathbb{E}_{U \sim \mu} f(U)| \leq e^{-m/M_{4,q}} q^{2n} \tag{E.34}$$

If $|\mathbb{E}_{U \sim \mu} f(U)| \leq q^{-cn}$, then $\mathbb{E}_{U \sim \nu^{*m}} f(U) \leq 2q^{-cn}$ whenever $m/n \geq (c+2)M_{4,q} \log q$.

Hastings' Schwinger-Dyson trick [305] gives

$$\mathbb{E}_{U \sim \mu} f(U) \leq 10N^{-2} = 10q^{-2n}. \tag{E.35}$$

Therefore, whenever $m/n \geq 4M_{4,q} \log q$, we have

$$\mathbb{E}_{U \sim \nu^{*m}} f(U) \leq 11q^{-2n}. \tag{E.36}$$

E.9   A mean field approximation

Ref. [230] argued, on the basis of Keldysh perturbation theory, that in various circumstances the out-of-time-order correlator would satisfy a traveling wave equation such as the Fisher-KPP equation (the details of this equation depending on the physical system). An example is the Fisher-KPP equation itself:

$$\partial_t \mathcal{C} = D\nabla^2 \mathcal{C} + \lambda \mathcal{C}(1 - \mathcal{C}). \tag{E.37}$$

The key feature is λ term, which means that if $\mathcal{C}$ is 'seeded' with a small nonzero value, it will increase to a value close to one on a timescale of order λ^{-1} (and then saturate). This equation has stable solutions describing a front propagating with a speed $v_B = 2\sqrt{D\lambda}$. This front does not broaden.

This phenomenology is very different from the picture which we have obtained from the random circuit and the mapping to classical growth processes. Recall that in 1D we related $\mathcal{C}$ to a homogeneous (linear) equation, and in higher dimensions we found that $\mathcal{C}$ was not governed by a partial differential equation.

The purpose of this Appendix is to show that a traveling wave picture can emerge from our mappings if we make a certain mean field approximation. This mean field approximation is not valid in the systems we have studied — it is an uncontrolled approximation which does not capture the true behaviour either at short or at large times. However in variant models a small parameter could be present which justified the mean field approximation up to some finite but large timescale. In this situation we expect that mean field will nevertheless break down at asymptotically long times, with the front eventually roughening in the manner discussed in the text.

Recall that for the random circuit we have

$$\overline{C}(x,t) = \frac{q^2}{q^2-1} \langle n(x,t) \rangle, \tag{E.38}$$

where $n(x,t)$ is the occupation number in the fictitious classical cluster growth problem. Let us consider the *joint* probability distribution $P(\{n\};t)$ for this occupation number. This distribution involves nontrivial correlations between sites which are crucial for capturing the correct asymptotic behaviour. Nevertheless let us explore the mean field approximation in which we pretend all sites are independent, $P(\{n\};t) = \prod_x P_x(n(x);t)$, with

$$P_x(n(x);t) = \left[1 - \langle n(x,t) \rangle \right] \delta_{n(x),0} + \langle n(x,t) \rangle \, \delta_{n(x),1}. \tag{E.39}$$

For simplicity, consider a model on the hypercubic lattice in d dimensions (with coordination number $z = 2d$) in which unitaries ('updates') are applied to bonds in a Poissonian fashion at rate $\Gamma/2$ per bond. This continuous time protocol does not change the basic point but it simplifies the equations. Write $m = \langle n \rangle$. Note that if we update a bond which contains at least one fictitious particle, the subsequent (conditionally) averaged density on that bond is $1 - p$. This implies

$$m(x, t + \Delta t) = (1 - z\Gamma\Delta t)m(x,t) + \Gamma\Delta t(1-p) \sum_{y \in x} \left\langle \left(1 - \delta_{n(x),0}\delta_{n(y),0}\right)\right\rangle, \tag{E.40}$$

where the first term is the probability that site x does not receive an update in the interval Δt. Making the mean field approximation, $\left\langle \delta_{n(x),0}\delta_{n(y),0}\right\rangle$ factorizes into $(1 - m(x))(1 - m(y))$, so that

$$\partial_t m(x,t) = \Gamma \sum_{y \in x} \left(- pm(x,t) + (1-p)m(y,t) - (1-p)m(x,t)m(y,t)\right). \tag{E.41}$$

The first term on the right is a 'death rate'. The second term is spreading. The third term is a correction to overcounting in the second term. An analogous equation could be written down for the regular circuit considered in the main text, but we would have to use discrete time. Eq. E.41 is a lattice traveling wave equation. This is most apparent if we make a formal expansion in the lattice spacing a to second order (valid, given the approximations already made, if the solution is slowly varying). Recalling $p = 1/(q^2 + 1)$ and Eq. E.38,

$$\Gamma^{-1}\partial_t \overline{C}(x,t) = a^2 \left((1-p) - (1-2p)\overline{C}\right)\nabla^2\overline{C} + 2d(1-2p)\overline{C}(1 - \overline{C}). \tag{E.42}$$

This differs from the Fisher-KPP equation only in the C–dependence of the diffusion constant, and we expect similar properties.

Above, the mean field limit was an unjustified formal approximation. We could of course construct random circuit models in which the (lattice) mean field approximation was quanti-

305

tatively accurate up to a large time, for example by using long range interactions or a large coordination number to reduce the effect of correlations. However at long times, in physical dimensionalities, we expect the front to roughen so that the mean field traveling wave picture breaks down. In (unphysically) high dimensions, mean field may be valid even at late times (recall that the phase diagram of the KPZ equation allows for a non-roughening phase in high dimensions, as discussed in the text).

Bibliography

[1] S. Vijay, T. H. Hsieh, and L. Fu, Phys. Rev. X **5**, 041038 (2015).

[2] S. Vijay and L. Fu, Phys. Scr. **T168**, 014002 (2016).

[3] S. Vijay and L. Fu, Phys. Rev. B **94**, 235446 (2016).

[4] S. Vijay and L. Fu, (2017), 1703.00459.

[5] S. Vijay, (2017), 1701.00762.

[6] S. Vijay, J. Haah, and L. Fu, Phys. Rev. B **92**, 235136 (2015).

[7] S. Vijay, J. Haah, and L. Fu, Phys. Rev. B **94**, 235157 (2016).

[8] S. Vijay and L. Fu, (2017), 1706.07070.

[9] A. Nahum, J. Ruhman, S. Vijay, and J. Haah, Phys. Rev. X **7**, 031016 (2017).

[10] A. Nahum, S. Vijay, and J. Haah, (2017), 1705.08975.

[11] S. Vijay and L. Fu, Phys. Rev. B **91**, 220101(R) (2015).

[12] S. Vijay and A. Vishwanath, (2018), 1803.08483.

[13] B. Russell, *The Conquest of Happiness* (Liveright Publishing Corporation, 1930).

[14] L. Fu and C. L. Kane, Phys. Rev. Lett. **100**, 096407 (2008).

[15] A. G. Fowler, M. Mariantoni, J. M. Martinis, and A. N. Cleland, Phys. Rev. A **86**, 032324 (2012).

[16] D. A. Ivanov, Phys. Rev. Lett. **86**, 268 (2001).

[17] C. Xu and C. Wu, Phys. Rev. B **77**, 134449 (2008).

[18] M. Creutz, L. Jacobs, and C. Rebbi, Phys. Rev. D **20**, 1915 (1979).

[19] A. Kitaev, Ann. Phys. **303**, 2 (2003).

[20] A. Einstein, B. Podolsky, and N. Rosen, Phys. Rev. **47**, 777 (1935).

[21] J. Preskill, (2012), 1203.5813v3.

[22] D. Poulin, A. Qarry, R. D. Somma, and F. Verstraete, Phys. Rev. Lett. **106**, 170501 (2011).

[23] W. Shakespeare, *Hamlet* (Arden Shakespeare, London, UK, 2006), .

[24] P. Shor, SIAM J. Sci. Statist. Comput. **26**, 1484 (1997).

[25] L. K. Grover, Proceedings, 28th Annual ACM Symposium on the Theory of Computing (STOC) , 212 (1996).

[26] E. Farhi *et al.*, Science **292**, 472 (2001).

[27] M. A. Nielsen and I. L. Chuang, Phys. Rev. Lett. **79**, 321 (1997).

[28] E. Knill and R. Laflamme, Phys. Rev. A **55**, 900 (1997).

[29] R. Laflamme, C. Miquel, J. P. Paz, and W. H. Zurek, Phys. Rev. Lett. **77**, 198 (1996).

[30] D. C. Tsui, H. L. Stormer, and A. C. Gossard, Phys. Rev. Lett. **48**, 1559 (1982).

[31] R. Laughlin, Phys. Rev. B **23**, 5632 (1981).

[32] R. B. Laughlin, Phys. Rev. Lett. **50**, 1395 (1983).

[33] X. G. Wen and Q. Niu, Phys. Rev. B **41**, 9377 (1990).

[34] E. Fradkin and S. Shenker, Phys. Rev. D **19**, 3682 (1979).

[35] S. C. Zhang, T. H. Hansson, and S. Kivelson, Phys. Rev. Lett. **62**, 82 (1989).

[36] X. G. Wen, Phys. Rev. B **44**, 2664 (1991).

[37] S. Sachdev and N. Read, Phys. Rev. Lett. **66**, 1773 (1991).

[38] T. Senthil and M. P. A. Fisher, Phys. Rev. B **62**, 7850 (2000).

[39] R. Moessner and S. L. Sondhi, Phys. Rev. Lett. **86**, 1881 (2001).

[40] M. Hermele, M. P. A. Fisher, and L. Balents, Phys. Rev. B **69**, 064404 (2004).

[41] B. I. Halperin, Phys. Rev. Lett. **52**, 1583 (1984).

[42] D. Arovas, J. R. Schrieffer, and F. Wilczek, Phys. Rev. Lett. **53**, 722 (1984).

[43] M. A. Levin and X. G. Wen, Phys. Rev. B **71**, 045110 (2005).

[44] A. Kitaev, Ann. Phys. **321**, 2 (2006).

[45] X. Chen, Z.-C. Gu, and X.-G. Wen, Phys. Rev. B **82**, 155138 (2010).

[46] J. Haah, Phys. Rev. A **83**, 042330 (2011).

[47] J. Haah, Commun. Math. Phys **324**, 351 (2013).

[48] S. Bravyi and J. Haah, Phys. Rev. Lett. **111**, 200501 (2013).

[49] R. Alicki, M. Fannes, and M. Horodecki, J. Phys. A: Mathematical and Theoretical **42**, 065303 (2008).

[50] P. Calabrese and J. Cardy, J. Stat. Mech. **0504**, P04010 (2005).

[51] P. Calabrese and J. Cardy, Journal of Physics A: Mathematical and Theoretical **42**, 504005 (2009).

[52] P. Calabrese and J. Cardy, Journal of Statistical Mechanics: Theory and Experiment **2016**, 064003 (2016).

[53] C. T. Asplund, A. Bernamonti, F. Galli, and T. Hartman, Journal of High Energy Physics **9**, 110 (2015), 1506.03772.

[54] M. Fagotti and P. Calabrese, Phys. Rev. A **78**, 010306 (2008).

[55] I. Peschel and V. Eisler, Journal of Physics A: Mathematical and Theoretical **42**, 504003 (2009).

[56] J. Schachenmayer, B. P. Lanyon, C. F. Roos, and A. J. Daley, Phys. Rev. X **3**, 031015 (2013).

[57] P. Hauke and L. Tagliacozzo, Phys. Rev. Lett. **111**, 207202 (2013).

[58] A. Coser, E. Tonni, and P. Calabrese, Journal of Statistical Mechanics: Theory and Experiment **2014**, P12017 (2014).

[59] A. S. Buyskikh, M. Fagotti, J. Schachenmayer, F. Essler, and A. J. Daley, Phys. Rev. A **93**, 053620 (2016).

[60] V. Alba and P. Calabrese, (2016), 1608.00614.

[61] A. M. Lauchli and C. Kollath, Journal of Statistical Mechanics: Theory and Experiment **2008**, P05018 (2008).

[62] H. Kim and D. A. Huse, Phys. Rev. Lett. **111**, 127205 (2013).

[63] L. Zhang, H. Kim, and D. A. Huse, Phys. Rev. E **91**, 062128 (2015).

[64] W. W. Ho and D. A. Abanin, Phys. Rev. B **95**, 094302 (2017).

[65] M. Žnidarič, T. c. v. Prosen, and P. Prelovšek, Phys. Rev. B **77**, 064426 (2008).

[66] J. H. Bardarson, F. Pollmann, and J. E. Moore, Phys. Rev. Lett. **109**, 017202 (2012).

[67] M. Serbyn, Z. Papić, and D. A. Abanin, Phys. Rev. Lett. **110**, 260601 (2013).

[68] D. A. Huse, R. Nandkishore, and V. Oganesyan, Phys. Rev. B **90**, 174202 (2014).

[69] R. Vosk and E. Altman, Phys. Rev. Lett. **110**, 067204 (2013).

[70] A. Chandran and C. R. Laumann, Phys. Rev. B **92**, 024301 (2015).

[71] D. J. Luitz, N. Laflorencie, and F. Alet, Phys. Rev. B **93**, 060201 (2016).

[72] F. Verstraete, V. Murg, and J. Cirac, Advances in Physics **57**, 143 (2008), http://dx.doi.org/10.1080/14789940801912366.

[73] R. Islam *et al.*, Nature **528**, 77 (2015).

[74] A. M. Kaufman *et al.*, Science **353**, 794 (2016).

[75] A. J. Daley, H. Pichler, J. Schachenmayer, and P. Zoller, Phys. Rev. Lett. **109**, 020505 (2012).

[76] S. Leichenauer and M. Moosa, Phys. Rev. D **92**, 126004 (2015).

[77] H. Casini, H. Liu, and M. Mezei, Journal of High Energy Physics **7**, 77 (2016), 1509.05044.

[78] X. Chen, T. Zhou, D. A. Huse, and E. Fradkin, Annalen der Physik (2016).

[79] T. Hartman, S. A. Hartnoll, and R. Mahajan, Phys. Rev. Lett. **119**, 141601 (2017).

[80] J. Cotler, N. Hunter-Jones, J. Liu, and B. Yoshida, JHEP **1711**, 048 (2017).

[81] J. Haah, Phys. Rev. B **89**, 075119 (2014).

[82] M. Kardar, G. Parisi, and Y.-C. Zhang, Physical Review Letters **56**, 889 (1986).

[83] E. Majorana, Nuovo Cimento **14**, 171 (1937).

[84] A. Kitaev, Phys.-Usp. **44**, 131 (2001).

[85] G. Moore and N. Read, Nucl. Phys. B **360**, 362 (1991).

[86] N. Read and D. Green, Phys. Rev. B **61**, 10267 (2000).

[87] J. Alicea, Rep. Prog. Phys **75**, 076501 (2012).

[88] C. W. J. Beenakker, Annu. Rev. Cond. Mat. Phys. **4**, 113 (2013).

[89] R. M. Lutchyn, J. D. Sau, and S. D. Sarma, Phys. Rev. Lett. **105**, 077001 (2010).

[90] Y. Oreg, G. Refael, and F. von Oppen, Phys. Rev. Lett. **105**, 177002 (2010).

[91] A. C. Potter and P. A. Lee, Phys. Rev. Lett. **105**, 227003 (2010).

[92] S. Nadj-Perge, I. K. Drozdov, B. A. Bernevig, and A. Yazdani, Phys. Rev. B **88**, 020407(R) (2013).

[93] V. Mourik *et al.*, Science **336**, 1003 (2012).

[94] A. Das *et al.*, Nat. Phys. **8**, 887 (2012).

[95] S. Nadj-Perge *et al.*, Science **346**, 6209 (2014).

[96] J.-P. Xu *et al.*, Phys. Rev. Lett. **114**, 017001 (2015).

[97] H.-J. Kwon, K. Sengupta, and V. M. Yakovenko, European Phys. Journal B **37**, 349 (2004).

[98] L. Fu and C. L. Kane, Phys. Rev. B **79**, 161408(R) (2009).

[99] L. Fu, Phys. Rev. Lett. **104**, 056402 (2010).

[100] S. Bravyi and A. Kitaev, Quantum Computers and Computing **2**, 43 (2001).

[101] M. H. Freedman and D. A. Meyer, Found. Comput. Math **1**, 325 (2001).

[102] R. Raussendorf and J. Harrington, Phys. Rev. Lett. **98**, 190504 (2007).

[103] R. Raussendorf, J. Harrington, and K. Goyal, New J. Phys **9**, 199 (2007).

[104] A. G. Fowler, A. M. Stephens, and P. Groszkowski, Phys. Rev. A **80**, 052312 (2009).

[105] E. Dennis, A. Kitaev, A. Landahl, and J. Preskill, J. Math. Phys. **43**, 4452 (2002).

[106] R. Barends *et al.*, Nature **508**, 500 (2014).

[107] J. Kelly *et al.*, Nature **519**, 66 (2015).

[108] A. D. Córcoles *et al.*, Nature Commun. **6**, 6979 (2015).

[109] S. Bravyi, B. Terhal, and B. Leemhuis, New. J. Phys. **12**, 083039 (2010).

[110] C. Xu and L. Fu, Phys. Rev. B **81**, 134435 (2010).

[111] X.-G. Wen, Phys. Rev. Lett. **90**, 016803 (2003).

[112] J. C. Y. Teo, J. Phys. C **28**, 143001 (2016).

[113] D. V. Harlingen, private communication.

[114] B. van Heck, F. Hassler, A. R. Akhmerov, and C. W. J. Beenakker, Phys. Rev. B **84**, 180502(R) (2011).

[115] R. Hutzen, A. Zazunov, B. Braunecker, A. L. Yeyati, and R. Egger, Phys. Rev. Lett. **109**, 166403 (2012).

[116] B. van Heck, A. R. Akhmerov, F. Hassler, M. Burrello, and C. W. J. Beenakker, New. J. Phys **14**, 035019 (2012).

[117] J. Koch *et al.*, Phys. Rev. A **76**, 042319 (2007).

[118] M. Veldhorst *et al.*, Nature Mat **11**, 417 (2012).

[119] J. R. Williams *et al.*, Phys. Rev. Lett. **109**, 056803 (2012).

[120] F. Yang *et al.*, Phys. Rev. B **86**, 134504 (2012).

[121] J. B. Oostinga *et al.*, Phys. Rev. X **3**, 021007 (2013).

[122] I. Sochnikov *et al.*, Nano Lett. **13**, 3086 (2013).

[123] S. Cho *et al.*, Nature Communications **4**, 1689 (2013).

[124] C. Kurter, A. D. K. Finck, P. Ghaemi, Y. S. Hor, and D. J. V. Harlingen, Phys. Rev. B **90**, 014501 (2014).

[125] J. D. Sau, R. M. Lutchyn, S. Tewari, and S. D. Sarma, Phys. Rev. Lett. **104**, 040502 (2010).

[126] J. Alicea, Phys. Rev. B **81**, 125318 (2010).

[127] A. P. Higginbotham *et al.*, Nature Phys. **11**, 1017 (2015).

[128] B. M. Terhal, F. Hassler, and D. P. DiVincenzo, Phys. Rev. Lett. **108**, 260504 (2012).

[129] Z. Nussinov, G. Ortiz, and E. Cobanera, Phys. Rev. B **86**, 085415 (2012).

[130] C. K. Chiu, D. I. Pikulin, and M. Franz, Phys. Rev. B **91**, 165402 (2015).

[131] D. S. Wang, A. G. Fowler, and L. C. L. Hollenberg, Phys. Rev. A **83**, 020302(R) (2011).

[132] D. S. Wang, A. G. Fowler, A. M. Stephens, and L. C. L. Hollenberg, Quant. Inf. Comput. **10**, 456 (2010).

[133] F. Hassler, A. R. Akhmerov, and C. W. J. Beenakker, New Journal of Physics **13**, 095004 (2011).

[134] L. Sun *et al.*, Phys. Rev. Lett. **108**, 230509 (2012).

[135] A. G. Fowler, Quantum Information & Computation **12**, 970 (2012).

[136] J. Edmonds, Canad. J. Math **17**, 449 (1965).

[137] A. G. Fowler, A. C. Whiteside, and L. C. L. Hollenberg, Phys. Rev. Lett. **108**, 180501 (2012).

[138] L. Jiang, C. L. Kane, and J. Preskill, Phys. Rev. Lett. **106**, 130504 (2011).

[139] H.-H. Sun *et al.*, Phys. Rev. Lett. **116**, 257003 (2016).

[140] J. Alicea, Y. Oreg, G. Refael, F. von Oppen, and M. P. A. Fisher, Nature Phys. **7**, 412 (2011).

[141] D. Aasen *et al.*, Phys. Rev. X **6**, 031016 (2016).

[142] F. L. Pedrocchi and D. P. DiVincenzo, Phys. Rev. Lett. **115**, 120402 (2015).

[143] J. D. Sau, D. J. Clarke, and S. Tewari, Phys. Rev. B **84**, 094505 (2011).

[144] T. Karzig, F. Pientka, G. Refael, and F. von Oppen, Phys. Rev. B **91**, 201102(R) (2015).

[145] M. A. Nielsen, Physics Letters A **308**, 2 (2003).

[146] P. Bonderson, M. Freedman, and C. Nayak, Phys. Rev. Lett. **101**, 010501 (2008).

[147] S. M. Albrecht *et al.*, Nature **531**, 206 (2016).

[148] B. van Heck, R. M. Lutchyn, and L. I. Glazman, Phys. Rev. B **93**, 235431 (2016).

[149] C. M. Marcus, private communication.

[150] V. Khemani, R. Nandkishore, and S. Sondhi, Nat. Phys. **11**, 560 (2015).

[151] A. Prem, J. Haah, and R. Nandkishore, Phys. Rev. B **95**, 3 (2017).

[152] F. L. Pedrocchi, N. E. Bonesteel, and D. P. DiVincenzo, Phys. Rev. B **92**, 115441 (2015).

[153] S. Plugge, A. Rasmussen, R. Egger, and K. Flensberg, (2016), 1609.01697.

[154] T. Karzig *et al.*, Phys. Rev. B **95**, 235305 (2017).

[155] L. A. Landau *et al.*, Phys. Rev. Lett. **116**, 050501 (2016).

[156] B. I. Halperin *et al.*, Phys. Rev. B **85**, 144501 (2012).

[157] S. Plugge *et al.*, Phys. Rev. B **94**, 174514 (2016).

[158] A. F. Andreev, JETP **22** (1966).

[159] L. Yu, Acta Phys Sin. **21**, 75 (1965).

[160] H. Shiba, Prog. Theor. Phys **40**, 435 (1968).

[161] A. I. Rusinov, Sov. J. Exp. Theor. Phys. Lett. **9**, 85 (1969).

[162] C. Janvier *et al.*, Science **349**, 1199 (2015).

[163] S. Bravyi and A. Kitaev, Annals of Physics **298**, 210 (2002).

[164] P. J. de Visser *et al.*, Phys. Rev. Lett. **112**, 047004 (2014).

[165] M. Zgirski *et al.*, Phys. Rev. Lett. **106**, 257003 (2011).

[166] S. M. Albrecht *et al.*, Phys. Rev. Lett. **118**, 137701 (2017).

[167] M. T. Deng *et al.*, Science **354**, 1557 (2016).

[168] S. Hoffman, C. Schrade, J. Klinovaja, and D. Loss, Phys. Rev. B **94**, 045316 (2016).

[169] S. Plugge, A. Rasmussen, R. Egger, and K. Flensberg, New J. Phys. **19**, 012001 (2017).

[170] D. Rainis and D. Loss, Phys. Rev. B **85**, 174533 (2012).

[171] D. Gottesman, *Stabilizer Codes and Quantum Error Correction*, PhD thesis, California Institute of Technology, 1997.

[172] F. J. MacWilliams and N. J. A. Sloane, *The Theory of Error-Correcting Codes* (North-Holland Publishing Company, 1977).

[173] A. R. Calderbank and P. W. Shor, Phys. Rev. A. **54**, 1098 (1996).

[174] P. W. Shor, Phys. Rev. A. **52**, R2493 (1995).

[175] D. Gottesman, Phys. Rev. A **54**, 1862 (1996), quant-ph/9604038.

[176] A. M. Steane, Phys. Rev. Lett. **77**, 793 (1996).

[177] S. Bravyi, B. Leemhuis, and B. Terhal, Ann. of Phys. **326**, 839 (2011).

[178] C. Chamon, Phys. Rev. Lett. **94**, 040402 (2005).

[179] B. Yoshida, Phys. Rev. B **88**, 125122 (2013).

[180] C. Castelnovo and C. Chamon, Philosophical Magazine **29**, 1 (2011).

[181] B. M. Terhal, Rev. Mod. Phys. **87**, 307 (2015).

[182] I. H. Kim and J. Haah, Phys. Rev. Lett. **116**, 027202 (2016).

[183] G. K. Savvidy and F. J. Wegner, Nucl. Phys. B **413**, 605 (1994).

[184] G. K. Savvidy and K. G. Savvidy, Physics Letters B **324**, 72 (1994).

[185] G. K. Savvidy and K. G. Savvidy, Modern Physics Letters A **11**, 1379 (1996).

[186] R. Pietig and F. J. Wegner, Nucl. Phys. B **525**, 549 (1998).

[187] A. Lipowski, D. Johnston, and D. Espriu, Phys. Rev. E **62**, 3404 (2000).

[188] P. Dimopoulos, D. Espriu, E. Jané, and A. Prats, Phys. Rev. E **66**, 056112 (2002).

[189] F. Wegner, J. Math Phys. **12**, 2259 (1971).

[190] C. D. Batista and Z. Nussinov, Phys. Rev. B **72**, 045137 (2005).

[191] Z. Nussinov and E. Fradkin, Phys. Rev. B **71**, 195120 (2005).

[192] A. E. Lipstein and R. A. Reid-Edwards, JHEP **09**, 034 (2014).

[193] D. A. Johnston, Phys. Rev. D **90**, 107701 (2014).

[194] D. Eisenbud, *Commutative algebra with a view toward algebraic geometry* (Springer-Verlag, 1994).

[195] D. A. Buchsbaum and D. Eisenbud, Journal of Algebra **25**, 259 (1973).

[196] S. Bravyi, M. Hastings, and S. Michalakis, J. Math. Phys. **51**, 093512 (2010).

[197] D. Williamson, Phys. Rev. B **94**, 155128 (2016).

[198] M. Pretko, Phys. Rev. B **95**, 115139 (2017).

[199] A. Hamma, P. Zanardi, and X.-G. Wen, Phys. Rev. B **72**, 035307 (2005).

[200] S. S. Bullock and G. K. Brennen, J. Phys. A **40**, 3481 (2007).

[201] F. Wilczek, Phys. Rev. Lett. **957**, 49 (1982).

[202] J. M. Leinaas and J. Myrheim, Nuovo Cimento B **37**, 1 (1977).

[203] N. Read, Physics Today **65** (2012).

[204] A. Stern, Nature **464**, 187 (2010).

[205] T. Lan, L. Kong, and X. g. Wen, (2016), 1602.05946.

[206] P. Deligne, Moscow Math. Journal **2**, 227 (2002).

[207] J. C. Y. Teo and C. L. Kane, Phys. Rev. Lett. **104**, 046401 (2010).

[208] C. Nayak, Nature **464**, 693 (2010).

[209] H. Ma, E. Lake, X. Chen, and M. Hermele, Phys. Rev. B **95**, 6 (2017).

[210] T. H. Hsieh and G. B. Halasz, Phys. Rev. B **96**, 5 (2017).

[211] B. Shi and Y.-M. Lu, (2017), 1705.09300.

[212] E. H. Lieb and D. W. Robinson, The finite group velocity of quantum spin systems, in *Statistical Mechanics*, pp. 425–431, Springer, 1972.

[213] H. Liu and S. J. Suh, Phys. Rev. Lett. **112**, 011601 (2014).

[214] M. Mezei and D. Stanford, (2016), 1608.05101.

[215] P. Hayden and J. Preskill, Journal of High Energy Physics **2007**, 120 (2007).

[216] Y. Sekino and L. Susskind, Journal of High Energy Physics **2008**, 065 (2008).

[217] W. Brown and O. Fawzi, (2012), 1210.6644.

[218] N. Lashkari, D. Stanford, M. Hastings, T. Osborne, and P. Hayden, Journal of High Energy Physics **2013**, 22 (2013).

[219] P. Hosur, X.-L. Qi, D. A. Roberts, and B. Yoshida, Journal of High Energy Physics **2016**, 4 (2016).

[220] R. Oliveira, O. C. O. Dahlsten, and M. B. Plenio, Phys. Rev. Lett. **98**, 130502 (2007).

[221] O. C. O. Dahlsten, R. Oliveira, and M. B. Plenio, Journal of Physics A: Mathematical and Theoretical **40**, 8081 (2007).

[222] M. Žnidarič, Phys. Rev. A **78**, 032324 (2008).

[223] F. G. S. L. Brandao, A. W. Harrow, and M. Horodecki, Commun. Math. Phys. **346**, 397 (2016), 1208.0692v2.

[224] S. H. Shenker and D. Stanford, Journal of High Energy Physics **2015**, 132 (2015).

[225] A. Larkin and Y. N. Ovchinnikov, Sov Phys JETP **28**, 1200 (1969).

[226] A. Kitaev, Hidden correlations in the hawking radiation and thermal noise, in *Talk given at the Fundamental Physics Prize Symposium*, 2014.

[227] S. H. Shenker and D. Stanford, Journal of High Energy Physics **2014**, 67 (2014).

[228] S. H. Shenker and D. Stanford, Journal of High Energy Physics **2014**, 46 (2014).

[229] J. Maldacena, S. H. Shenker, and D. Stanford, Journal of High Energy Physics **2016**, 106 (2016).

[230] I. L. Aleiner, L. Faoro, and L. B. Ioffe, Annals of Physics **375**, 378 (2016).

[231] D. Stanford, Journal of High Energy Physics **2016**, 9 (2016).

[232] A. A. Patel and S. Sachdev, Proceedings of the National Academy of Sciences **114**, 1844 (2017), http://www.pnas.org/content/114/8/1844.full.pdf.

[233] S. Banerjee and E. Altman, Phys. Rev. B **95**, 134302 (2017).

[234] Y. Gu, X.-L. Qi, and D. Stanford, (2016), 1609.07832.

[235] D. A. Roberts and B. Swingle, Phys. Rev. Lett. **117**, 091602 (2016).

[236] D. Chowdhury and B. Swingle, (2017), 1703.02545.

[237] A. A. Patel, D. Chowdhury, S. Sachdev, and B. Swingle, (2017), 1703.07353.

[238] B. Swingle and D. Chowdhury, Physical Review B **95**, 060201 (2017).

[239] A. Nahum, J. Ruhman, and D. Huse, 1705.10364.

[240] Y. Huang, Y.-L. Zhang, and X. Chen, Annalen der Physik (2016).

[241] Y. Chen, (2016), 1608.02765.

[242] R.-Q. He and Z.-Y. Lu, Physical Review B **95**, 054201 (2017).

[243] R. Fan, P. Zhang, H. Shen, and H. Zhai, Science Bulletin (2017).

[244] A. Chapman and A. Miyake, (2017), 1704.04405.

[245] D. A. Roberts and D. Stanford, Physical review letters **115**, 131603 (2015).

[246] B. Dóra and R. Moessner, (2016), 1612.00614.

[247] A. Bohrdt, C. Mendl, M. Endres, and M. Knap, (2016), 1612.02434.

[248] D. J. Luitz and Y. B. Lev, (2017), 1702.03929.

[249] E. Leviatan, F. Pollmann, J. H. Bardarson, and E. Altman, (2017), 1702.08894.

[250] G. Zhu, M. Hafezi, and T. Grover, Physical Review A **94**, 062329 (2016).

[251] B. Swingle, G. Bentsen, M. Schleier-Smith, and P. Hayden, Phys. Rev. A **94**, 040302 (2016).

[252] N. Y. Yao *et al.*, (2016), 1607.01801.

[253] M. Gärttner *et al.*, (2016), 1608.08938.

[254] J. Li *et al.*, (2016), 1609.01246.

[255] K. X. Wei, C. Ramanathan, and P. Cappellaro, (2016), 1612.05249.

[256] D. A. Roberts, D. Stanford, and L. Susskind, Journal of High Energy Physics **2015**, 51 (2015).

[257] A. Pagnani and G. Parisi, Physical Review E **92**, 010101 (2015).

[258] K. Johansson, Comm. Math. Phys. **209**, 437 (2000).

[259] M. Prähofer and H. Spohn, Phys. Rev. Lett. **84**, 4882 (2000).

[260] P. Calabrese, P. L. Doussal, and A. Rosso, EPL (Europhysics Letters) **90**, 20002 (2010).

[261] V. Dotsenko, EPL (Europhysics Letters) **90**, 20003 (2010).

[262] T. Sasamoto and H. Spohn, Phys. Rev. Lett. **104**, 230602 (2010).

[263] T. Sasamoto and H. Spohn, Nuclear Physics B **834**, 523 (2010).

[264] T. Sasamoto and H. Spohn, Journal of Statistical Physics **140**, 209 (2010).

[265] G. Amir, I. Corwin, and J. Quastel, Communications on Pure and Applied Mathematics **64**, 466 (2011).

[266] P. Calabrese and P. Le Doussal, Phys. Rev. Lett. **106**, 250603 (2011).

[267] S. Prolhac and H. Spohn, Phys. Rev. E **84**, 011119 (2011).

[268] P. L. Doussal and P. Calabrese, Journal of Statistical Mechanics: Theory and Experiment **2012**, P06001 (2012).

[269] T. Imamura and T. Sasamoto, Phys. Rev. Lett. **108**, 190603 (2012).

[270] T. Imamura and T. Sasamoto, Journal of Statistical Physics **150**, 908 (2013).

[271] D. Gottesman, (1998), quant-ph/9807006.

[272] J. Gütschow, S. Uphoff, R. F. Werner, and Z. Zimborás, J. Math. Phys. **51**, 015203 (2010).

[273] D. P. DiVincenzo, D. W. Leung, and B. M. Terhal, IEEE Trans. Inf Theory **48**, 580 (2002), quant-ph/0103098v1.

[274] P. Hayden *et al.*, Journal of High Energy Physics **11**, 9 (2016), 1601.01694.

[275] A. Hamma, S. Santra, and P. Zanardi, (2011), 1109.4391v4.

[276] A. Hamma, S. Santra, and P. Zanardi, (2012), 1204.0288v3.

[277] P. Zanardi, (2013), 1303.2832v4.

[278] L. Saul, M. Kardar, and N. Read, Physical Review A **45**, 8859 (1992).

[279] C. A. Tracy and H. Widom, Communications in Mathematical Physics **159**, 151 (1994).

[280] P. Forrester, Nuclear Physics B **402**, 709 (1993).

[281] M. Eden, A two-dimensional growth process, in *Proceedings of the Fourth Berkeley Symposium on Mathematical Statistics and Probability, Volume 4: Contributions to Biology and Problems of Medicine*, pp. 223–239, Berkeley, Calif., 1961, University of California Press.

[282] A.-L. Barabási and H. E. Stanley, *Fractal concepts in surface growth* (Cambridge university press, 1995).

[283] D. Richardson, Random growth in a tessellation, in *Mathematical Proceedings of the Cambridge Philosophical Society* Vol. 74, pp. 515–528, Cambridge Univ Press, 1973.

[284] R. Durrett and T. M. Liggett, The Annals of Probability , 186 (1981).

[285] R. Savit and R. Ziff, Phys. Rev. Lett. **55**, 2515 (1985).

[286] J. Kertész and D. E. Wolf, Physical review letters **62**, 2571 (1989).

[287] J. Krug, J. Kertész, and D. Wolf, EPL (Europhysics Letters) **12**, 113 (1990).

[288] T. Sasamoto and H. Spohn, Journal of Statistical Mechanics: Theory and Experiment **2010**, P11013 (2010).

[289] T. Kriecherbauer and J. Krug, Journal of Physics A: Mathematical and Theoretical **43**, 403001 (2010).

[290] I. Corwin, Random Matrices: Theory and Applications **01**, 1130001 (2012).

[291] T. Halpin-Healy and K. A. Takeuchi, Journal of Statistical Physics **160**, 794 (2015).

[292] K. A. Takeuchi, M. Sano, T. Sasamoto, and H. Spohn, Scientific Reports **1**, 34 EP (2011).

[293] K. A. Takeuchi and M. Sano, Journal of Statistical Physics **147**, 853 (2012).

[294] P. Deift, A. Its, and I. Krasovsky, Communications in Mathematical Physics **278**, 643 (2008).

[295] J. Baik, R. Buckingham, and J. DiFranco, Communications in Mathematical Physics **280**, 463 (2008).

[296] P. Freche, D. Stauffer, and H. E. Stanley, Journal of Physics A: Mathematical and General **18**, L1163 (1985).

[297] R. Hirsch and D. E. Wolf, Journal of Physics A: Mathematical and General **19**, L251 (1986).

[298] P. Meakin, Phys. Rev. A **38**, 418 (1988).

[299] D. E. Wolf, Journal of Physics A: Mathematical and General **20**, 1251 (1987).

[300] J. Krug, H. Spohn, and C. Godrèche, Solids far from equilibrium (1991).

[301] J. Krug and H. Spohn, Phys. Rev. A **38**, 4271 (1988).

[302] T. Prosen, Journal of Physics A: Mathematical and Theoretical **40**, 7881 (2007).

[303] T. Prosen and I. Pižorn, Phys. Rev. A **76**, 032316 (2007).

[304] C. Jonay, D. A. Huse, and A. Nahum, (In preparation) .

[305] M. B. Hastings, 0706.0556v1.

[306] P. Zanardi, C. Zalka, and L. Faoro, Phys. Rev. A **62**, 030301 (2000), quant-ph/0005031v1.

[307] J. Cardy *Scaling and Renormalization in Statistical Physics* Vol. 5 (Cambridge University Press, 1996).

[308] T. Halpin-Healy and Y.-C. Zhang, Physics Reports **254**, 215 (1995).

[309] D. A. Huse and C. L. Henley, Phys. Rev. Lett. **54**, 2708 (1985).

[310] D. Forster, D. R. Nelson, and M. J. Stephen, Phys. Rev. A **16**, 732 (1977).

[311] J. Baik, P. Deift, and K. Johansson, Journal of the American Mathematical Society **12**, 1119 (1999).

[312] C. A. Tracy and H. Widom, Probability Theory and Related Fields **119**, 350 (2001).

[313] M. Kardar, G. Parisi, and Y.-C. Zhang, Phys. Rev. Lett. **56**, 889 (1986).

[314] D. A. Huse, C. L. Henley, and D. S. Fisher, Phys. Rev. Lett. **55**, 2924 (1985).

[315] T. Halpin-Healy, Phys. Rev. E **58**, R4096 (1998).

[316] S. Ryu and T. Takayanagi, Phys. Rev. Lett. **96**, 181602 (2006).

[317] B. Swingle, Phys. Rev. D **86**, 065007 (2012).

[318] F. Pastawski, B. Yoshida, D. Harlow, and J. Preskill, Journal of High Energy Physics **2015**, 1 (2015).

[319] O. C. O. Dahlsten, R. Oliveira, and M. B. Plenio, Journal of Physics A: Mathematical and Theoretical **40**, 8081 (2007).

[320] M. Žnidarič, Phys. Rev. A **78**, 032324 (2008).

[321] D. N. Page, Phys. Rev. Lett. **71**, 1291 (1993).

[322] C. Nadal, S. N. Majumdar, and M. Vergassola, Journal of Statistical Physics **142**, 403 (2011).

[323] D. Perez-Garcia, F. Verstraete, M. M. Wolf, and J. I. Cirac, Quantum Info. Comput. **7**, 401 (2007).

[324] C. Chamon and E. R. Mucciolo, Phys. Rev. Lett. **109**, 030503 (2012).

[325] P. Meakin, P. Ramanlal, L. M. Sander, and R. C. Ball, Phys. Rev. A **34**, 5091 (1986).

[326] J. M. Kim and J. M. Kosterlitz, Phys. Rev. Lett. **62**, 2289 (1989).

[327] In preparation .

[328] G. Evenbly and G. Vidal, Journal of Statistical Physics **145**, 891 (2011).

[329] M. Kardar, Phys. Rev. Lett. **55**, 2923 (1985).

[330] M. Kardar, *Statistical Physics of Fields* (Cambridge University Press, 2007).

[331] D. A. Roberts and L. S. D. Stanford, Journal of High Energy Physics **2015**, 1 (2015).

[332] E. H. Lieb and D. W. Robinson, *The Finite Group Velocity of Quantum Spin Systems* (Springer Berlin Heidelberg, Berlin, Heidelberg, 2004), pp. 425–431.

[333] A. Hamma, R. Ionicioiu, and P. Zanardi, Phys. Rev. A **71**, 022315 (2005).

[334] A. Hamma, R. Ionicioiua, and P. Zanardi, Physics Letters A **337**, 22 (2005).

[335] O. C. O. Dahlsten and M. B. Plenio, Quant. Inf. Comp. **6**, 527 (2006).

[336] ITensor, http://itensor.org.

[337] T. Nattermann, Journal of Physics C: Solid State Physics **18**, 6661 (1985).

[338] M. Kardar, Journal of Applied Physics **61**, 3601 (1987).

[339] D. S. Fisher, Phys. Rev. Lett. **56**, 1964 (1986).

[340] A. A. Middleton, Phys. Rev. E **52**, R3337 (1995).

[341] F. D. M. Haldane, J. Phys. C **14**, 2585 (1981).

[342] F. D. M. Haldane, Phys. Rev. Lett **47**, 1840 (1981).

[343] C. L. Kane and M. P. A. Fisher, Phys. Rev. Lett. **68**, 1220 (1992).

[344] C. L. Kane and M. P. A. Fisher, Phys. Rev. B **46**, 15233 (1992).

[345] S. Elitzur, R. B. Pearson, and J. Shigemitsu, Phys. Rev. D **19**, 3698 (1979).

[346] A. Ukawa, P. Windey, and A. H. Guth, Phys Rev. D **21**, 1013 (1980).

[347] M. Creutz, L. Jacobs, and C. Rebbi, Phys. Rev. Lett. **42**, 1390 (1979).

[348] B. Svetitsky and L. G. Yaffe, Nucl. Phys. B **210**, 423 (1982).

[349] J. V. José, L. P. Kadanoff, S. Kirkpatrick, and D. R. Nelson, Phys. Rev. B **16**, 1217 (1977).

[350] A. Casher, Nucl. Phys. B **151**, 353 (1979).

[351] G. t'Hooft, Nucl. Phys. B **138**, 1 (1978).

[352] J. Jersák, C. B. Lang, and T. Neuhaus, Phys. Rev. Lett. **77**, 1933 (1996).

[353] J. Jersák, T. Neuhaus, and H. Pfeiffer, Phys. Rev. D **60**, 054502 (1999).

[354] H. G. Evertz, T. Jersak, T. Neuhaus, and P. M. Zerwas, Nucl. Phys. B **251**, 279 (1985).

[355] G. Arnold, B. Bunk, T. Lippert, and K. Schilling, Nucl. Phys. B **119**, 864 (2003).

[356] A. Rasmussen, Y.-Z. You, and C. Xu, (2016), 1601.08235.

[357] D. Rokhsar and S. Kivelson, Phys. Rev. Lett. **61**, 2376 (1988).

[358] E. Ardonne, P. Fendley, and E. Fradkin, Ann. of Phys. **310**, 493 (2004).

[359] C. L. Henley, J. Phys. C **16**, S891 (2004).

[360] C. Castelnovo, C. Chamon, and D. Sherrington, Phys. Rev. B **81**, 184303 (2010).

[361] C. Castelnovo, C. Chamon, C. Mudry, and P. Pujol, Ann. of Phys. **318**, 216 (2005).

[362] C. Castelnovo and C. Chamon, Phys. Rev. B **77**, 054433 (2008).

[363] D. A. Johnston and R. P. K. C. M. Ranasinghe, J. Phys A: Math. Theor. 44, 295004 (2011).

[364] D. A. Johnston and R. P. K. C. M. Ranasinghe, (2011), 1106.0325.

[365] A. R. Calderbank, E. M. Rains, P. W. Shor, and N. J. A. Sloane, Phys. Rev. Lett. **78**, 405 (1997), quant-ph/9605005.

[366] A. Klappenecker and M. Rotteler, IEEE Transactions on Information Theory **48**, 2396 (2002).

[367] N. Linden, F. Matus, M. B. Ruskai, and A. Winter, The Quantum Entropy Cone of Stabiliser States, in *8th Conference on the Theory of Quantum Computation, Communication and Cryptography (TQC 2013)*, edited by S. Severini and F. Brandao, , Leibniz International Proceedings in Informatics (LIPIcs) Vol. 22, pp. 270–284, Dagstuhl, Germany, 2013, Schloss Dagstuhl–Leibniz-Zentrum fuer Informatik, 1302.5453.

[368] G. Roósz, R. Juhász, and F. Iglói, Phys. Rev. B **93**, 134305 (2016).

[369] L. Saul, M. Kardar, and N. Read, Phys. Rev. A **45**, 8859 (1992).

[370] I. Peschel, Journal of Physics A: Mathematical and General **36**, L205 (2003).

[371] T. Halpin-Healy, Phys. Rev. A **42**, 711 (1990).